# A-7 Strut Braced Wing Concept
# Transonic Wing Design

by
Andy Ko, William H. Mason,
B. Grossman and J.A. Schetz

VPI-AOE-275
July 12, 2002

Prepared for:
National Aeronautics and Space Administration
Langley Research Center

Contract No.: NASA PO #L-14266

Covering the period June 3, 2001– Nov. 30, 2001

Multidisciplinary Analysis and Design Center for Advanced Vehicles
Department of Aerospace and Ocean Engineering
Virginia Polytechnic Institute and State University
Blacksburg, VA 24061

## Executive Summary

The Multidisciplinary Analysis and Design (MAD) Center at Virginia Tech has investigated the strut-braced wing (SBW) design concept for the last 5 years. Studies found that the SBW configuration showed savings in takeoff gross weight of up to 19%, and savings in fuel weight of up to 25% compared to a similarly designed cantilever wing transport aircraft. In our work we assumed that computational fluid dynamics (CFD) would be used to achieve the target aerodynamic performance levels. No detailed CFD design of the wing was done.

In this study, we used CFD to do the aerodynamic design for a proposed SBW demonstration using a re-winged A7 aircraft. The goal was to design a standard constant isobar transonic cruise wing, together with the strut. The wing/pylon/strut junction would be an integral part of the aerodynamic design. We did this work in consultation with NASA Langley Configuration Aerodynamics branch members through a weekly teleconference, using PDF files to allow them to visualize the progress. They provided us with the codes required to do the work, although one of the codes assumed to be available was not.

We selected a high aspect ratio (AR=11.4) planform previously studied, and appropriate for the A-7, but with a modification to the strut sweep (reduction from 19.4$^{o}$ to 4.1$^{o}$) to avoid the landing gear bay.

A suite of two-dimensional (2-D) and three-dimensional (3-D) CFD software was used in this project. We used MSES, a code developed at the MIT Computational Aerospace Sciences Laboratories for the 2-D analysis and design work. For the 3-D

analysis and design tasks, we had initially planned to use FPS3D, a viscous analysis and design code written by Dave Kinney at NASA Ames. However, it was not available, and therefore at NASA's suggestion, we used FELISA, an inviscid analysis code, and RAM (Rapid Aircraft Modeler) as the geometric modeler. Both were developed by NASA. Other support software was developed in-house. Also, we collaborated with Andy Hahn at NASA Ames, who helped us translate complex RAM geometries for use with FELISA.

Two primary tasks were conducted in parallel. The first was the design of the 2-D airfoil sections at various spanwise stations. The other task was the 3-D wing design, with the design of the wing/pylon/strut intersection the most critical aspect of this task.

In the 2-D tasks, airfoils for four different spanwise sections were designed. This was done starting with a NASA supercritical airfoil design and modifying its shape by adding or subtracting a sixth-order polynomial thickness distribution to improve the airfoil performance at the required design conditions. Table A provides a summary of the airfoil design requirements that were used. Off- design performances of the airfoils were also considered in the design process. Simple sweep theory was used to translate the 2-D airfoil into sections that can be used in a 3-D wing.

Table A: Table of the 3- and 2-dimension requirements of the airfoil at the wing spanwise station candidates.

| **Station** | **η** | **three-dimensional** | | | **two-dimensional** | | |
|---|---|---|---|---|---|---|---|
| | | **M** | $C_l$ | **t/c** | **M** | $C_l$ | **t/c** |
| **Root** | 0.00 | 0.85 | 0.434 | 0.133 | 0.757 | 0.547 | 0.1490 |
| **Break** | 0.67 | 0.85 | 0.742 | 0.062 | 0.757 | 0.935 | 0.0696 |
| **Max $C_l$** | 0.80 | 0.85 | 0.753 | 0.065 | 0.757 | 0.948 | 0.0730 |
| **Tip** | 1.00 | 0.85 | 0.000 | 0.075 | 0.757 | 0.000 | 0.0842 |

For the 3-D wing design, an inviscid CFD analysis of a preliminary A7 SBW wing geometry together with the fuselage was done to identify key design issues. The twist distribution for this geometry was obtained from a linear theory solution. After initial full configuration analysis, to reduce the design cycle time, design modifications were made to a geometry that did not include the fuselage. First, modifications to the wing twist were made to create a more nearly constant isobar wing.

Much work was done in the area of the wing/pylon/strut intersection to reduce drag. Prior to detailed aerodynamic design, CFD inviscid analysis indicated that a strong shock occurred in the wing/strut/pylon area, causing large interference drag. Parametric studies involving the change of the pylon toe, strut incidence and strut twist were done to understand the effects of these changes on the flow characteristics at the intersection. The effect of the presence of the pylon was also investigated. We observed that the wing/strut/pylon intersection was behaving like a 2-D nozzle, choking the flow at a minimum area point and expanding the flow downstream with the expansion terminating in a strong shock near the trailing edge of the strut. A solution to this problem was devised by flattening the upper surface of the strut near the wing/pylon/strut intersection, which effectively reduced the shock strength and in some cases eliminated it. Thus the interference drag at the wing/pylon/strut intersection was reduced significantly and possibly can be eliminated with additional aerodynamic design.

In this study, we identified the key issues and resolved them for the transonic design of the A7 SBW demonstrator aircraft wing. The main achievement was the elimination of the shock at the wing/pylon/strut intersection, which reduced the intersection drag at that section. New airfoils, modified from various NASA supercritical airfoils, were designed for the require lift and thickness of the SBW demonstrator. Additional work using complete viscous analysis is required for the wing twist, especially in the presence of the strut, to finalize the constant isobar wing. Viscous analysis is also required to design the tip airfoil section of the strut. Although inviscid analysis has allowed us to define the majority of the design, a viscous analysis and design capability is needed to complete the work.

# Table of Contents

## Nomenclature

| | |
|---|---|
| $C_l$ | two-dminesional lift coefficient |
| $C_L$ | three-dimensional wing lift coefficient |
| e | Oswald's span efficiency factor |
| $L/D$ | Lift to Drag ratio |
| M | Mach number |
| Re | Reynolds number |
| $t/c$ | Thickness to chord ratio |
| $x/c$ | position of wing relative to the chord of the wing |
| $\alpha$ | angle of attack |
| $\Lambda$ | Wing reference sweep |
| $\Lambda_{\mathrm{LE}}$ | Wing leading edge sweep |
| $\eta$ | Normalized wing spanwise position. |

## List of Figures

## List of Tables

# Acknowledgments

We would like to acknowledge several people for their direct and indirect contribution to this project:

- Dick Campbell and Francis Capone at NASA Langley for their invaluable insight they provide during the weekly teleconference and also for their help in obtaining the necessary software needed for this project.
- Andrew Parker for his help in designing the airfoil sections.
- Andrew Hahn from NASA Ames for his help in modeling the geometry and creating the grid for the A-7 geometry and his insight into using RAM.
- Dan McCormick for his help in modeling the A7 aircraft geometry.
- Karen L. Bibb from NASA Langley for her help and technical insight on using the FELISA system.
- Dr. M. Drela at MIT for allowing us to use MSES.

## 1. Introduction

The strut-braced wing (SBW) design concept has been implemented today in many general aviation aircraft designs. However, the SBW concept has never been used on a transonic passenger transport aircraft. However, this is not an entirely new idea. Werner Pfenniger at Northrop first proposed this idea in the early 1950's [1]. Later, other SBW aircraft investigations followed, notably Kulfan et al. [2], Park [3] and Turriziani et al. [4]. In the last 5 years, the Multidisciplinary Analysis and Design (MAD) Center at Virginia Tech, under the support of the NASA Langley Research Center has used Multidisciplinary Design Optimization (MDO) to extensively investigate the SBW concept on transonic passenger transport aircraft. Early in this investigation, Grasmeyer et al. [5],[6],[7] found that the SBW configuration allowed for a wing with higher aspect ratio and decreased wing thickness without any increase in wing weight relative to its cantilevered wing counterpart. The SBW configuration also has a lower wing sweep, allowing the wing to achieve natural laminar flow without incurring a penalty in wave drag. It was shown that the best SBW configuration had a 15% savings in takeoff gross weight (TOGW), 29% savings in fuel weight and a 28% increase in $L/D$ compared to its cantilevered wing counterpart. Later, Lockheed Martin Aeronautical Systems (LMAS) did an industry evaluation of the work by the MAD Center. Refinements were made to the MDO code during this time, and it was found that a fuselage mounted engines SBW configuration showed a 9% savings in TOGW over a similarly designed cantilever wing aircraft design [8]. Further refinements were made, improving the optimization architecture [9], and wing structural weight prediction method [10]. Optimization results indicated that a wing-mounted engines SBW configuration had savings in TOGW of up to 19% and fuel weight savings of almost 25% over a similarly designed cantilever wing aircraft design [9]. Figure 1 shows the general layout of the different configurations considered in this study. However, no detailed aerodynamic transonic wing design was done in these studies.

In 1999, we had proposed a demonstration of the SBW concept through the RevCon (Revolutionary Concepts) program funded by NASA. This proposal [11] was in partnership with LMAS and the NASA Langley Research Center. We proposed that the concept be demonstrated through the flight testing of a re-winged A7 aircraft using the SBW design. This demonstrator aircraft would be used to prove the aerodynamic and structural feasibility of the design. It would also be used to test the innovative strut design that would take loads only in tension. Figure 2 shows the proposed A7 SBW demonstrator aircraft concept. However, this proposal was not funded.

In 2000, a Virginia Tech senior class aerospace design team (Team RevCon) conceptually designed the aforementioned A-7 demonstrator aircraft [12]. Figure 3 shows a model of their design. In their design, the forward and aft fuselage fuel tanks would be augmented with a 450-gallon fuel cell, replacing the cannon and ammunition drum.

In all the Virginia Tech SBW designs that were made previously, we had assumed that Computational Fluid Dynamics (CFD) would be used for the detailed aerodynamic design and that it would be possible to achieve the target aerodynamic performance levels. Some CFD analysis to investigate the wing-strut interference drag of the model SBW configuration was done by Tetrault [13] in 2000. Information on wing-strut drag was obtained in this investigation although no detailed design was performed. To eliminate the question of potential aerodynamic problems with a transonic SBW design (for example, the high interference drag at the wing/pylon/strut juncture), NASA Langley tasked Virginia Tech to perform a detailed aerodynamic wing design for the A-7 demonstrator aircraft in preparation of the next round of REVCON concept selections. The final design would be a standard constant isobar transonic cruise wing, together with the strut. The wing/pylon/strut junction would also be included as an integral part in the design. The next phase of the REVCON program never materialized.

## *1.1. Design Approach*

The task order for the project required us to design a standard constant isobar transonic cruise wing and strut for the A7 RevCon SBW demonstrator aircraft. Many variations on the SBW concept had been studied previously, and the first task was to select the appropriate wing planform to use for the detailed design. This wing would be scaled appropriately to allow it to be placed on the fuselage of the A7 aircraft at a position where it would have minimal effect on the original stability of the aircraft. Issues of strut placement on the fuselage would also be considered.

Since the wing has a high aspect ratio, airfoil design would play an important role in the design. In addition, the appropriate analysis and design software had to be selected, evaluated and verified. Support software not available would be developed in-house. Selection of a baseline airfoil would be followed by modification to meet the specific requirements for this design. After the airfoil section was designed and placed in the wing, the analysis and design of the wing itself was required, taking into account the effects of the pylon and strut. The design of the wing/pylon/strut intersection is the most critical aspect of this work. The effect of the fuselage would also have to be taken into account.

Some of these tasks were done in parallel. For example, some of the airfoil design work was being done at the same time that some initial three-dimensional wing analyses were performed.

During the course of the project, we held weekly meetings with NASA Langley (Dick Campbell and Francis Capone primarily) via teleconferencing. These meetings proved invaluable as they provided us with insight into the design problem and also assisted us in selecting and obtaining necessary analysis and design software. However, even with help from NASA Langley, we encountered problems obtaining the appropriate software. Although we were originally going to use the FPS3D software developed by Dave Kinney from NASA Ames, it was unavailable. Thus this study was done primarily with a viscous 2D code (MSES) and an inviscid 3D code (FELISA).

## 2. Choosing the demonstrator wing

Wing data from different SBW aircraft designs were collected and tabulated to help in the selection of a suitable wing design for the SBW A-7 concept demonstrator. Table 1 shows this table of wing data. Based on the comparison, it was decided that the wing-mounted engines SBW design (Grasmeyer's mission [5],[6],[7]) was the most appropriate for this application. This is due to its high TOGW savings, low wing sweep and relatively high aspect ratio compared to a similarly designed cantilever aircraft. The wing was then scaled for the A-7, maintaining the aspect ratio, taper ratio, thickness to chord ratios, wing sweep and wing loading. By keeping the wing loading constant at 120 lb/ft$^2$, the scaled wing area for the demonstrator aircraft was calculated to be 270.8 ft$^2$. The wing chords, wing span and wing thickness were then computed.

The placement of the wing was then addressed. Critical factors in the placement of the wing were the static stability and the strut/fuselage junction relation to the landing gear bay. We wanted to place the wing at a location such that the static stability of the aircraft would be similar to the original A7 aircraft (see Appendix A). We found that if the wing was placed in a position to give a static stability of 9-10%, the strut/fuselage intersection coincided with the landing gear bay. Therefore, to solve this problem, the strut sweep was decreased to allow its attachment aft of the landing gear bay. The strut sweep was reduced from 19.4° to 4.1°. Figure 4 shows the final dimensions of the wing and strut of the A7 demonstrator aircraft. An analysis of the effect of the reduced strut sweep on the original SBW aircraft showed only a 900 lbs (0.2%) reduction in TOGW, but with minor violations in the constraints (Range was reduced from 7300 nmi to 7230 nmi and the upper slack load factor increased from 0.8 to 0.86).

Figure 5 gives the $C_l$ distribution for the selected SBW aircraft wing. We see that the maximum section $C_l$ occurs at a distance of about 80% span from the root. This position is not very far from the wing/strut intersection (which is at 67% span from the root).

Early in the project, there were concerns that the wing would be too thin to manufacture. Therefore, the thickness distribution of the A-7 demonstrator wing was also obtained, shown in Figure 6. The strut is 1.5 inches thick, while the wing thickness at the tip (where it is the least) is 1.8 inches.

Table 1: Table of wing data from different SBW designs and configurations

|  |  | LMAS Mission |  |  | Grasmeyer's Mission |  |  |  |
|---|---|---|---|---|---|---|---|---|
|  | **8300 nmi Wing Mounted Engines SBW** | **Fuselage Mounted Engines SBW** | **Wing Mounted Engines SBW** | **Tip Mounted Engines SBW** | **Fuselage Mounted Engines SBW** | **Wing Mounted Engines SBW** | **Tip Mounted Engines SBW** | **LMAS SBW Design** |
| % TOGW savings | 20.3 | 10 | 14.3 | 13.8 | 10.5 | 19 | 16.8 | 11.1? |
| TOGW (lbs) | 508021 | 546708 | 521023 | 523563 | 530469 | 480229 | 493006 | 504835 |
| Wing Half Span (ft) | 109.5 | 106.6 | 101.8 | 95.6 | 106.5 | 106.6 | 99 | 109.6 |
| 1/4 Chord Sweep (deg) | 27.4 | 32.1 | 31.5 | 32.1 | 29.5 | 27 | 29.8 | 31.2 |
| Wing Root Chord (ft) | 30.9 | 34.3 | 33 | 62.6 | 31.5 | 29.7 | 33.6 | 32.66 |
| Wing Mid Chord (ft) |  |  |  |  |  |  |  |  |
| Wing Tip Chord (ft) | 7.9 | 6.74 | 7.06 | 10.3 | 10 | 7.8 | 9.6 | 6.86 |
| Wing Centerline t/c | 0.132 | 0.14 | 0.14 | 0.15 | 0.137 | 0.133 | 0.149 | 0.1 (avg) |
| Wing Break t/c | 0.061 | 0.066 | 0.074 | 0.098 | 0.07 | 0.062 | 0.091 | 0.1 (avg) |
| Wing Tip t/c | 0.091 | 0.078 | 0.076 | 0.076 | 0.075 | 0.075 | 0.097 | 0.1 (avg) |
| Wing Aspect Ratio | 11.27 | 10.39 | 10.17 | 8.92 | 10.3 | 11.4 | 9.16 | 11.1 |
| Position of Wing/Strut Intersection (% half-span) | 0.69 | 0.71 | 0.61 | 0.9 | 0.84 | 0.67 | 0.59 | 0.68 |
| 1/4 chord strut sweep (deg) | 21.5 | 20 | 20.4 | 30.4 | 12.6 | 19.4 | 24.3 | 19 |
| Strut Chord (ft) | 8.2 | 7.36 | 6.95 | 4.43 | 4.34 | 6.08 | 7.91 | 6.7 |
| Reference Area (ft2) | 4252.6 | 4369.6 | 4077.5 | 4102.3 | 4420.5 | 4001.9 | 4278.4 | 4333.6 |
| Cruise Lift Coefficient | 0.53 | 0.54 | 0.54 | 0.55 | 0.47 | 0.53 | 0.52 | 0.55 |

Although the wing will be relatively thin, after discussion with NASA Langley, it was determined that the wing was not too thin to manufacture. To compare, Figure 7 shows the *t/c* ratio distribution of the A7 demonstrator aircraft wing obtained from the MDO results. Notice that although the *t/c* ratio at the tip is greater than the *t/c* ratio at the wing break station, the thickness at the tip is smaller than that at the wing break station.

Table 2 below also gives a summary of the scaled SBW wing for the demonstrator aircraft.

Table 2: Summary of the dimensions of the wing for the A7 SBW demonstrator aircraft.

| | **A7 demonstrator wing** |
|---|---|
| **Wing Root chord** | 7.72 ft |
| **Wing Tip chord** | 2.03 ft |
| **Wing Root *t/c*** | 0.133 |
| **Wing Break *t/c*** | 0.062 |
| **Wing Tip *t/c*** | 0.075 |
| **Wing $\Lambda_{LE}$** | 29.28° |
| **Wing Break $\eta$** | 0.67 |
| **Wing Area** | 270.8 $ft^2$ |
| **Wing Span** | 55.57 ft |
| **Wing Taper Ratio** | 0.262 |
| **Wing Aspect Ratio** | 11.4 |
| **Strut Chord** | 1.58 |
| **Strut *t/c*** | 0.08 |
| **Strut $\Lambda_{LE}$** | 4.1° |
| **Strut Span** | 18.62 ft |

# 3. Software

This section describes the software we used. Most of the programs were obtained from NASA. Some of these programs were used independently while others were used concurrently, with the data from one program used as input in another. In addition to previously existing programs, we developed our own software to do tasks such as data translation and post processing. Some of the programs are scripts that automate tasks between the use of two or more programs. This approach helped us reduce the design cycle time. We made sure that we did software verification of the codes. This process also allowed us to learn how to use the programs.

## *3.1. Description of software used*

### 3.1.1. VLM4997 and JKayVLM

VLM4997 is a vortex lattice program written by John Lamar at NASA Langley. This program, written in FORTRAN, is designed to estimate the subsonic aerodynamic characteristics of up to four complex planforms using up to 400 panels. References [14] to [17] describe the theory and use of the program. JKayVLM is another FORTRAN vortex lattice program written by Jacob Kay at Virginia Tech. Reference [18] explains this program in detail. Both vortex lattice programs were used to estimate static margin and stability derivatives to be used to verify Team RevCon's design [12].

### 3.1.2. Lamdes

Lamdes, short for the Lamar design program, uses a vortex lattice method to find the spanload that minimizes the induced drag [19]. It has been modified to include pressure drag and to include a spanload as input to give the span efficiency factor *e*, for multiple lifting non-planar surfaces including canards and winglets [20]. An associated camber distribution for subsonic flow can also be found.

### 3.1.3. Rapid Aircraft Modeler – RAM

The Rapid Aircraft Modeler, or RAM, was developed for the Systems Analysis Branch at NASA Ames. As the name suggests, it is a CAD tool that can be used to create three-dimensional objects of complete aircraft or aircraft systems. Since it is designed to create aircraft geometries, objects such as wings, tails, the fuselage and cockpit can be easily created. It also provides for the creation of flaps and slats, including control surfaces. Wing twist and dihedral can also be incorporated easily. Although RAM has only a small library of airfoils, it has provision for use of custom designed airfoils via an input file. Currently, RAM does not export to the IGES file format, and therefore an external translator is needed for this purpose. RAM runs on any UNIX workstation with OpenGL support.

### 3.1.4. FLO36

FLO36 is Jameson's transonic potential flow airfoil analysis code. It uses ADI and multigrid to provide very fast computing times. The boundary conditions are satisfied exactly using conformal mapping. Because it is fast, it provides a quick and easy tool for transonic airfoil analysis. Reference [21] provides detailed information about FLO36.

### 3.1.5. MSES

MSES is a multi-element airfoil analysis and design system that was developed by Professor Mark Drela at the MIT Fluid Dynamics Research Laboratory. The following is a quote from the lab's summary of MSES's capabilities [22].

“MSES is a numerical airfoil development system. It includes capabilities to analyze, modify, and optimize single and multi-element airfoils for a wide range of Mach and Reynolds numbers. The range of validity includes low-Reynolds numbers and transonic Mach numbers. Flows with transitional separation bubbles, shock waves, trailing edge and shock-induced separation can be predicted. Surface pressure and aerodynamic force predictions are accurate just past stall. Transition can be forced or predicted as part of the flow calculation.

Airfoil design is accomplished by interactive specification of surface pressures, with the resultant airfoil geometry being computed. Analysis calculations may be performed at any time during the design process. Automated calculation of angle-of-attack and Mach number sweeps is provided. All analysis results may be displayed graphically.

An interactive optimization driver is provided. Optimization procedures center on the iterative minimization of drag or any relevant objective function over one or more operating points. Arbitrary geometry mode shapes associated with the geometric degrees of freedom can be prescribed.

The numerical formulation of MSES consists of a finite-volume discretization of the steady Euler equations on an intrinsic streamline grid. The boundary layers and trailing wakes are described by a two-equation integral formulation with lagged-dissipation closure. The inviscid and viscous regions are fully coupled via the displacement thickness. The airfoil surfaces admit a solid-body boundary condition in the direct analysis mode, and a prescribed pressure boundary condition in the inverse “design” mode. The overall system is solved using a full Newton method.”

### 3.1.6. FELISA

The FELISA system was written by J. Peiro from the Department of Aeronautics at Imperial College, London, K. Morgan at the Department of Civil Engineering at the University College of Swansea at Swansea, U.K. and J. Peraire from the Department of Aeronautics and Astronautics at MIT for NASA Langley. The following is a quote from the introduction section of the FELISA system manual that explains the FELISA system [23].

"The FELISA system provides a capability for generating and adapting unstructured tetrahedral meshes within three dimensional computational domains of general shape and for solving the equations of steady compressible inviscid flow on such meshes. It also provides tools for visualizing the computed flow solutions and the geometrical data employed"

The manual goes on to say about the mesh generation: "The tetrahedral mesh generation is accomplished by a procedure which is a variant of the advancing front method, in which both nodal points and tetrahedral elements are simultaneously created.

The starting point for the generation of the unstructured mesh for the three dimensional volume is the triangulation of the boundary surface of the computational domain. This surface is described mathematically in terms of the composite curves and surfaces, which are commonly employed in CAD systems. This triangulation of the boundary surface is accomplished by using a modified version of a two-dimensional advancing front method. The assembly of the resulting triangular faces forms the initial front for the tetrahedral generation process.

The triangular surface elements and the tetrahedral volume elements are generated according to a spatial distribution of local mesh size and stretching which is defined by the user."

In addition to this, the manual explains the flow solution section of the FELISA system. "The flow algorithm is developed by applying a Galerkin finite element method in space to obtain coupled sets of ordinary differential equations in time. The steady-state solution of this equation set is achieved by advancing the system using an explicit Runge-Kutta type marching scheme. Artificial viscosity, which is designed so as to maintain the second order accuracy of the method, is added to stabilize the solution. The convergence of this basic algorithm is further enhanced by the use of local time stepping and residual averaging."

Also bundled with the FELISA system is a suite of programs that can be used for post-processing, written by other FELISA users. All of the data obtained from FELISA was post-processed and visualized using Tecplot v8.0.

### 3.1.7. In-house developed software

As mentioned earlier, software was developed in-house to be used in addition to the other analysis codes obtained.

#### *3.1.7.1. Airfoil modification tools*

To help in the airfoil design for the A7 SBW wing, several simple programs were written in FORTRAN to perform certain modifications to the airfoil geometry based on an input airfoil geometry. All of the programs written can output to a format readable in MSES or in RAM.

The program *Scale* was written to scale the input airfoil to any specified user input *t/c* ratio. Multiplying the thickness coordinates of the original airfoil with an appropriate factor does this. It allows a designed airfoil to be scaled to any *t/c* ratio needed in the wing design. It also provides us with a tool with which we can observe the effects of airfoil thickness scaling.

The program *Bump* adds (or subtracts) a sixth order polynomial thickness distribution onto an airfoil surface. The user determines the position, amplitude and span at which this distribution is added to the airfoil. A description of this thickness distribution and its effects can be found in reference [24] and [25].

#### *3.1.7.2. Convert*

*Convert* is a program written in UNIX script language (*csh*) and FORTRAN. It is a translator program that takes the output from RAM and converts it to a geometry definition file that can be used by FELISA. *Convert* was written to translate only three different types of geometries that are created in RAM and therefore is not a 'robust' translation software between RAM and FELISA. The first two geometries that *Convert* can translate are wing-only geometries. The first geometry is the standard wing geometry created in RAM that consists of the wing lofted between the root and tip airfoil sections. The second geometry is the 'multi-wing' geometry, which is a wing-alone configuration that consists of two intermediate airfoil stations in between the root and tip airfoils. The wing is lofted between the airfoil stations. The third geometry that can be handled by *Convert* is a wing/pylon/strut configuration. The wing section is the 'multi-wing' geometry. A pylon intersects the bottom surface of the wing, and a strut intersects the pylon. A major hurdle in programming *Convert* to translate the wing/pylon/strut configuration is determining the intersection curves between the wing, pylon and strut. AutoCad is used to obtain the intersection curves. When a wing/pylon/strut geometry is made in RAM, an AutoCad script input file can be easily created. From this input file, the intersection curves between the different elements can be obtained and saved in individual output files. These files are then used by *Convert* to create a FELISA geometry definition file. Although this process seems complicated, the entire process can be completed in as little as 15 minutes from the creation of the RAM geometry to the output of the FELISA geometry file.

### 3.1.8. Software verification

We ran the two key codes, MSES and FELISA, for standard test cases to make sure we understood how to apply them properly before using them in our design work.

#### *3.1.8.1. MSES verification*

To verify MSES, results were compared to solutions obtained from other analysis codes such as FLO36 and XFOIL [26], and with existing experimental wind tunnel data. XFOIL is an Euler airfoil analysis program, using panel methods. Like MSES, Professor Mark Drela developed this code at the MIT Computational Aerospace Sciences Laboratory.

To check the accuracy of these programs at low Mach numbers, we compared the force and moment predictions for the NACA 0012 (Figure 8) and 4412 (Figure 9) airfoils to experimental data at a Reynolds number of 6 million [27]. Figures 11 to 13 show the results of these comparisons, demonstrating that both programs work well for low speeds.

Analysis of a more modern airfoil was done by comparing the MSES solution to the pressure distribution prediction from XFOIL of a GA(W)-1 airfoil (Figure 13), shown in Figure 14.

When the NACA 4412 airfoil was originally run with XFOIL, a bump in the data similar to a drag bucket appeared around a $C_l$ of 0.75. This bump was traced to a problem with the transition point of the airfoil. XFOIL and MSES employ the $e^n$ method, where $n$ represents the log of the amplification factor of the most-amplified frequency that triggers transition [28]. The default value is 9, representing a normal wind tunnel. The drag bucket was diminished when we used a value of 6, which represents an older wind tunnel that was not designed to produce a clean and quite flow.

MSES's accuracy at transonic Mach numbers was then checked, by comparing inviscid pressure distribution predictions for a NACA 0012 airfoil at M=0.75 with predictions from a full potential code (FLO36) and a small disturbance theory code (TSFOIL2). Figure 15 shows the result of this comparison. The shock location predicted by MSES is ahead of the shock predictions from the other methods. This is the expected trend comparing the Euler equations result from MSES with the more approximate methods.

#### *3.1.8.2. FELISA verification*

To assess the accuracy of the FELISA grid generator and flow solver, it was necessary to compute the solution to a well know wing test case. The ONERA M6 wing in transonic flow was chosen as the test case. The wing has a round wing tip with a root chord of 0.8059 m, half-span of 1.1963 m, leading edge sweep of 30$^{\circ}$, and a taper ratio equal to 0.562. The experimental data for this wing can be found in the AGARD Advisory Report (No. 138) [30]. The freestream condition chosen for this test case was M = 0.84 at an angle of attack $\alpha = 3.06^{o}$. Note that there is a small difference between the modeled geometry and the actual experimental test case in that the modeled geometry has a flat wing tip, while the wind tunnel model has a round wing tip. However, we did not expect that this difference to alter the flow solution significantly.

The computational boundary used for this flow solution extended to approximately 20 root chords away to the wing. The final solution used a mesh of 1,209,176 tetrahedra, which was generated by an adaptive re-meshing program, called REMESH, included with FELISA software distribution. Figure 16 shows the surface triangulation of the final mesh that was used for the solution.

Figure 17 shows the Mach contours and also pressure coefficient distributions on the upper surface of the wing at various spanwise stations along the wing. We can see that the solution resolved the lamda-shock on the upper surface accurately. The pressure distributions at various spanwise stations are compared to experimental data in Figure 18 to Figure 24. In general, there is good agreement between the experimental and computational solutions, which are from an inviscid solution. Small differences in the data appear in the position and resolution of the shock. The plots show that the main shock from the inviscid CFD solution was stronger than the shock found in the experiment. Also, the first shock (closer to the leading edge) was predicted to be farther aft than found in the experiment at the 65% and 80% span stations. The results shown for the 99% span cut are “noisy” due to the lack of enough computed data points to make good chordwise cuts. However, the trend in the data still follows the experimental results closely.

Since the solution captures the principal flow features of this test case, we concluded that we had learned how to use the FELISA flow solver and it was an appropriate flow solver for this design application.

## 4. Airfoil Design

In this section we explain the airfoil design process used for the A7 SBW demonstrator aircraft wing. To start, we select a NASA supercritical airfoil section from the catalog in NASA TP 2969, by Harris [31]. Since these NASA supercritical airfoils were not designed for the operating conditions or thicknesses that we need in our application, modifications to the selected airfoils to improve their performance at design operating conditions were required.

Note that some of this work was done in parallel with the three-dimensional wing analysis and design effort. Only the later three-dimensional wing design work incorporates the final airfoils.

The first step in the process was the analysis and selection of appropriate baseline NASA supercritical airfoils to modify and use at different wing spanwise stations. The airfoils were chosen to have properties such as *t*/*c* ratio and camber that were close to those required at the various wing spanwise stations. Initially, airfoils for 3 wing spanwise stations were selected. Another station was added later to allow for a better wing twist distribution.

Next, several methods to modify these airfoils for minimum drag at the design operating conditions and to satisfy geometric requirements were investigated. Several surprises were encountered during this process.

Once a method to modify the NASA supercritical airfoils was selected, we began modifying and analyzing the airfoils for the different wing spanwise stations. The process was divided into two parts: designing airfoils for the outboard wing spanwise stations and airfoils for the inboard wing spanwise stations. These airfoils were grouped this way since the *t/c* requirements for the airfoils in these groups were close to each other and therefore lessons learned from the design of one airfoil could be applied to the other, or the same baseline NASA airfoil could serve as a similar starting point. The design process also took into account the off-design performance of the airfoils.

The wing outboard airfoil designs were based on an airfoil that had already been designed during the airfoil modification method selection process. Although this airfoil was designed for a different $C_l$ and *t/c* ratio than that which was required at the outboard wing spanwise stations, it was close enough that only minor modifications was needed.

Before proceeding, we describe our experience with the NASA airfoil coordinates cataloged in Harris's NASA report, TP 2969 [31].

## *4.1. Lesson learned: NASA airfoil coordinates problem*

Performing initial analysis of several of the airfoils in Harris's NASA report TP 2969 [31], we found that the airfoil coordinates had several problems. Figure 25 shows the FLO36 analysis of the SC(2)-0406 airfoil using the original coordinates found in the report. As can be clearly seen, the airfoil pressure distribution curve contains "wiggles".

Upon examination, we found that the airfoil coordinates contained in the report actually consist of a series of straight lines defining the airfoil shape. Apparently, a smaller number of coordinates were ‘enhanced’ by adding points to the data set using linear interpolation. This is illustrated in Figure 26. The airfoil geometry was described by a much smaller number of coordinate points and then, quite apparently, linearly interpolated to increase the total number of coordinate points for the airfoil. Once these “extra” points were removed, the pressure distributions predicted by FLO36 were smooth. The other deficiency in the airfoil coordinates was that there was not enough points at the leading edge to adequately define the surface. This resulted in the erratic pressure distributions at the leading edge, also seen in Figure 25. To solve this problem, more points were added to the leading edge using a cubic spline through the available points. Figure 27 shows the result of fixing these two deficiencies on the SC(2)-0406 airfoil at different angles of attack.

## *4.2. Initial Airfoil Selection and analysis*

Several spanwise stations on the wing were identified as control stations to define the two-dimensional airfoils. The wing shape was then determined by straight line wrap lofting between the airfoils at these stations. Four stations were identified: the wing root, wing break, wing tip and the maximum $C_l$ station. Upon examining these stations, we found that the maximum $C_l$ station was at approximately the 80% half-span position, while the wing break station was close by, at the 67% half-span position. Also, the $C_l$ and *t/c* ratio requirement at these two stations were similar. Since the wing break station was also a design variable in the SBW optimization code that was used to optimize the original SBW wing, we eliminated the maximum $C_l$ station.

The three-dimensional requirements ($t/c$ and $C_l$) at these stations were then converted to the equivalent two-dimensional conditions using simple sweep theory. Table 3 gives the relation between the three-dimensional and two-dimensional design problem.

Table 3: Table of the three- and two-dimension requirements of the airfoil at the wing spanwise station candidates.

| **Station** | **η** | **three-dimensional** | | | **two-dimensional** | | |
|---|---|---|---|---|---|---|---|
| | | **M** | $C_l$ | $t/c$ | **M** | $C_l$ | $t/c$ |
| **Root** | 0.00 | 0.85 | 0.434 | 0.133 | 0.757 | 0.547 | 0.1490 |
| **Break** | 0.67 | 0.85 | 0.742 | 0.062 | 0.757 | 0.935 | 0.0696 |
| **Max $C_l$** | 0.80 | 0.85 | 0.753 | 0.065 | 0.757 | 0.948 | 0.0730 |
| **Tip** | 1.00 | 0.85 | 0.000 | 0.075 | 0.757 | 0.000 | 0.0842 |

For the wing break spanwise station, 3 supercritical airfoils were considered for analysis.

- SC(2)-1006 (6% thick, design $C_l = 1.0$)
- SC(2)-1010 (10% thick, design $C_l = 1.0$)
- SC(2)-0706 (6% thick, design $C_l = 0.7$)

Figure 28 shows the FLO36 result comparison between the three different airfoils. Recall that FLO36 is an inviscid full potential code. The SC(2)-1006 airfoil was run at a Mach number of 0.7 while the other airfoils were run at the design Mach number of 0.757. The SC(2)-1006 was run at Mach number 0.7 because we could not get a converged solution using FLO36 at any higher Mach number for this airfoil due to the presence of a strong shock. All three airfoils were at zero angle of attack.

Figure 29 and Figure 30 shows the analysis at different angles of attack of the SC(2)-0406 and SC(2)-0706 airfoils respectively. No analysis was made on the SC(2)-1010 due to difficulties converging a solution using FLO36 at the design Mach number. From the figures, we can see that the SC(2)-0706 reaches a $C_l$ close to the target $C_l$ of 0.95, while having a *t/c* ratio of 7% (the target t/c ratio is 7.3% for this station). Hence, the SC(2)-0706 was chosen to be used as the nominal airfoil to be further analyzed and modified.

FLOMG was initially chosen to perform a more detailed viscous analysis of the nominal airfoil. However, FLOMG requires that the airfoil have pointed trailing edges. After investigating different methods of closing the trailing edge of the airfoil without significantly changing its aerodynamic characteristics, we decided to use a code that could handle finite thickness trailing edge airfoils. So instead, at the suggestion of Dick Campbell at NASA LaRC, we used MSES, written by Professor Mark Drela of the MIT Computational Aerospace Sciences Laboratories.

Figure 31 shows a viscous solution obtained from MSES on the SC(2)-0706 airfoil. Note that the viscous solution now gives a lower $C_l$ than what was obtained by FLO36 under the same conditions. Also, the shock is closer to the leading edge of the airfoil in the viscous solution.

## *4.3. Airfoil modification method evaluation and selection*

One of the reasons MSES was chosen as the airfoil analysis code was its capability to do inverse-design. This capability allows the user to specify changes in the pressure distribution on the surface of the airfoil. MSES then attempts to make changes to the airfoil geometry to match that pressure distribution.

The SC(2)-0406 and SC(2)-0706 airfoils were used as test cases for the inverse design capability of MSES. Figure 32 shows an inviscid solution of the SC(2)-0406 airfoil obtained from MSES prior to modification.

We experimented with several changes to the pressure distribution using MSES's inverse design capabilities. Referring to Figure 32, they were to:

i. Move the shock (which is at about 40% chords from the leading edge) further towards the trailing edge.

ii. Soften the expansion around the leading edge, to reduce the maximum velocity

iii. Reduce the intensity of the shock

iv. Smooth out any "kinks" in the pressure distribution

As novice users, several problems were encountered while trying to meet these goals, mainly because it was difficult for MSES to make changes near the stagnation point of the airfoil (as documented in the User's Guide [28]). This was a problem since modifications (i),(ii) and (iii) require a change of the shape of the leading edge of the airfoil. Attempts at directly changing the airfoil shape to achieve the desired goals met with limited success. These changes included thickening and thinning the leading edge of the airfoil. An attempt at flattening the top surface of the airfoil in order to mover the shock further aft and to reduce the shock strength was also made.

Another problem encountered early-on in the use of MSES's inverse design capabilities was that the resultant modified airfoil from MSES had small 'wiggles' and ‘bumps’ in the shape. The addition of these ‘wiggles’ and ‘bumps’ would result in the desired pressure distribution. However, it is impractical to use this airfoil design for two reasons. Manufacturing a wing using this airfoil shape would be too expensive. Also, the airfoil would perform poorly away from the design point. We later found that using the Modal-Inverse design method in MSES solved the ‘wiggles’ and ‘bumps’ problem.

### *4.4. Lesson learned: the ‘shock-free’ airfoil*

Figure 33 shows a viscous MSES solution of the SC(2)-0706 airfoil at $M = 0.757$, $C_l = 0.918$ and $Re = 36x10^{6.}$. The inverse design capability of MSES was then used to reduce the shock strength on the airfoil. This produced an unexpected result. Figure 34 shows the resulting modified surface pressure distribution. We see that it looks as if the designed airfoil is shock free. The discontinuity at 70% chord is probably a result of a discontinuity in the geometry (MSES was constrained not to change the geometry aft of this point).

However, when we look at the contour plots of this solution given in Figure 35, we see clearly that a shock still exists in the flowfield. This was referred to by Volpe [29] as a hanging or secondary shock. Volpe showed similar results in which an apparent ‘shock-free’ airfoil was designed but a hanging shock was found. The occurrence of this shock was associated with a concave section on the upper side of the airfoil ahead of the shock. It was suggested that a constraint on the curvature could be implemented to avoid such a solution. In our case (Figure 35) we find that the boundary layer thickness where the shock occurs is much thicker than that ahead of the shock. Although the actual surface of the airfoil is not concave, it is clear that the thick boundary layer changes the effective inviscid curvature of the airfoil. This change in curvature, although we are not certain that it is concave, could explain the presence of a hanging shock.

Investigating further, the modified airfoil coordinates were obtained from MSES and its shape smoothed with the use of cubic splines. The airfoil was then reanalyzed using MSES. Figure 36 shows the results of the analysis on the modified airfoil. We can clearly see that the surface pressure distribution has not drastically changed from the original SC(2)-0706 surface pressure distribution at that same operating conditions.

In this exercise, we learned to look at the results with a ‘grain of salt’. Careful attention to the physics of the solution was necessary, especially when a solution looked ‘too good to be true’. More experience on the part of the use was required to use the inverse design option in MSES.

### *4.5. Closing the trailing edge*

We mentioned earlier that an airfoil with a finite thickness trailing edge caused analysis problems when using the program FLOMG. Using MSES solved this problem. Later on, we found that the FELISA solver that we used for the three-dimensional analysis did not accept geometries that have finite thickness trailing edge airfoils. For example, on a wing, an open surface would exist when there is a gap between the trailing edge of the upper surface and lower surface of the wing. Creating an additional surface joining the upper and lower wing surface trailing edges with another surface, essentially adding a finite thickness base, would solve this problem. However, since FELISA is an inviscid solver, the sharp corner leads to extreme flow acceleration as the flow turns the corner at the trailing edge instead of separating, as it would occur in the real flow. Since the baseline supercritical airfoils have finite thickness trailing edges (which are usually defined with the upper and lower surface trailing edges separated by a gap), using these airfoils to model the three-dimensional geometry would produce open surfaces at the wing trailing edge. Thus we needed to use airfoils with zero thickness, pointed trailing edges. Using an airfoil with a pointed trailing edge eliminates these problems. The airfoil should have essentially the same flow characteristics as a finite thickness trailing edge airfoil design. Rivers and Wahls [32], and Van Dam [33] discuss the different methods used to overcome the finite trailing edge thickness problem. Based on the work by Rivers and Wahls [32], we decided that a 'sliver' of thickness should be removed from the bottom surface, varying linearly from the trailing edge to the leading edge. The effect of this modification was analyzed using MSES (inviscid analysis). Figure 37 shows a geometric comparison between a SC(2)-0406 airfoil with a finite thickness trailing edge, and its modified version with a pointed trailing edge. The difference in the inviscid surface pressure coefficient distribution caused by this modification is shown in Figure 38. This figure shows that the modification caused the shock location to move slightly forward while reducing the $C_l$ at this angle of attack by only 0.02. This result shows that a pointed trailing edge airfoil design can be used without major deviations in performance from a finite thickness trailing edge airfoil.

## *4.6. Airfoil design method*

Since there were limitations in our skill in using the inverse design capability in MSES, and the inverse designs from MSES created small local 'bumps' on the airfoil, we adopted a different design approach.

It was decided that, to have more control over the airfoil shape design and characteristics, and to gain insight into conventional airfoil design techniques, the method of adding and subtracting long 'bumps' to the upper and lower surface of the airfoil was used. Unlike the local 'bumps' used in the inverse design method in MSES, this method adds (or subtracts) a shape that provides continuous curvature at the beginning and end of the bump. The user defines the start, end, and maximum thickness position locations of the bump on the airfoil and also determines the magnitude of the maximum thickness. This method has been called the 'Grumman cubic bump method', although the bump is actually defined by a 6th order polynomial. Airfoil designers at Grumman conducted parametric studies of the effects of various 'bump' shapes added to airfoils and found this to be a practical approach. Reference [24] provides detail of the Grumman cubic bump. This reference is also included in this report as Appendix D. Mason and Miller [25] provide an example of its use to eliminate a shockwave.

The first step toward understanding the effect of adding and subtracting the 'bump' to the airfoil is to systematically add and subtract the 'bump' distribution at various locations along the upper surface of the airfoil. The bump was directly added or subtracted vertically along to the airfoil surface. An inviscid analysis using MSES was used to evaluate the performance of the modified airfoils. It was determined that the process should be started with a bump with a maximum height of 0.5% chord spanning the entire chord. The bump thickness distribution was added to the upper surface of a SC(2)-0406 airfoil (modified with a closed trailing edge), varying the location of the maximum height along the chord. Figure 39 shows the wave drag predictions from MSES as a function of maximum bump height location at a design $C_l$ of 0.757. Contrary to intuition, Figure 39 indicates that subtracting the bump thickness distribution increases the wave drag of the airfoil, whereas adding a thickness distribution reduces the wave drag on the airfoil by as much as 50 counts. Keep in mind that the inviscid shock location predicted by MSES on the closed trailing edge SC(2)-0406 airfoil is at the 39% chord location. Figure 39 shows that the lowest wave drag is achieved when a bump is added with its maximum thickness position placed close to the shock location of the original design.

Next, an investigation into the effects of the maximum height of the thickness distribution was done. Since it was found previously that placing the maximum height at the 40% chord location produced the lowest wave drag, this case will be used to investigate the effect of the maximum thickness. The maximum thickness of the bump was varied between 0.5% and 1.4% chords and an inviscid analysis of the modified airfoil was done using MSES. Figure 40 shows the wave drag predictions from MSES as a function of the maximum bump thickness. It can be deduced from this figure that the larger the maximum thickness of the bump, the lower the wave drag on the airfoil. Also, we find that the savings in wave drag diminish after a maximum thickness of 1.2%. Figure 41 shows a comparison of the pressure coefficient distribution as a result of the different maximum thickness. We can see that with a large thickness, a double shock develops on the upper surface of the wing, which is undesirable. The start of this double shock can be seen in the solution with the case where a 1.2% maximum thickness distribution was added. Therefore, a maximum limit of approximately 1.2% was set to the maximum thickness of the added distribution.

The effect of using a combination of 2 or 3 bumps added to the upper surface of the airfoil was then investigated. This investigation also involved observing the off-design characteristics of the designed airfoils. It is essential that together with designing the airfoil for low drag at the design condition, the off-design characteristics of the airfoil also be considered [34],[35].

Viscous and inviscid analyses were used in determining the performance of 5 different airfoil designs. These airfoils were designed by adding 2 or 3 bumps at different locations and amplitudes on the closed trailing edge SC(2)-0406 airfoil mentioned earlier. The placement and amplitude of the bumps were selected based on estimating where the addition of a bump might improve off-design conditions. Figure 42 provides a summary of the 5 different airfoil designs analyzed.

Figure 43 shows the pressure coefficient distribution on the airfoils at the two-dimensional design condition of M=0.757 and $C_l$ of 0.75. We can see that the case D and case E airfoils had weaker shocks than the other designs. Figure 44 shows the drag polars for the 5 airfoil designs, and again, case D and case E stand out as having the least drag. In fact, the only difference in performance between case D and case E was that the case E airfoil has lower drag at lower $C_l$. Figure 45 shows the viscous drag polars of the airfoils, at a much smaller $C_l$ range to better differentiate between the performance of the airfoils better. Case B and C were also eliminated from this chart because although their performance was better than the original SC(2)-0407 airfoil, they were not as good as case D or E. This analysis was done using MSES, at a Reynolds number of 32 million. We can see that although the single bump design has less drag at the design point, its performance is not as good as the double and triple bump cases at off design conditions.

As noted earlier, case E has less drag at lower $C_l$ compared to case D. These observations can also be seen in Figure 46, which is the drag rise plot of the different airfoils. In this plot however, case E performs much better than case D at lower Mach numbers. Therefore case E was chosen as the airfoil design that was to be modified and used for the outboard sections of the A7 SBW demonstrator aircraft.

### *4.7. Outboard airfoil designs*

For the design of the wing outboard sections, airfoils at the 70% span and wing tip will be designed. Recall that in section 4.2, we had chosen the break station (which is at 67% span) in addition to the root and tip wing stations as locations whose airfoils will be designed. The airfoil for the root station will be designed later at the inboard airfoil design section. The 67% span station was changed to the 70% span station because of complications that arose due to modeling the three-dimensional wing. In the three-dimensional design of the wing, the twist distribution of the wing is determined by specifying the twist at the selected span stations. This results in a 'kink' in the twist distribution at those span stations. Since the pylon intersects the wing at the break station of the wing, it was not advisable to also have a 'kink' in the twist distribution at this point. The span station therefore was moved to the 70% station.

To preserve the results of the design work done in the previous section, the previously designed airfoil (Case E) was used as a starting point for the wing outboard station airfoils. We then modified the Case E airfoil, to match the required thickness of the 70% span and tip stations. The required thickness and $C_l$ of the two wing outboard station and the Case E airfoil is summarized in Table 4.

Table 4: Summary of the thickness and $C_l$ requirements for the outboard span stations compared to the Case E airfoil.

| | **70% span station** | **Tip station** | **Case E airfoil** |
|---|---|---|---|
| ***t/c* ratio** | 0.0696 | 0.0842 | 0.0711 |
| **$C_l$** | 0.9420 | 0.0000 | 0.7500 |

To match the 6.96% thickness, a Grumman bump centered on the point of maximum thickness and with negative amplitude was used to remove thickness from the bottom of the Case E airfoil. The specific bump used had an amplitude of -0.16% at 35% chord length, stretching from 0 to 70% of the airfoil length. Scaling the Case E airfoil by multiplying the airfoil thickness by an appropriate factor created the 8.42% thickness airfoil.

The new airfoils are shown in Figure 47 and Figure 48. The drag polars and drag rise plots for these new airfoils, compared to the original SC(2)-0406 airfoil, are shown in Figure 49 and Figure 50. The improvement over the NASA supercritical airfoil is apparent, and may stem from the fact that the SC(2)-0406 airfoil was designed for a $C_l$ of 0.4, while the airfoil we needed for our purposes needed a design $C_l$ around 0.75. Figure 51 shows the pressure distribution at the design conditions.

### *4.8. Inboard airfoil designs*

After designing the outboard airfoil sections, the next task was to design the inboard airfoil sections. Two airfoil sections were designed; to be used at the root and 15% span station. The additional 15% span station was included as an additional wing span station to more accurately define the wing twist distribution (that will be explained later in section 6). A summary of the *t/c* and $C_l$ requirements of the airfoils at these span stations is given in Table 5.

Table 5: *t/c* and $C_l$ requirement of the inboard airfoil designs.

| | **Root station** | **15% span station** |
|---|---|---|
| ***t/c* ratio** | 0.149 | 0.139 |
| **$C_l$** | 0.547 | 0.612 |

Again, the Grumman cubic bump method was used to design the airfoils. The SC(2)-0614 airfoil was chosen as the baseline airfoil for the root and 15% span stations since both the *t/c* ratio and design $C_L$ are close to the requirements. The airfoil was modified to have a closed trailing edge by subtracting thickness off the bottom surface using the same method used with the outboard airfoil designs.

For the root station airfoil, the design process starts with a viscous investigation into the effects of subtracting and adding bumps and varying their maximum amplitude position along the chord. The start and end of the bump were set at the leading and trailing edge respectively. A maximum amplitude of 0.5% chord length was chosen as the thickness to be added and subtracted. Figure 52 shows the drag variation as a function of position of the maximum amplitude of the bumps added and removed from the airfoil. It shows that removing bumps at the 30% and 40% chord positions produce the best drag savings.

The next step was to determine the best value for the maximum amplitude of the bumps to be removed from the airfoil. The 40% chord location was selected as the position where the maximum thickness of the bump would be placed. Figure 53 shows the results of this study. We can see that removing a thickness of 0.3% to 0.4% chord length produced the best reduction in drag. It was therefore decided that the designed airfoil would be a closed trailing edge SC(2)-0614 airfoil with a 0.3% chord length maximum amplitude Grumman cubic bump removed at the 40% chord position starting from the leading edge and ending at the trailing edge. Multiplying the airfoil thickness by an appropriate factor to match the t/c ratio requirement of 0.149 then scaled the airfoil.

An investigation into using more than one bump was also performed to see if using a secondary bump would reduce the wave drag further on the scaled designed airfoil. In this investigation, bumps of 0.2% chord length maximum amplitude were added and removed from the scaled design airfoil. The position of the maximum amplitude of the bump was varied along the chord, with the bump start and end being at 40% and at the trailing edge respectively. Figure 54 shows the results of this study. It can be seen that adding bumps at the 70% to 80% chord position reduces the drag of the previously designed airfoil by almost 1 drag count. A study was also done to find out the best thickness of the secondary bump that should be added to the 70% chord position. Figure 55 shows the result of this investigation. Although it seems that adding an 0.8% chord length bump would produce an airfoil with the best drag performance, the pressure distributions on this design revealed the presence of double shocks on the airfoil, similar to that which we observed in Figure 41. Only adding a 0.3% bump or smaller did not produce the aforementioned double shocks. Therefore, it was determined that adding a secondary bump of 0.3% maximum amplitude at the 70% chord position was a design to be studied further.

In picking the airfoil design to use for the root section, the performance of the different designed airfoils needed to be evaluated at both on- and off-design conditions. In the off design condition analysis, the airfoil with only one bump removed, the scaled airfoil with one bump removed and the airfoil with one bump removed with a secondary bump added were considered. The SC(2)-0614 airfoil was also analyzed to serve as a reference case. Note that the SC(2)-0614 airfoil ($t/c = 0.14$) and the airfoil with one bump removed ($t/c = 0.134$) are thinner than the required thickness of $t/c = 0.149$ at the root station.

Figure 56 shows the pressure coefficient distribution of the four designs that were considered. These results were obtained from viscous solutions using MSES, at a Mach number of 0.757 and at a design $C_l$ of 0.547. Figure 57 and Figure 58 show the drag polar and drag rise of the considered airfoil respectively. As can be seen on the drag polar, although the design with two bumps has lower drag at the design condition, its off design performance is worse than that of the scaled one bump design. This characteristic is also exhibited on the drag rise plot. Although the plots show that the one bump design has the best performance overall, as mentioned earlier, this airfoil is thinner than that is required for the root station. Therefore, the scaled one bump design was chosen as the airfoil to be used on at the root station.

For the 15% span station airfoil, the same design process used for the root station airfoil was adopted. Since the design $C_l$ at this station is different from that of the root airfoil, the results from the root station airfoil design cannot be used. The design at this station required an airfoil of $t/c$ ratio of 0.139 operating at a Mach number of 0.757 and a $C_l$ of 0.612. Figure 59 shows the results for the bump position study performed on the closed trailing edge using the SC(2)-0614 airfoil as the airfoil modified. Unlike the root airfoil design, the results do not show a position where a minimum drag design occurs. Therefore, thickness studies on removing bumps at maximum thickness position of 20%, 30% and 40% chord locations were studied. Figure 60 shows the results of this study. This figure shows that removing bumps of maximum amplitude of 0.5% chord length produce the largest reduction in drag. However, although the plot shows that the bump should be removed from the 20% chord position, the pressure coefficient distribution showed the formation of double shocks. Therefore, a design with 0.5% chord length maximum amplitude bump removed from the 30% chord position was chosen for further study. As was done in the design of the other airfoils, the airfoil was then scaled to match the required airfoil *t/c* ratio of 0.139. Studies on adding or removing secondary bumps were also conducted, but the results showed no significant reduction in drag.

Figure 61, Figure 62 and Figure 63 show the pressure coefficient distribution at the design conditions, the drag polar, and drag rise of the designed airfoils respectively. The drag polar shows only a small difference between the scaled design and that of the airfoil with one bump removed. Also, although the scaled design has a slightly higher wave drag at lower Mach numbers, it has the same drag as that of the design with one bump removed at the design conditions. It should be noted that the airfoil with one bump removed is not at the required thickness of the 15% span station. From these figures, it was decided that the scaled airfoil design would be used for the 15% span station.

## 5. The Airfoil-Wing Connection

To relate the two-dimension airfoil design and analysis to the three-dimension conditions, several theories can be used. Simple sweep theory relates the pressure distribution on an airfoil to a swept wing based on the local normal Mach number [36]. The theory relates the two-dimension and three-dimension conditions by:

$\mathbf{M}_{2D} = \mathbf{M}_{3D} \cdot \cos(\mathbf{\Lambda})$

$\mathbf{t/c}_{2D} = \mathbf{t/c}_{3D} / \cos(\mathbf{\Lambda})$

$\mathbf{C}_{\mathbf{L},2D} = \mathbf{C}_{\mathbf{L},3D} / \cos^2(\mathbf{\Lambda})$

$\mathbf{C}_{\mathbf{P},2D} = \mathbf{C}_{\mathbf{P},3D} / \cos^2(\mathbf{\Lambda})$

where $\mathbf{\Lambda}$ is the sweep of selected reference line on the wing.

Boppe [37] proposed the sweep-taper theory (building on Lock's sweep theory) for tapered wings, which relates the pressure distribution from a cut in the wing along a line that is tangent to the local sweep with that of an airfoil. Van Der Velden et al. [38] refined these theories by accounting for the influence of local taper, local sweep and three-dimensional induced velocities.

To determine which method would best relate the airfoil and wing pressure distributions, a comparison was made using simple sweep theory and sweep-taper theory, using the shock sweep as the reference sweep. The Mach number used in the airfoil analysis was the two-dimension Mach number based on the shock sweep. Pressure distributions from one of our interim designs were used. This design was analyzed at an angle of attack of 5° and the solution predicted a $C_L$ of 0.732. This $C_L$ is higher than the design $C_L$. However, we decided that this should not affect the comparison that we are making. In addition to this, the shock location of this configuration is at approximately mid-chord of the wing, about where we would like the final design shock to be located. Figure 64 shows the pressure distribution on the upper surface of the wing and the positions at which the comparison with the two-dimensional airfoil analysis were made. At these positions, simple sweep theory and sweep taper theory were applied. The pressure coefficient distribution was then plotted, and the two-dimensional $C_l$ was calculated. Next, the airfoil shape corresponding to the simple sweep theory cut is analyzed using MSES (inviscid solution), matching the two-dimensional $C_l$ at those stations.

Figures 65 to 68 give the pressure coefficient comparison at the four cuts. As we can see, the results from MSES predict a slightly sharper shock than of the wing solution from FELISA. However, the shock location predicted by MSES is in reasonably good agreement with the shock location obtained from the FELISA wing solution. Also, the overall pressure distribution from the MSES airfoil analysis follows the FELISA wing solution closely. Only small differences in the pressure coefficient distribution are seen near the leading edge. This applies to the results both from simple sweep theory and sweep taper theory. Hence, it was decided that simple sweep theory was appropriate to use as a link between the two-dimensional airfoil design and the three-dimensional wing analysis.

## 6. Wing design

In the three-dimensional wing design process, we used RAM as the geometry modeler, FELISA as the grid generator and flow solver, and *Convert* as a translator between RAM and FELISA. This process started with the design of the wing alone (without the pylon or strut). In this step, the twist distribution of the wing and control span station positions were decided. It should be noted that as this step was being done, the airfoil design work described in the previous section was also being performed. Hence, we only used NASA supercritical airfoils in the first few wing analysis.

One of the major stumbling blocks early on in the three-dimensional wing design process was the difficulty in translating RAM geometry data into a format suitable for FELISA. At this point, *Convert* was only written to translate wing-alone geometries between the two programs. To be able to convert complex geometries such as the full A7 SBW demonstrator aircraft geometry required additional programming. The difficulty in this case was the calculation of intersection curves between intersecting entities (such as the intersection between wing and the fuselage). This calculation involved complex algorithms that were beyond our capabilities given the time constraints. A program that did the translation between the two programs had already been written at NASA, but it could not be made available to us. We resolved this problem by collaborating with Andy Hahn at the NASA Ames Research Center. Andy Hahn, who had access to this translation software, had offered to help us translate and create the grid for us, once a design was made in RAM.

With Andy Hahn's help we were able to create a full A7 SBW demonstrator aircraft geometry, create a grid and run a flow solution. This initial analysis of the aircraft provided us with greater insight into the issues that would have to be addressed in the design. However, we found that the cycle time between the design in RAM and the calculation of the flow solution was not fast enough for us to design the wing by our deadline.

After considering the data obtained from the flow solution of the complete A7 SBW demonstrator aircraft, we found that we could consider only the wing/pylon/strut geometry without the fuselage to perform much of the design work. With this in mind, we improved *Convert* to be able to translate wing/pylon/strut geometries from RAM to

FELISA. The intersection curves in this geometry was obtained from AutoCad and input into *Convert* as an additional input file. By concentrating only on the wing/pylon/strut configuration, we reduced our cycle time to one flow solution per day (compared to a cycle time of 1 to 1.5 weeks if sent to NASA Ames).

With this new capability, a study on the effect of the fuselage was first carried out. If the fuselage had a great impact on the flow characteristics of the SBW configuration, the design work would have to involve the fuselage. However, the study revealed that the fuselage had only a minimal effect on the flow solution, and therefore we could decide on most of the design changes based on analysis of the wing/pylon/strut only geometry.

Several other studies were done, investigating the effect of changing geometric properties such as pylon toe and strut twist. The purpose of these studies was to understand the flow occurring at the wing/pylon/strut juncture, and ultimately reduce the shock strength (and therefore reducing the interference drag) at this juncture. These studies led us to conclude that the flow at this juncture was similar to flow through a two-dimensional nozzle. With this understanding, we were able to shape the strut to reduce the shock strength and even eliminate the shock altogether at this wing/pylon/strut juncture.

The following sections describe in detail the wing design and analysis work that was done.

## *6.1. Wing-only configuration*

To start the design of the A7 strut-braced wing configuration, a simple swept trapezoidal wing was developed using RAM, the geometric modeler. This wing matches the planform and wing area of the scaled SBW wing described earlier. The twist distribution was prescribed as a straight line wrap between the root and tip stations of the wing.

The twist at the root and tip stations were obtained from a linear theory solution. LAMDES [19],[20] was employed to obtain the full twist distribution. Given the geometry of the wing planform and the design $C_L$, LAMDES finds the spanload distribution that produces the minimum induced drag for the wing (in this case, a classic elliptic spanload). The twist distribution is calculated based on the spanload distribution and an assumed chord load using linear aerodynamics. Experience has shown that this provides a good initial estimate for use in transonic wing design. Based on the LAMDES results, it was found that a 6.371° wing tip wash-out angle was required (referenced from the root station) with a root $\alpha=5^\circ$. Although a straight line wrap between the root and tip creates a twist distribution that is a poor approximation of the linear theory twist distribution, this configuration serves as a starting point.

Figure 69 and Figure 70 are the inviscid solutions obtained using FELISA for the wing alone configuration designed with the SC(2)-0706 airfoil. Figure 69 shows the pressure contours on the upper surface of the wing, and Figure 70 gives the pressure coefficient distribution at various spanwise stations along the wing. It can be seen that the shock on this wing is too far aft of wing for a good design. Also, the shock at this location is too strong to be an efficient wing. Both characteristics indicate that the airfoil shape contains too much camber for the operating Mach number. Hence, using the SC(2)-0406 airfoil should result in better design since it has a smaller camber.

Figure 71 and Figure 72 are the solutions obtained from FELISA fot the wing alone configuration with the SC(2)-0406 airfoil. Figure 71 shows the pressure contours on the upper surface of the wing, and Figure 72 shows the pressure coefficient distribution at various cuts along the wing. In contrast to Figure 70, the shock on the wing is weaker, and at a much more desirable location, at about 60% of the chord. The configuration shock (or also known as lamda-shock) extends to about 30% span of the wing, after which, the shock follows the sweep of the wing, which is an indication of a constant isobar wing. This condition deviates slightly at the tip, where the shock un-sweeps. Root and tip modifications would be necessary to change the shock characteristics at the tip and at the region of the configuration shock. In addition to this, the $C_L$ calculated for this wing is 0.732. The angle of attack needs to be decreased to achieve the target $C_L$ of 0.53.

It was found after several analysis runs that a $C_L$ of 0.527 can be achieved at an $\alpha$= 4.0°. Figure 73 shows the pressure contours on the upper surface of the wing at this angle of attack. We can see that the shock on the wing has moved further forward on the wing. Also, the shock moves closer to the leading edge at sections closer to the wing tip. Figure 74 shows the pressure coefficient distribution at several spanwise stations along the wing. Although the shock on the upper surface is weaker than in the previous case (Figure 72), the shock observed at the 60% span station cut can be reduced in strength by tailoring the airfoil shape. Also, as mentioned earlier, the pressure coefficient distribution shows that this wing is far from a 'constant' isobar wing design.

The next step in the design of the A7 wing involves determining the twist distribution at various stations on the wing other than at the root and the tip of the wing. Figure 75 shows the difference between the linear theory twist distribution and the straight line wrap twist distributions. As we can see, the twist distribution of a straight line wrap wing with the twist fixed at the root and tip values varies significantly from the linear theory twist distribution. However, by using additional control stations at the 10% and 30% span stations, we can nearly match the linear theory twist distribution.

A wing with the additional control stations at the 10% and 30% span stations was designed. The closed trailing edge SC(2)-0406 airfoil was used in this wing and an inviscid analysis using FELISA was done. Figure 76 shows the pressure contours on the upper surface of the wing with at an angle of attack of 4.0º. At a first glance, we observe the absence of any shocks on the upper surface of the wing. However, the calculated $C_L$ for this solution is 0.26, only slightly more than half of the target coefficient. The reason for this is that, from Figure 75, we see that overall, the wing is operating at a much lower angle of attack with the more appropriate detailed twist distribution. Figure 77 shows the pressure coefficient distribution of this wing at the 20%, 60% and 95% span station.

Next, the wing was modified by replacing the SC(2)-0406 airfoil with the designed inboard and outboard airfoil shapes discussed in Section 4. Also, the position of the span stations on the wing was changed to using the root, 30% span, 70% span and wing tip (as opposed to the root, 10% span, 30% span and wing tip used in the previous case) to accommodate the use of the designed airfoils.

An invicid FELISA analysis was done for the new wing alone configuration. Figure 78 shows the pressure contours on the upper surface of the wing at an $\alpha$=4.0º.

Here, a shock is present on the wing, and the $C_L$ for this wing is 0.518. Even with the overall decreased angle of attack for the wing, the new airfoils almost provide the target $C_L$. One of the major reason of this is that the wing has a higher *t/c* ratio compared to using only the SC(2)-0406 airfoil (which is 6% thick). Figure 79 gives the pressure coefficient distribution on the top and bottom surfaces of the wing at various span stations. We see a fairly strong shock at the 20% span station, while the shock at the 60% span station is acceptably weak. We would like to reduce the strength of the shock near the root to a strength shown at the 60% span station. One way to do this is to untwist the wing at the root, to reduce the load there, transferring it more to the tip. This sort of tailoring also would help in creating a constant isobar wing.

## *6.2. Full A7 geometry – Initial analysis*

One of the main challenges of this project was obtaining access to necessary programs and analysis codes. An integral part of the suite of programs needed to complete the tasks of the project was a geometry translator that would interface between RAM and FELISA. Since we could not obtain access to this translator, as described above, Andy Hahn at NASA Ames agreed to help in refining the A7 SBW demonstrator geometry, especially with aspects concerning the fuselage details. He also would help with the grid generation of the A7 SBW geometry. Therefore, the design process would start with the design of the A7 SBW geometry modeled in RAM at Virginia Tech, then sent to Andy Hahn at NASA Ames to be modified and the grid generated. This grid would then be sent back to Virginia Tech, for the flow solution to be computed. As a first step, the grid for a general aircraft configuration was sent to Virginia Tech, to investigate if this process was feasible and if the computational time to obtain the flow solution was reasonable. In the next step, the A7 SBW geometry with the wings containing NASA supercritical airfoils and the pylon and strut using the NACA 0008 airfoil was used. The design of the supercritical airfoils discussed in section 4 had not been completed yet at this point in time, and therefore could not be used. Figure 80 shows the geometry that was created in RAM that was to be used to in the analysis of the A7 SBW demonstrator aircraft design. Due to difficulties arising in creating a grid for this complex geometry, the cockpit section in this geometry was removed, to simplify the geometry. This geometry is shown in Figure 81. The first computational grid was created with this simplified geometry and sent to Virginia Tech. The surface triangulation of this grid is show in Figure 82. Using this grid, a FELISA inviscid flow solution was obtained at a Mach number of 0.85.

Figure 83 to Figure 86 show the FELISA inviscid results of this flow solution. Figure 83 shows the pressure contour plots on the entire geometry. Figure 84, Figure 85 and Figure 86 shows pressure contour plots on the surfaces of the wing, strut and pylon respectively. Figure 87 and Figure 88 show the pressure coefficient distributions at various spanwise stations along the wing and strut respectively. Figure 89 shows the pressure coefficient distribution on a section of the pylon. From these plots, several observations can be made.

- There is still a strong shock on the upper surface of the wing positioned close to the trailing edge of the wing. However, it must be noted that only the designed airfoils for the outboard sections were used in this geometry. For the inboard airfoils, a NASA SC(2)-0614 airfoil was used in the root section and NASA

SC(2)-0712 airfoil at the 15% span station. It can be expected that using the designed airfoils at the inboard sections would improve the pressure distribution on the upper surface of the wing.

- There is a strong shock on the bottom surface of the wing close to the pylon, where the wing and the strut create a ‘channel effect’ in the flow. This shock is positioned close to the trailing edge of the pylon.
- There is also a shock near the root on the bottom surface of the wing. This could be due to the wing/fuselage intersection. In a detailed design, this intersection would be blended with the fuselage to prevent a shock like this from appearing.
- The shock on the upper surface of the strut is strong and needs to be weakened considerably.
- The isobars on the upper surface of the strut are curved, and hence need to be designed to a more ‘constant’ distribution. The lower surface of the strut has a relatively more ‘constant’ distribution.

These observations identify key sections where design changes need to be made. A clear change to the design, as mentioned earlier is to use the designed airfoils in all the wing specified inboard and outboard wing stations. Also, the airfoil sections in the pylon and strut should be changed from a NACA 0008 to an uncambered NASA supercritical airfoil. It was decided that a SC(2)-0010 airfoil, with its trailing edge closed, and scaled by multiplying the airfoil thickness with an appropriate factor to a *t/c* of 8% should be used. To close the airfoil’s trailing edge, a ‘sliver’ of thickness was removed from the upper and lower surface to prevent from introducing any camber into the airfoil section.

Other initial changes that could be made would be to change the pylon toe, introduce twist into the strut and to change the strut incidence.

We know that the pylon toe, strut twist and incidence have to be changed. The key question in the design process is determining the magnitude of these changes. With only one flow solution of the full configuration, there was no easy way of determining sensitivities to make changes. Another key consideration in this endeavor is that the cycle time from creation the RAM geometry, submission it to NASA Ames for the grid to be created and the completion the flow solution would take as long as 1 to 1.5 weeks.

## *6.3. Wing/strut/pylon only configuration*

Considering the long cycle time, we needed to be able to evaluate design changes on a daily basis. Reviewing the results, we decided that the critical aspect of the wing design was the wing/strut/pylon design.

To speed up the design process, we found that if we considered the wing/strut/pylon configuration without the fuselage, we could generate the grid for FELISA ourselves, from a geometry created in RAM, eliminating the need and time expense of sending it to NASA Ames at every iteration. To do this, a program to translate the RAM geometry definition (for a wing/strut/pylon configuration) to a geometry definition suitable for FELISA was written. This reduced the overall cycle time to approximately one day. This capability allowed us to assess design changes much more rapidly.

## 6.4. Fuselage Effects

In adopting the strategy of only analyzing a wing/strut/pylon configuration, the first task was to investigate the effect of the fuselage on wing/strut/pylon configuration. Hence, the full A7 SBW design was compared to the wing/strut/pylon alone configuration. Figure 90 to Figure 97 show the comparison between the flow solutions with and without the fuselage. We can see from these figures that the results are similar, with only minor differences. The main difference between the solutions is the reduction of the overall $C_L$ from 0.529 to 0.518 with the removal of the fuselage. Also, the pressure peak at the leading edge of the outboard sections is higher compared to the case with the fuselage. Another difference is that the shock on the top surface of the strut near the root is closer to the trailing edge for the case with the fuselage. With only minor differences, we concluded that most of the design changes and analysis can be made for only the wing/strut/pylon configuration before performing analysis and design on the complete A7 SBW demonstrator aircraft geometry.

## 6.5. Wing/Pylon/Strut only configuration studies

To start to understand the flow at the intersection of the wing, pylon and strut, the local sensitivity and effect on the surrounding flow to geometric changes, parametric studies were done by changing the geometric properties of the intersection including pylon toe and strut incidence. As a comparison, a baseline design was chosen for each study to be used as a comparison. Also, certain stations on the strut and pylon were chosen where the pressure coefficient distributions would be compared. The goal of these studies was to reduce the shock strength at the wing/pylon/strut intersection and to unload the strut and pylon. Three stations on the strut were chosen, at position *y*=18 (96.7% span of strut), position *y*=12 (64.5% span of strut) and at position *y*=6 (32.2% span of strut). Figure 98 shows the location of these stations that will be used to assess design changes. On the pylon, the pressure coefficient at position *z*=1.5 was also examined. Figure 99 shows the position (*z*=1.5 position) where the pressure coefficient will be examined on the pylon for the various studies.

### 6.5.1. Effect of pylon toe

For the pylon toe study, the baseline design was the wing/pylon/strut geometry using the airfoils designed in section 4 in the wing. A closed trailing edge SC(2)-1010 airfoil scaled to 8% thickness was used for the strut and pylon. The pylon and strut have no twist or incidence relative to the root section of the wing.

For pylon toe-out, cases with 1° and 2° pylon toe-out were investigated. The effect on the strut is given in Figures 101 to 102. Figure 103 shows the effects of the pylon toe-out angles on the pylon itself. Pylon toe-out does not seem to affect the pressure coefficient distribution on the strut very much. There are small changes in the shock strength and position on the upper surface of the strut in Figure 101 and Figure 102, but these differences are minor. However, as shown in Figure 103 we do see changes in the pressure coefficient distribution along the outboard surface of the pylon due to pylon toe-out. The inboard surface of the pylon, like the strut, does not seem to be affected by this change, though. Figure 103, shows that increasing pylon toe-out increases the pressure peak near the leading edge of the section.

For pylon toe-in, cases for angles of up to 4° were investigated. Figures 104 to 107 show the effects of pylon toe-in. Again, as found in the results for the pylon toe-out investigation, the results show that pylon toe-in does not affect the pressure distribution on the strut nor the inboard surface of the pylon. As expected, based on the pylon toe-out investigation, the pressure peak near the leading edge of the section reduces with increasing pylon toe-in. It can therefore be concluded that pylon toe affects mainly the pressure distribution on the outboard surface of the pylon, with only minor effects on the strut and inboard surface of the pylon.

### 6.5.2. Effect of strut incidence

The effects of strut incidence were studied next. In this study, the same baseline design used for the pylon toe study was used as a comparator. This baseline design has the same angle of attack as the root section of the wing. The study investigated strut incidence angles of up to –3° (relative to the root section of the wing). Figures 108 to 111 show the effects of strut incidence on the strut and pylon.

In Figure 108, which is a section on the strut near the pylon, decreasing the strut incidence results in only a slight reduction in shock strength. There is essentially almost no change in the shock position at this station due to strut incidence. A larger change in the pressure coefficient distribution is seen on the bottom surface of the strut due to strut incidence change. We see that decreasing strut incidence increases the pressure peak and lengthens the supersonic plateau on the bottom surface. Also, based on the –3° strut incidence pressure distribution plot on the bottom surface, we see a weak shock forming with decreasing strut incidence.

A more dramatic change in pressure coefficient distribution due to strut incidence can be seen when we look at Figure 109, which is the distribution further away from the pylon. This result shows that with decreasing strut incidence, the loading on the strut decreases and the shock on the upper surface of the strut at that section decreases in strength (and ultimately disappears) while moving towards the leading edge of the section. Conversely, the pressure distribution on the lower surface increases with decreasing strut incidence. We see that the strut is unloaded at about –3° strut incidence at this section (at position $y$=12), although the pressure coefficient distribution shapes on the upper and lower surface are not similar. This uneven local loading will produce a torsional load on the strut.

In Figure 110, we see the effect of strut incidence on a section of the strut farther away from the pylon. Here, the effect of strut incidence change is quite pronounced, with shock disappearing on the upper surface and the pressure distribution increasing on the lower surface with decreasing strut incidence. At this section, the strut unloads at about –2° incidence. A –3° strut incidence (which was what was required to unload the strut at the $y$=12 station) causes the strut at this section to produce negative lift. Also, at –2°, the strut is somewhat evenly loaded, and hence would not produce a significant torsional load.

Figure 111 shows the effect of strut incidence on the pressure coefficient distribution on the pylon. Although the effect is small, strut incidence does reduce the shock strength on the inboard surface of the pylon slightly, at about the same magnitude seen at the upper surface of the strut at the $y$=18 section. This is expected since this is the same shock that is on the strut. No discernable trends on the outboard surface of the pylon can be seen due to strut incidence.

Based on these results, it would be safe to conclude that the effects of strut incidence are large away from the pylon but small in the wing/pylon/strut junction. This result shows that strut twist should be used to unload the strut, at least at sections away from the pylon. Other geometric changes have to be made in the wing/pylon/strut juncture to reduce the shock strength.

### 6.5.3. Effect of strut twist

The next step in investigating the effect of geometric changes to the design was to examine strut twist. The same untwisted, 0° strut incidence (relative to the wing root section) design that was used in the previous studies was again used as the baseline design. Based on the results obtained from the strut incidence study, two twist cases were studied. To unload the strut, a strut incidence of –1° (relative to the wing root section) was used, with a –3° and –4° strut twist for the two respective cases. This means that for the –3° strut twist case, the root section of the strut would be at –1° incidence relative to the wing root section while the tip section of the strut (attached to the pylon) would be at a –4° incidence relative to the wing root (i.e. there would be a –3° difference between the root and tip sections). For the –4° strut twist case, the strut tip section would be at a –5° incidence angle relative to the wing root (i.e. a –4° difference between the root and tip sections). The strut is linearly lofted between the root and the tip.

Figures 112 to 115 show the results from the strut twist study. Figure 112 gives the pressure coefficient distribution at the $y$=18 section on the strut, close to the pylon. We can see that on the upper surface, although the pressure distribution is lower when the section is at a lower incidence, there is still a strong shock. This plot shows that the net effect on the upper surface of the strut due to the change in twist and incidence was only to lower the pressure coefficient distribution. On the bottom surface, we see a greater effect with the pressure distribution becoming supercritical and a shock emerging with increasing strut twist.

Figure 113 gives the pressure coefficient distribution at *y*=12 on the strut, which is further away from the pylon. On this plot we find similar results obtained from the strut incidence study. It also shows that a –4° strut twist produces negative lift on the strut, while the –3° strut twist design results in a nearly unloaded strut. It would seem that a little more twist (perhaps 0.1° or 0.2°) from the –3° twist design is needed to fully unload the strut. Figure 114, which is the pressure distribution at *y*=6, farthest away from the pylon, shows a similar result. In examining these results collectively, it can be concluded that a combination of strut incidence and strut twist can be used to unload the strut evenly, away from the strut/pylon juncture.

Figure 115 shows the effect of strut twist on the pressure coefficient distribution on the pylon. On the inboard surface of the pylon, the same effect of shifting the pressure coefficient distribution down seen on the strut (at *y*=18) occurs on the pylon. As seen in the other studies, any changes to the strut that has an effect on the shock at the wing/pylon/strut intersection also determines the loading and pressure distribution on the inboard section of the pylon. As for the outboard section of the pylon, strut twist has only a small effect on the pressure distribution. Increasing (negative) strut twist seems to increase the pressure distribution on the outboard surface of the pylon at the leading edge half of the section. However, it does not seem to have any effect towards the trailing edge of the pylon.

### 6.5.4. The ‘channel’ effect

As seen in the previous studies, we observed that changing pylon toe, strut twist and incidence resulted in only very minor changes to the strong shock near the wing/pylon/strut intersection. Clearly, something other than the cumulative aerodynamic effect of the individual components was influencing the flow at this section. Observing the pressure distributions, it appeared that the flow in the juncture was acting like a nozzle, choking the flow at a minimum area point at the intersection and expanding the flow downstream, with the expansion terminating in a strong shock (near the trailing edge of the strut). To test this hypothesis, the area distribution which the flow ‘sees’ going through the intersection was examined. Since the area through the intersection is ‘open’ on one side (i.e. there is no wall bounding the intersection going towards the root), an imaginary wall was placed at $y$=16. Figure 116 provides a graphical illustration of this area. It should be noted that the frontal three-dimensional area was calculated instead of calculating the two-dimensional area across a cut near the intersection since the airfoil shape of the pylon also contributes to the flow characteristics at this section. Using the two-dimensional area would eliminate the geometric effect of the pylon. However, we will examine the effect of the pylon later.

In our first try at investigating the area effects on the flow properties through the juncture region, two different designs having different area distributions were made by changing the strut twist, changing the length of the pylon and by changing the location of the pylon and strut relative to the wing. For a comparison, the same baseline design that was used in the other studies, except with a –3° strut twist was chosen as a reference design. Figure 117 illustrates the differences between the designs. Figure 118 gives the three-dimensional area distribution of the three different designs. As we can see, the 2nd design has a smaller area distribution, and a shallower slope than the reference. Also, the position of the minimum area is further aft in the second design compared to the reference. The third design has a much higher area distribution, although the slope of the area distribution is similar to that of the reference design for most of the section. The position of the minimum area for the third design is closer towards the leading edge of the strut than the other two designs.

Figure 119 to Figure 121 show the pressure coefficient distributions at the various stations on the strut. In Figure 119, we see that the strength of the shock was not reduced in any of the designs. The only net effect of the different designs was to move the position of the shock relative to the strut. As expected, the bottom surface of the strut does not seem to be affected by the change in the intersection area. We only observe the effects of twist on the bottom surface. Moving away from the junction, Figure 120 does not show the presence of any shock, as seen in the strut twist study. It is interesting that although the twist for the second and third designs are the same, the effects of twist are amplified in the third design due to the change in pylon chord and, strut and pylon position. This same effect can be seen in Figure 121.

To test the hypothesis that the flow is choked at the minimum area location, the area and Mach number variations were examined. Figure 122 shows the result. The Mach number plots are at the $y$=18 section, close to the pylon. However, the area distribution plots are the three-dimensional frontal area calculated through this intersection as shown in Figure 116. From this plot we can see that indeed the flow reaches a Mach number of 1 close to or at the location of minimum area, confirming the hypothesis that the flow is behaving as if it was through a nozzle. This also explains why changes in the pylon toe, strut twist and incidence did not affect the strength of the shock very much.

### 6.5.5. Effect of the pylon

Next, we looked at the pylon. If the pylon had a large impact on the strength of the shock through the intersection, perhaps the use of a slotted pylon would relieve the accelerating flow through the intersection and reduce the strength of the shock. As an 'extreme slot', we removed the pylon entirely and did a flow analysis of the wing and strut alone. This case shows us the explicit effect of the pylon on the flow through the intersection. Therefore a comparison was made with a –3° strut twist and –1° strut incidence design with and without a pylon.

Figure 123 shows the results of that comparison. Here we only provide the pressure coefficient distribution at the $y$=18 section since we are only concerned with the flow near the pylon and the strength of the shock there. We see that there is only a small reduction of the strength of the shock due to the absence of the pylon. Also the position of the shock moved forward by about 10% of the chord. We can conclude therefore that the pylon has a minor effect on the flow. This result also indicates that since the pylon has only a minor effect, and the strut sweep is very small (4.1°), the nozzle-like flow through the intersection is even more two-dimensional-like than first thought. This is a favorable finding since we need only to change the two-dimensional area distribution between the strut and wing to affect the flow characteristics.

### 6.5.6. Solving the 'channel' effect

With an understanding of the cause of the accelerating flow through the wing/pylon/strut intersection, geometric changes can be made to weaken the shock at this location. One way is to prevent the flow from choking, by increasing the area at the throat, or in this instance, the location of minimum area, to an extent that the ratio of $A/A^*$, which is the ratio of the inlet area to the throat area is less than the critical 'choking' value of 1.027 (calculated at M=0.85). Figure 124 shows the orientation of the strut and wing sections at $y$=18, near the pylon. On inspection, we see that most of the change in area occurs due to the upper surface of the strut. Hence, if that surface were made flat, there would be little variation in the area distribution as the flow passes through.

Two designs were made with the upper surface of the strut near the pylon changed to be flat. In the first design, the lower half of the airfoil section at the tip of the strut (intersecting the pylon) was kept while leaving the upper portion flat. This essentially reduces the airfoil thickness by half from 8% to 4% *t/c*. The symmetric airfoil section at the strut root is kept, and the strut is linearly lofted between tip and the root sections. It should be noted that the airfoil section at the strut tip has a sharp leading, due to the intersection between the lower half of the airfoil and the flat top. We expect to have a pressure peak at the leading due to this sharp leading edge. The second design builds on the first design, where at the strut tip, the flat upper surface of the airfoil section is kept, and thickness is added to the lower surface to increase the strut thickness to 8% t/c. The leading edge of this airfoil section was also rounded. All the designs have the strut at a $-3^\circ$ twist angle and a $-1^\circ$ incidence angle relative to the wing root section. As a baseline design, the same design using the symmetric airfoil section at the tip was analyzed. Figure 125 shows the differences between the designs at a section at *y*=18, near the pylon.

Figure 126 shows the surface contour result comparison between the 3 different designs. As we can see, the shock strength was weakened considerably in the 4% *t/c* flat strut design, and the shock eliminated in the 8% t/c flat strut design. Figure 127 gives the pressure coefficient distribution at the *y*=18 station on the strut. As seen from the pressure contours, the strong shock on the upper surface of the strut was considerably weakened and eliminated from the 4% *t/c* flat strut design to the 8% *t/c* flat strut design. Also, as expected, there is a sharp pressure spike at the leading edge of the 4% *t/c* flat strut design. This spike is reduced in magnitude, due to the rounding of the leading edge of the tip strut airfoil in the 8% *t/c* flat strut design. Several observations should also be made about the bottom surface pressure coefficient distribution of the strut. We notice that there is a strong shock that has formed on the bottom surface of the 8% *t/c* flat strut design. This is to be expected due to the extra thickness that was added to there to make up the thickness. Airfoil shaping on this bottom surface should result in weakening the shock to an acceptable level. Also, we see that for both the 4% *t/c* and 8% *t/c* flat strut designs, the strut is producing negative lift. Based on the strut incidence and strut twist studies, we feel that changing the incidence and twist of the strut can unload the strut.

Figure 128 shows the pressure coefficient distribution on the pylon for the three designs that were analyzed. As seen on the strut, the shock on the inboard surface of the pylon is weak for the 4% t/c flat strut design and is eliminated for the 8% *t/c* flat strut design. It is interesting to note also that on the outboard surface of the pylon, the 8% *t/c* flat strut design produced a weak shock at about the 0.75 *x*/*c* location. As with the strut, we believe that changing the pylon toe can unload the pylon.

## 7. Conclusions

In this study, we identified the key aerodynamic issues and resolved them for the transonic design of the A7 SBW demonstrator aircraft wing. The primary accomplishments are:

- We selected a wing planform for the A7 SBW demonstrator aircraft based on previous SBW studies. The wing was scaled to meet the A7's wing loading requirements and the strut sweep reduced to prevent it from coinciding with the landing gear bay.
- Airfoil sections at four different span stations for the wing were designed by performing parametric studies involving the addition and subtraction of a 6th order polynomial thickness distribution on the upper and lower surface of an existing NASA supercritical airfoil section. MSES was used to analyzed the airfoil performance.
- Inviscid analysis on the entire A7 SBW demonstrator aircraft geometry (including the fuselage) was done. Key design issues were identified. Most notable was the presence of a strong shock at the wing/pylon/strut intersection.
- Parametric studies involving the design of the wing/pylon/strut intersection were performed to understand the flow characteristics at the intersection. The effects of pylon toe, strut incidence, strut twist and presence of the pylon were investigated. It was found that the flow at the intersection behaves like to a two-dimensional

nozzle. The strength of the shock at this intersection was reduced and even eliminated by flattening the upper surface of the strut near the intersection.

Although it was previously assumed that the interference drag caused by the wing/pylon/strut intersection would be manageable with CFD, no detailed aerodynamic design had been done. Now, it has been shown that the intersection can be designed to have minimal drag at the intersection. Also, specific airfoil sections had not been designed for use on the SBW. These airfoils are now available. The sensitivities obtained in the parametric studies involving pylon toe, strut twist and incidence studies will be useful in any future SBW design. The study has provided us with a baseline transonic wing design for the A7 SBW demonstrator aircraft

## 8. Recommendations

Although the key issues were addressed in the design of the A7 SBW demonstrator aircraft wing, several other issues need to be addressed. These include:

1. Although the airfoil section designs on the wing have been completed, additional work on the wing twist is needed, mainly to weaken the shock near the root, and transfer some of the wing loads to the tip. Also, some modification to the root and tip sections of the wing will be needed to account for 3-D effects.
2. Further design is required for the tip airfoil of the strut (intersecting the pylon), especially the lower strut surface.
3. The proper combination of pylon toe and strut twist needs to be determined to fully unload the strut. It is preferred that the strut be evenly loaded on both and upper and lower surfaces. This may be difficult near the pylon.

4. This wing/pylon/strut configuration has to be analyzed including the fuselage to address fuselage interference effects.

The three-dimensional CFD analysis done in this study was inviscid. Viscous analysis and design is required to complete the work. During the course of the project, viscous analysis and design codes that were needed for this task were not made available to us. The availability of these codes is critical to the completion and continuation of this work.

# 9. Figures

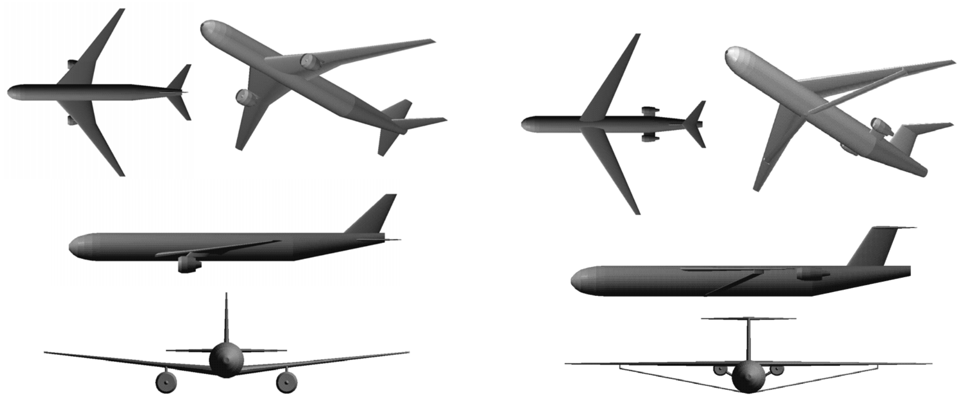

Cantilever baseline design configuration

Fuselage mounted engine strut-braced wing design

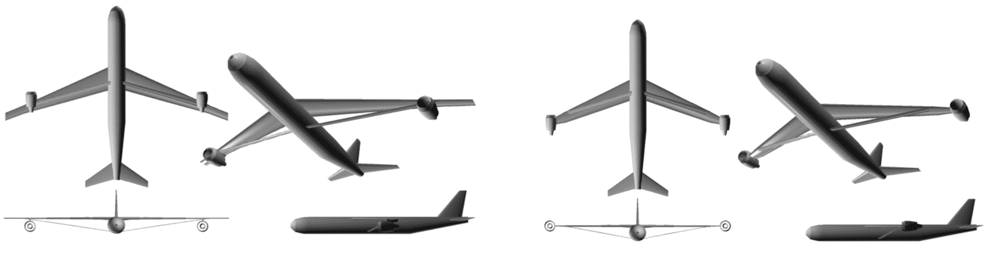

Wing mounted engine strut-braced wing design

Tip mounted engine strut-braced wing design

Figure 1: General configuration layouts of different designs investigated.

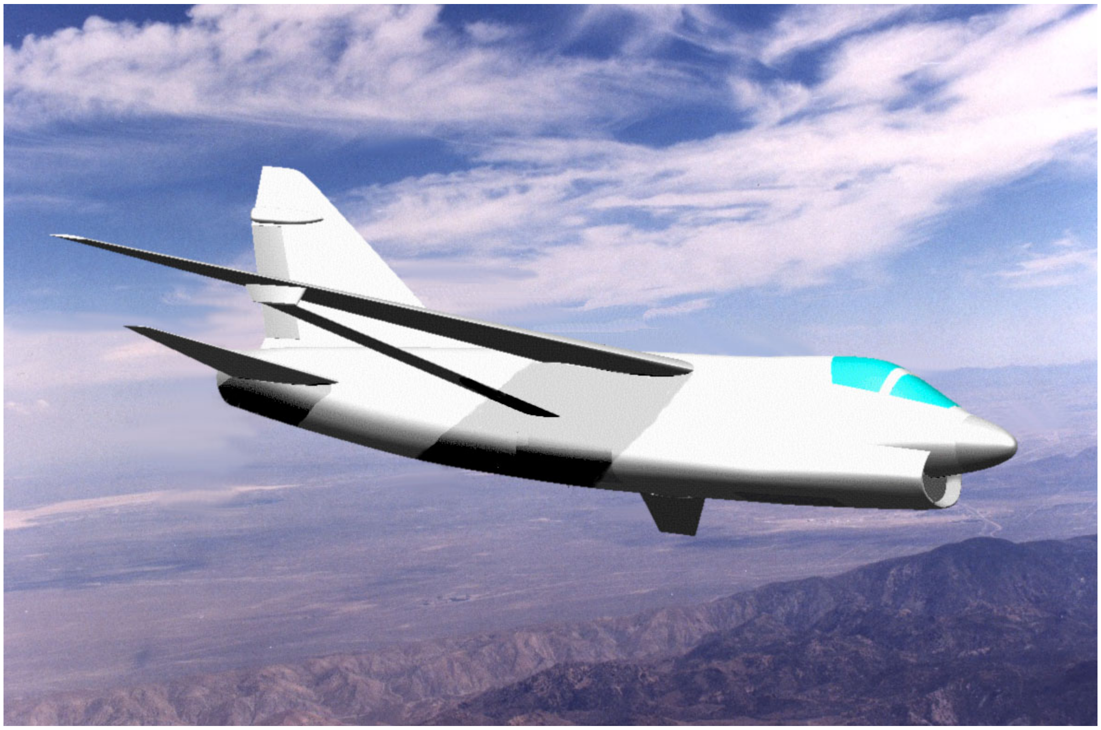

Figure 2: Proposed A7 SBW demonstrator aircraft for the 2000 RevCon project.

Figure 3: Picture of the A7 SBW demonstrator aircraft made by the senior class design team ( Team RevCon).

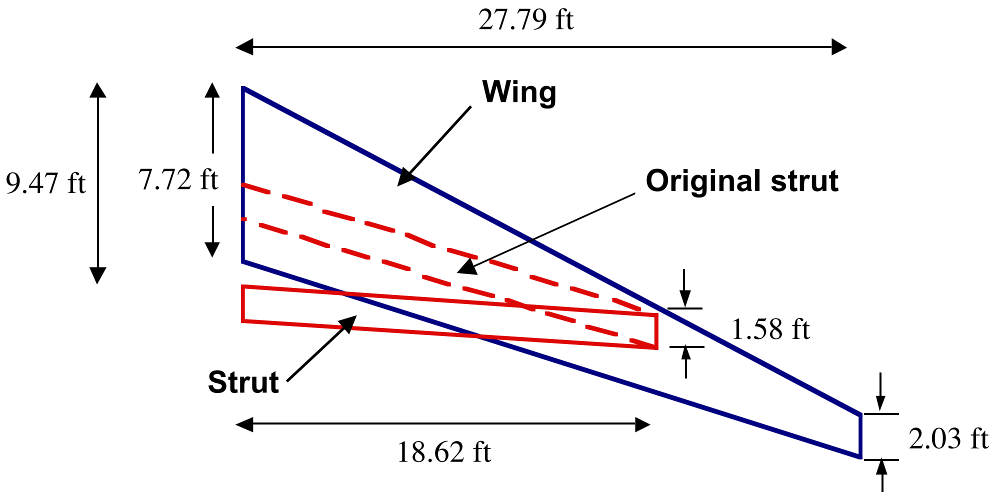

Wing leading edge sweep = 29.2°
Strut leading edge sweep = 4.09°
Strut original leading edge sweep = 19.4 °
Pylon height = 0.77 ft
Strut dihedral = 13.6°
Vertical distance between wing and strut = 5.27 ft

Figure 4: Dimensions of the scaled selected A-7 SBW demonstrator wing and strut.

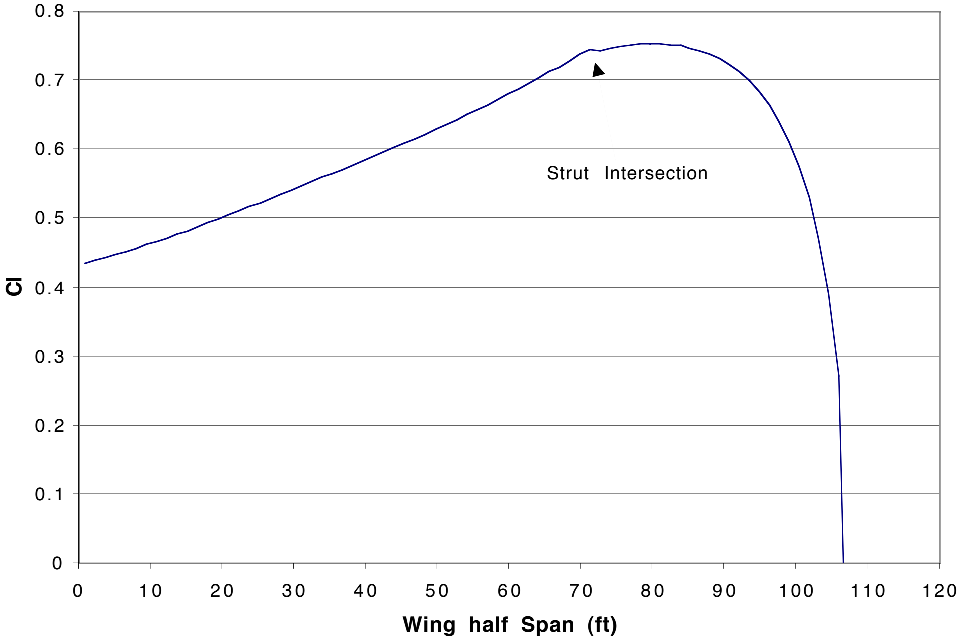

Figure 5: Lift coefficient distribution on the selected optimized SBW configuration wing.

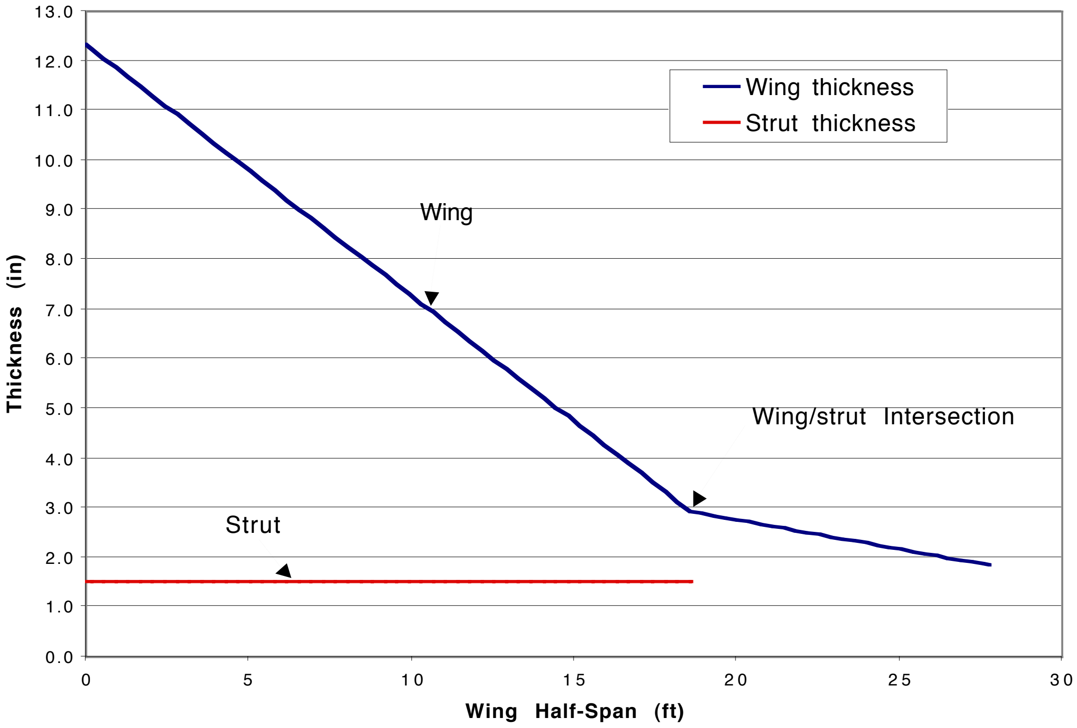

Figure 6: Thickness distribution on the A7 SBW demonstrator wing and strut

Figure 7: t/c distribution on the A7 SBW demonstrator wing and strut.

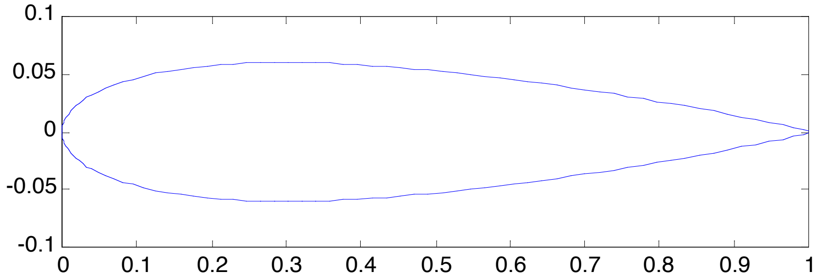

Figure 8: NACA 0012 airfoil (produced by XFOIL)

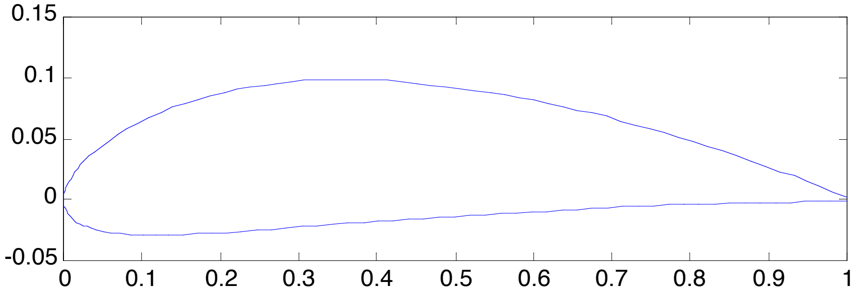

Figure 9: NACA 4412 airfoil (produced by XFOIL)

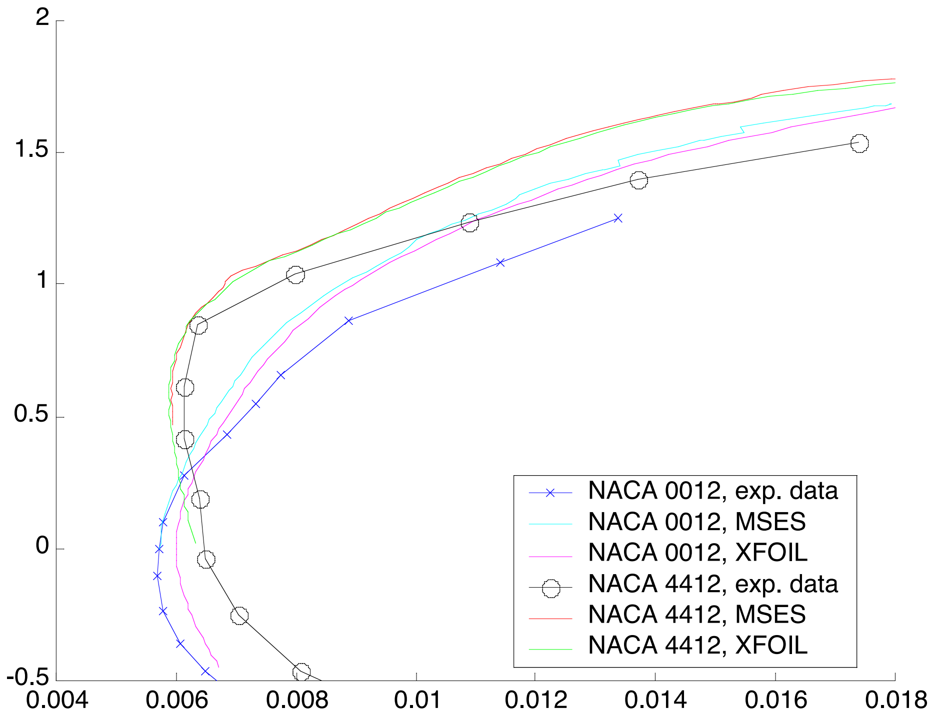

Figure 10: Comparison of drag polar predictions with experimental data. Re=6 x $10^{6.}$

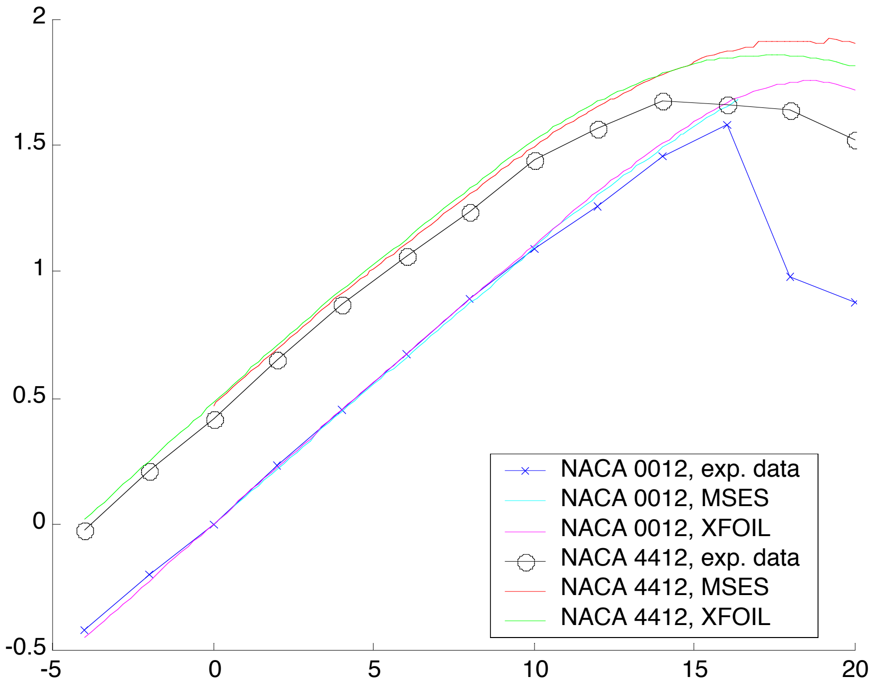

Figure 11: Comparison of lift predictions with experimental data. Re=6x10$^6$.

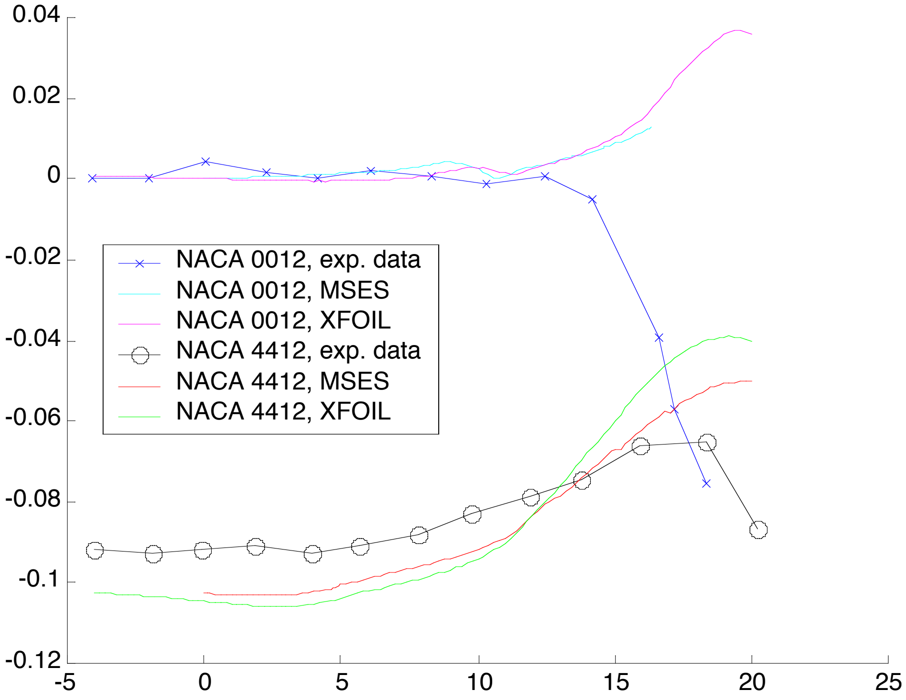

Figure 12: Comparison of moment predictions with experimental data. Re=6x10$^6$.

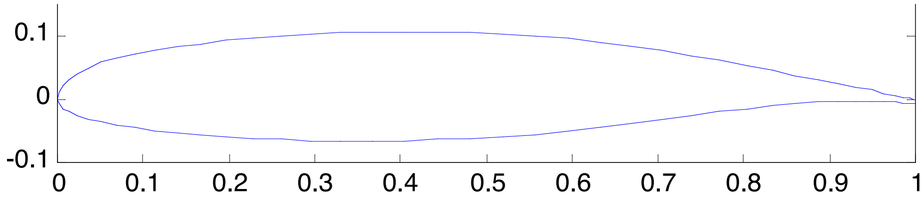

Figure 13: GA(W)-1 airfoil.

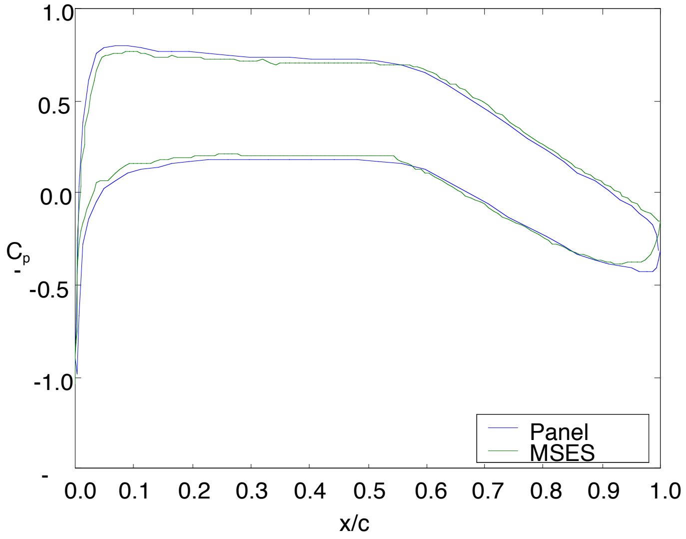

Figure 14: Comparison of the pressure coefficient distribution predictions of the GA(W)-1 airfoil.

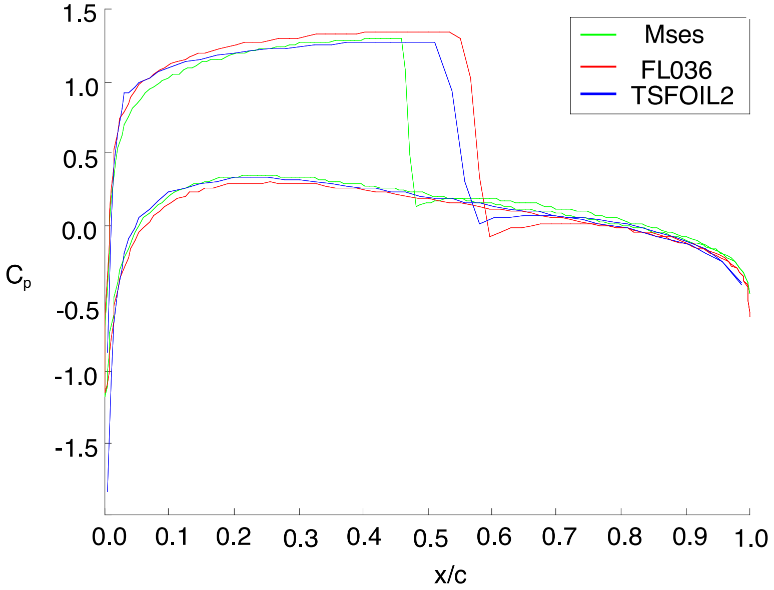

Figure 15: Comparison of different calculations of pressure coefficient for a NACA 0012 airfoil. M=0.75, $\alpha=2^o$.

Figure 16: Surface triangulation of the ONERA M6 wing (re-meshed case)

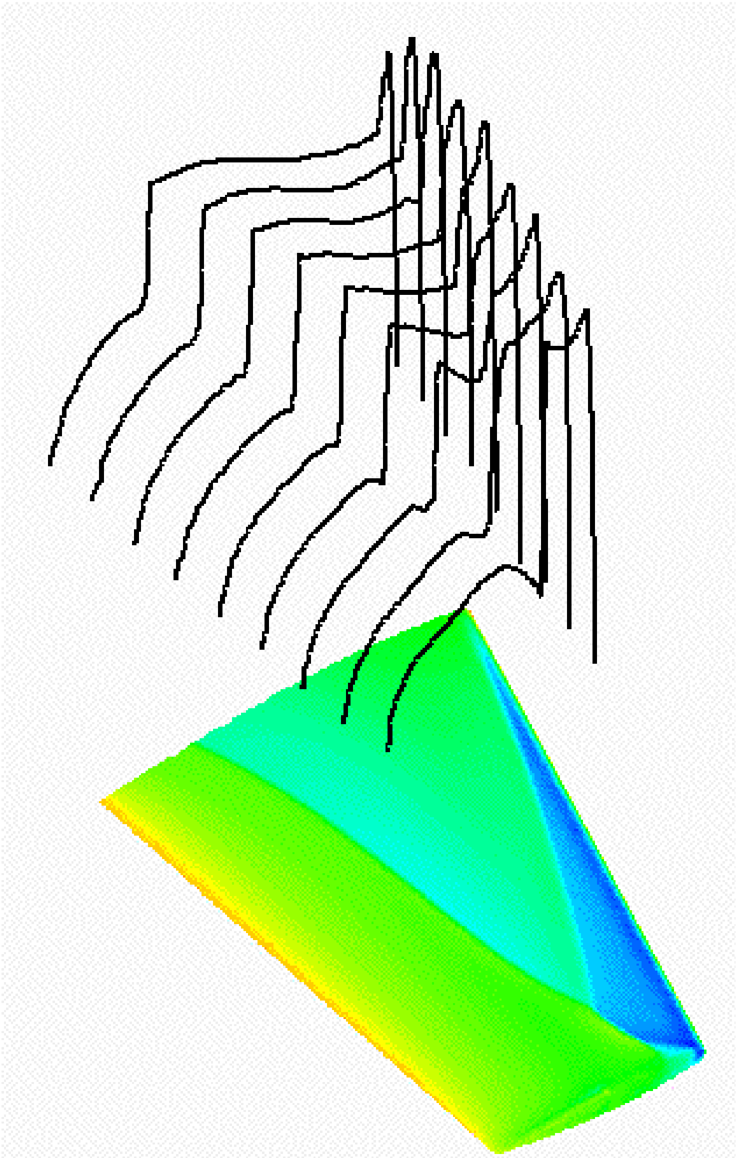

Figure 17: Pressure coefficient contours and plots at various spanwise stations for the ONERA M6 Wing test case. FELISA inviscid solution, M=0.84, $\alpha$=3.06°

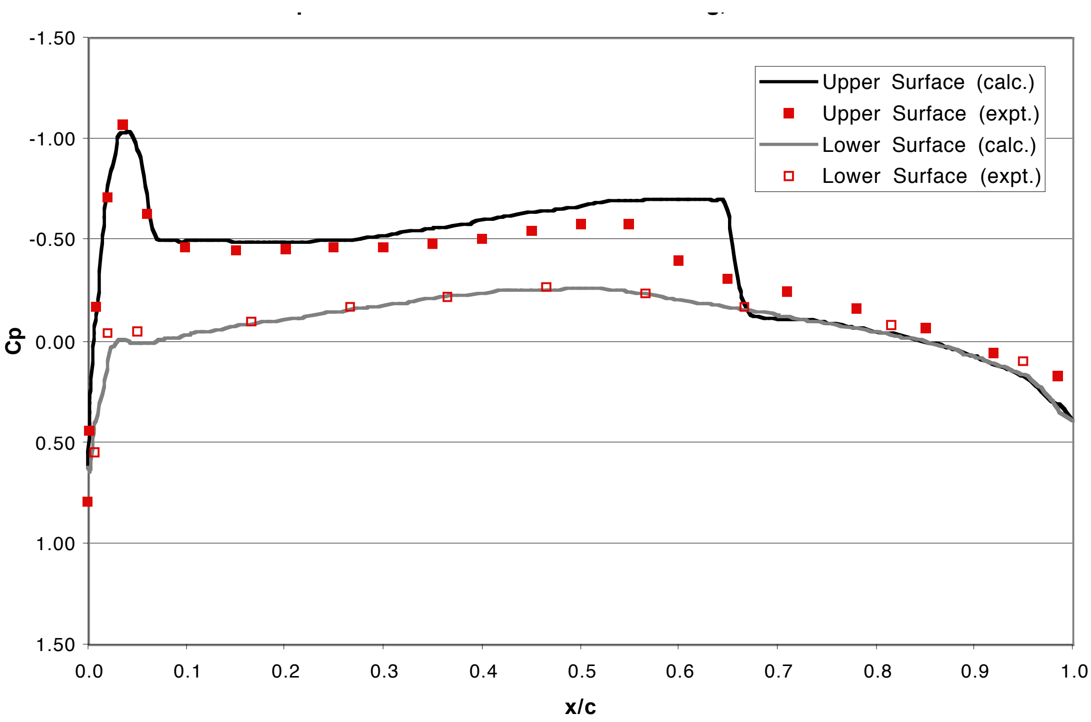

Figure 18: Comparison of pressure coefficient data from the FELISA inviscid solution and experimental data for the ONERA M6 wing. M=0.84, α=3.06°, η=0.2.

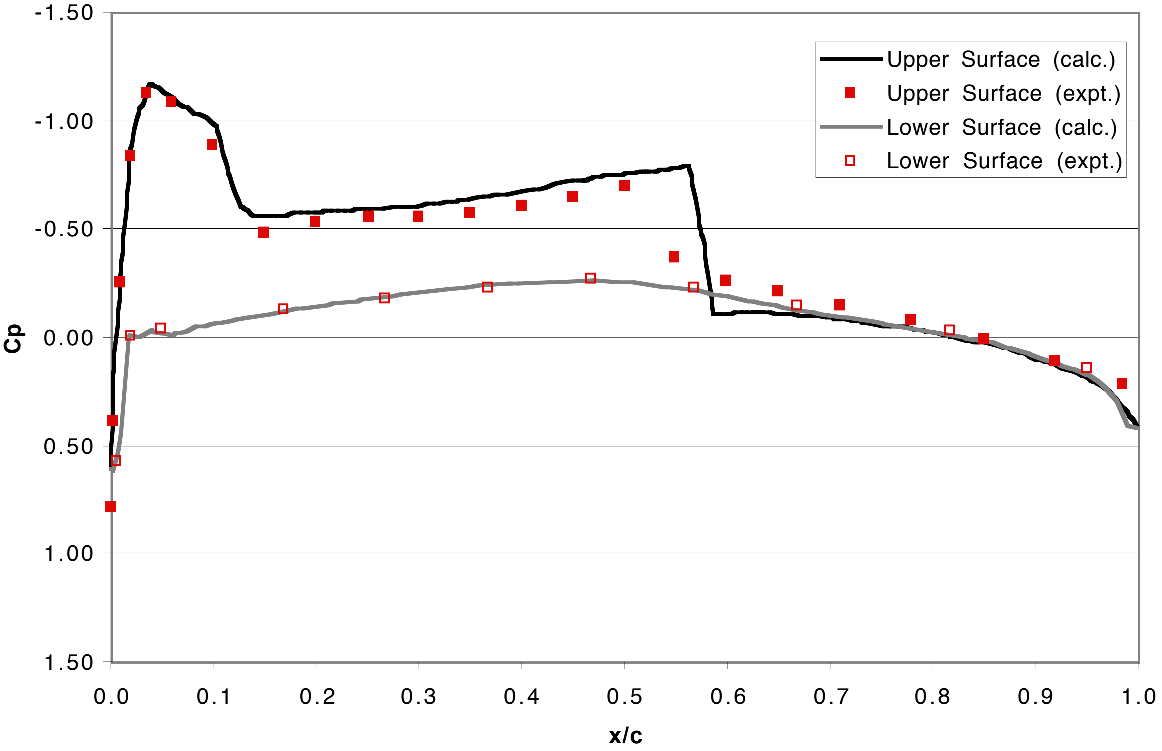

Figure 19: Comparison of pressure coefficient data from the FELISA inviscid solution and experimental data for the ONERA M6 wing. M=0.84, α=3.06°, η=0.44.

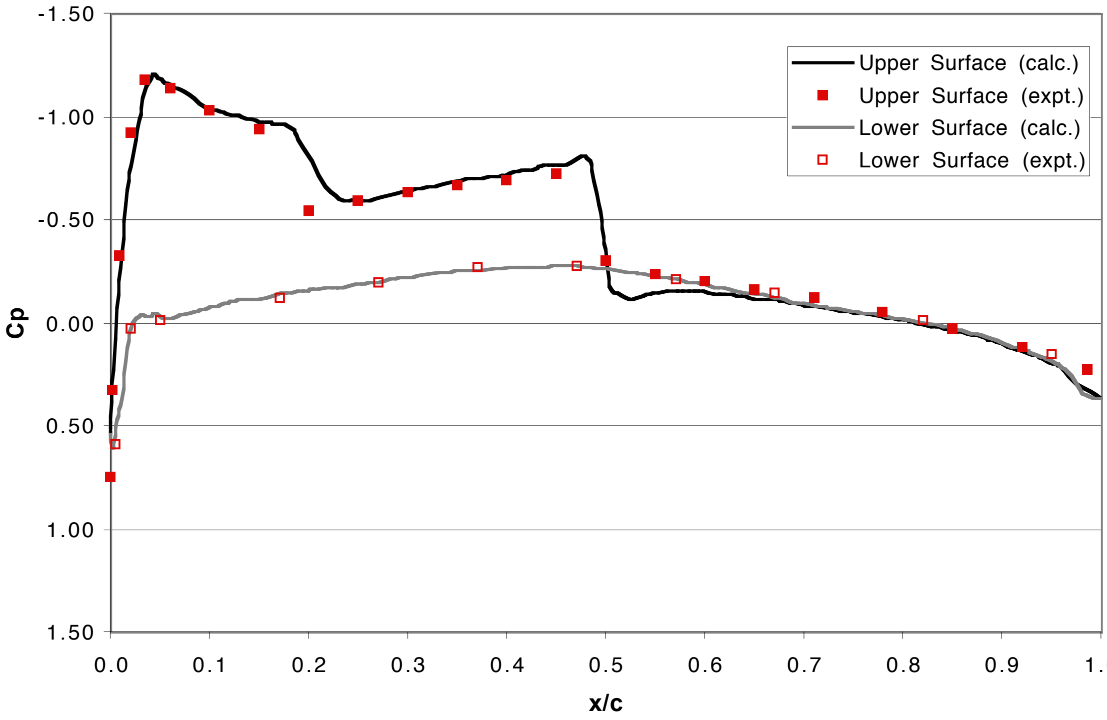

Figure 20: Comparison of pressure coefficient data from the FELISA inviscid solution and experimental data for the ONERA M6 wing. M=0.84, $\alpha$=3.06°, $\eta$=0.65.

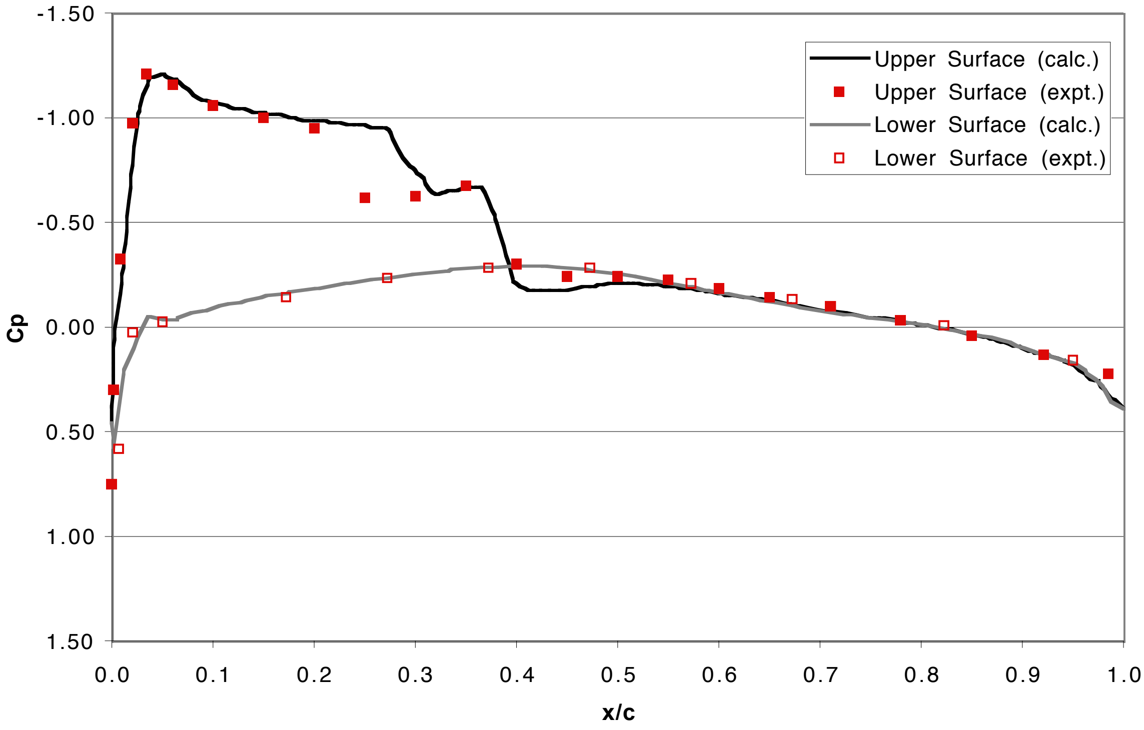

Figure 21: Comparison of pressure coefficient data from the FELISA inviscid solution and experimental data for the ONERA M6 wing. M=0.84, $\alpha$=3.06°, $\eta$=0.8.

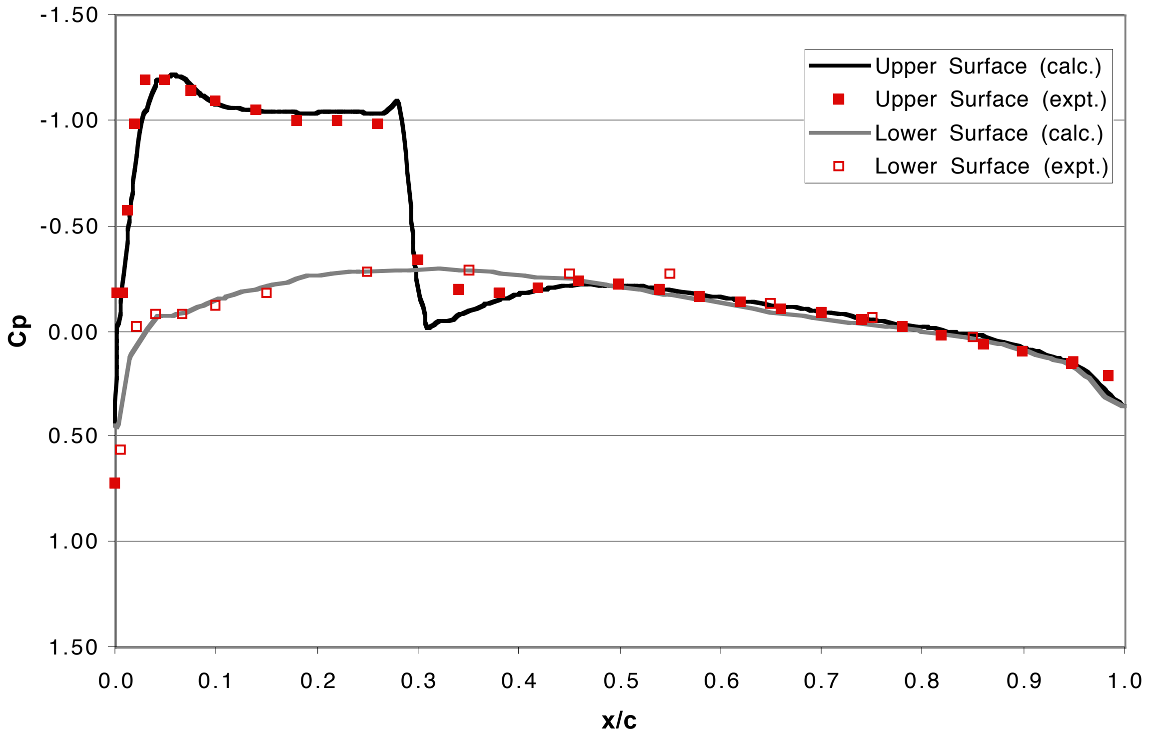

Figure 22: Comparison of pressure coefficient data from the FELISA inviscid solution and experimental data for the ONERA M6 wing. M=0.84, $\alpha$=3.06°, $\eta$=0.9.

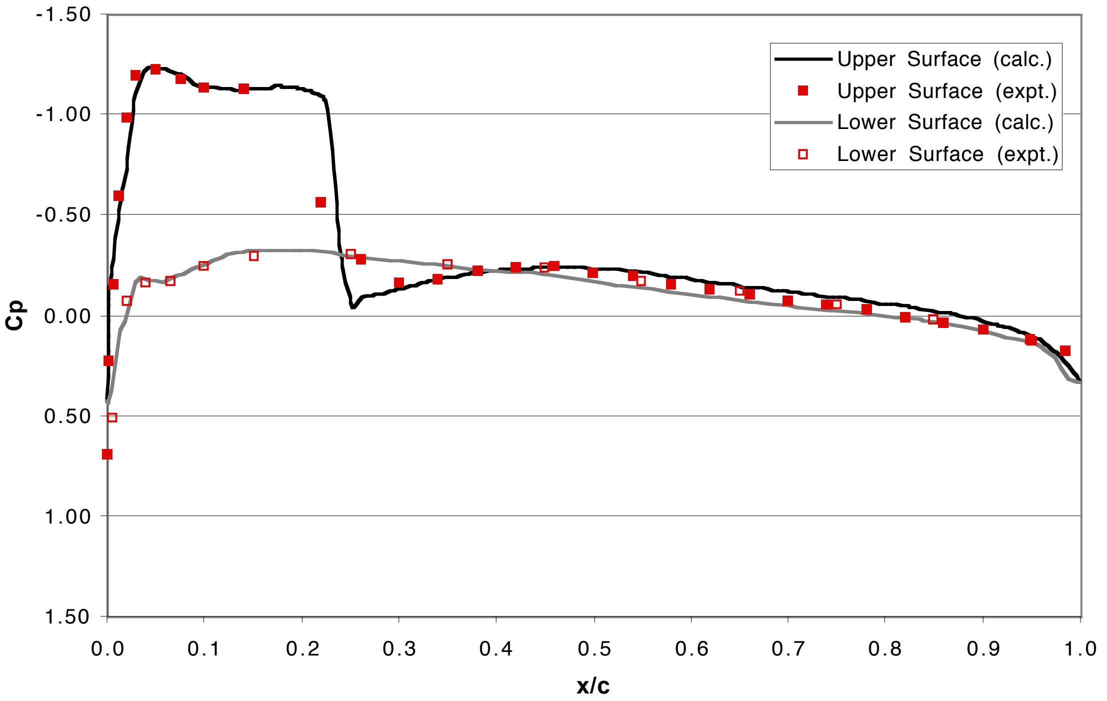

Figure 23: Comparison of pressure coefficient data from the FELISA inviscid solution and experimental data for the ONERA M6 wing. M=0.84, $\alpha$=3.06°, $\eta$=0.95.

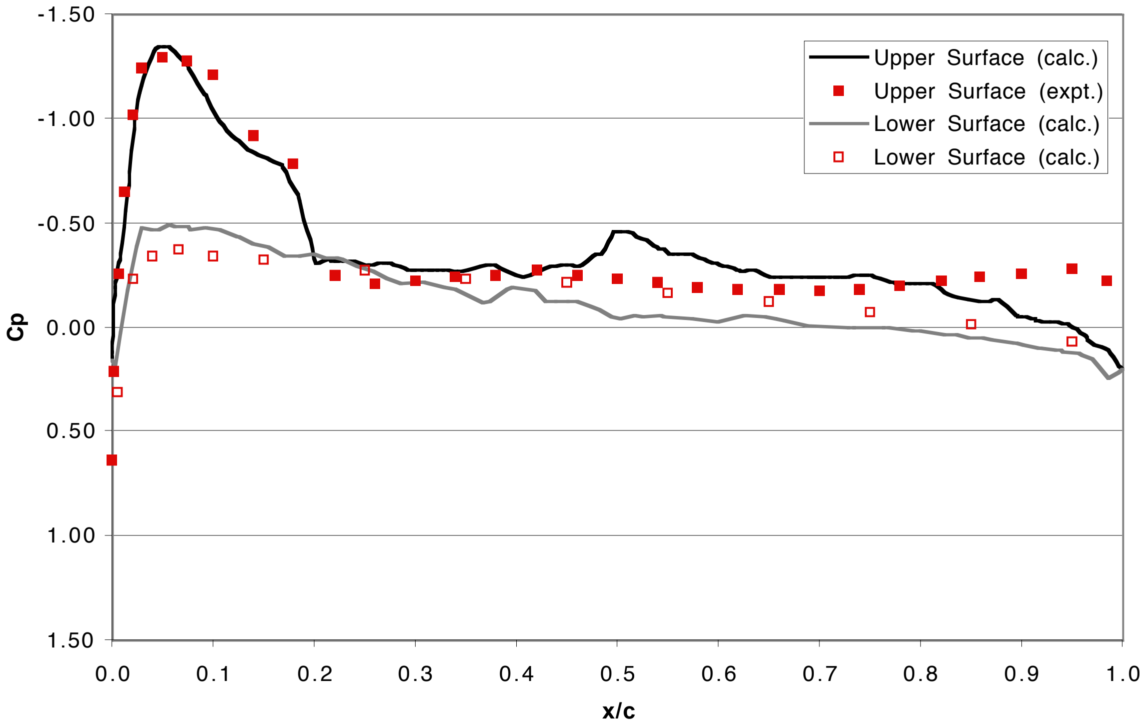

Figure 24: Comparison of pressure coefficient data from the FELISA inviscid solution and experimental data for the ONERA M6 wing. M=0.84, $\alpha$=3.06°, $\eta$=0.99.

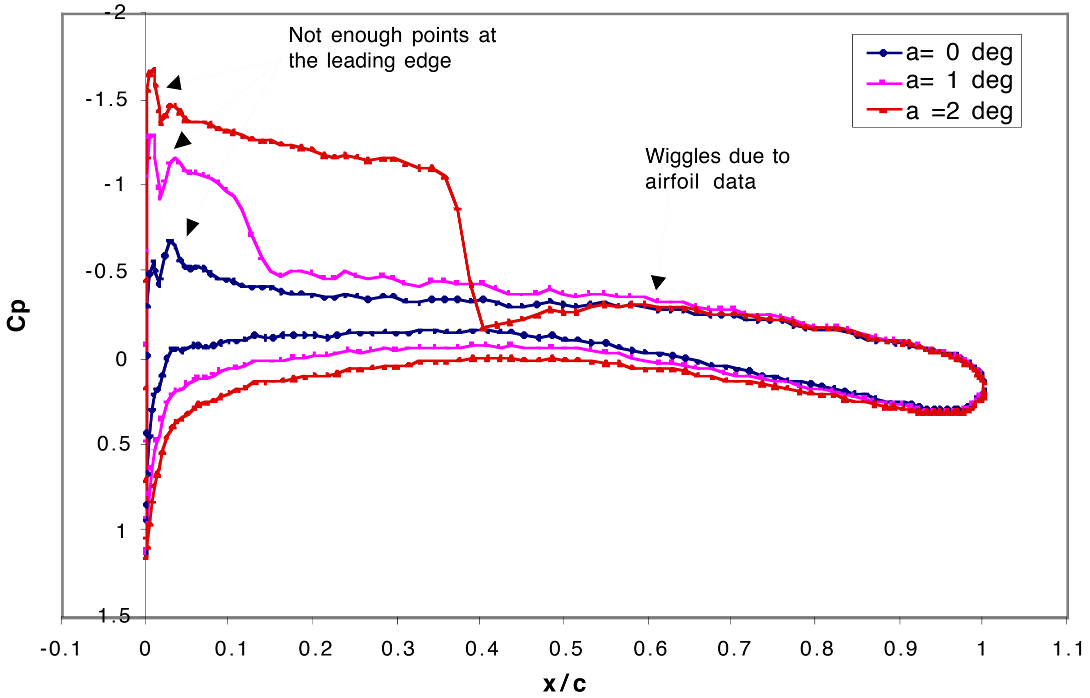

Figure 25: FLO36 analysis of the SC(2)-0406 airfoil at different angles of attack. M=0.75. Plot shows that deficiencies in airfoil coordinates causes irregularities in analysis results.

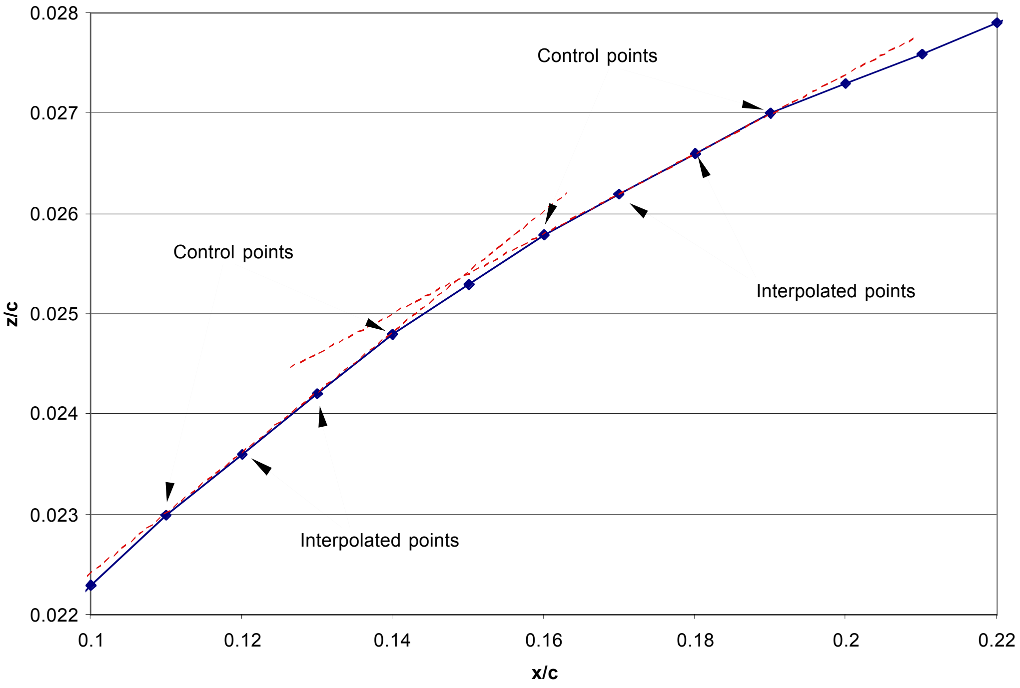

Figure 26: Plot of a magnified section (top surface) of the SC(2)-0406 airfoil. Blue line with blue tick marks show the original NASA airfoil coordinates. Red dotted lines show interpolated sections of the airfoil. The red lines reveal that some of the coordinates supplied by NASA are interpolated points between the actual airfoil control points.

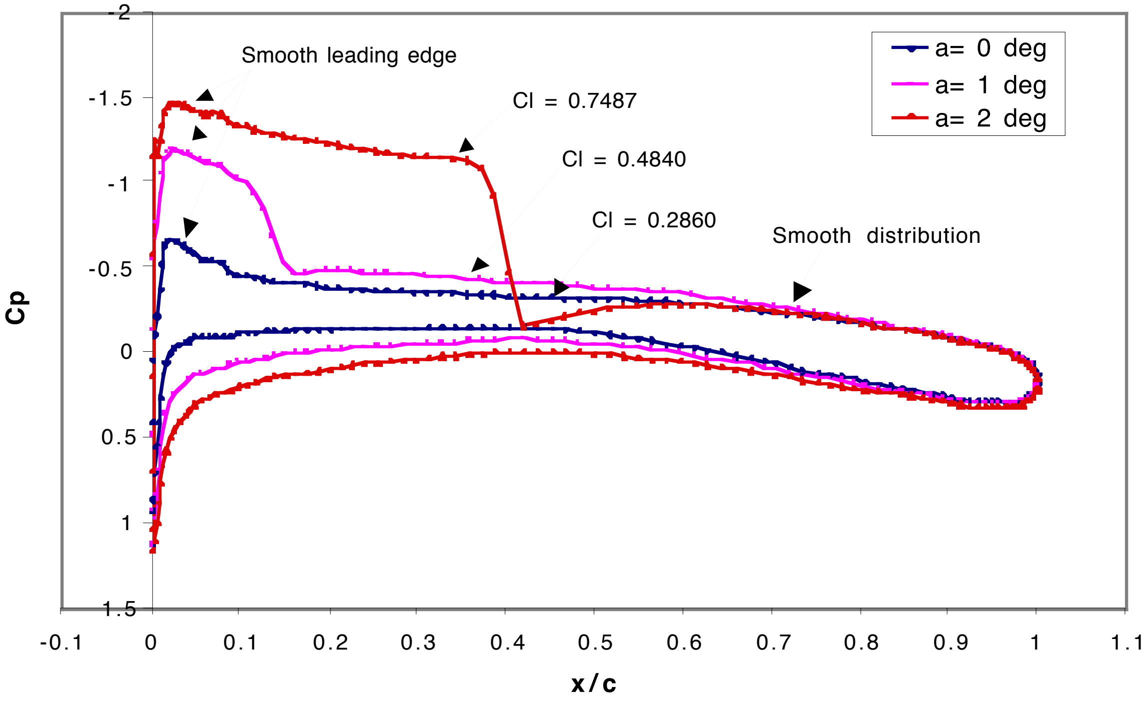

Figure 27: FLO36 analysis of the SC(2)-0406 airfoil at different angles of attack using 'cleaned-up' airfoil coordinates. M=0.75.

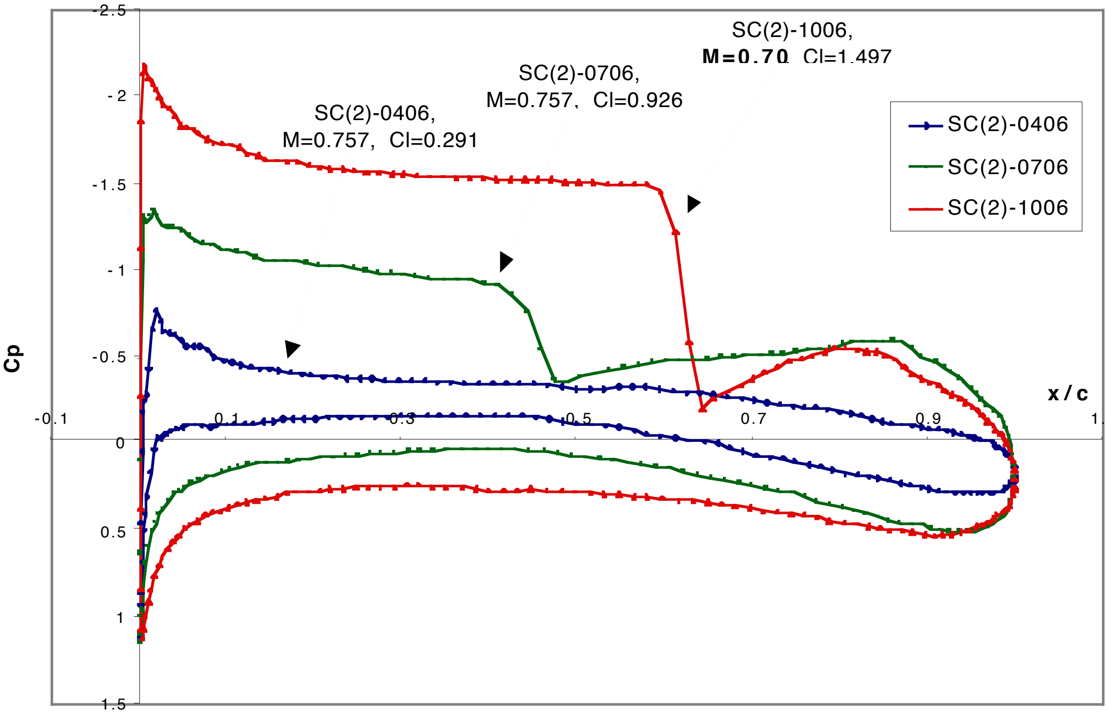

Figure 28: FLO36 results comparing the pressure coefficient distribution on three different airfoils. $\alpha=0^{\circ}$

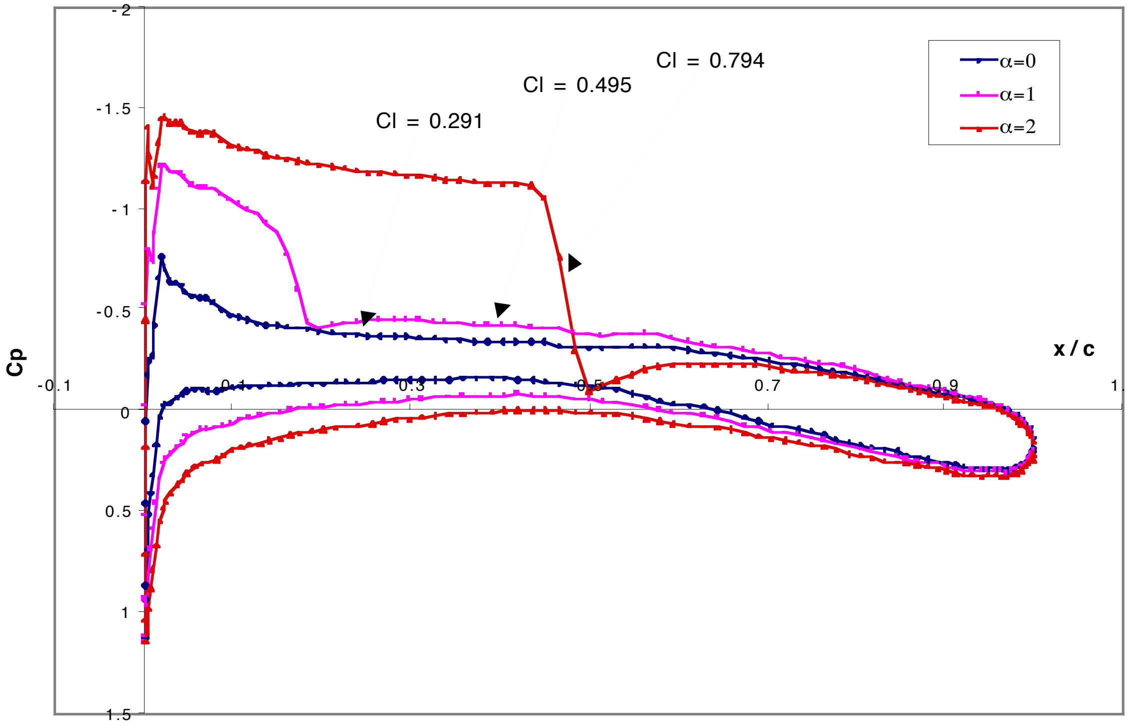

Figure 29: FLO36 pressure coefficient results on the SC(2)-0406 airfoil at different angle of attacks.

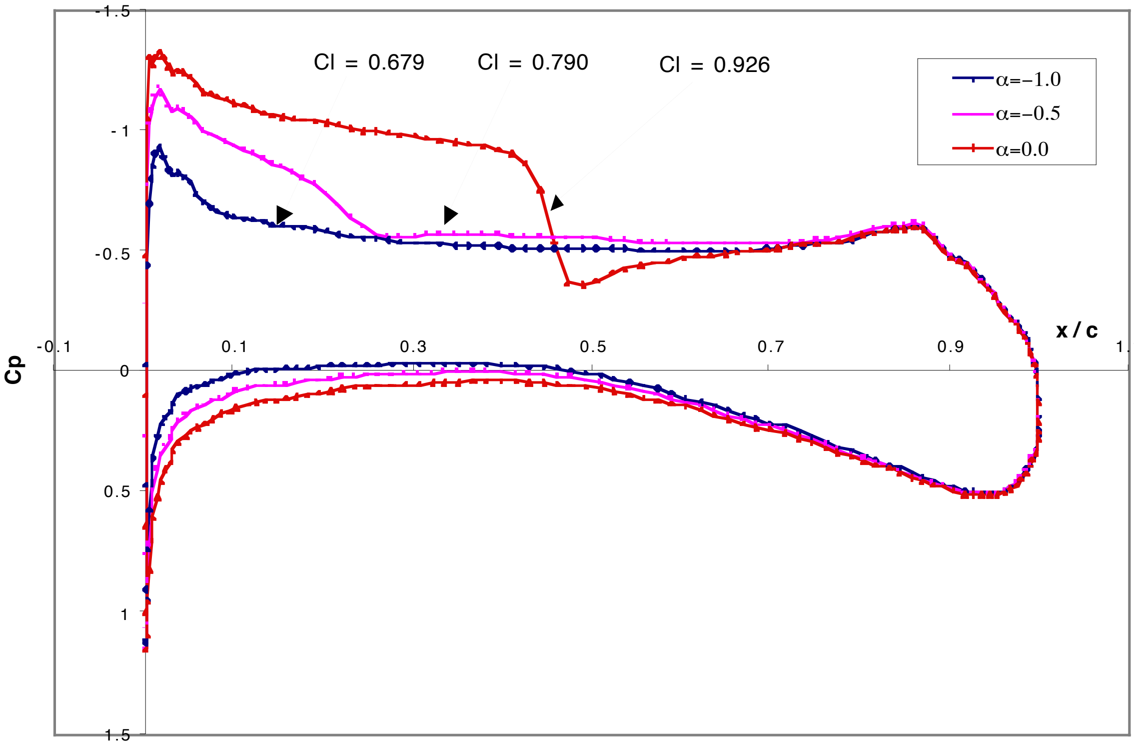

Figure 30: FLO36 pressure coefficient results on the SC(2)-0706 airfoil at different angle of attacks.

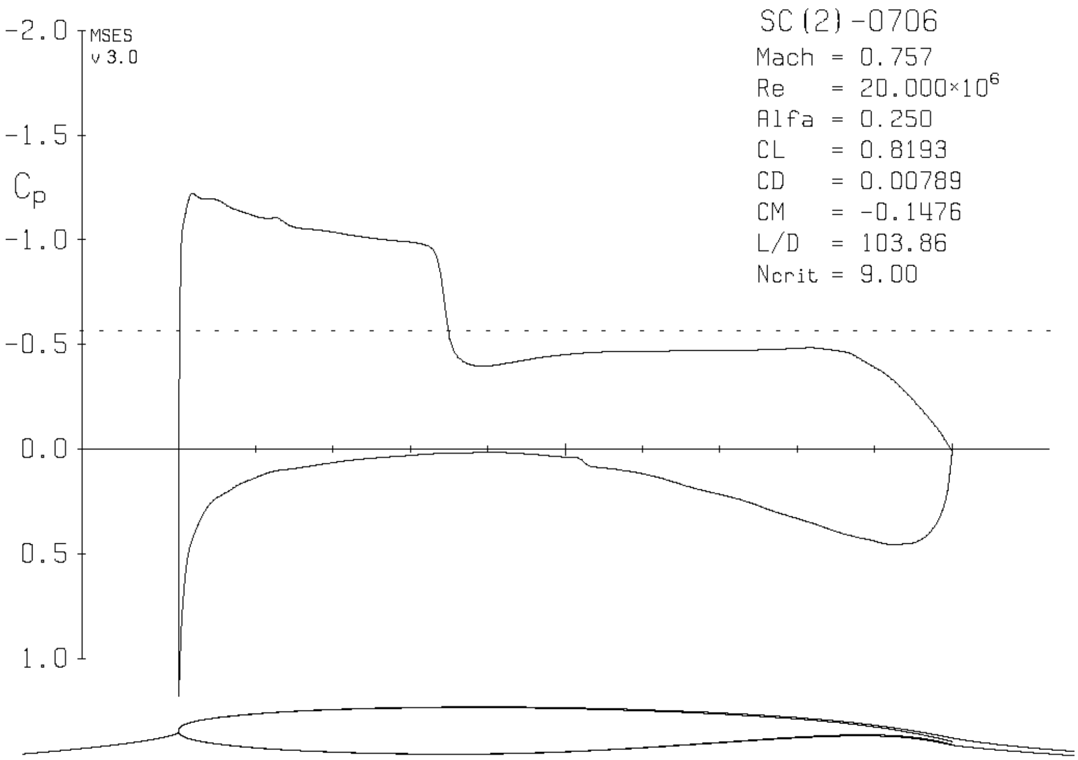

Figure 31: MSES viscous results on the SC(2)-0706 airfoil.

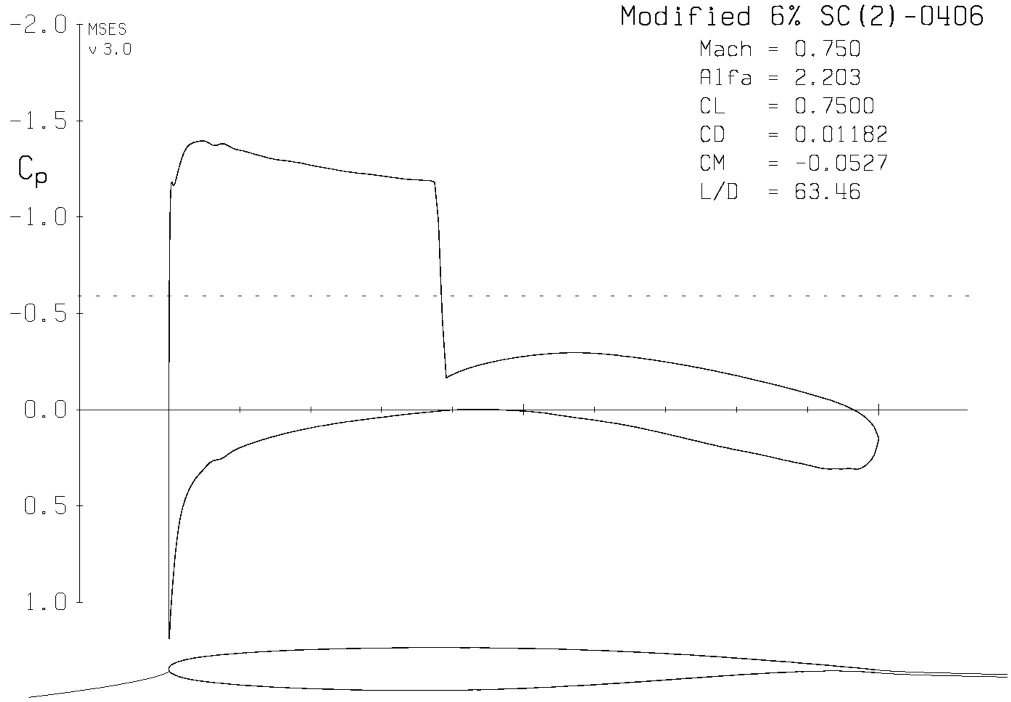

Figure 32: Inviscid MSES solution of the SC(2)-0406 airfoil.

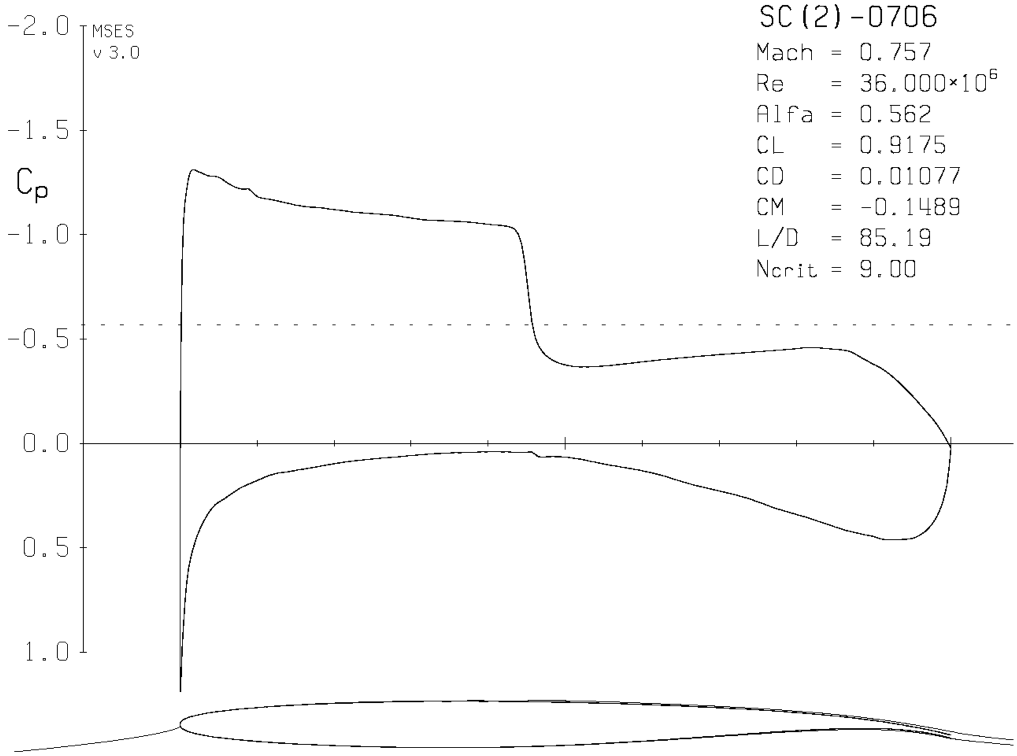

Figure 33: Viscous MSES solution of the SC(2)-0706 airfoil.

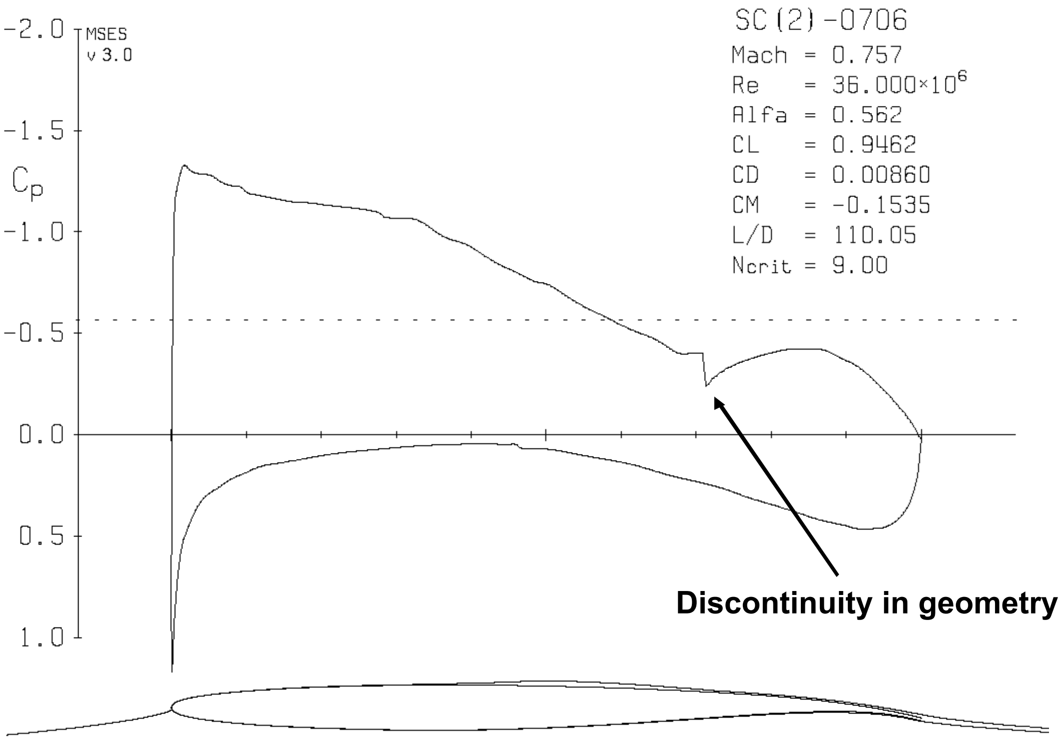

Figure 34: MSES viscous analysis of a modified SC(2)-0706 using the MSES inverse design capability. Pressure coefficient distribution shows an apparent shock-free airfoil.

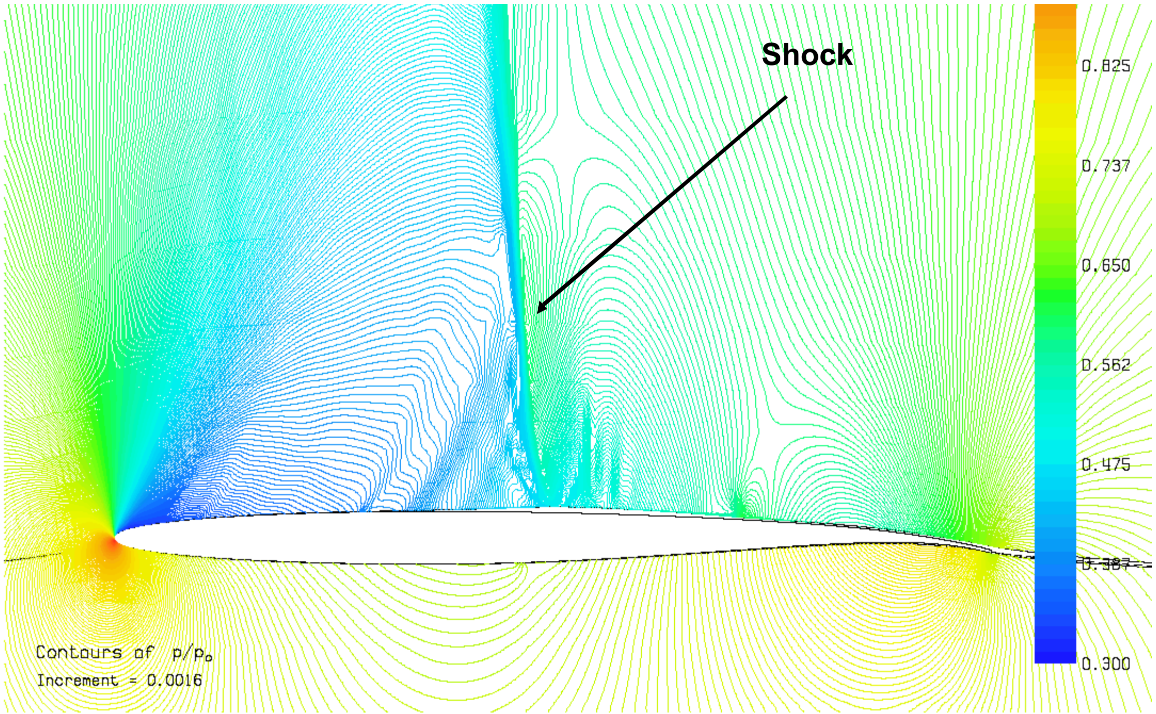

Figure 35: Pressure contour plot of an MSES viscous solution of the modified apparent 'shock-free' SC(2)-0706 airfoil. Although the surface pressure coefficient plot does not show the presence of the shock, it is clear that a shock still exists on the upper surface.

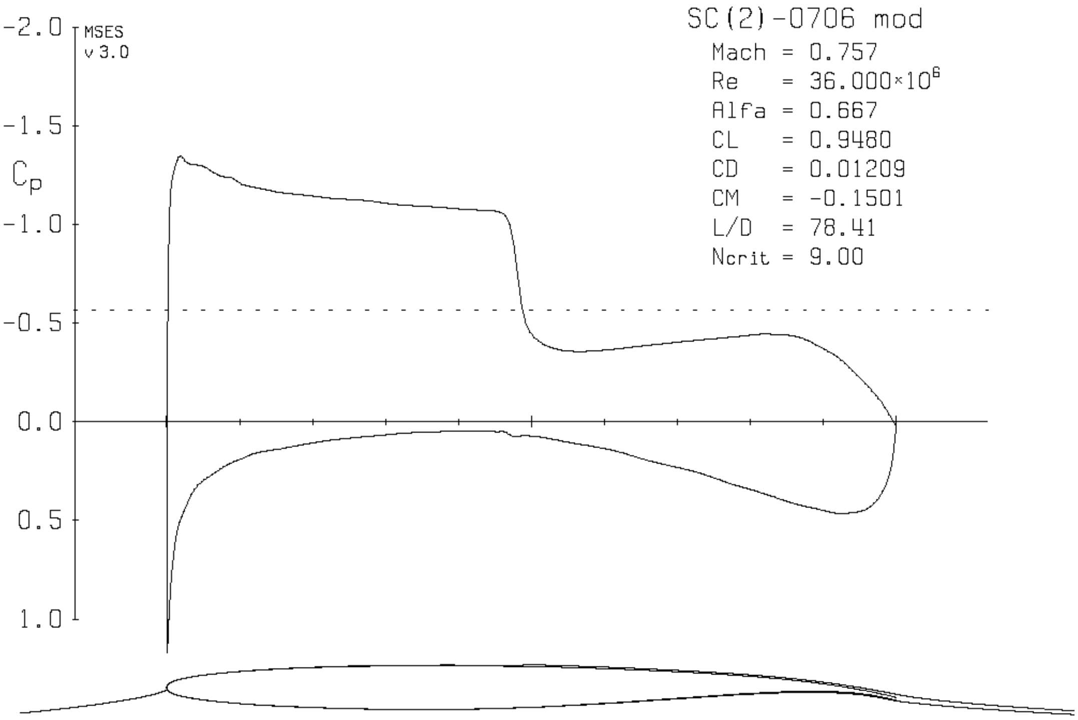

Figure 36: MSES viscous solution of the modified SC(2)-0706 that was apparently 'shock-free'. This solution was from the resultant airfoil coordinates that was smoothed.

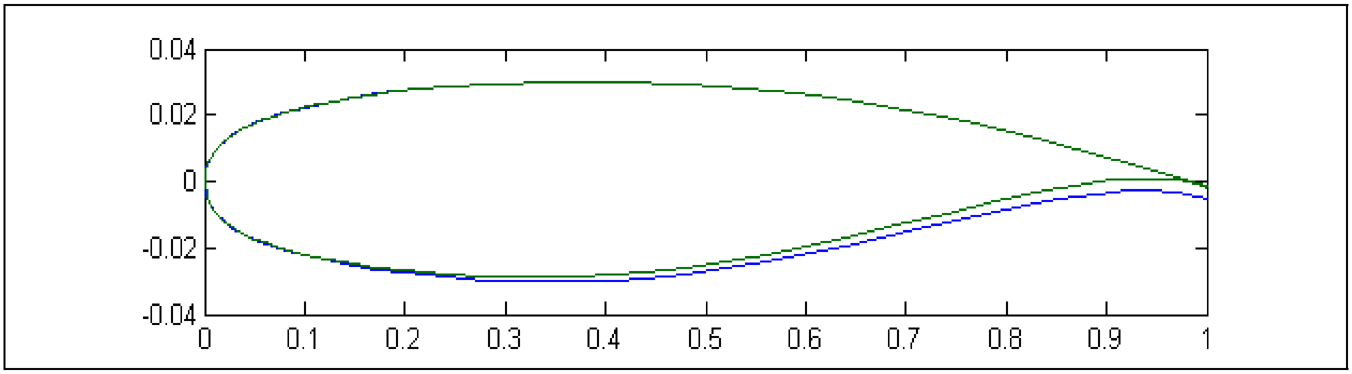

Figure 37: Comparison between the closed trailing edge and open trailing edge SC(2)-0406 airfoil

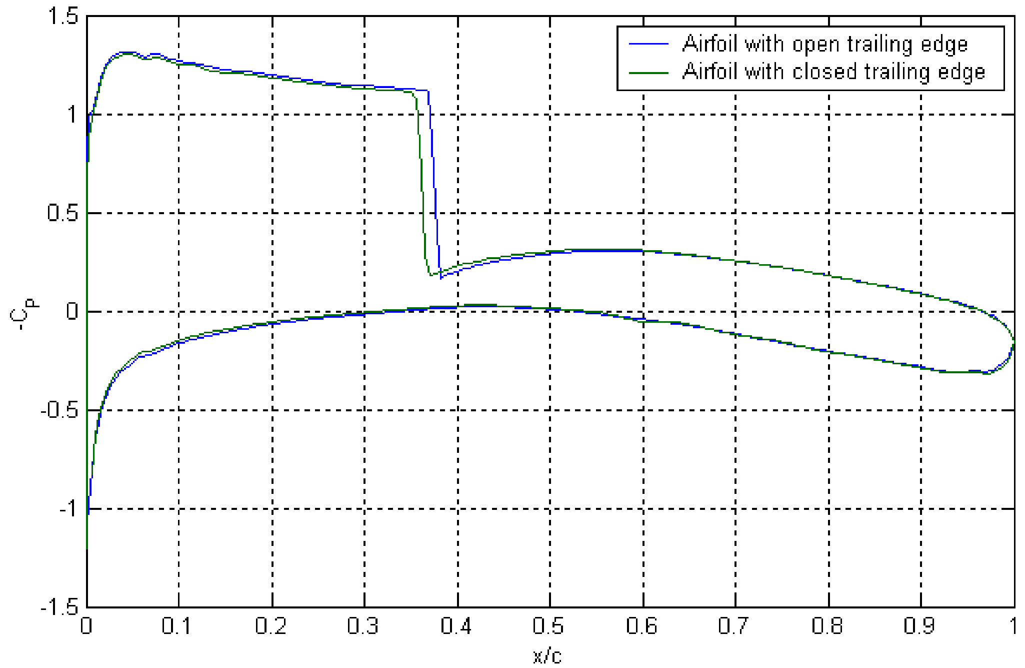

Figure 38**:** Comparison of the pressure coefficient distribution between the closed trailing edge and open trailing edge SC(2)-0406 airfoil at M=0.757, α = 2°. Inviscid solution from MSES

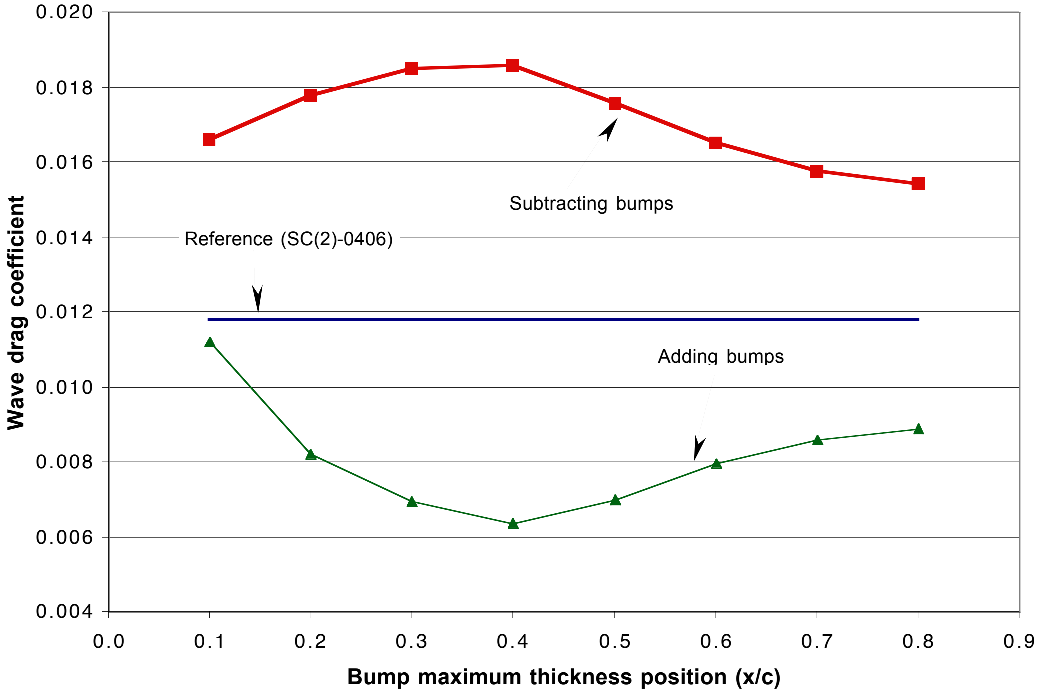

Figure 39: Variation of wave drag coefficient of the SC(2)-0406 airfoil with the addition and subtraction of ‘bumps’. MSES inviscid solution, M=0.757, $C_l$=0.75.

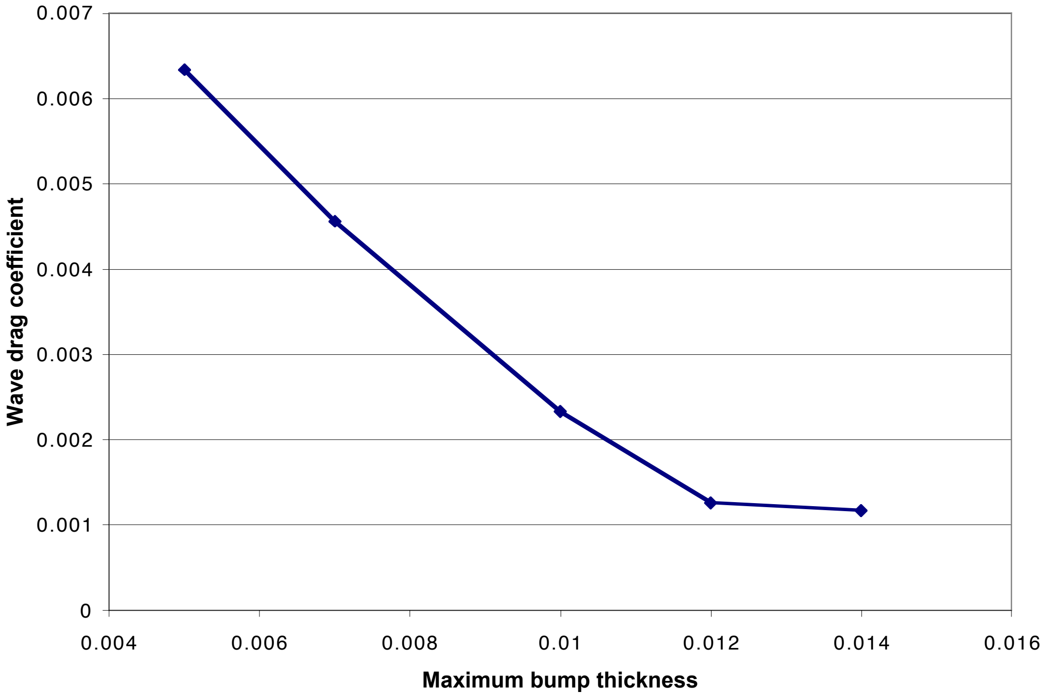

Figure 40: Variation of wave drag coefficient on a SC(2)-0406 airfoil with respect to the maximum bump thickness when a 'bump' is added. MSES inviscid solution, M=0.757, $C_l = 0.75$.

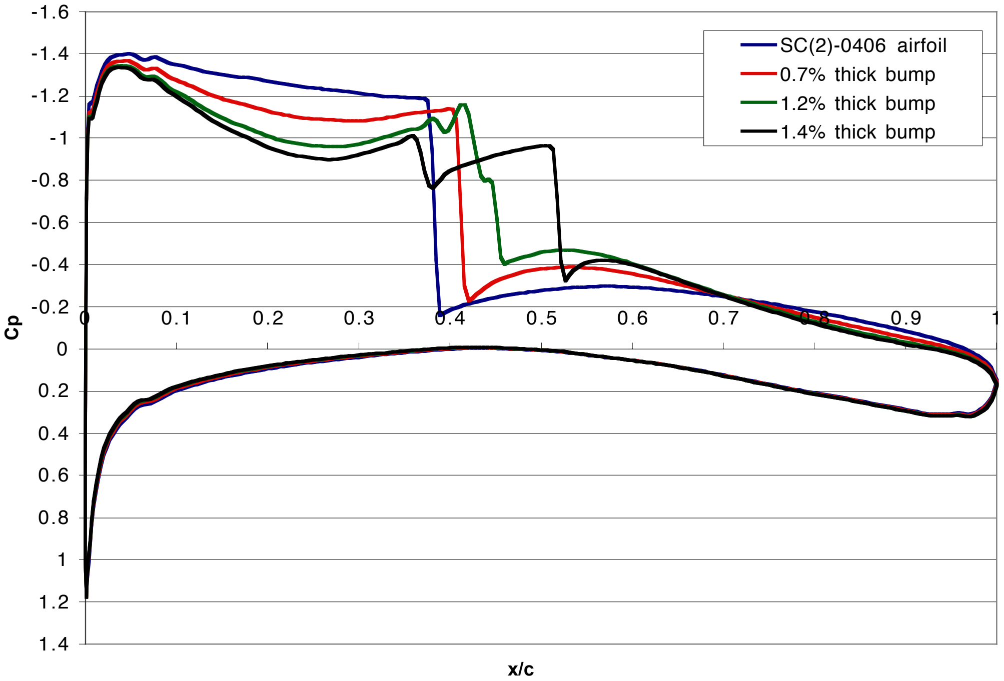

Figure 41: Comparison of pressure coefficient distribution on a SC(2)-0406 with 'bumps' added with different maximum thickness. MSES inviscid solution, M=0.757, $C_l$=0.75.

| Case | Description of Bumps | Airfoil Shape |
|---|---|---|
| A | - 0.7% bump at 40% c for entire length of the airfoil<br>- 0.2% bump at 10% c for 0 to 40% length |  |
| B | - 0.7% bump at 60% c for entire length of the airfoil<br>- 0.2% bump at 20% c for 0 to 60% length |  |
| C | - 0.7% bump at 70% c for entire length of the airfoil<br>- 0.2% bump at 250% c for 0 to 70% length |  |
| D | - 0.7% bump at 80% c for entire length of the airfoil<br>- 0.2% bump at 40% c for 0 to 80% length |  |
| E | - 0.7% bump at 80% c for entire length of the airfoil<br>- 0.3% bump at 40% c for 0 to 80% length<br>- 0.2% bump at 20% c for 0 to 40% length |  |

Figure 42: Summary of the multi-bump airfoils.

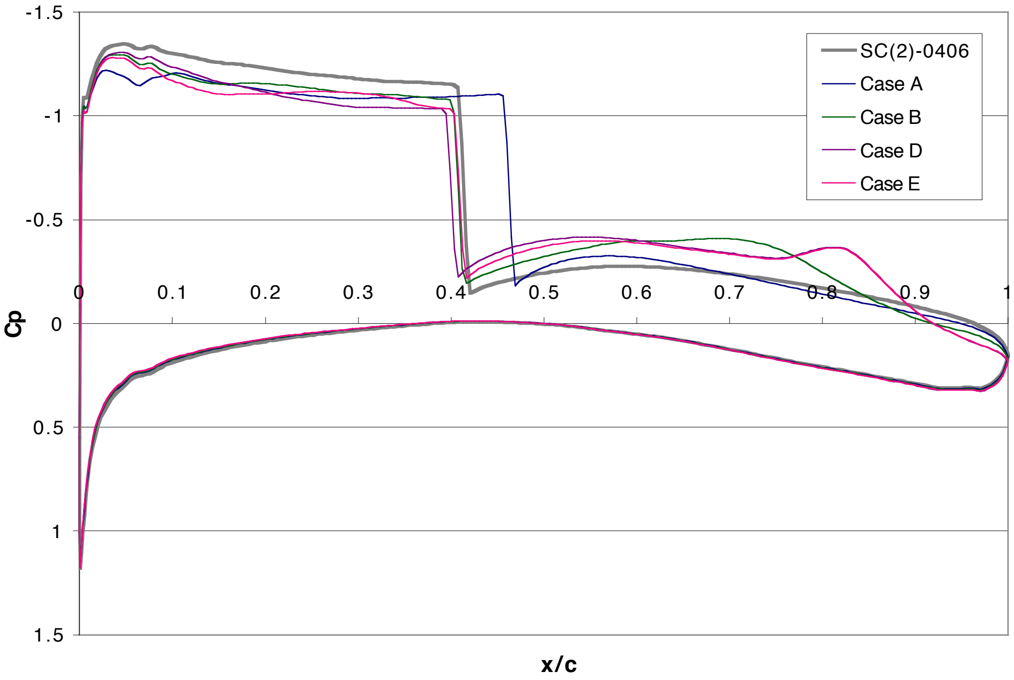

Figure 43: Pressure coefficient distribution on the multi-bump airfoils at design conditions (M=0.757, $C_l$=0.75) for the outboard wing stations. MSES inviscid solution.

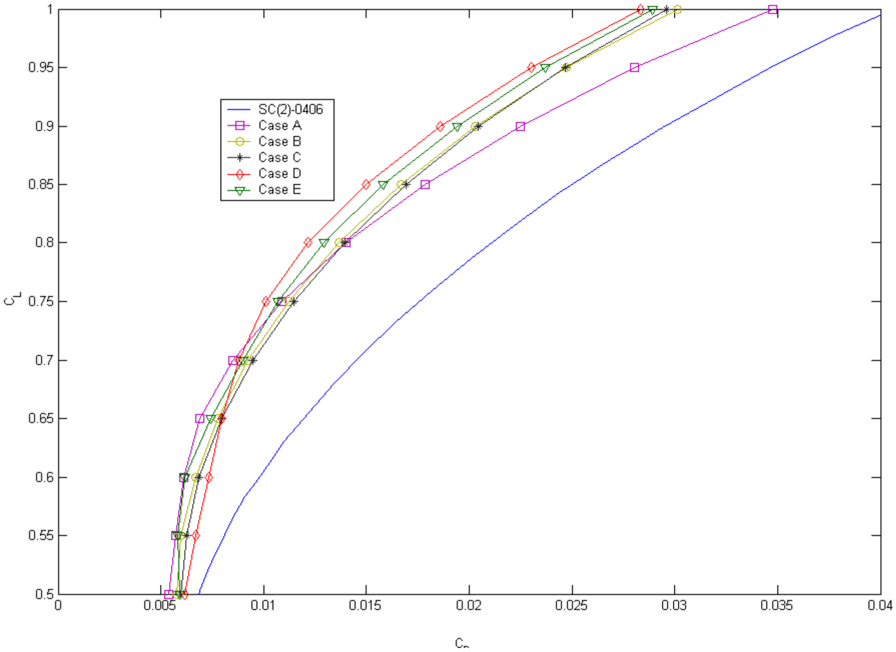

Figure 44**:** Comparison of the drag polars of the different multi-bump airfoil designs. MSES viscous solution, M=0.757. Re = 11.6 x $10^6$

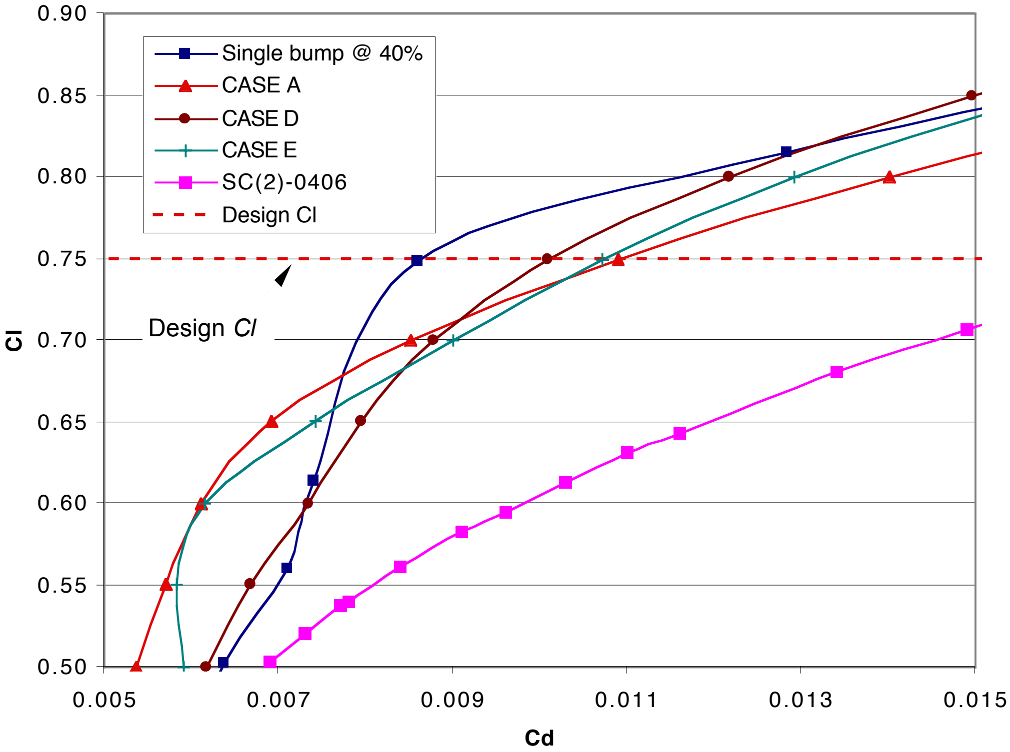

Figure 45: Comparison of drag polars of the different multi-bump airfoil designs. MSES viscous solution, M=0.757, Re=32x$10^6$.

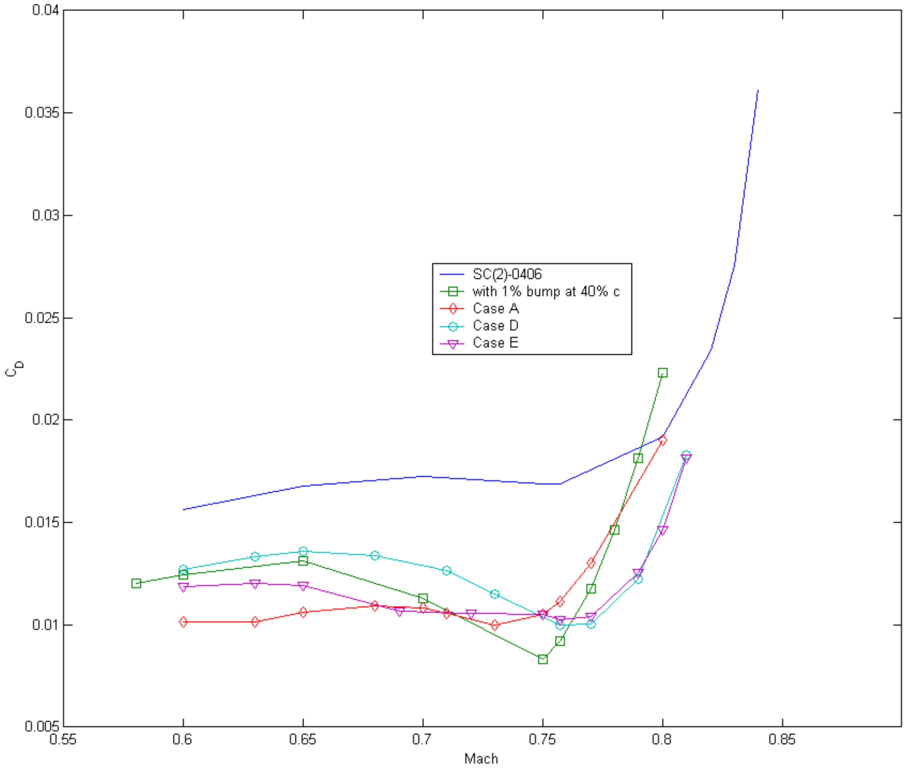

Figure 46: Drag rise comparison of the different multi-bump airfoil designs. MSES viscous solution, M=0.757, $C_l$ = 0.75, Re=32 x $10^6$.

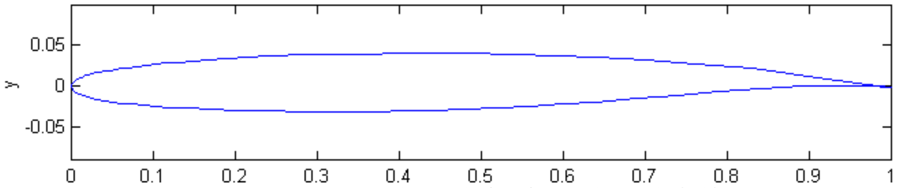

Figure 47: Designed 6.96% thick airfoil

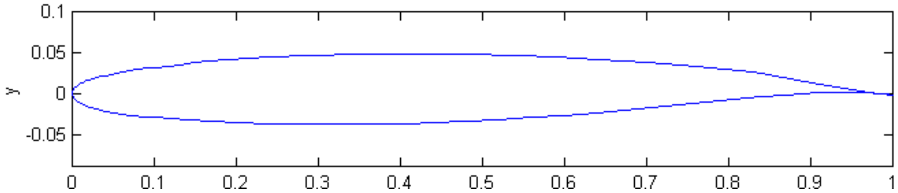

Figure 48: Designed 8.42% thick airfoil

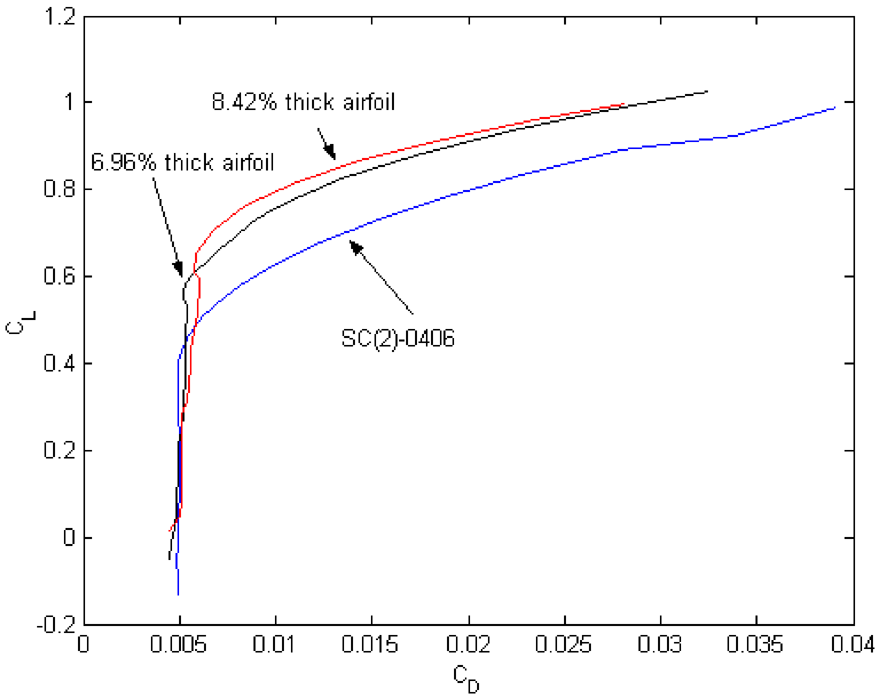

Figure 49**:** Drag polar comparison between the SC(2)-0406 airfoil and the designed outboard airfoils. MSES viscous solution, M=0.757. Re=32x$10^6$

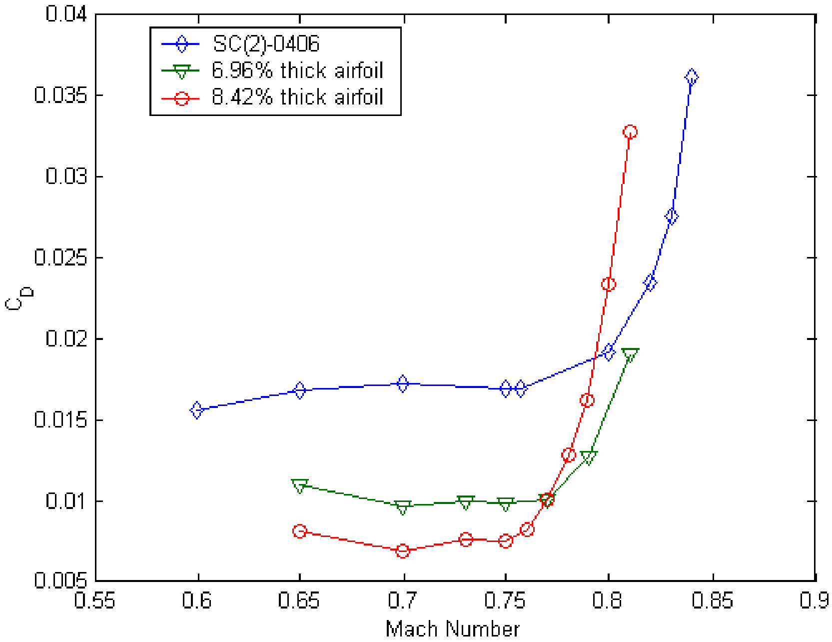

Figure 50: Comparison of the drag rise characteristics between the SC(2)-0406 airfoil and the designed outboard airfoils. MSES viscous solution. M=0.757, $C_l$=0.75, Re=32x$10^6$

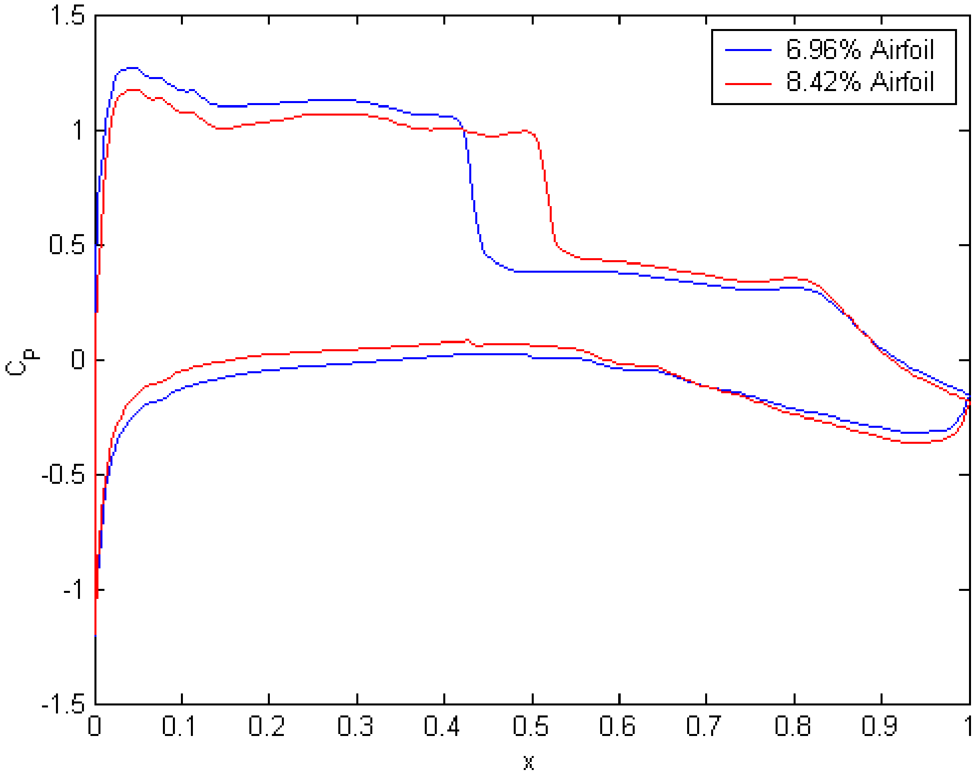

Figure 51: Comparison of the $C_p$ distribution at design conditions for the designed outboard airfoils. MSES viscous solution, M=0.757, $C_l$ =0.75, Re=32x$10^6$

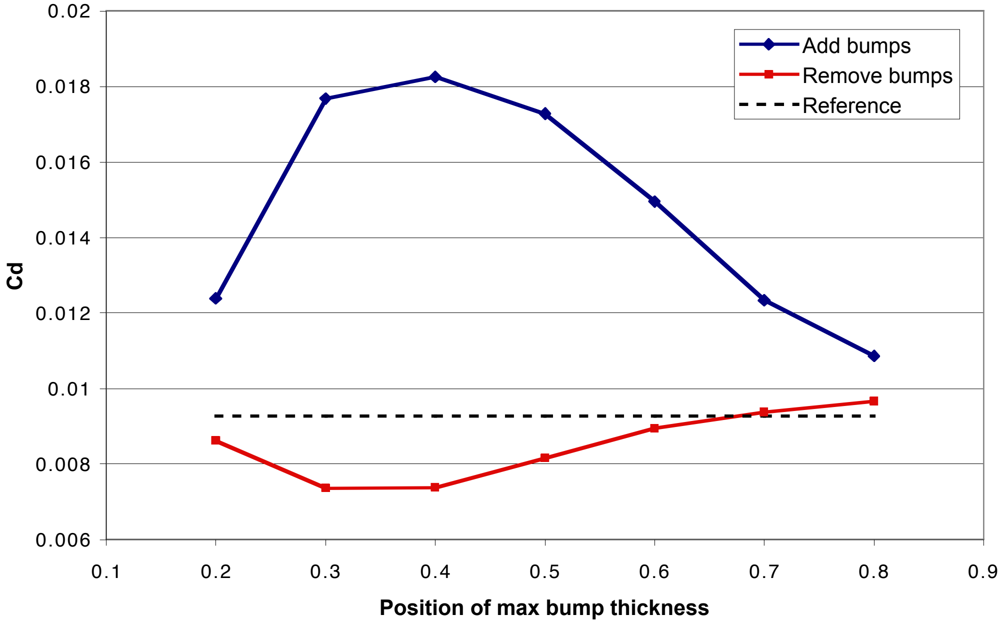

Figure 52: Variation of the drag coefficient of the SC(2)-0614 airfoil with the addition and subtraction of 'bumps' analyzed at M=0.757, $C_l$= 0.547, Re=32x$10^6$. MSES viscous solution.

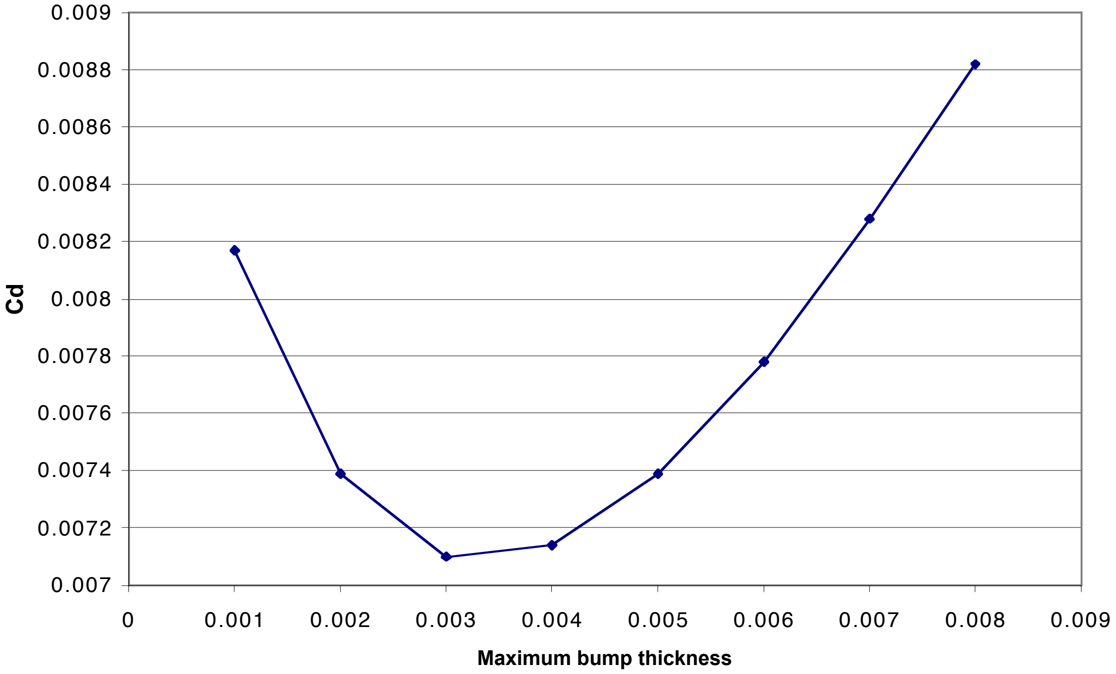

Figure 53: Variation of drag coefficient on a SC(2)-0614 airfoil with respect to the maximum bump thickness when a 'bump' is added at the 40% chord location. M=0.757, $C_l$=0.547, Re=32x$10^6$. MSES viscous solution.

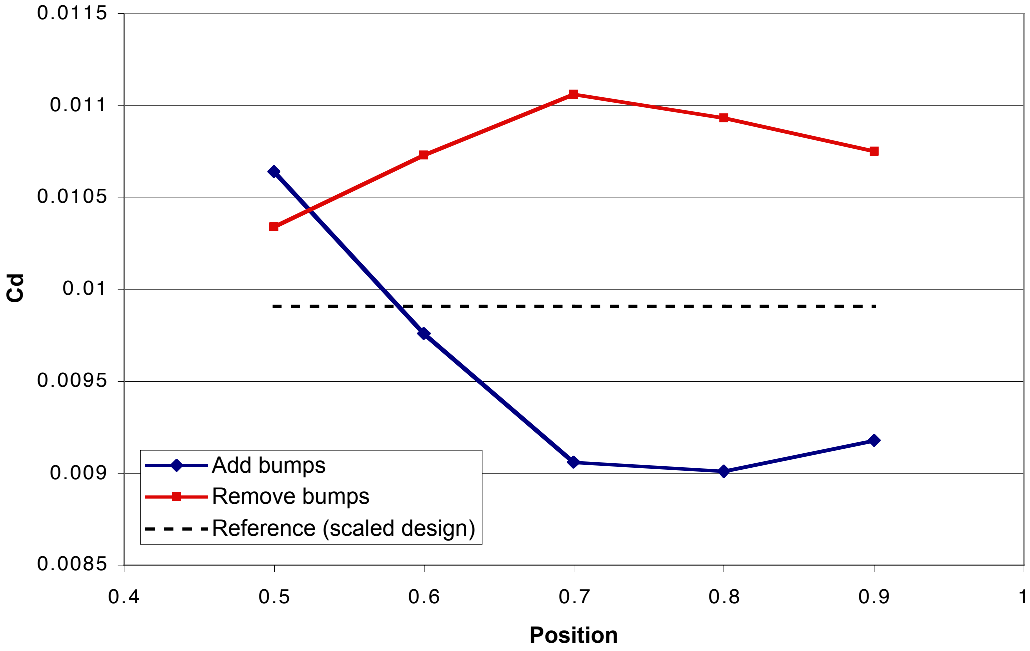

Figure 54: Variation of drag coefficient as a function of adding and subtracting a secondary bump on the root station scaled airfoil design. MSES viscous solution, M=0.757, $C_l$=0.547, Re=32x$10^6$.

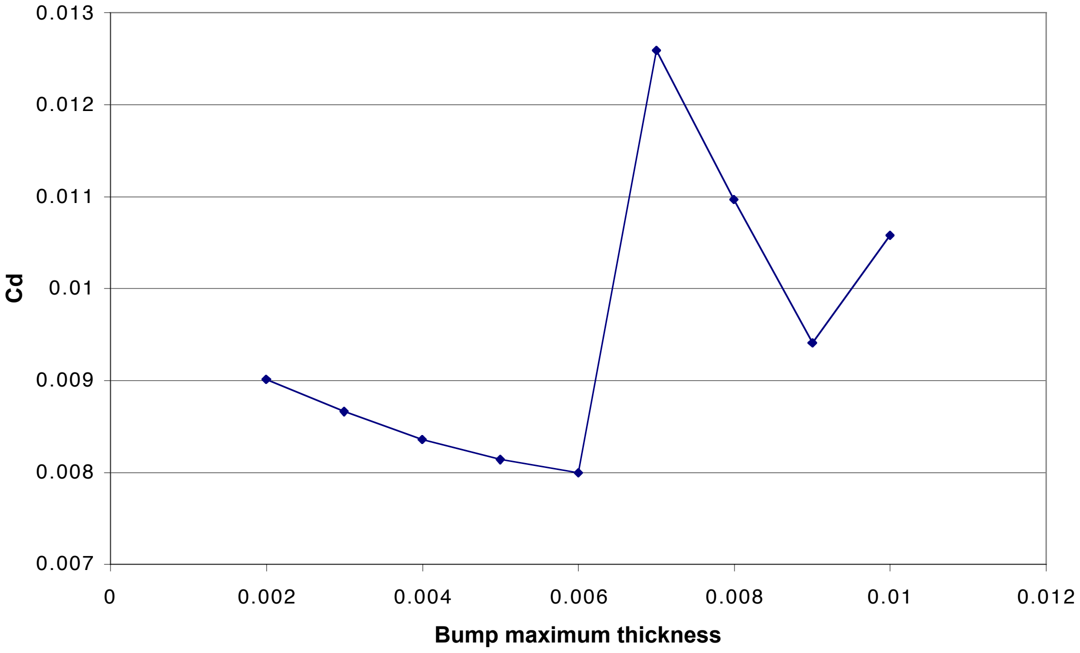

Figure 55: Variation of drag coefficient with respect to the maximum bump thickness of a secondary bump added at the 70% chord position on the root station scaled airfoil design. MSES viscous solution, M=0.757, $C_l$=0.547, Re=32x$10^6$.

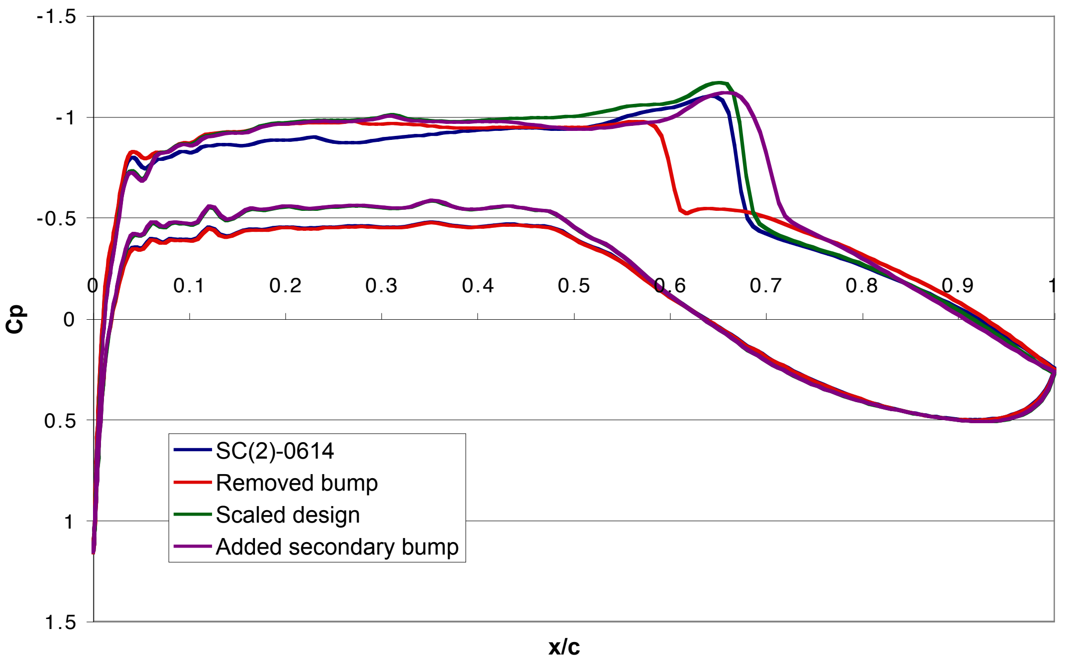

Figure 56: Pressure coefficient distribution comparison between the different designed airfoils for the root station. MSES viscous solution, M=0.757, $C_l$=0.547, Re=32x$10^6$.

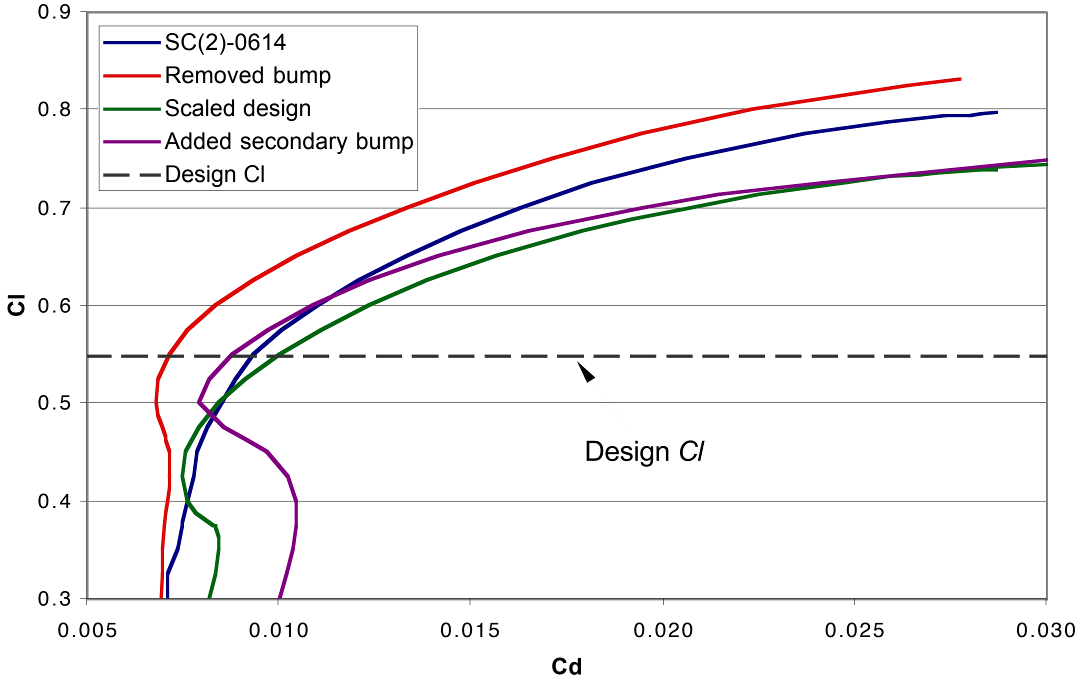

Figure 57: Comparison of drag polars between the different designed airfoils for the root station. MSES viscous solution, M=0.757, Re=32x10$^6$.

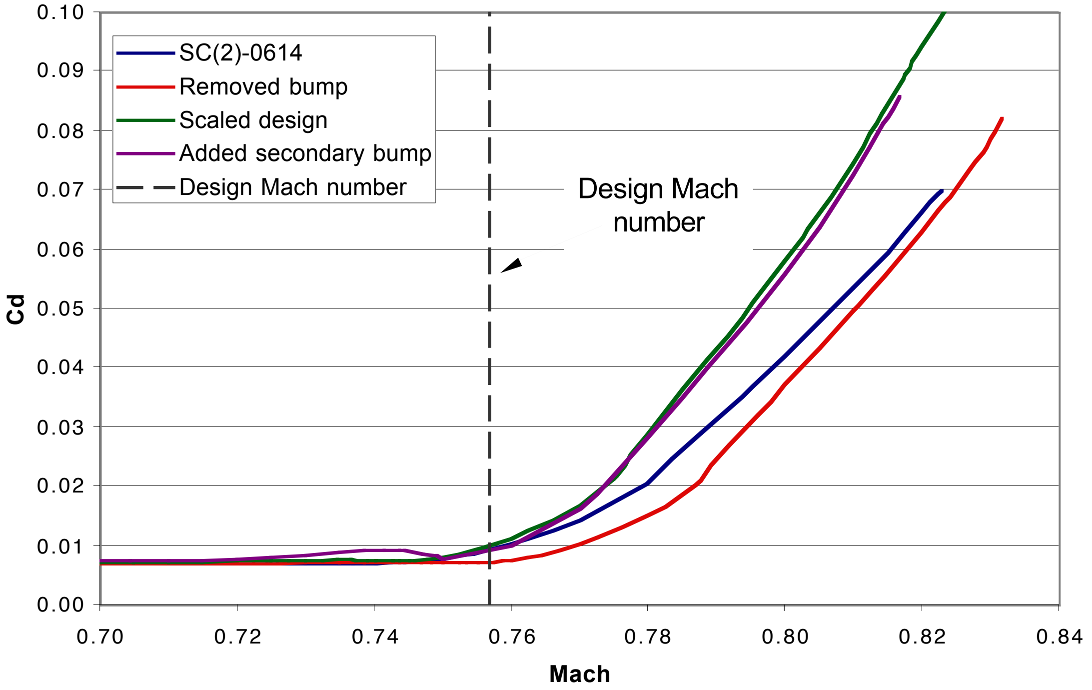

Figure 58: Comparison of the drag rise of the different designed airfoils for the root station. MSES viscous solution, $C_l$=0.547, Re=32x10$^6$.

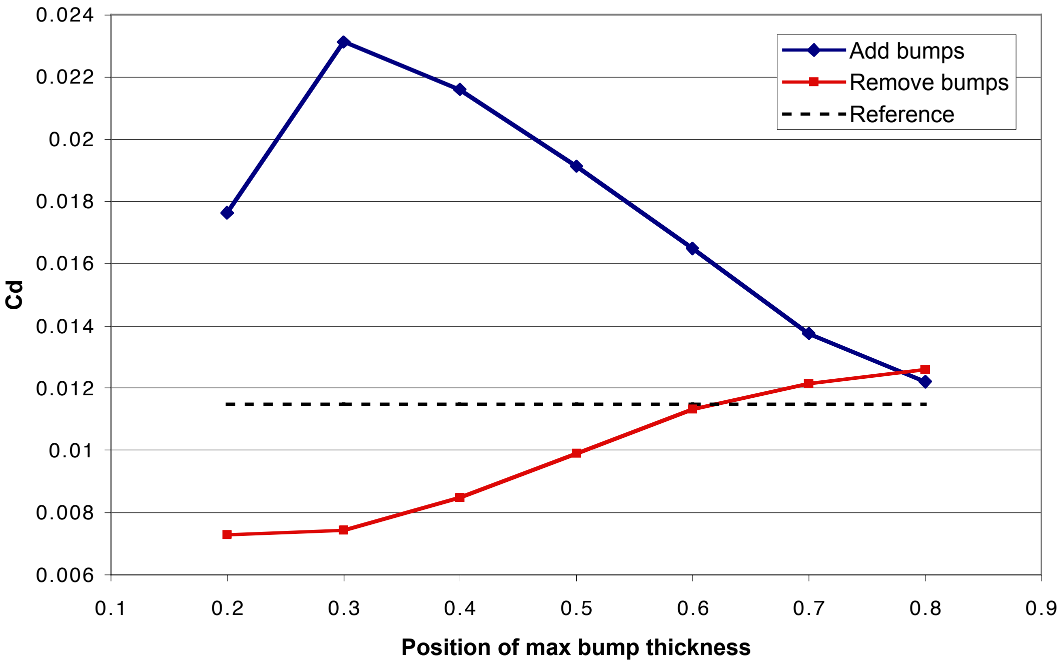

Figure 59: Variation of drag as a function of adding and removing bumps of thickness 5% chord at different locations on the upper surface of a closed trailing edge SC(2)-0614 airfoil. MSES viscous solution. M=0.757, $C_l$=0.612, Re=32x$10^6$.

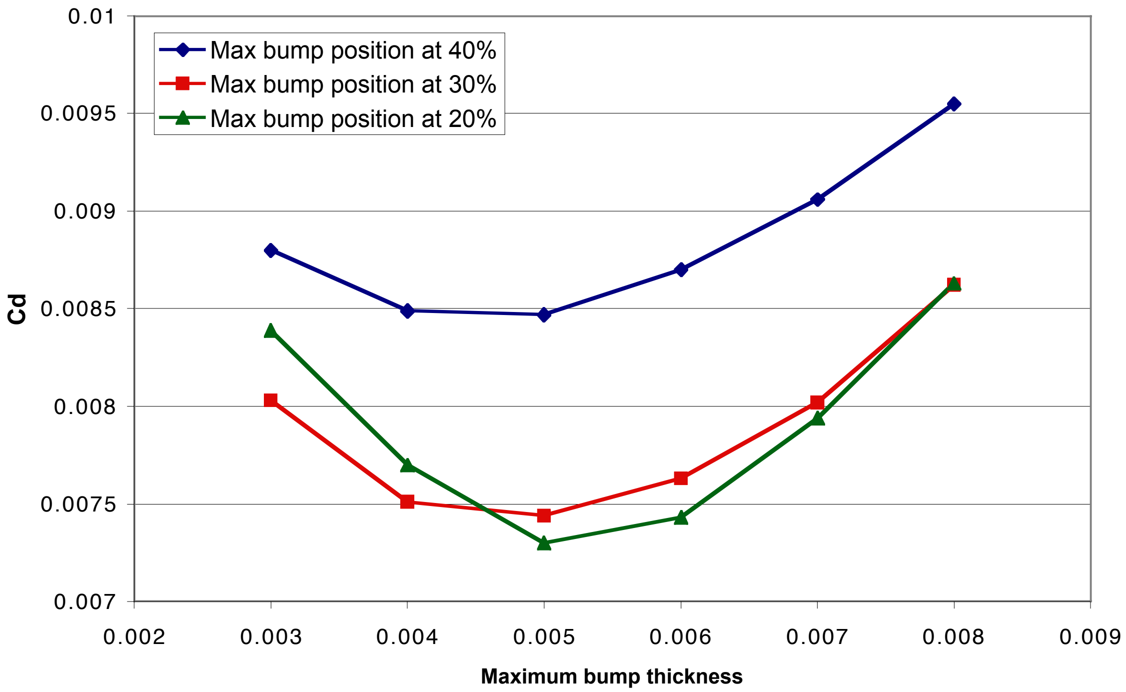

Figure 60: Comparison of drag coefficient as a function of maximum bump thickness removed from a closed trailing edge SC(2)-0614 airfoil at different positions on the airfoil. MSES viscous result, M0.757, $C_l$=0.612, Re=32x$10^6$.

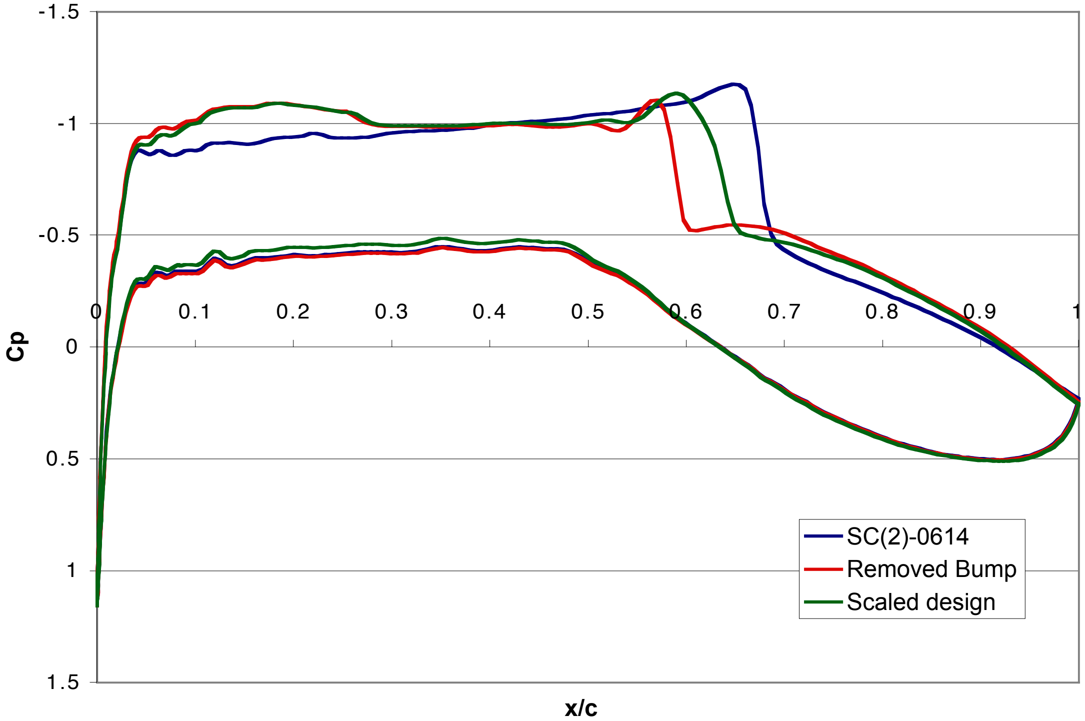

Figure 61: Comparison of pressure coefficient distribution of the airfoils designed for the 15% station. MSES viscous results, M=0.757, $C_l$ =0.612, Re=32x10$^6$.

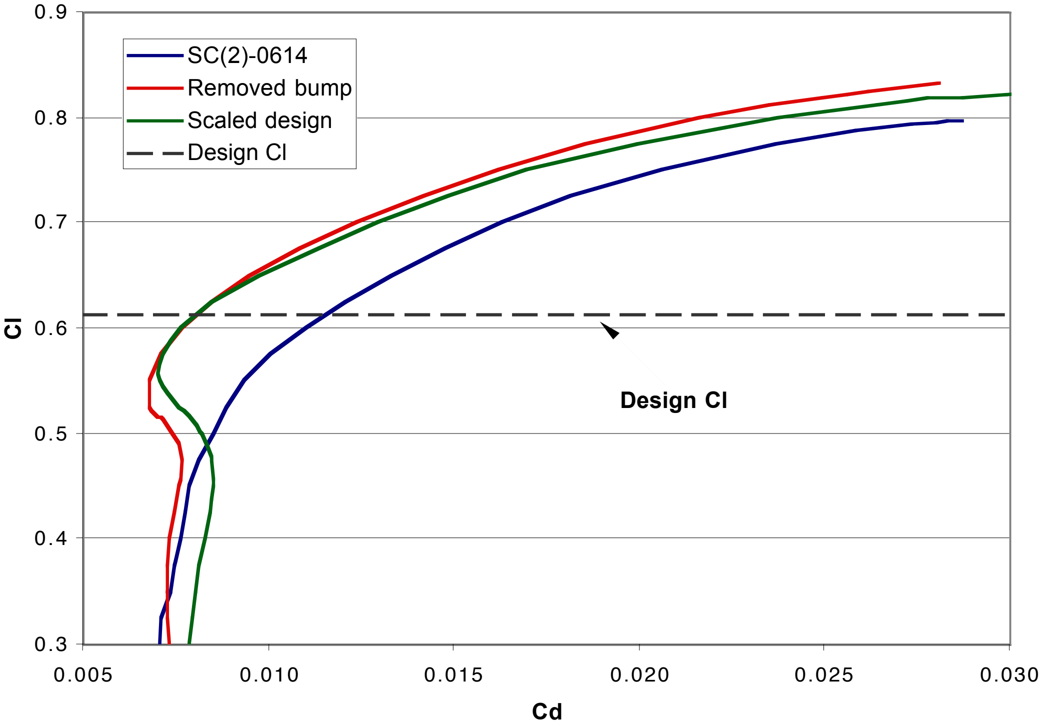

Figure 62: Comparison of drag polars of the designed airfoils for the 15% span station. MSES viscous solution, M=0.757, Re=32x10$^6$.

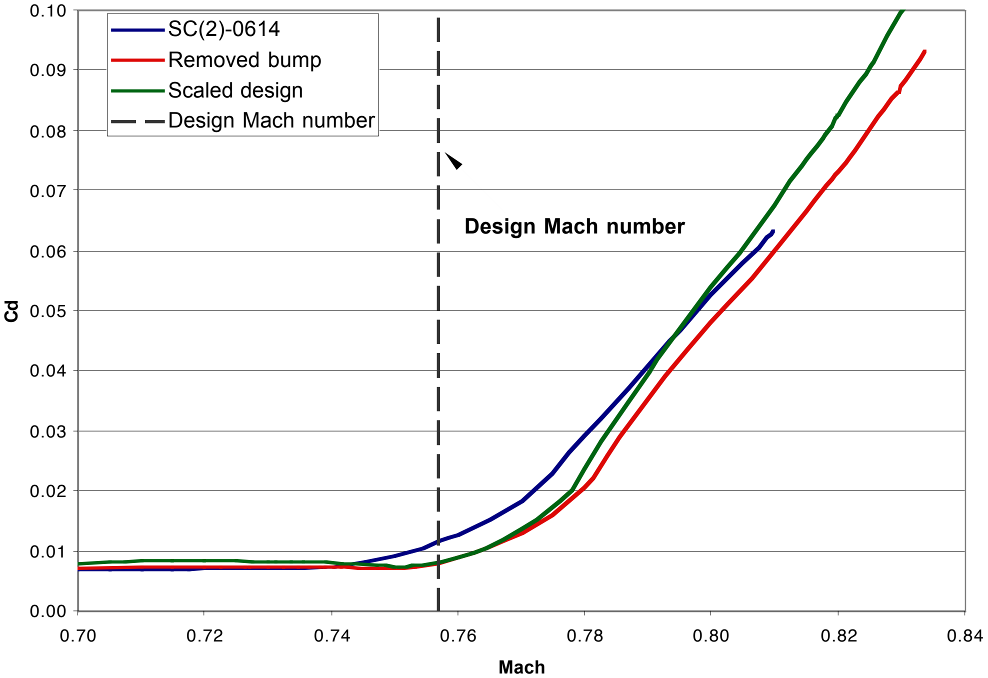

Figure 63: comparison of the drag rise of the airfoils designed for the 15% span station. MSES viscous results, $C_l$=0.612, Re=32x10$^6$.

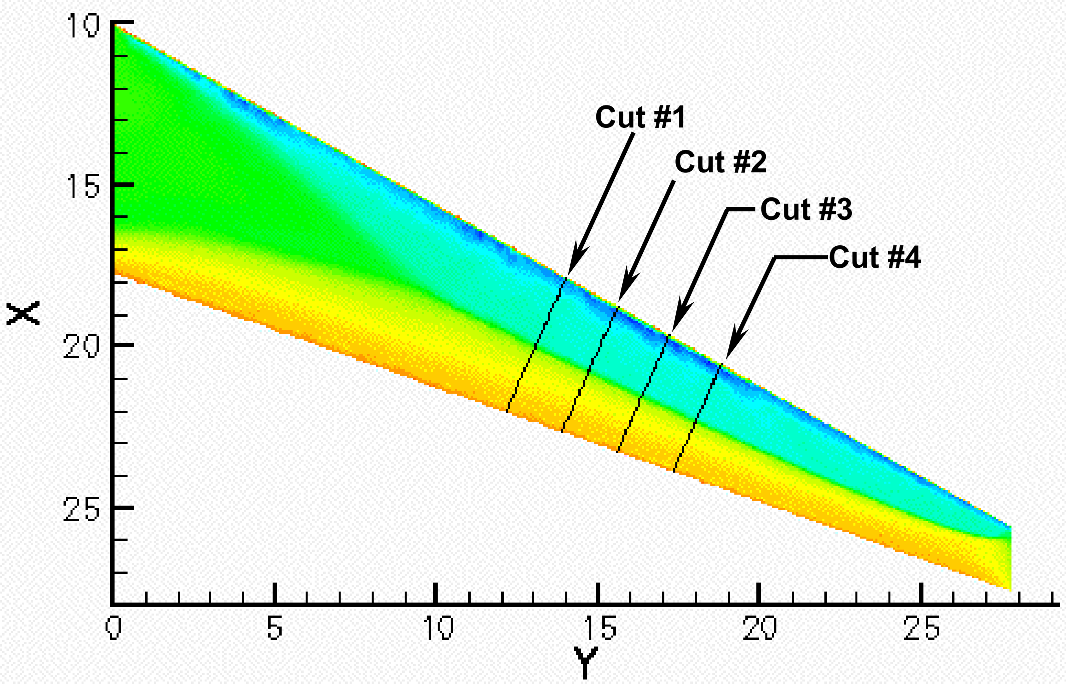

Figure 64: Pressure contours of the upper surface of the SBW A7 wing at $C_l$ = 0.359. Also shown are the positions where cuts were taken of the pressure coefficient distribution to compare with two-dimensional analysis results. FELISA inviscid solution, M=0.85.

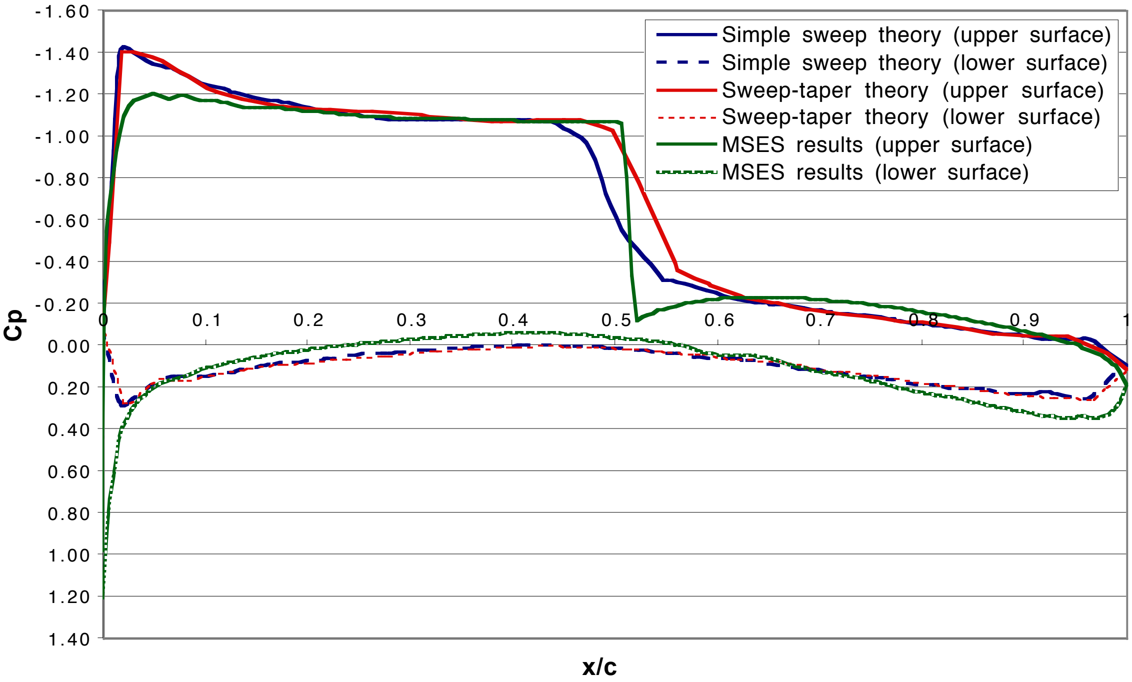

Figure 65: Comparison of the pressure coefficient distribution between cuts made from a wing and solution from an airfoil using simple sweep theory and sweep taper theory. Comparison is at Cut #1.

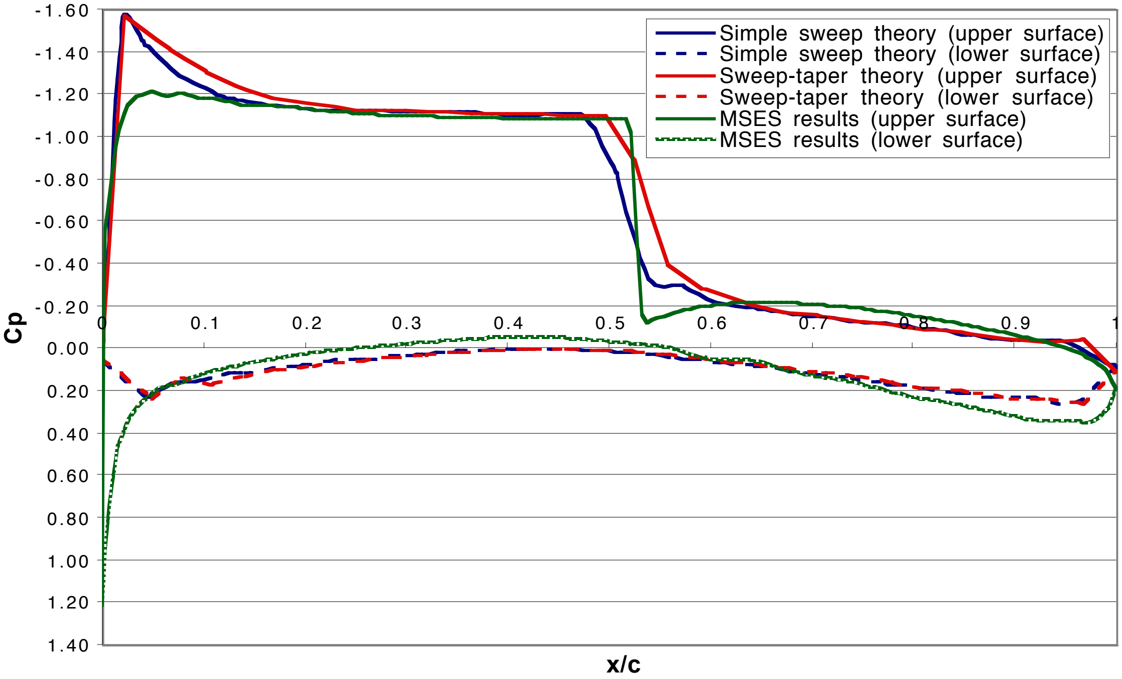

Figure 66: Comparison of the pressure coefficient distribution between cuts made from a wing and solution from an airfoil using simple sweep theory and sweep taper theory. Comparison is at Cut #2.

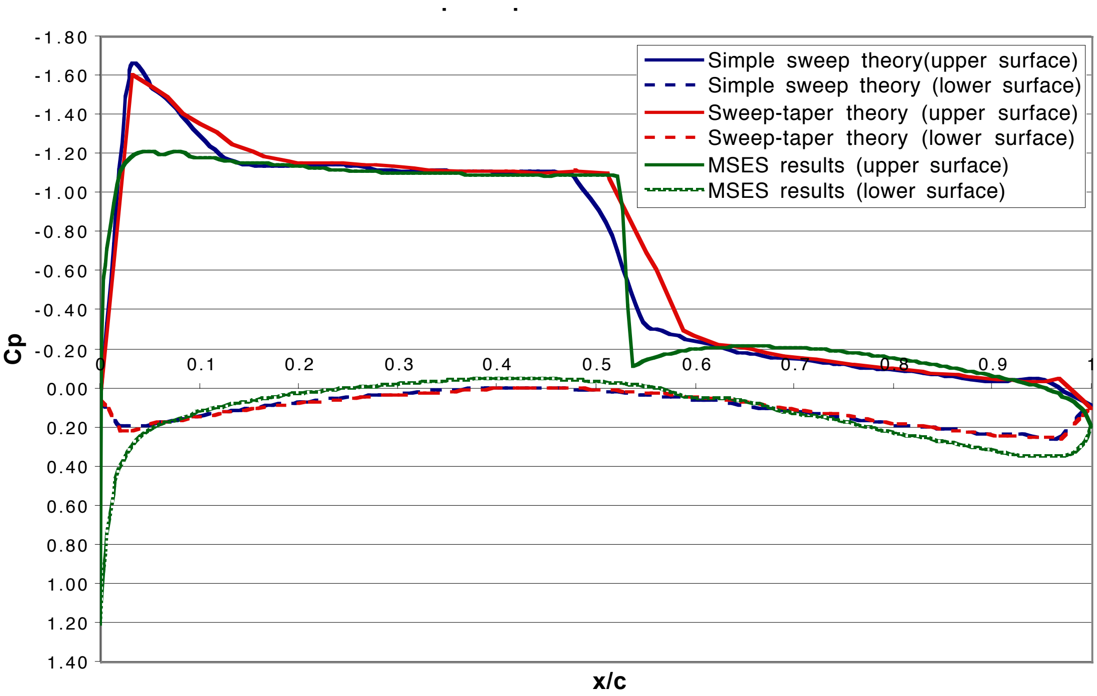

Figure 67: Comparison of the pressure coefficient distribution between cuts made from a wing and solution from an airfoil using simple sweep theory and sweep taper theory. Comparison is at Cut #3.

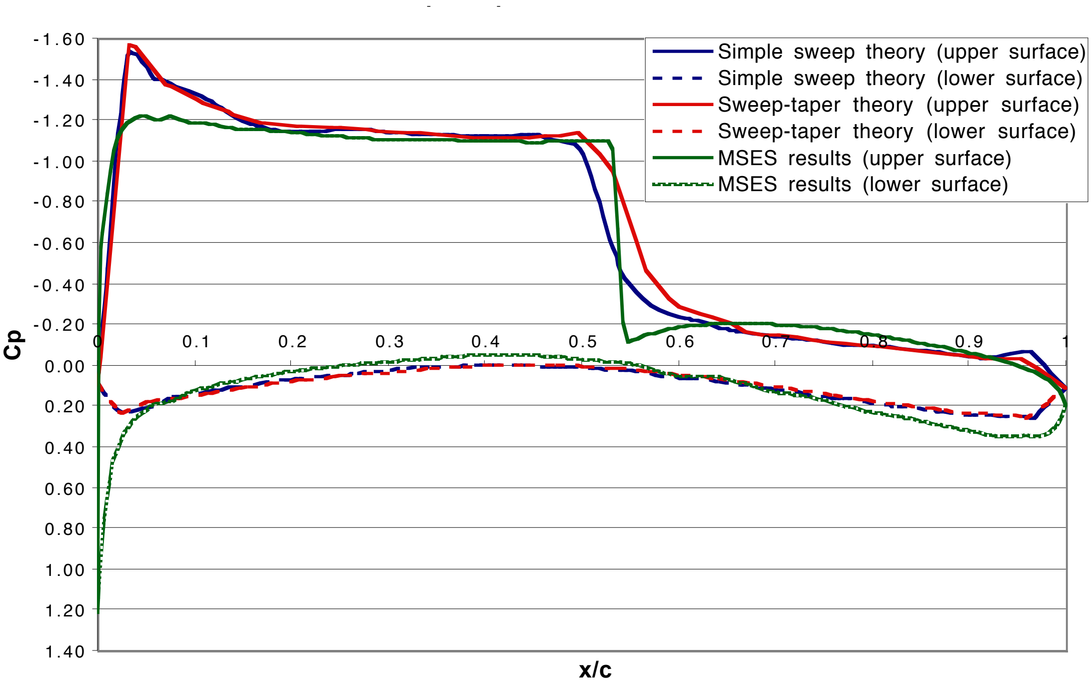

Figure 68: Comparison of the pressure coefficient distribution between cuts made from a wing and solution from an airfoil using simple sweep theory and sweep taper theory. Comparison is at Cut #4.

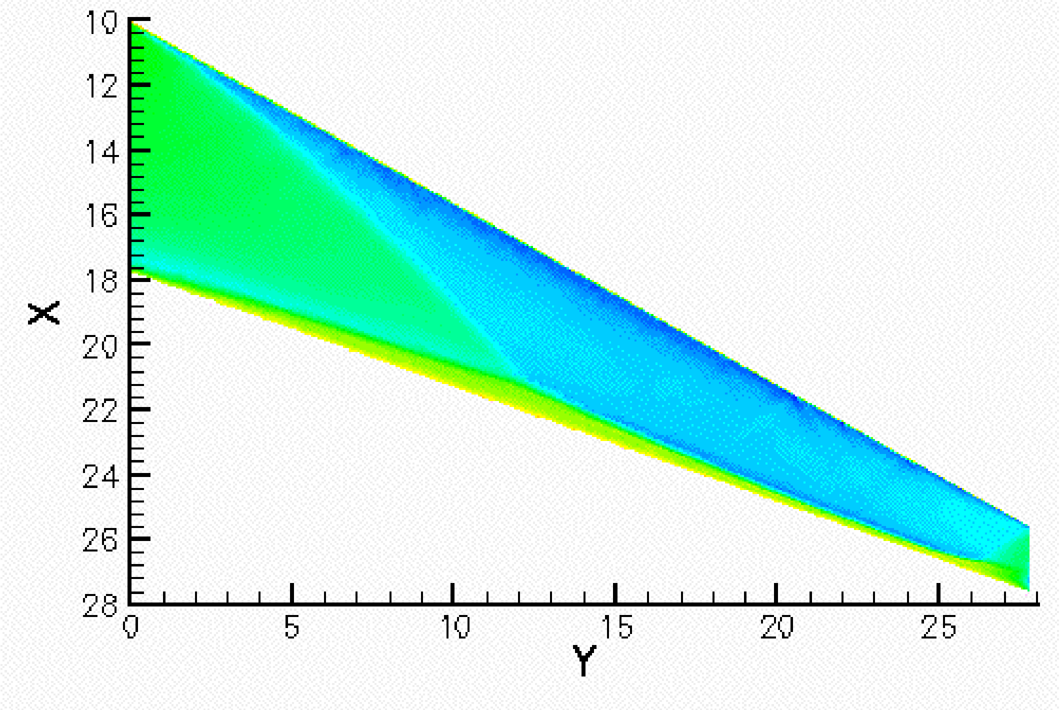

Figure 69**:** Pressure contour plot of the upper surface of the SBW A7 wing designed with a SC(2)-0706 airfoil. FELISA inviscid solution, M=0.85, α=5°.

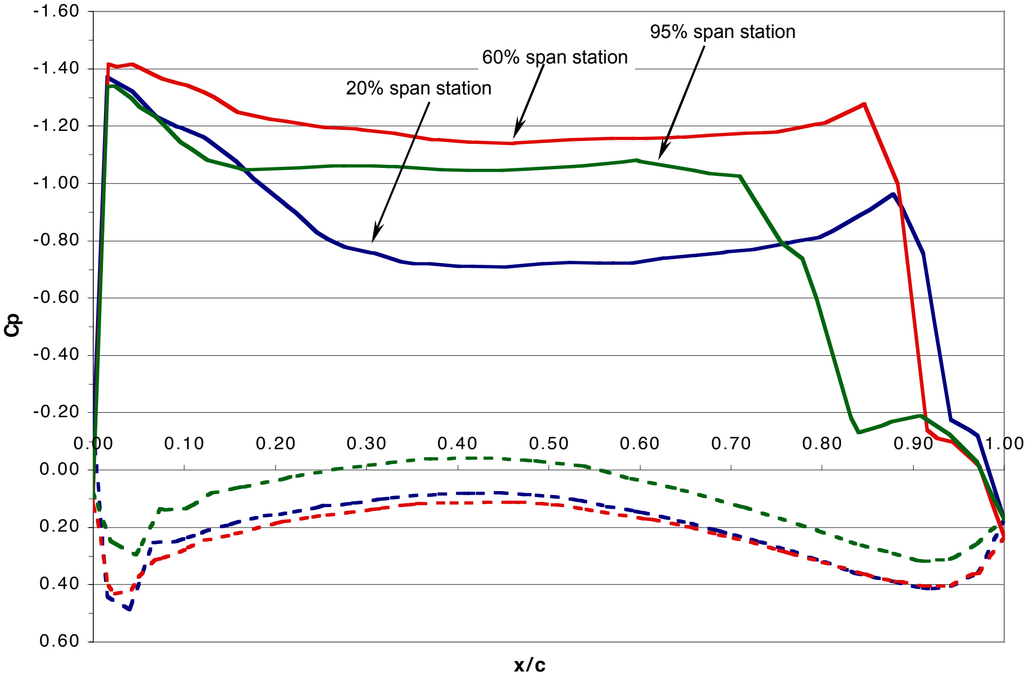

Figure 70: Pressure coefficient distributions on the SBW A7 wing designed with a SC(2)-0706 airfoil at different span stations. FELISA inviscid solution, M=0.85, α=5°.

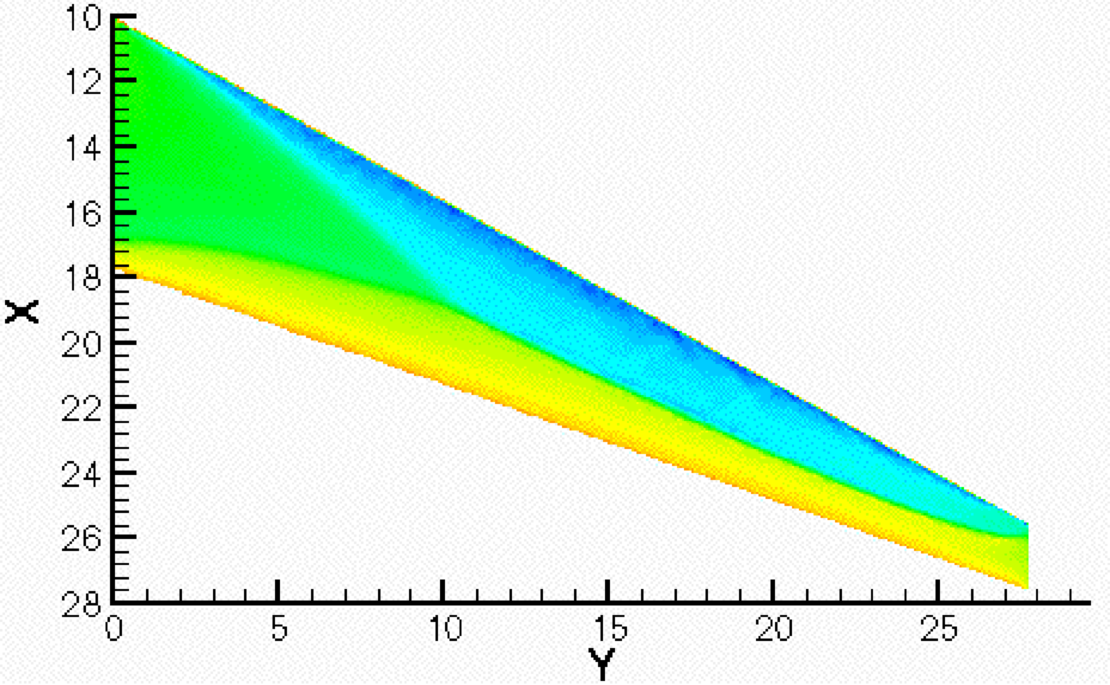

Figure 71: Pressure coutour of the upper surface of the SBW A7 wing designed with a SC(2)-0406 airfoil. FELISA inviscid solution, M=0.85, α=5°.

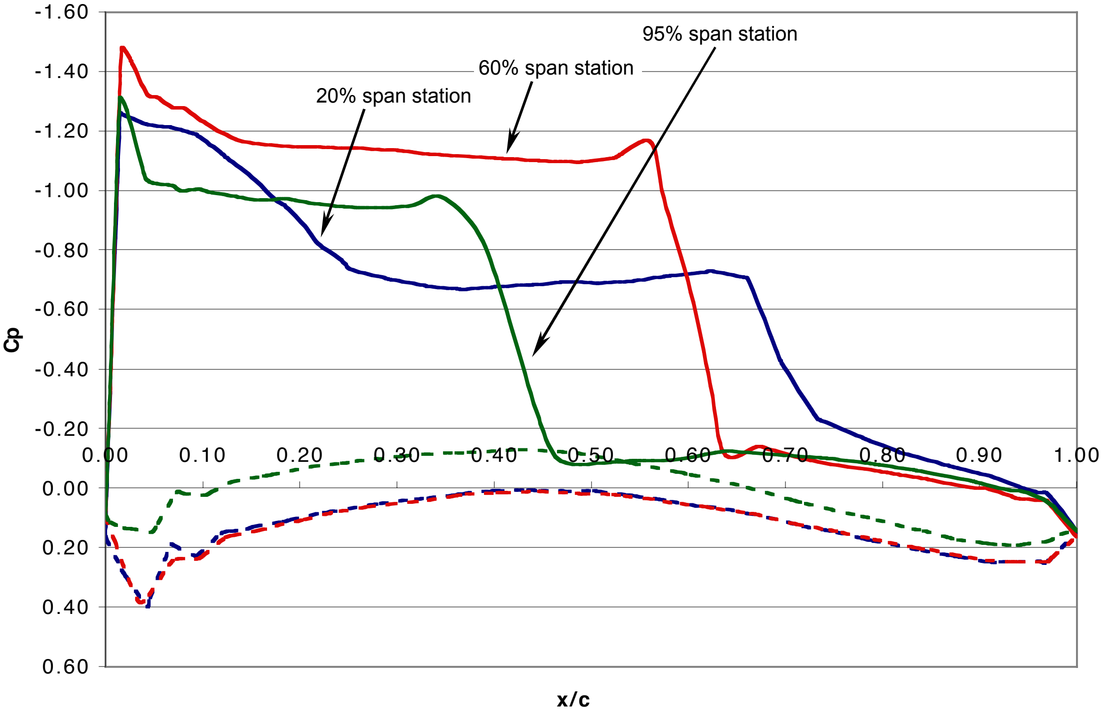

Figure 72: Pressure coefficient distribution on the SBW A7 wing designed with a SC(2)-0406 airfoil at different span stations. FELISA inviscid solution, M=0.85, α=5°.

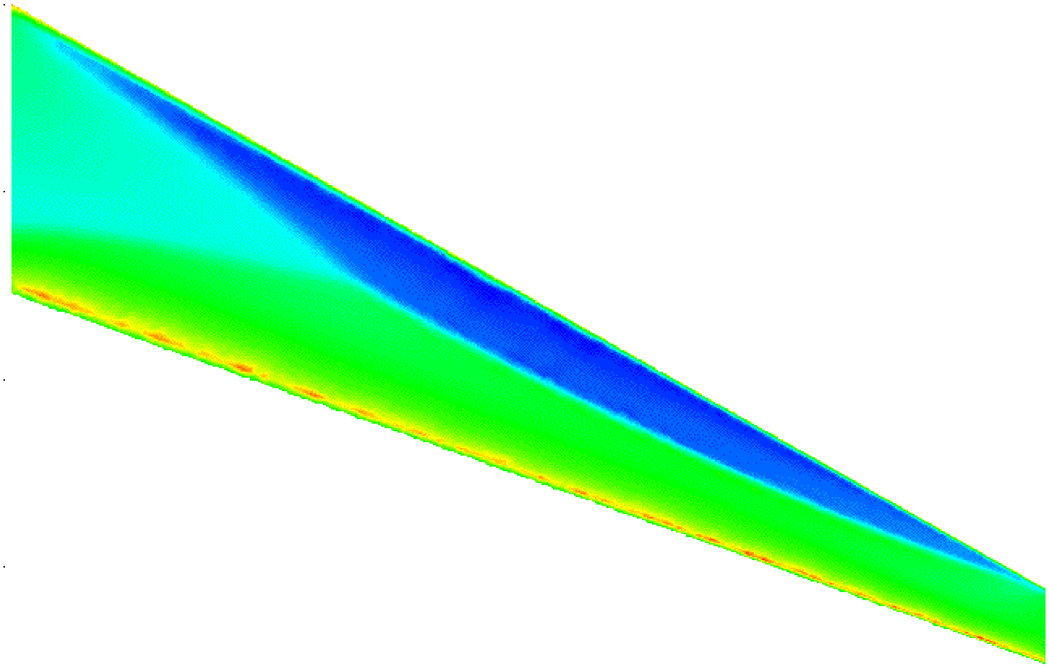

Figure 73: Pressure coutour of the upper surface of the SBW A7 wing designed with a SC(2)-0406 airfoil at $C_l$ =0.527. FELISA inviscid solution, M=0.85,

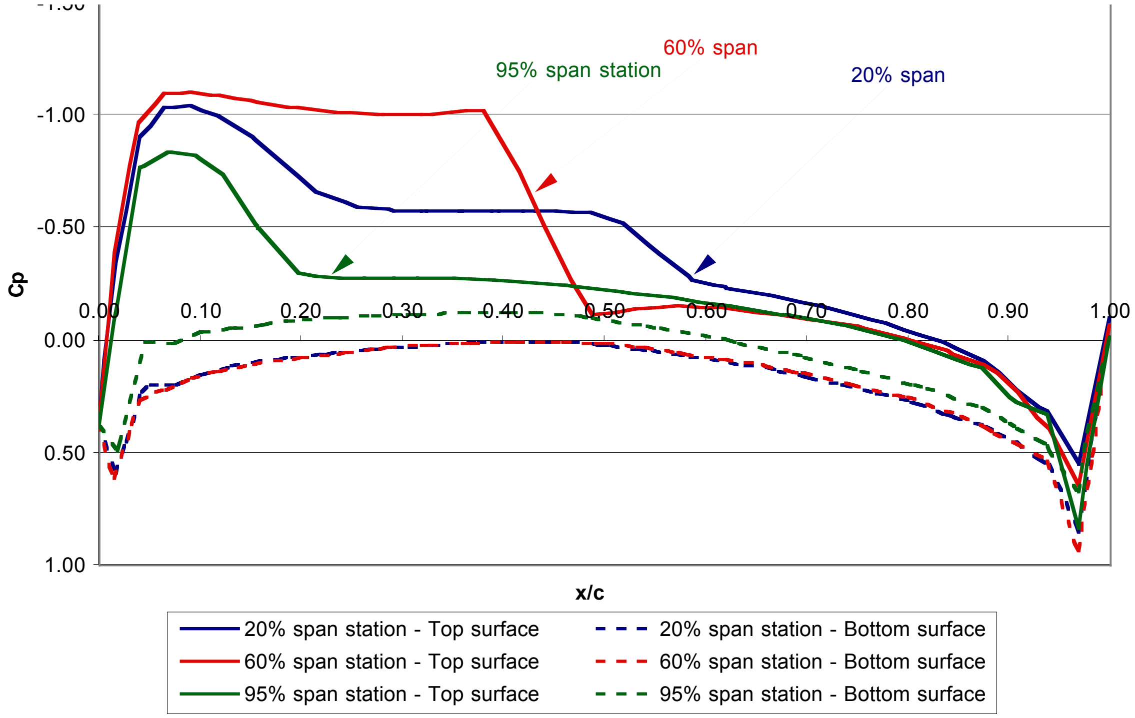

Figure 74**:** Pressure contours of the upper surface of the SBW A7 wing designed with an SC(2)-0406 airfoil at $C_l$ = 0.527. FELISA inviscid solution, M=0.85.

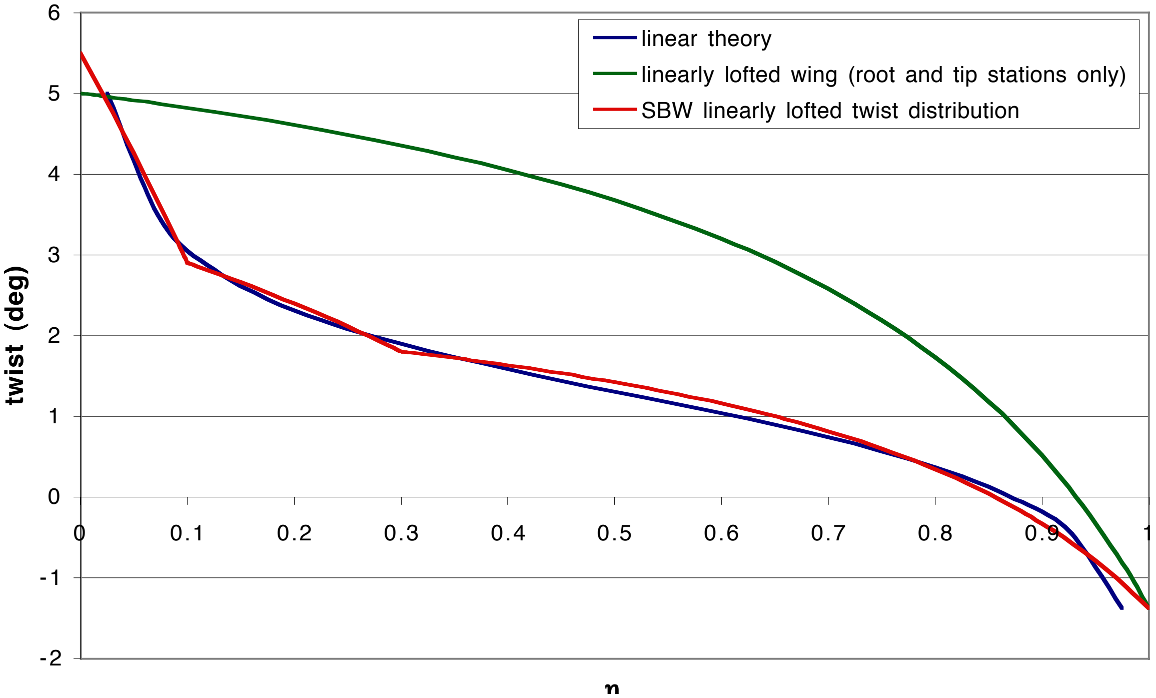

Figure 75: Difference between the twist distribution of the linear theory solution, a linearly lofted wing from only the root and tip stations, and the SBW linearly lofted wing from the root, 10% span, 30% span and tip station.

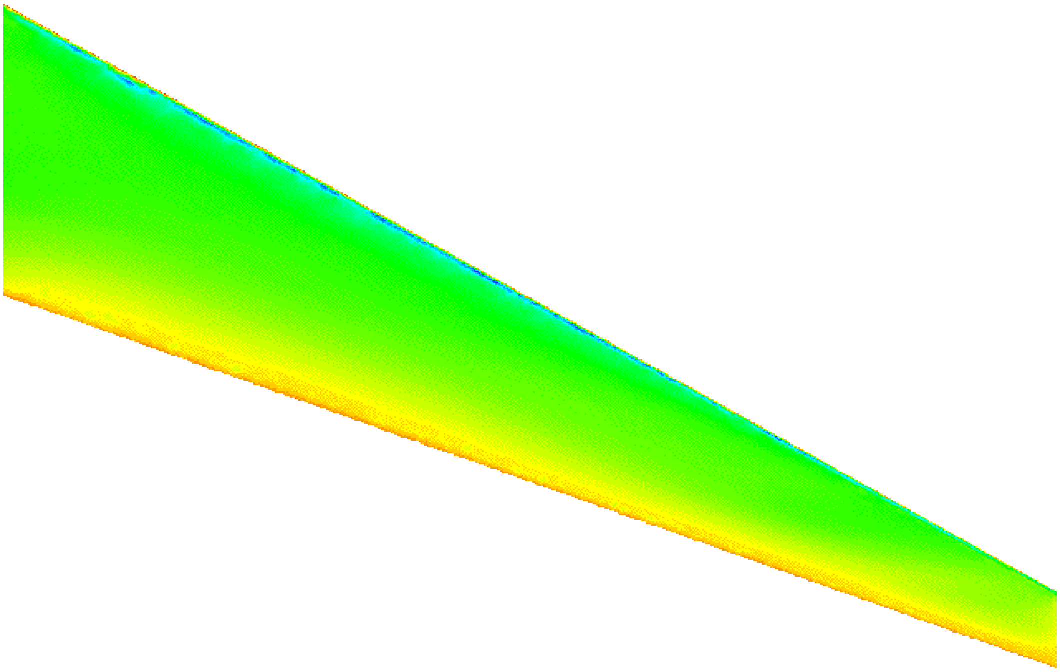

Figure 76: Pressure contours of the upper surface of the SBW A7 wing designed with an SC(2)-04060 airfoil at $C_l = 0.26$. Twist distribution of the wing was linearly lofted from the root, 10% span, 30% span and tip stations. FELISA inviscid solution, M=0.85.

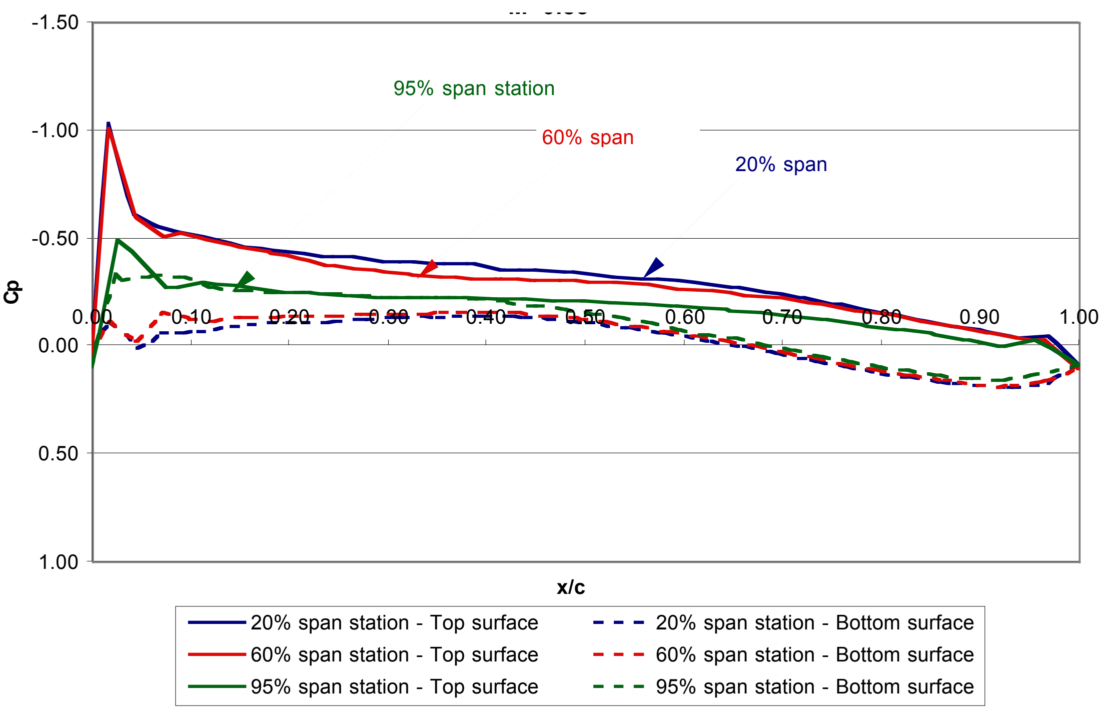

Figure 77**:** Pressure coefficient distribution on the SBW A7 wing designed with a SC(2)-0406 airfoil at $C_l$ =0.5. FELISA inviscid solution, M=0.85.

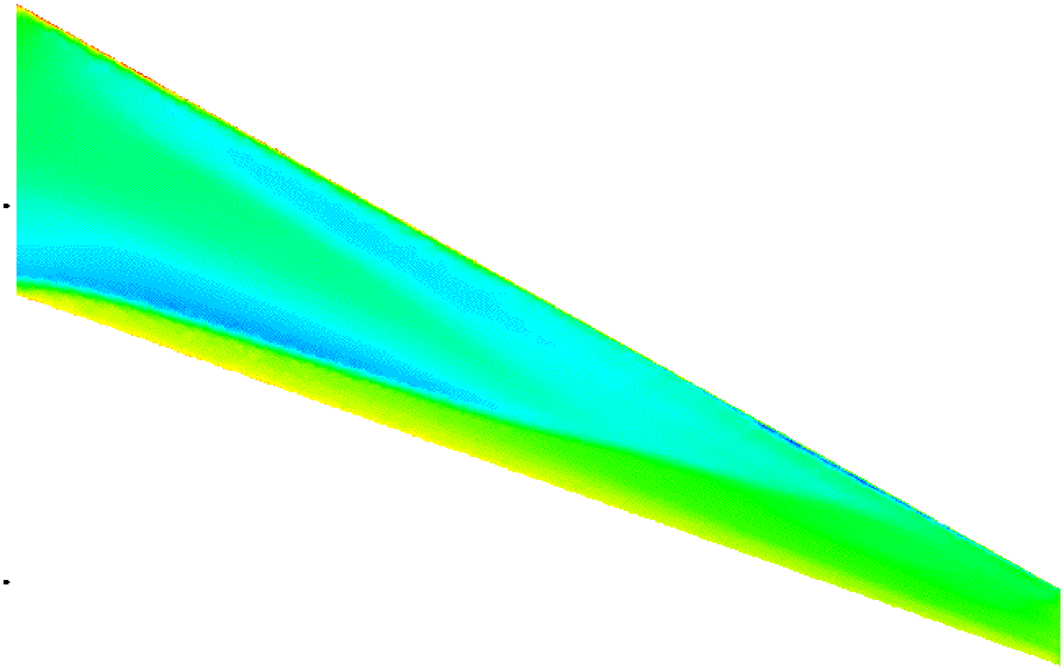

Figure 78: Pressure contours of the upper surface of the SBW A7 wing with designed supercritical airfoils, $C_l$ = 0.518. Twist distribution of the wing was linearly lofted from the root, 10% span, 30% span and tip stations. FELISA inviscid solution, M=0.85.

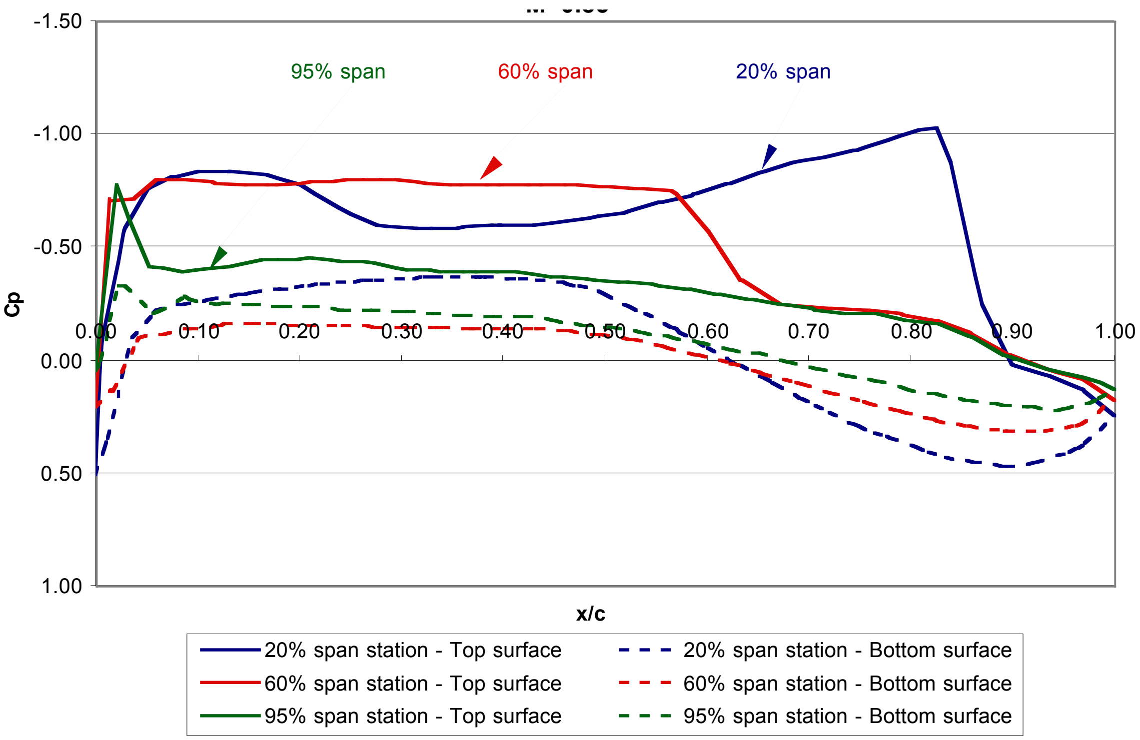

Figure 79: Pressure coefficient distribution on the SBW A7 wing with designed supercritical airfoils, $C_l$ =0.518. FELISA inviscid solution, M=0.85.

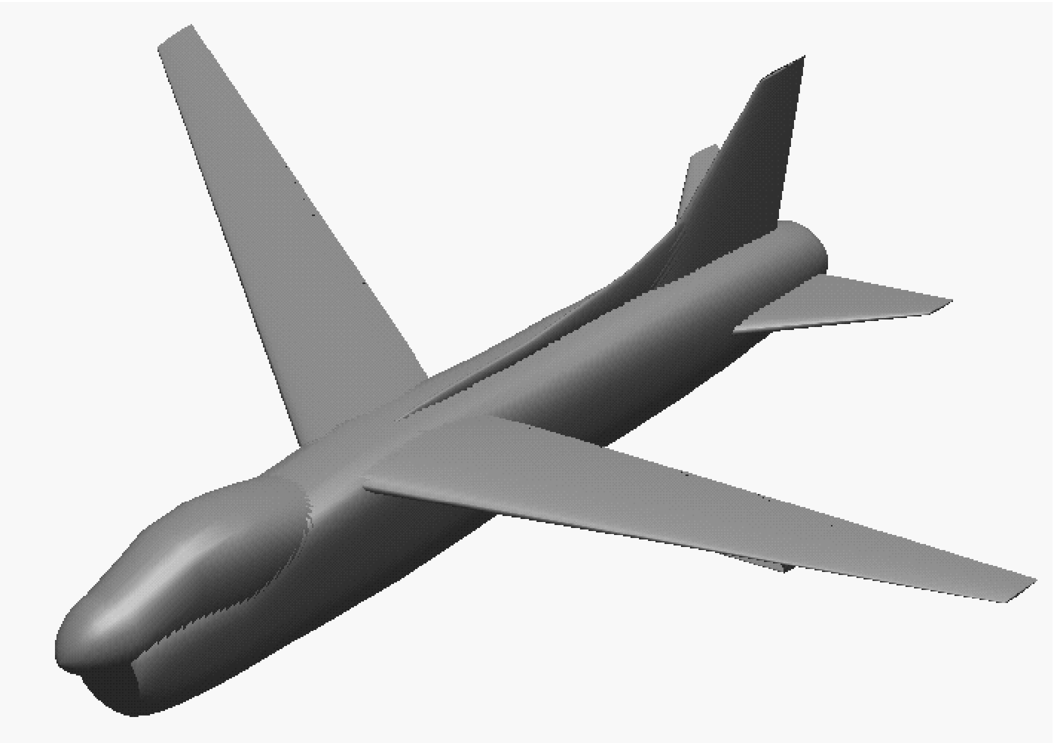

Figure 80**:** Rendered picture of the A7 SBW demonstrator aircraft geometry modeled in RAM

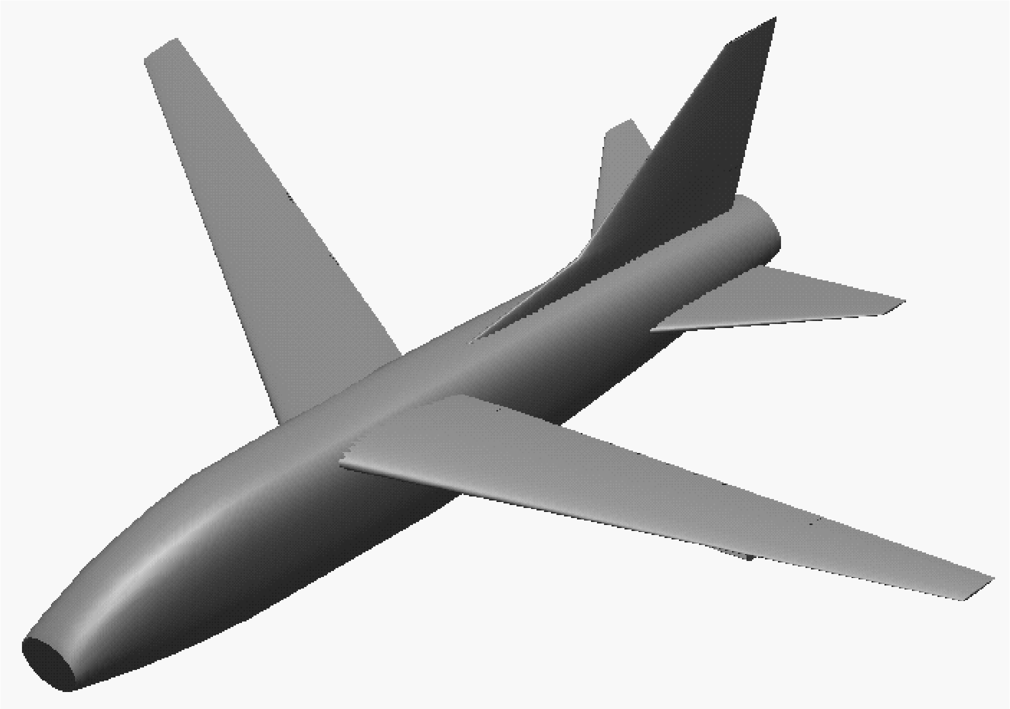

Figure 81: Rendered picture of the simplified A7 SBW demonstrator aircraft geometry modeled in RAM used to generate in the computational grid.

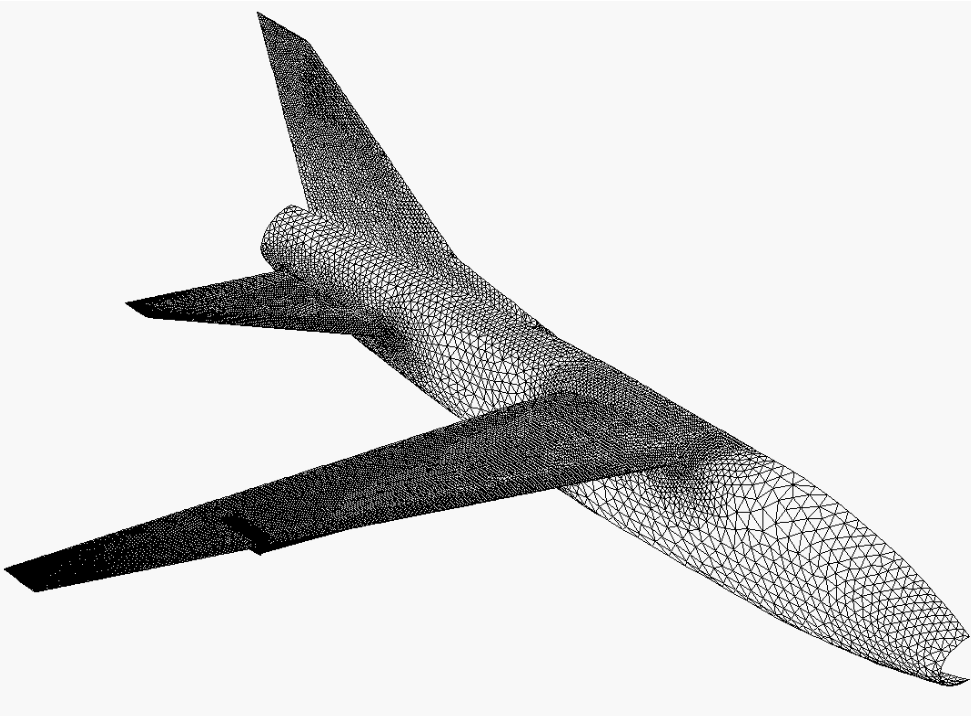

Figure 82: Surface triangulation of the simplified A7 SBW demonstrator aircraft geometry.

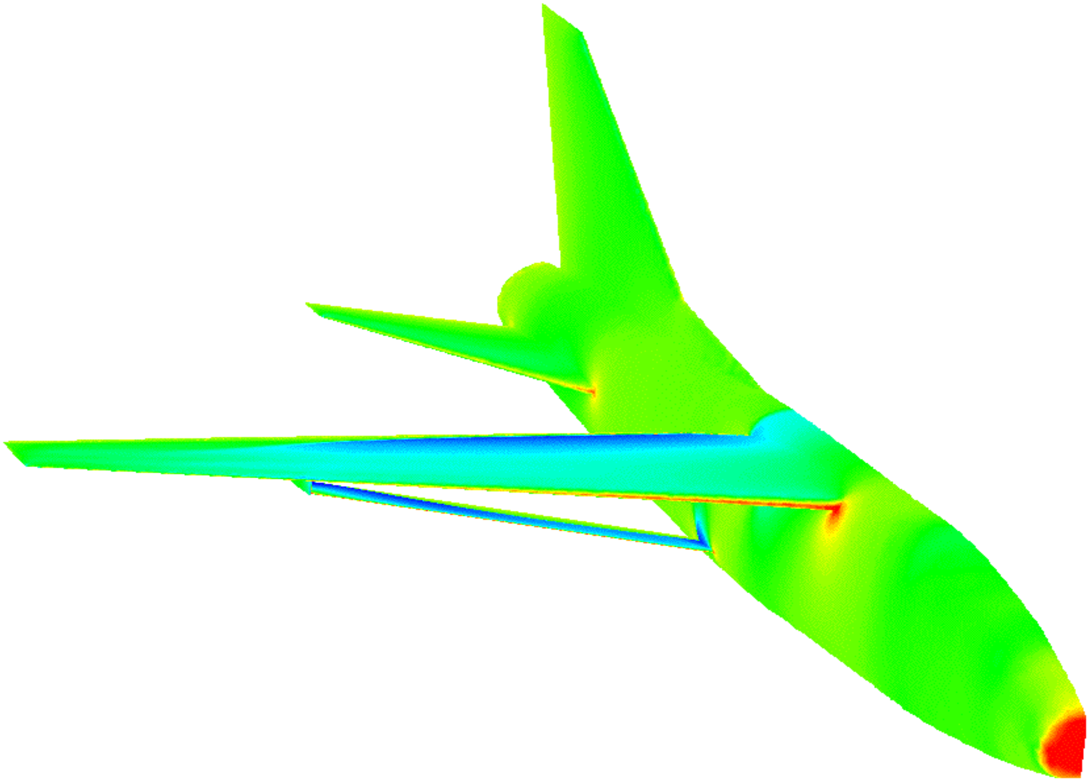

Figure 83: Pressure contours on the simplified A7 SBW geometry. FELISA inviscid solution, M=0.85, $\alpha$=2.85°.

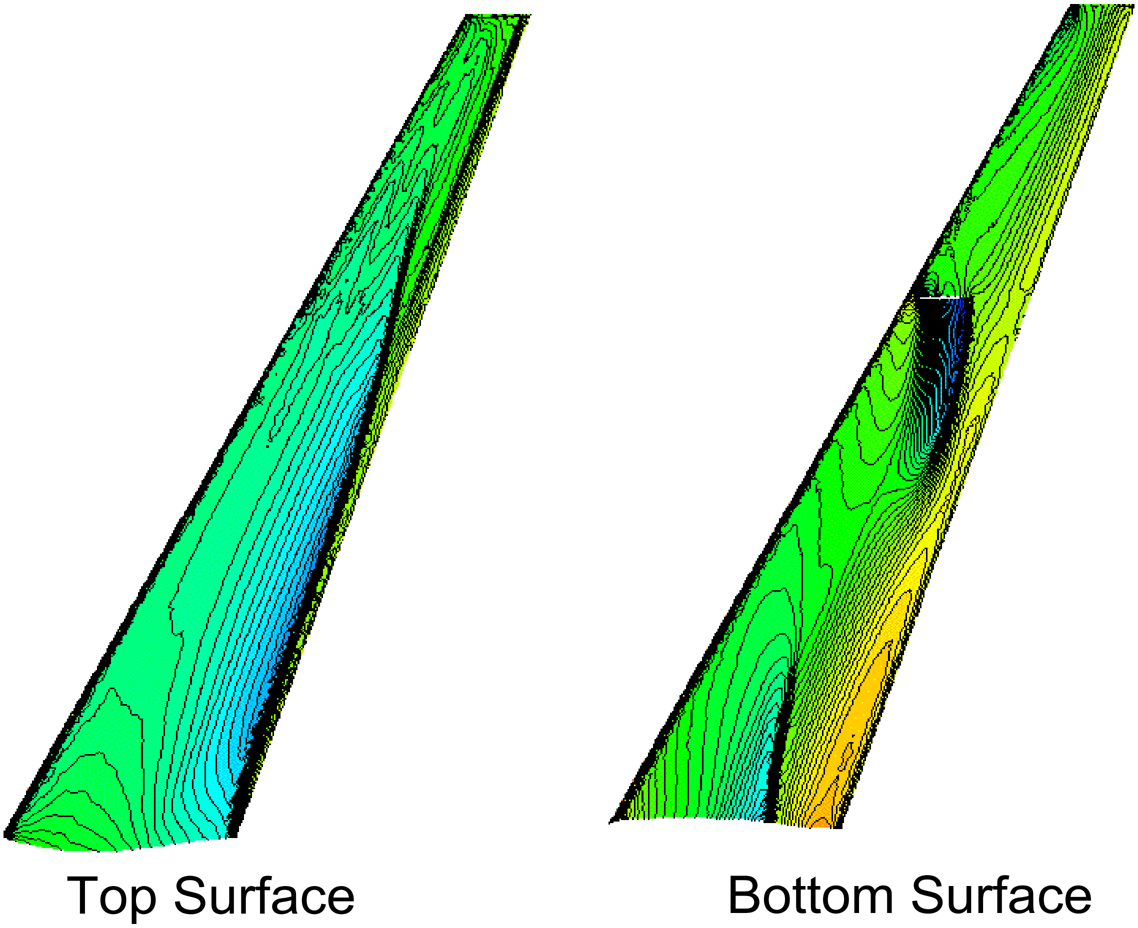

Figure 84: Pressure contours on the top and bottom surface of the wing on the simplified A7 SBW demonstrator aircraft. FELISA inviscid solution, M=0.85, $\alpha$=2.85°.

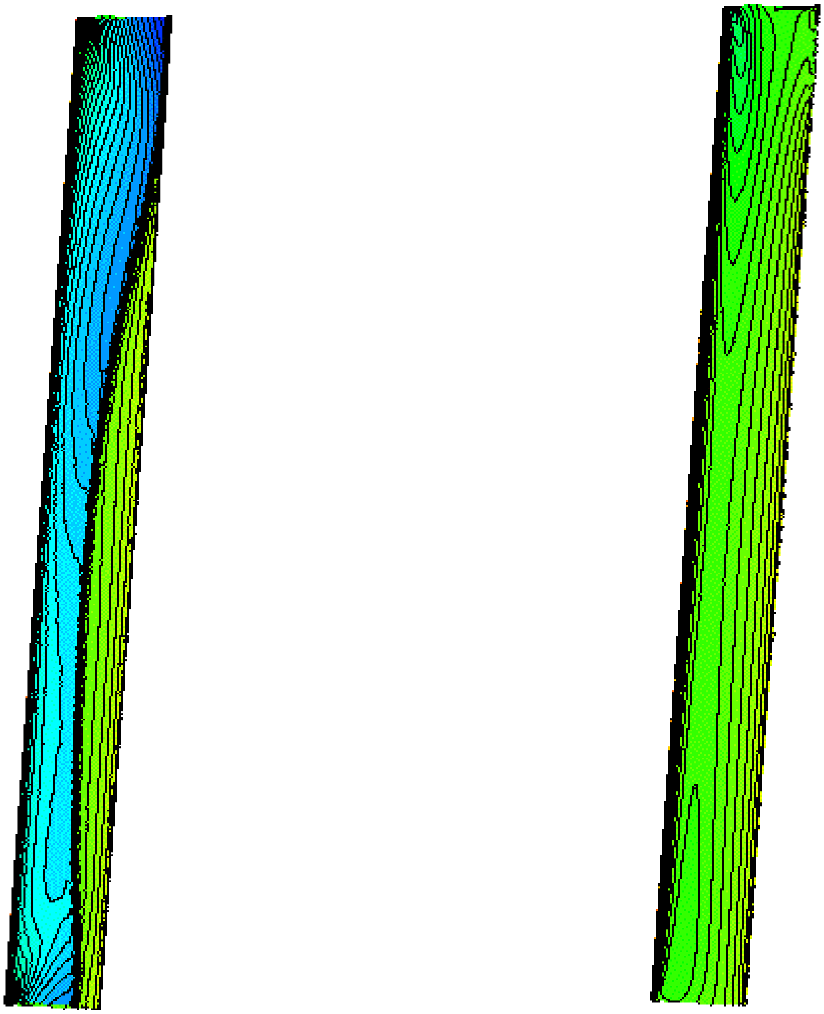

Top Surface

Bottom Surface

Figure 85: Pressure contours of the upper and lower surface of the strut on the simplified A7 SBW demonstrator aircraft. FELISA inviscid solution, M=0.85, $\alpha$=2.85°.

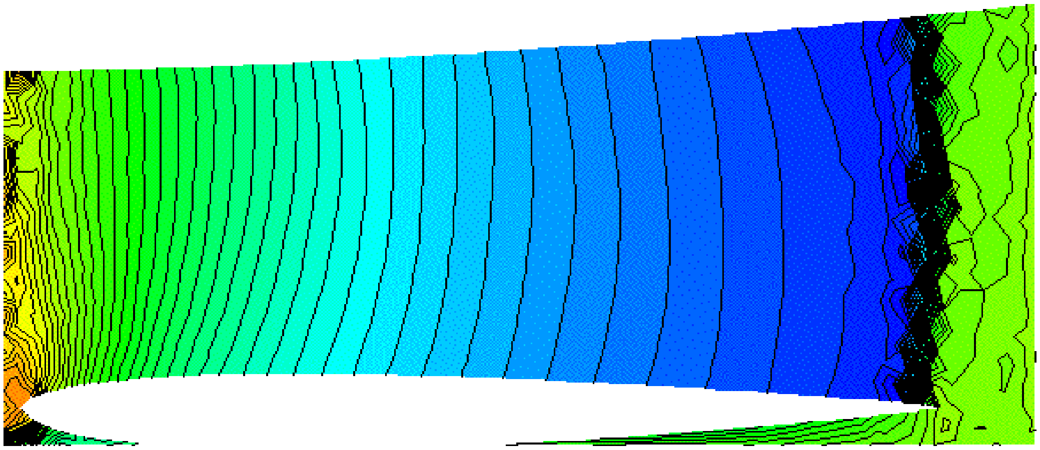

Inboard surface

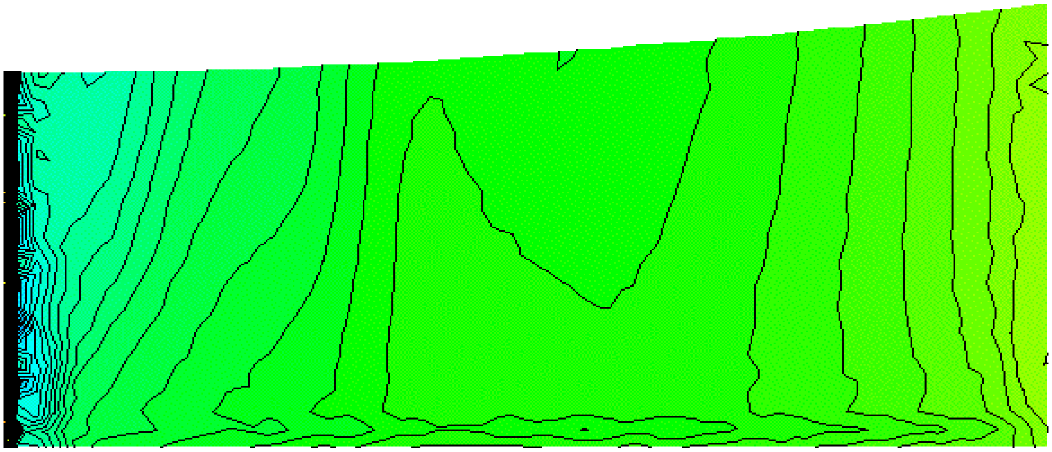

Outboard surface

Figure 86: Pressure contours of the inboard and outboard surface of the pylon on the simplified A7 SBW demonstrator aircraft. FELISA inviscid solution, M=0.85, $\alpha=2.85^{o}$.

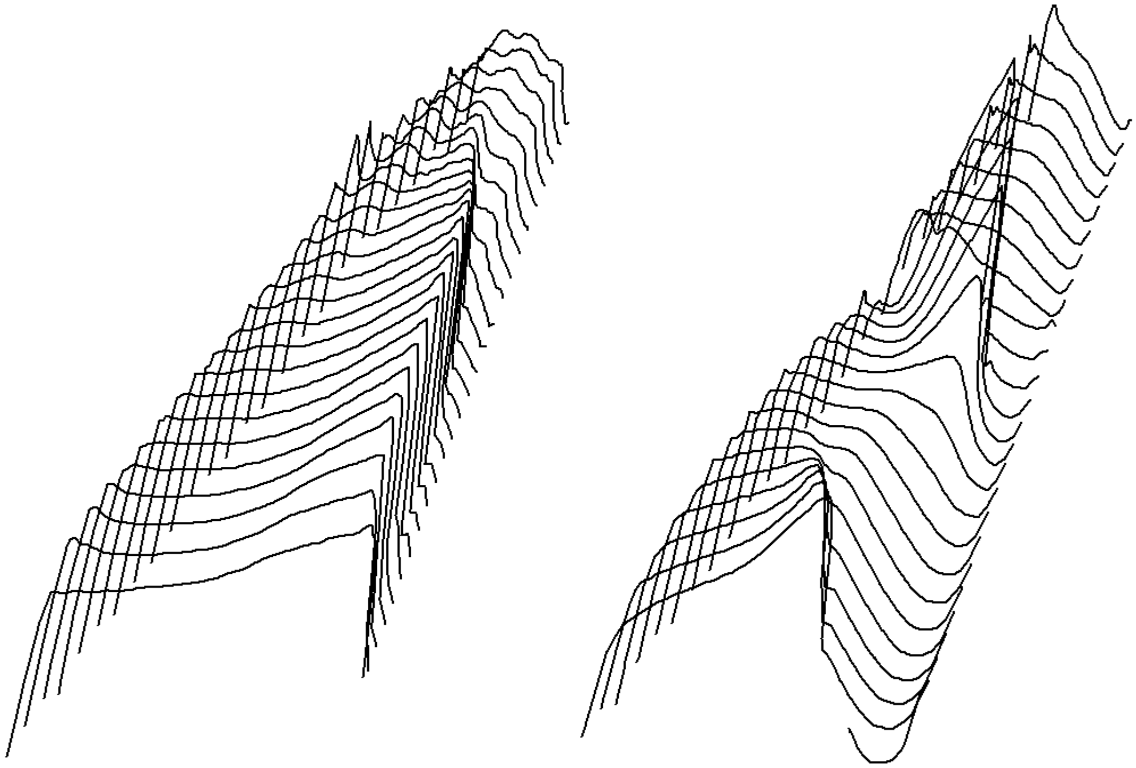

Top Surface Bottom Surface

Figure 87: Pressure coefficient distribution at various chordwise stations on the top and bottom surface of the wing on the simplified A7 SBW demonstrator aircraft. FELISA inviscid solution, M=0.85, $\alpha$=2.85°.

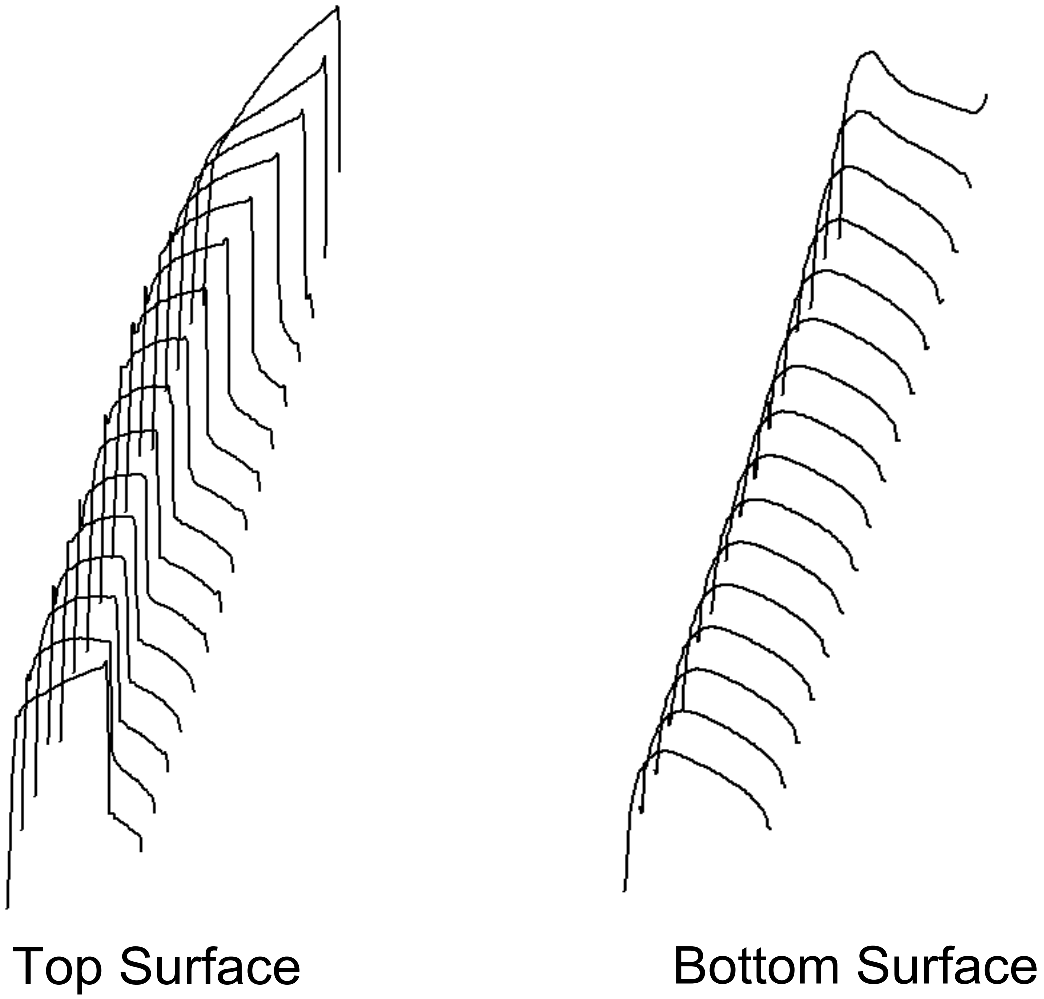

Top Surface

Bottom Surface

Figure 88: Pressure coefficient distribution at various chordwise stations on the top and bottom surface of the strut on the simplified A7 SBW demonstrator aircraft. FELISA inviscid solution, $M=0.85$, $\alpha=2.85^{\circ}$.

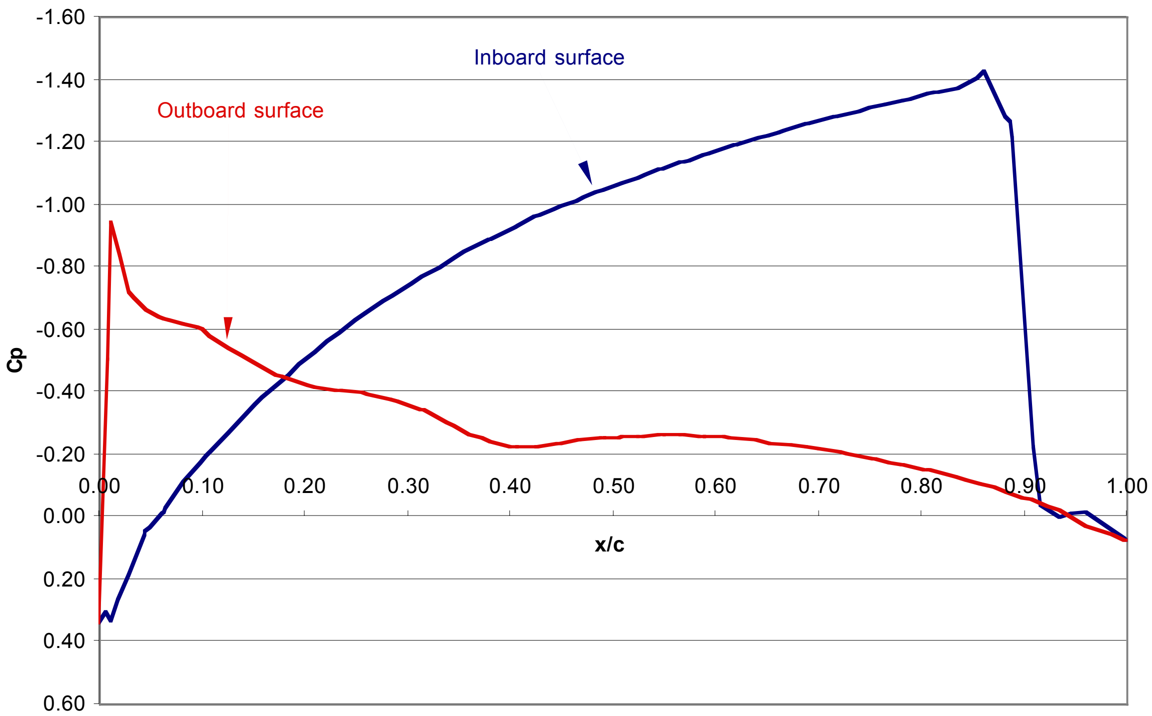

Figure 89: Pressure coefficient distribution at a chordwise station (*z*=1.5) on the inboard and outboard surface of the pylon on the simplified A7 SBW demonstrator aircraft. FELISA inviscid solution, M=0.85, α=2.85°.

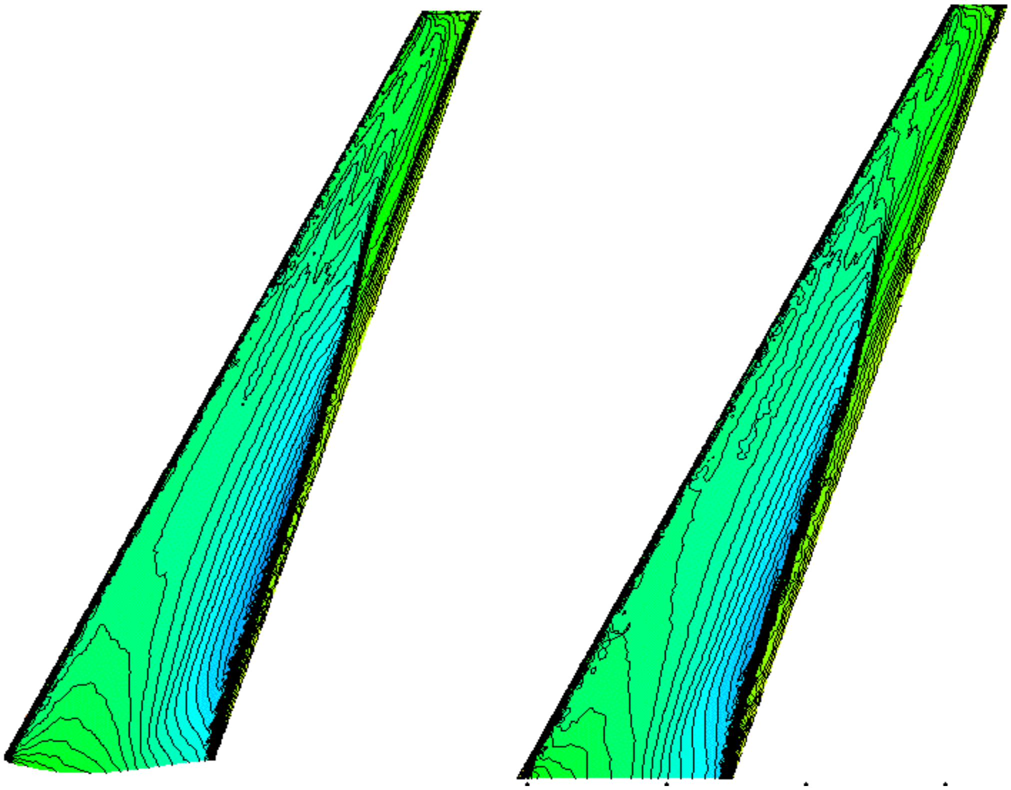

With fuselage, $C_L$=0.529 Without fuselage, $C_L$=0.518

Figure 90: Pressure contours of the upper surface of the wing. Comparing the effect of the fuselage. FELISA inviscid solution. M=0.85, $\alpha$=2.85º.

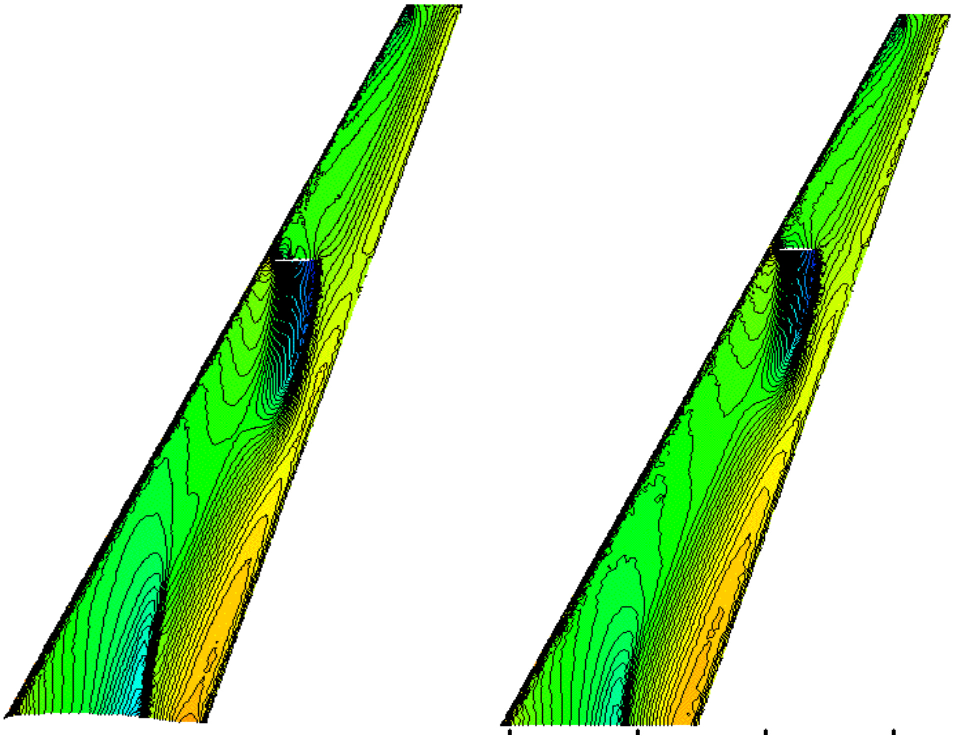

With fuselage, $C_L$=0.529 Without fuselage, $C_L$=0.518

Figure 91: Pressure contours of the lower surface of the wing. Comparing the effect of the fuselage. FELISA inviscid solution. M=0.85, $\alpha$=2.85°.

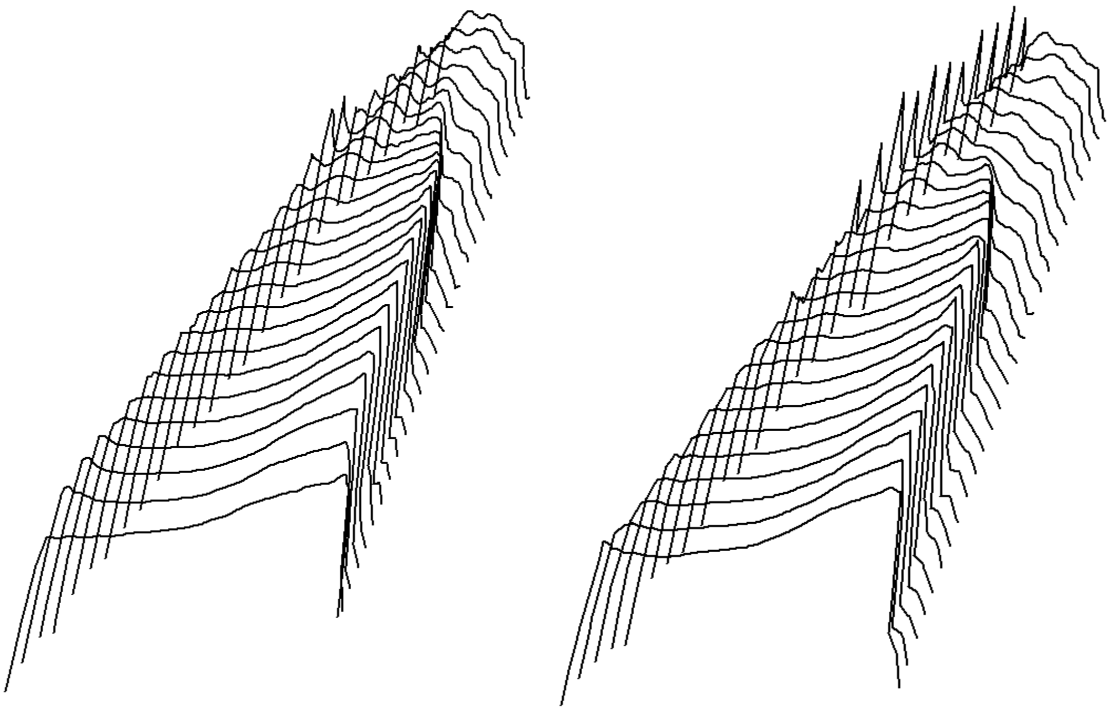

With fuselage, $C_L$=0.529 Without fuselage, $C_L$=0.518

Figure 92: Pressure coefficient distribution at various chordwise stations on the upper surface of the wing. Comparing the effect of the fuselage. FELISA inviscid solution. M=0.85, $\alpha$=2.85°.

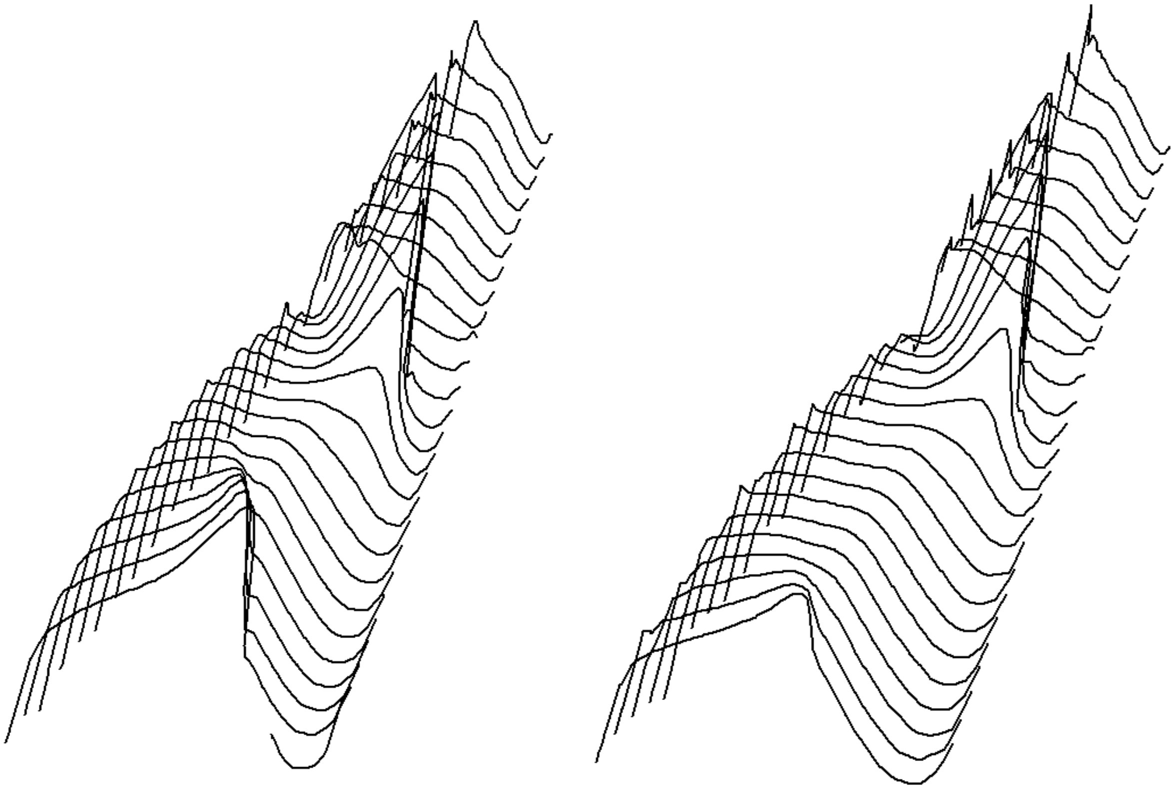

With fuselage, $C_L$=0.529 Without fuselage, $C_L$=0.518

Figure 93: Pressure coefficient distribution at various chordwise stations on the lower surface of the wing. Comparing the effect of the fuselage. FELISA inviscid solution. M=0.85, $\alpha$=2.85°.

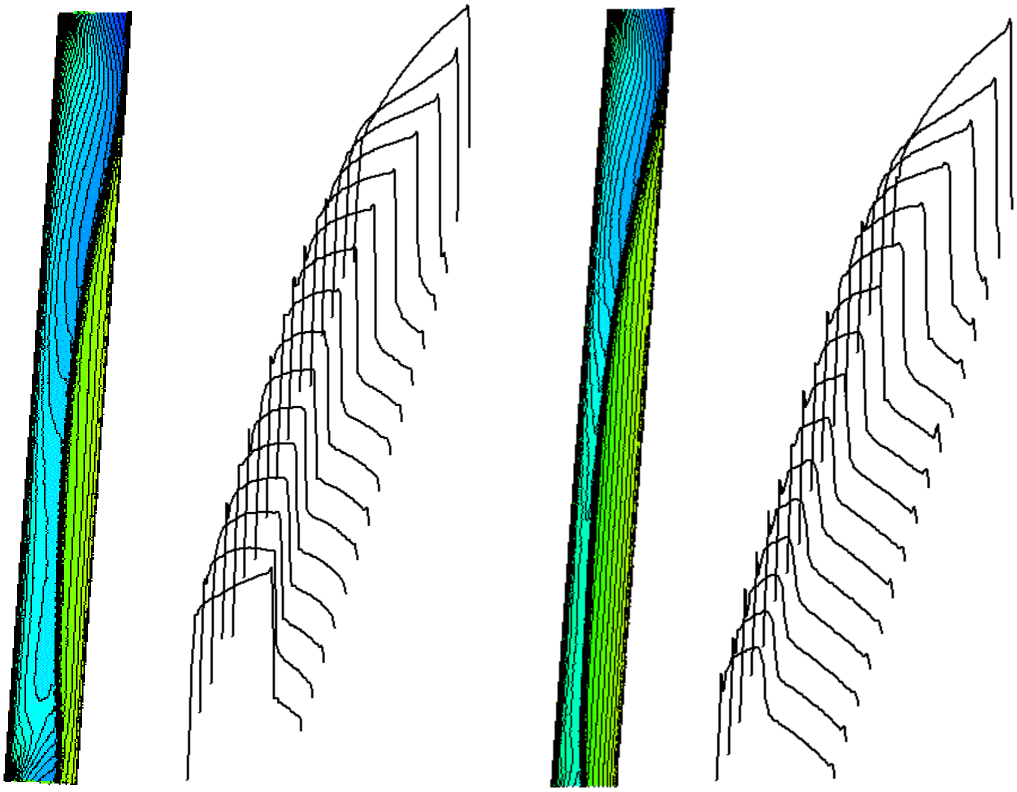

With fuselage, $C_L$=0.529 Without fuselage, $C_L$=0.518

Figure 94: Pressure contours and pressure coefficient distribution at various chordwise stations on the upper surface of the strut. Comparing the effect of the fuselage. FELISA inviscid solution. M=0.85, $\alpha$=2.85°.

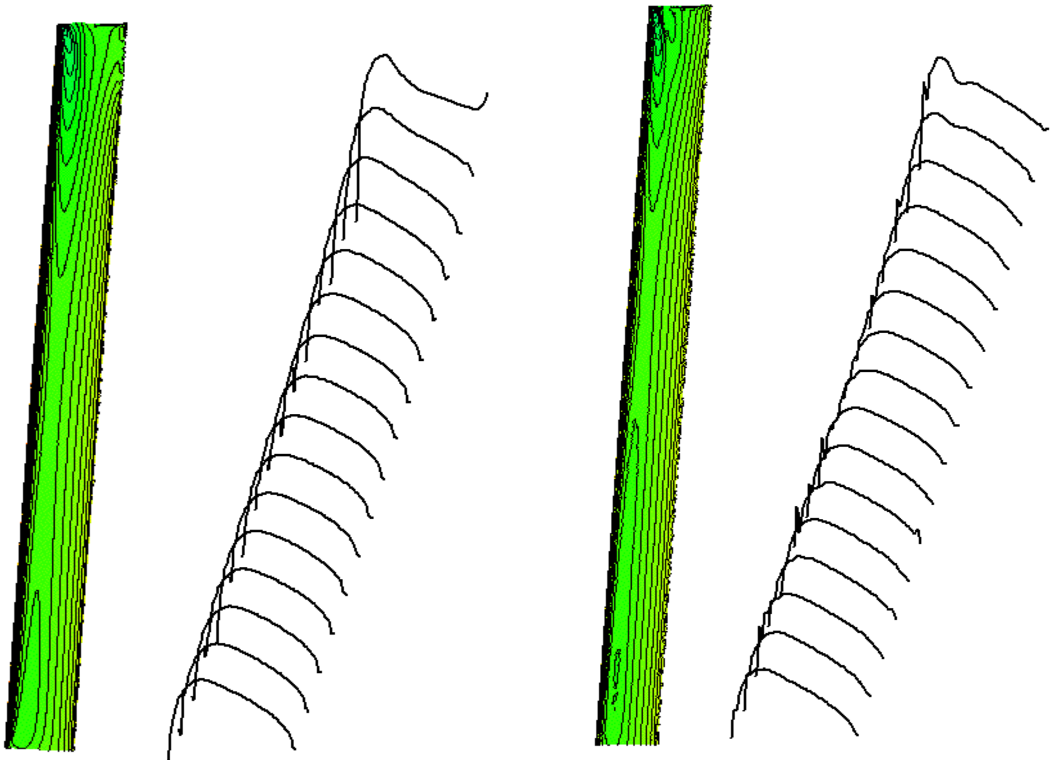

With fuselage, $C_L$=0.529 Without fuselage, $C_L$=0.518

Figure 95: Pressure contours and pressure coefficient distribution at various chordwise stations on the lower surface of the strut. Comparing the effect of the fuselage. FELISA inviscid solution. M=0.85, $\alpha$=2.85°.

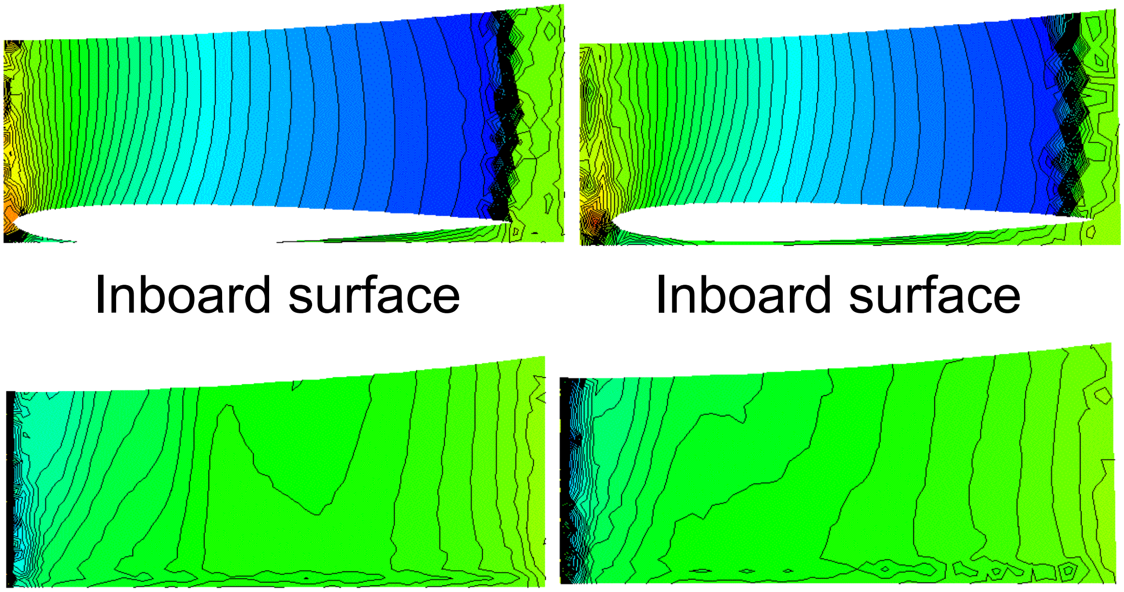

Inboard surface

Inboard surface

Outboard surface

Outboard surface

With fuselage, $C_L=0.529$

Without fuselage, $C_L=0.518$

Figure 96: Pressure contours on the inboard and outboard surfaces of the pylon. Comparing the effect of the fuselage. FELISA inviscid solution. M=0.85, $\alpha=2.85^o$.

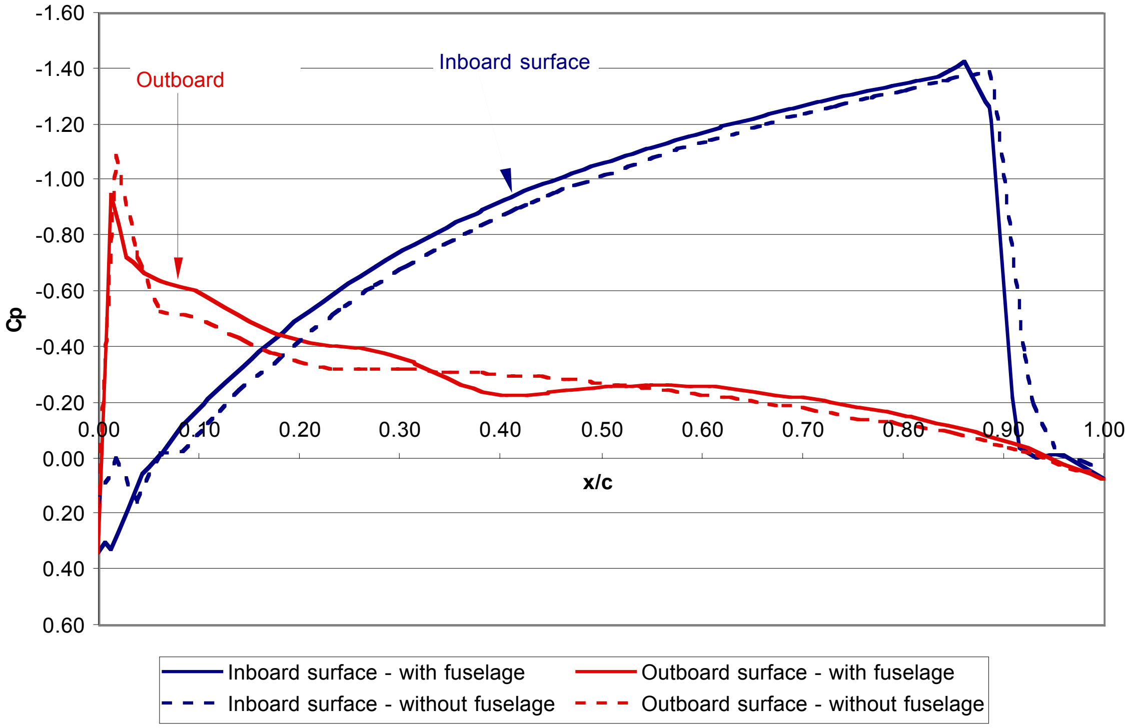

Figure 97: Pressure coefficient distribution of a section ($z$=1.5) on the inboard and outboard surfaces of the pylon. Comparing the effect of the fuselage. FELISA inviscid solution. M=0.85, $\alpha$=2.85º.

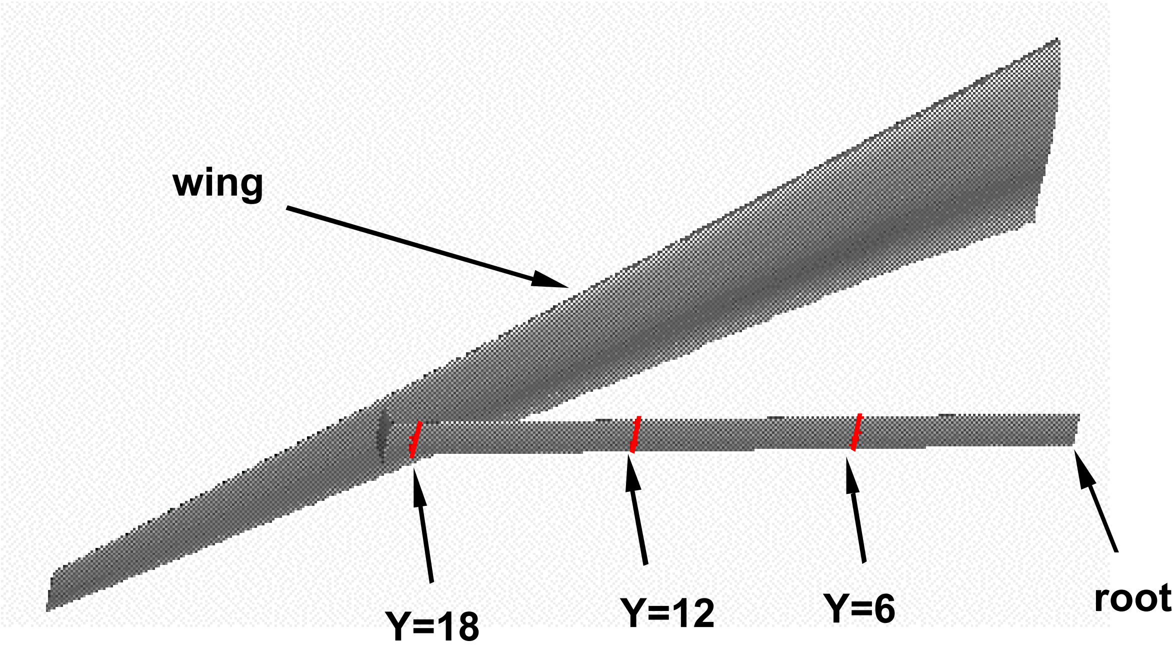

Figure 98: Illustration showing the wing, pylon and strut. Red lines show the position of the chordwise stations along the strut that where the pressure coefficient distribution will be examined in the various studies.

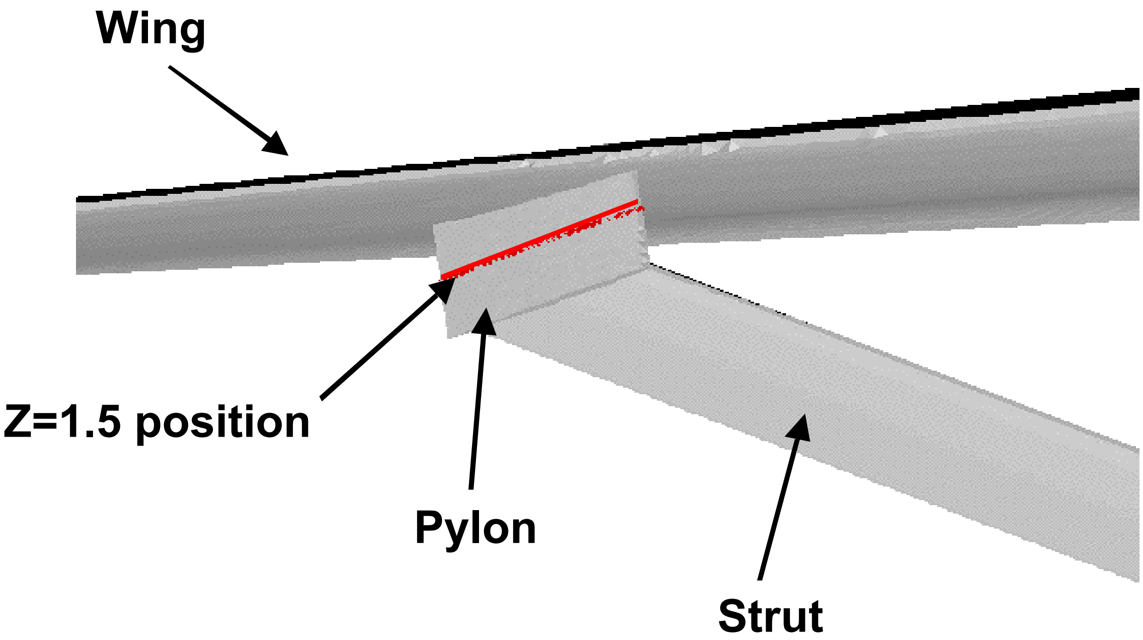

Figure 99: Illustration showing the wing,pylon and strut. The red line shows the position of the *z*=1.5 cut on the pylon where the pressure coefficient distribution will be examined in the various studies.

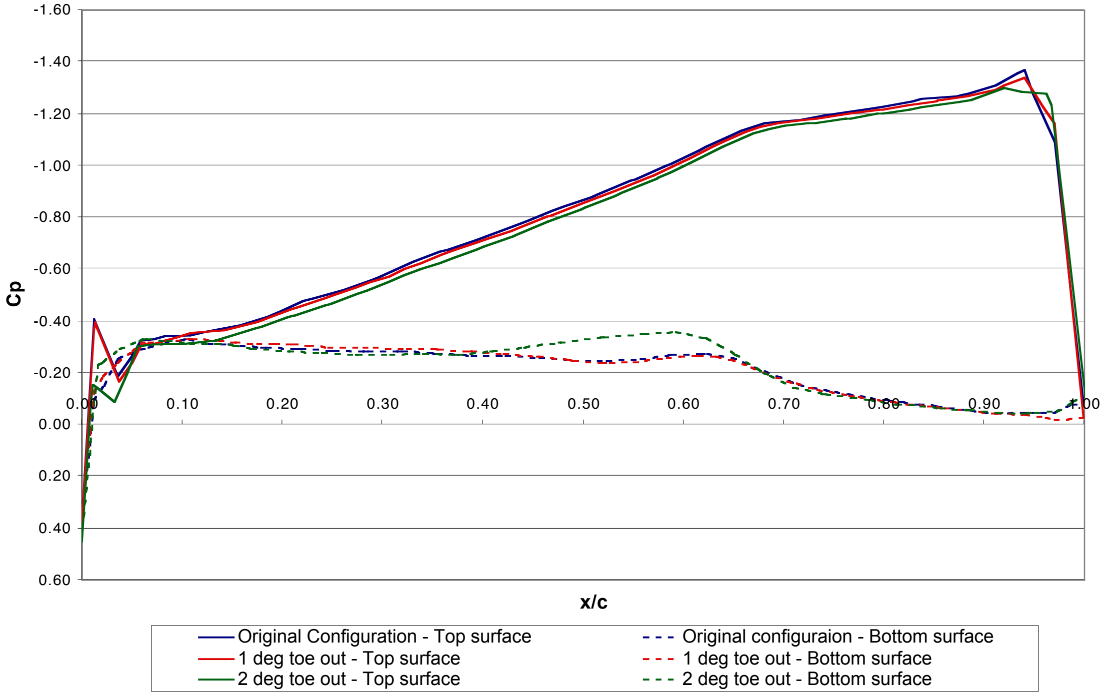

Figure 100: Pressure coefficient distribution on the strut at *y*=18 for the pylon toe-out study. FELISA inviscid solution, M=0.85.

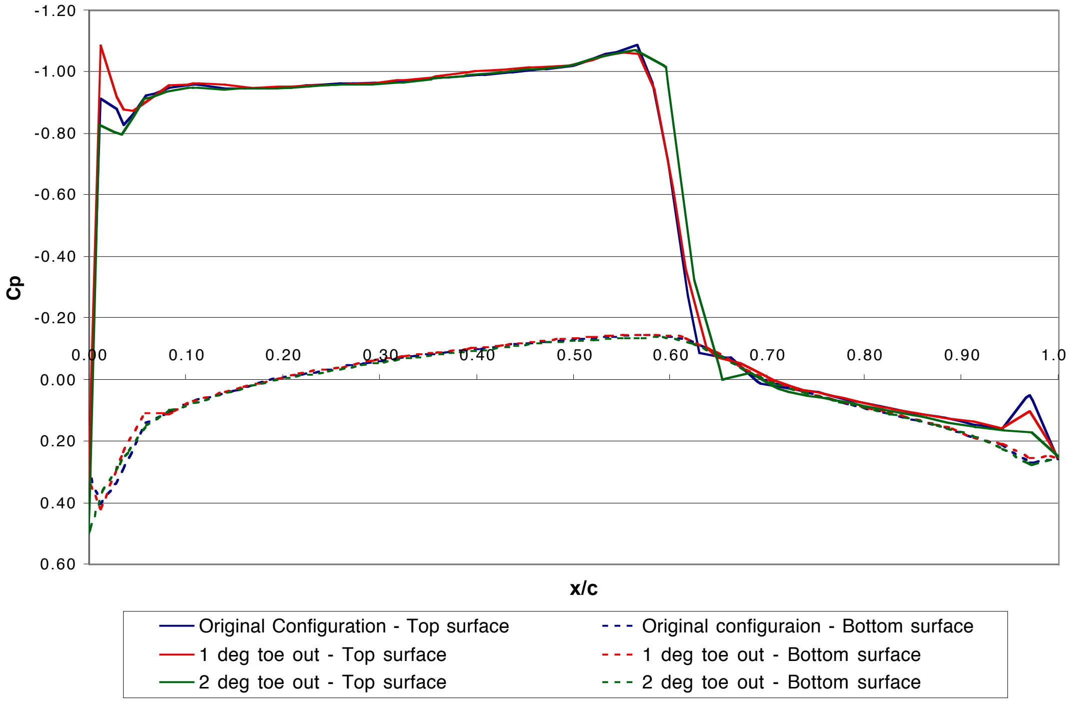

Figure 101: Pressure coefficient distribution on the strut at *y*=12 for the pylon toe-out study. FELISA inviscid solution, M=0.85.

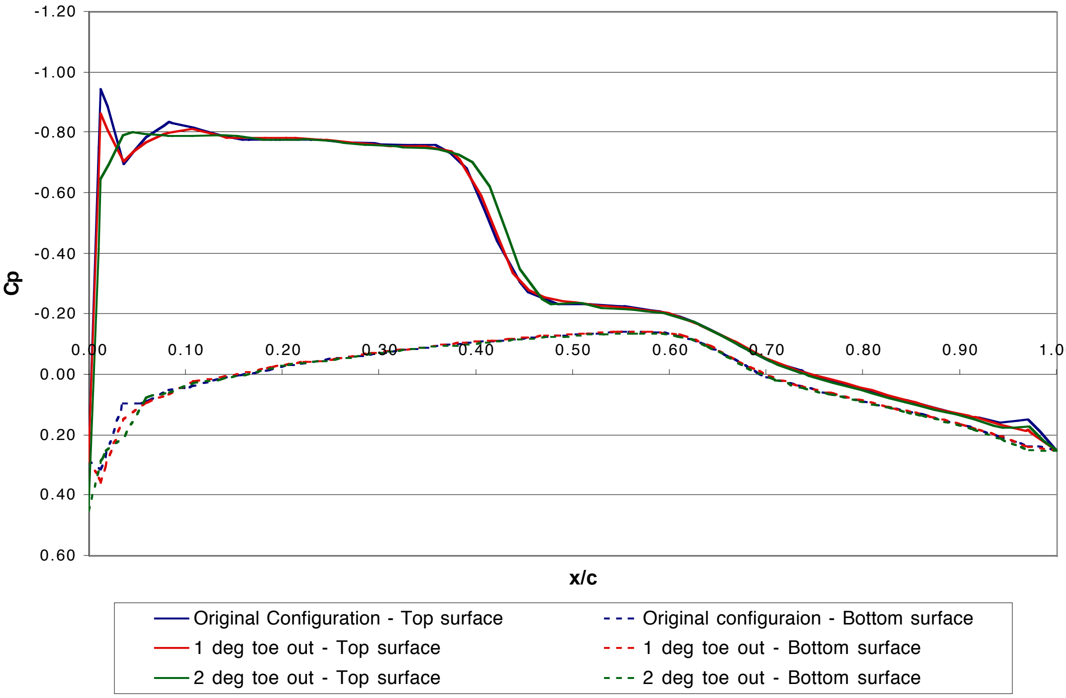

Figure 102: Pressure coefficient distribution on the strut at *y*=6 for the pylon toe-out study. FELISA inviscid solution, M=0.85.

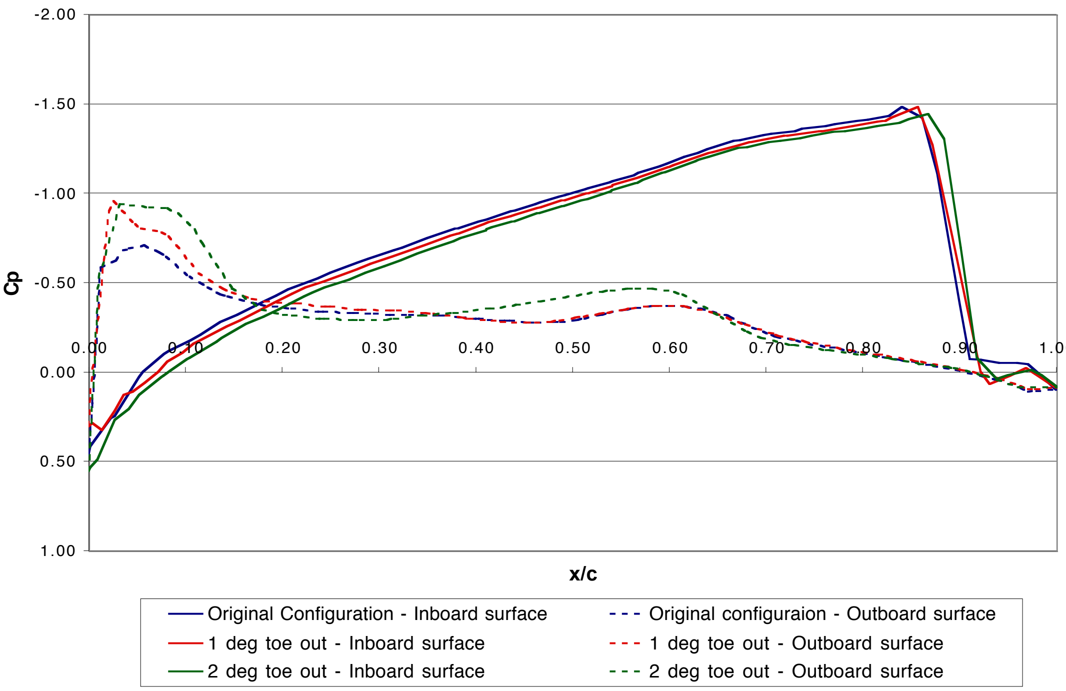

Figure 103: Pressure coefficient distribution on the pylon at *z*=1.5 for the pylon toe-out study. FELISA inviscid solution, M=0.85.

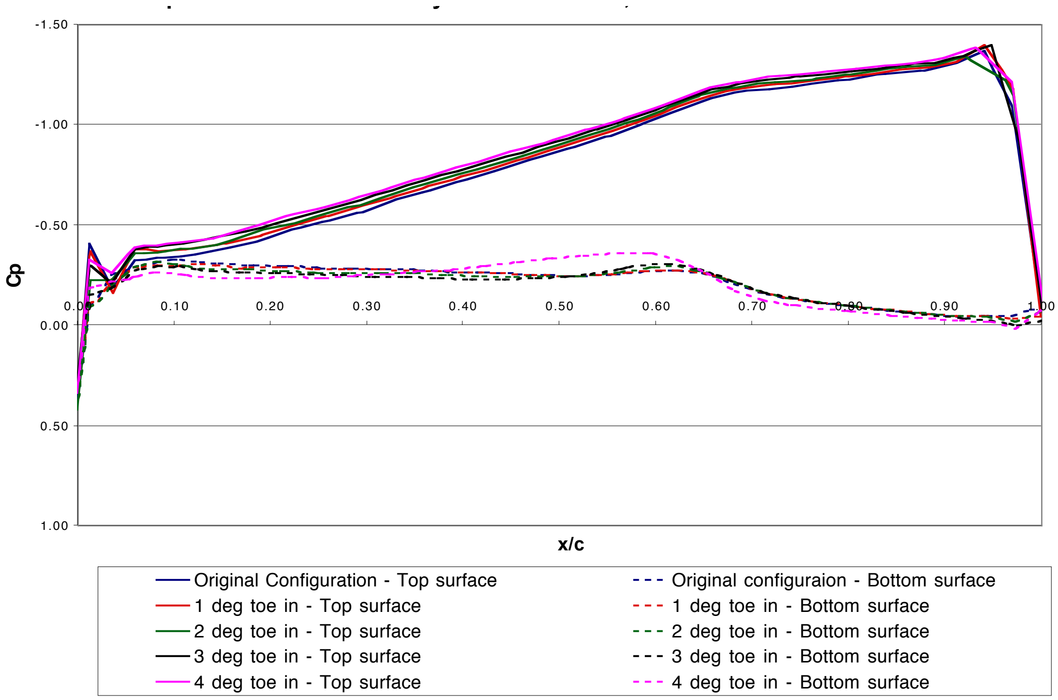

Figure 104: Pressure coefficient distribution on the strut at *y*=18 for the pylon toe-in study. FELISA inviscid solution, M=0.85.

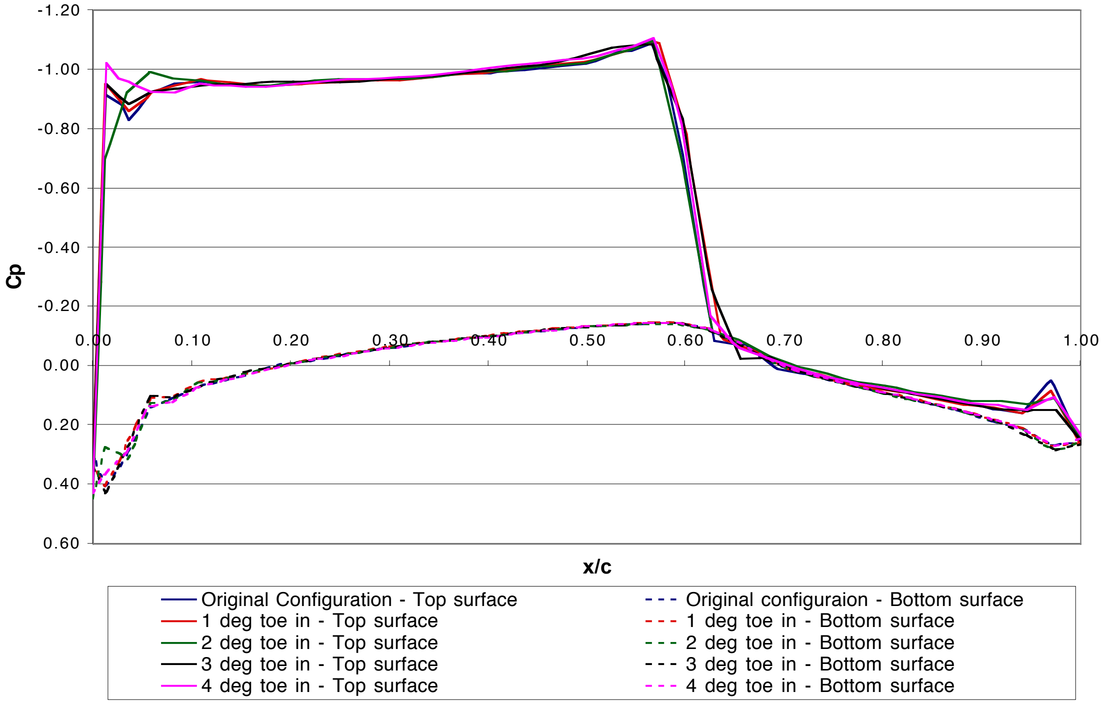

Figure 105: Pressure coefficient distribution on the strut at *y*=12 for the pylon toe-in study. FELISA inviscid solution, M=0.85.

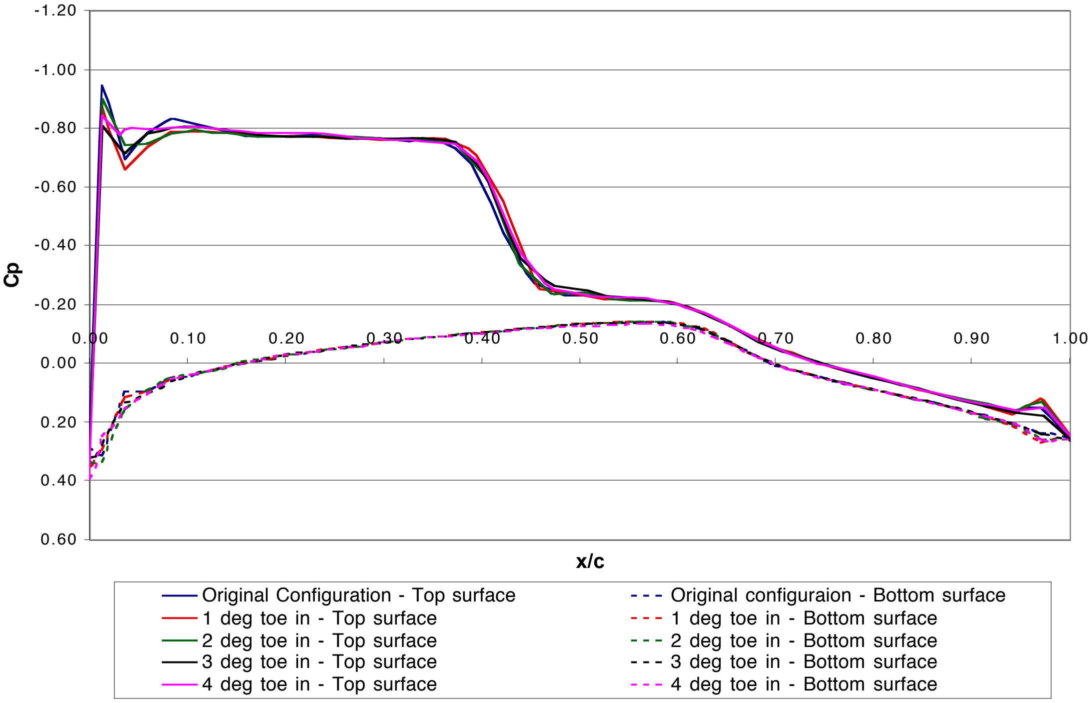

Figure 106: Pressure coefficient distribution on the strut at *y*=6 for the pylon toe-in study. FELISA inviscid solution, M=0.85.

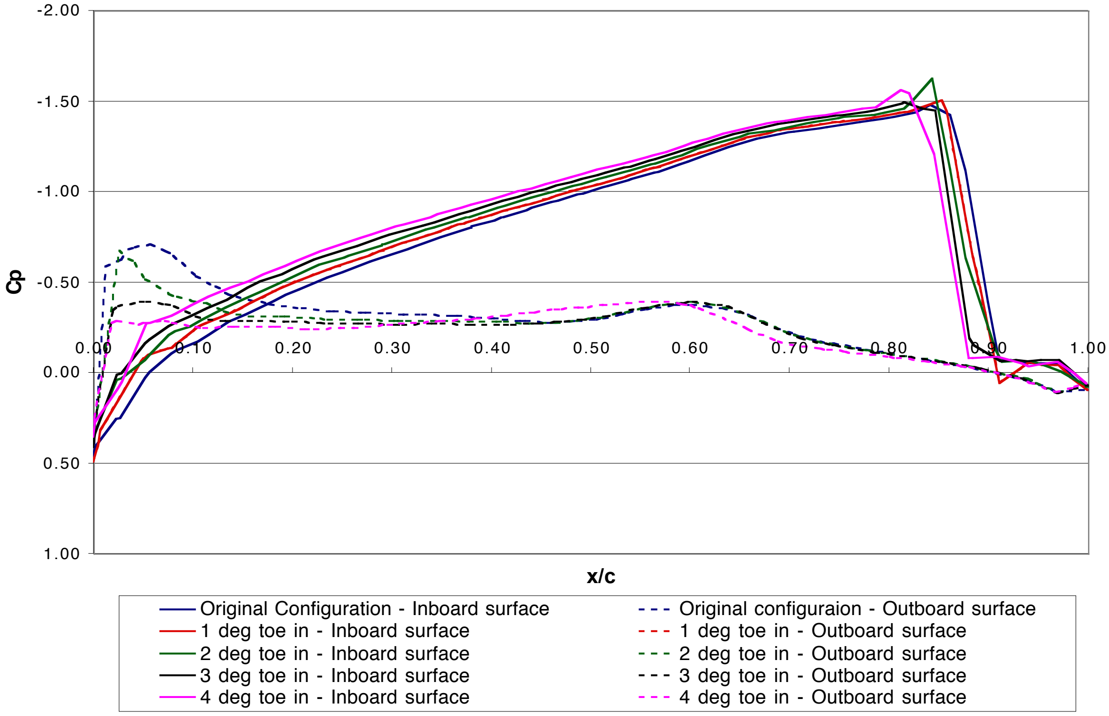

Figure 107: Pressure coefficient distribution on the pylon at *z*=1.5 for the pylon toe-in study. FELISA inviscid solution, M=0.85.

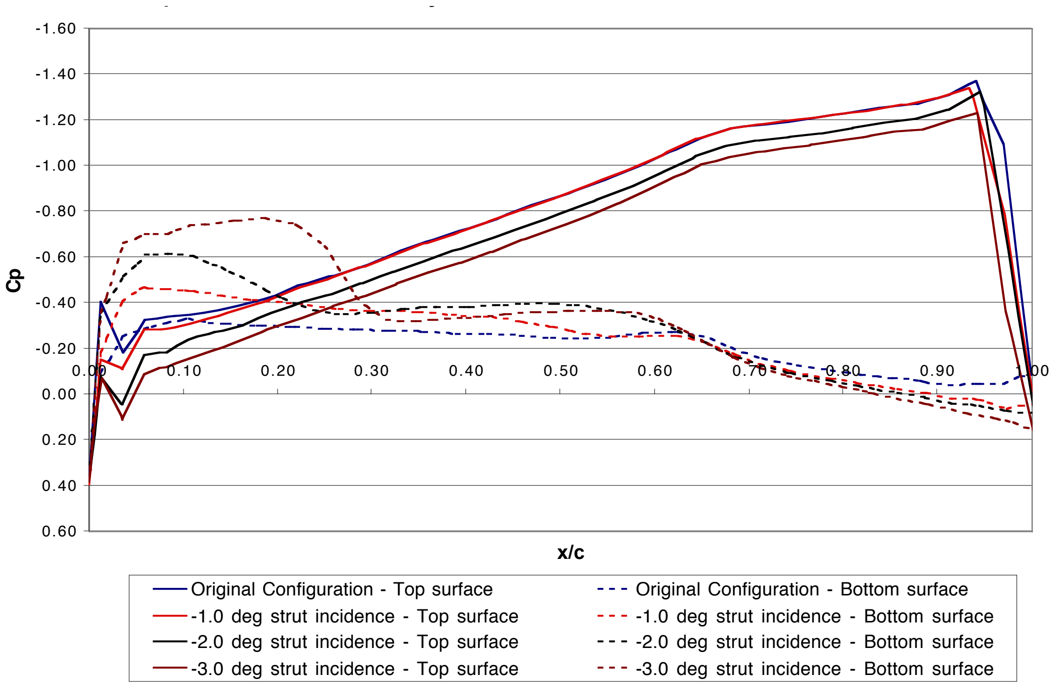

Figure 108: Pressure coefficient distribution on the strut at *y*=18 for the strut incidence study. FELISA inviscid solution, M=0.85.

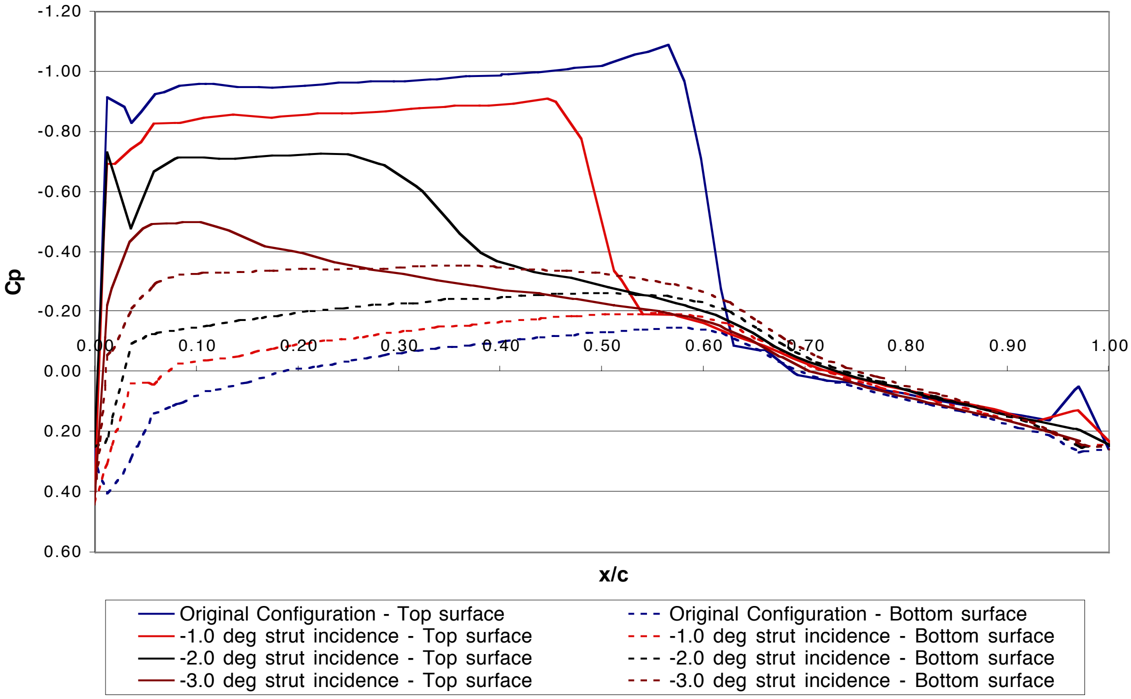

Figure 109: Pressure coefficient distribution on the strut at *y*=12 for the strut incidence study. FELISA inviscid solution, M=0.85.

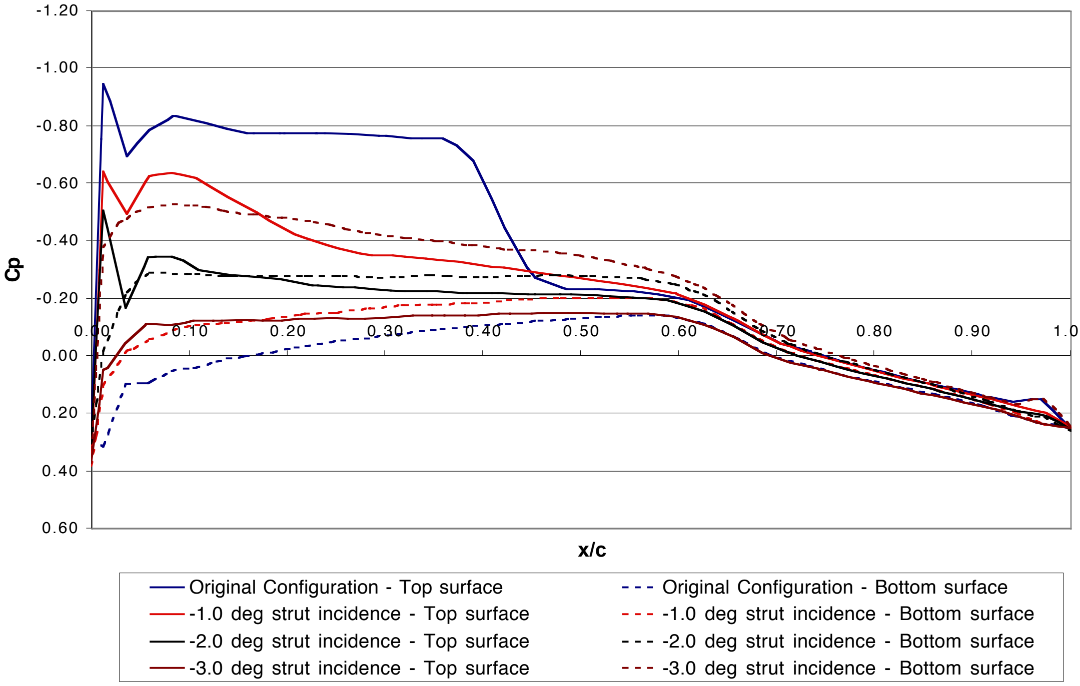

Figure 110: Pressure coefficient distribution on the strut at *y*=6 for the strut incidence study. FELISA inviscid solution, M=0.85.

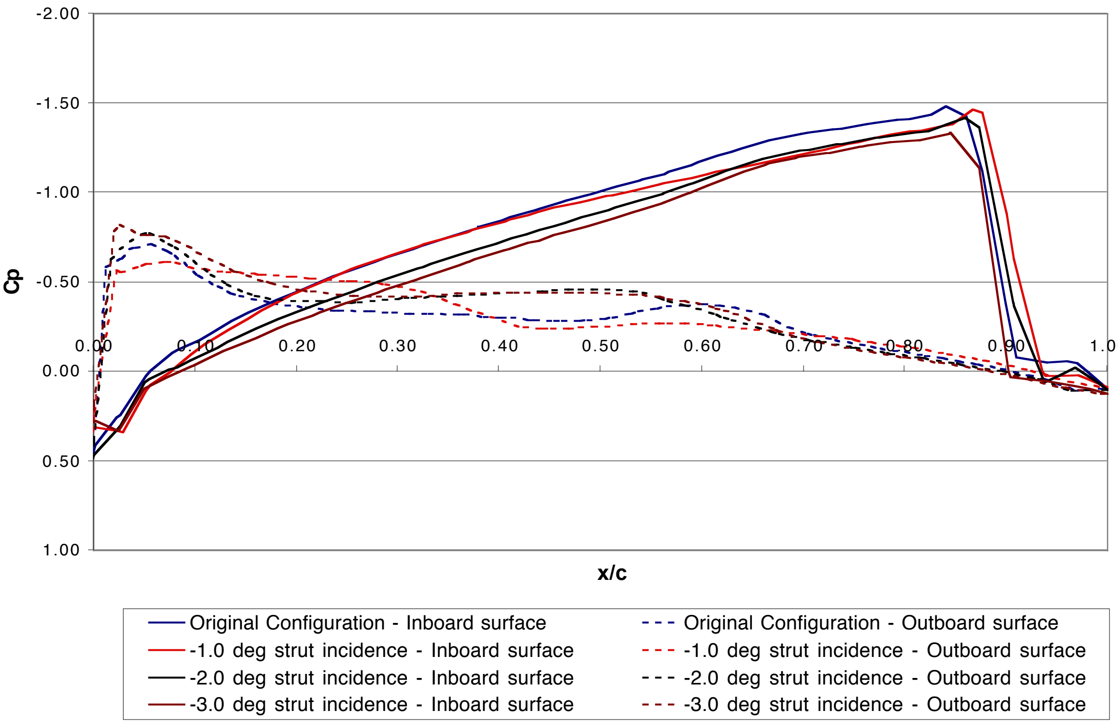

Figure 111: Pressure coefficient distribution on the pylon at *z*=1.5 for the strut incidence study. FELISA invisicid solution, M=0.85.

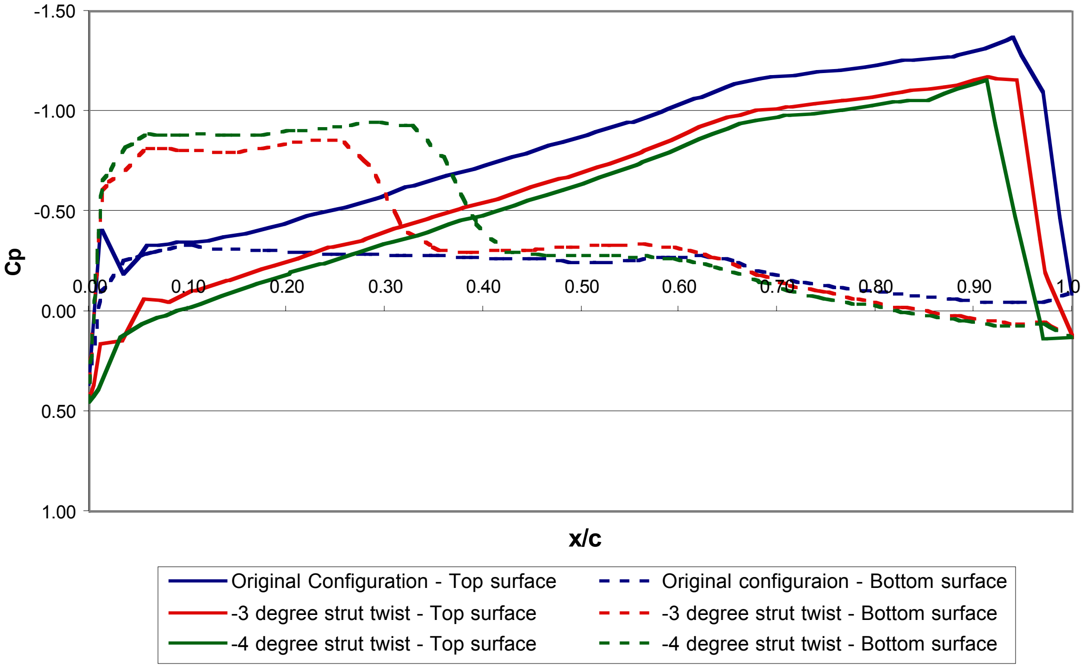

Figure 112: Pressure coefficient distribution on the strut at *y*=18 for the strut twist study. FELISA inviscid solution, M=0.85.

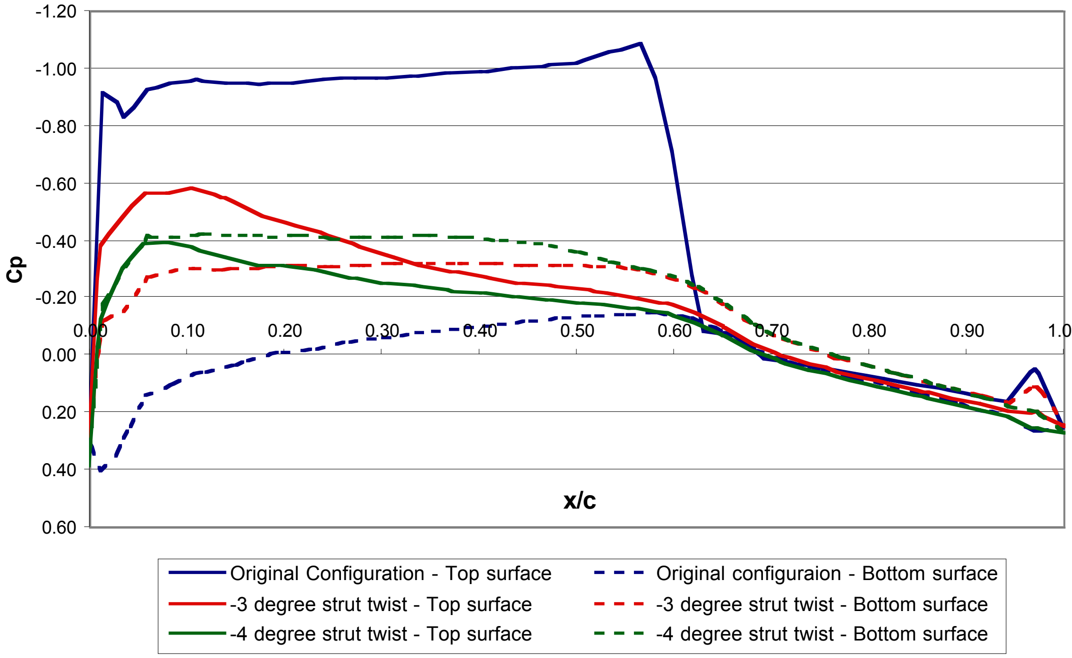

Figure 113: Pressure coefficient distribution on the strut at *y*=12 for the strut twist study. FELISA inviscid solution, M=0.85.

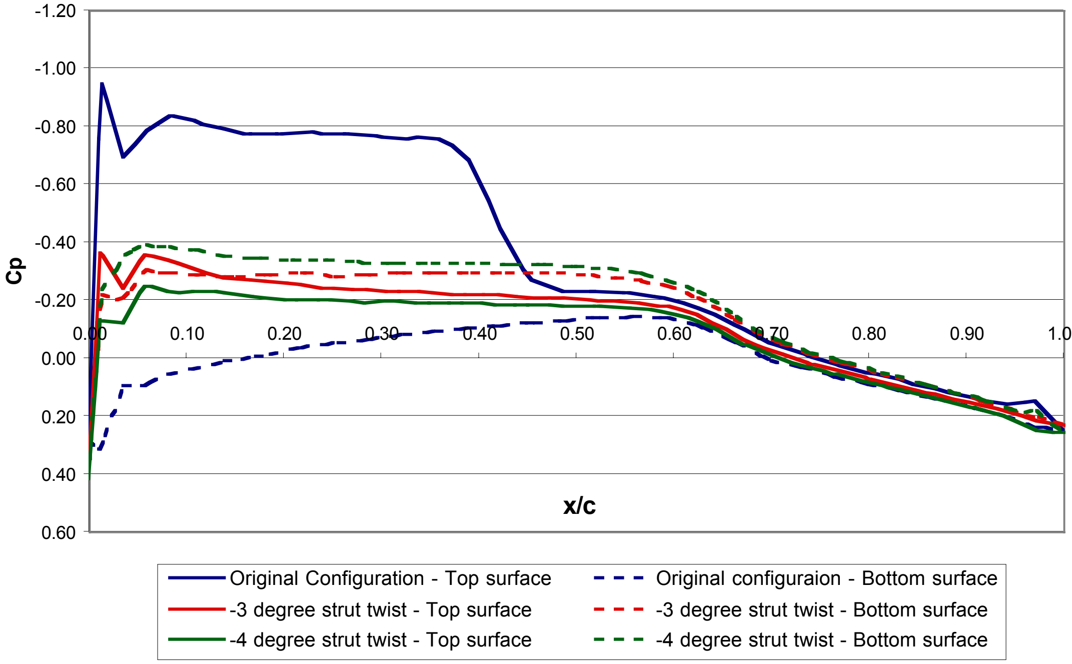

Figure 114: Pressure coefficient distribution on the strut at *y*=6 for the strut twist study. FELISA inviscid solution, M=0.85. Strut twist study.

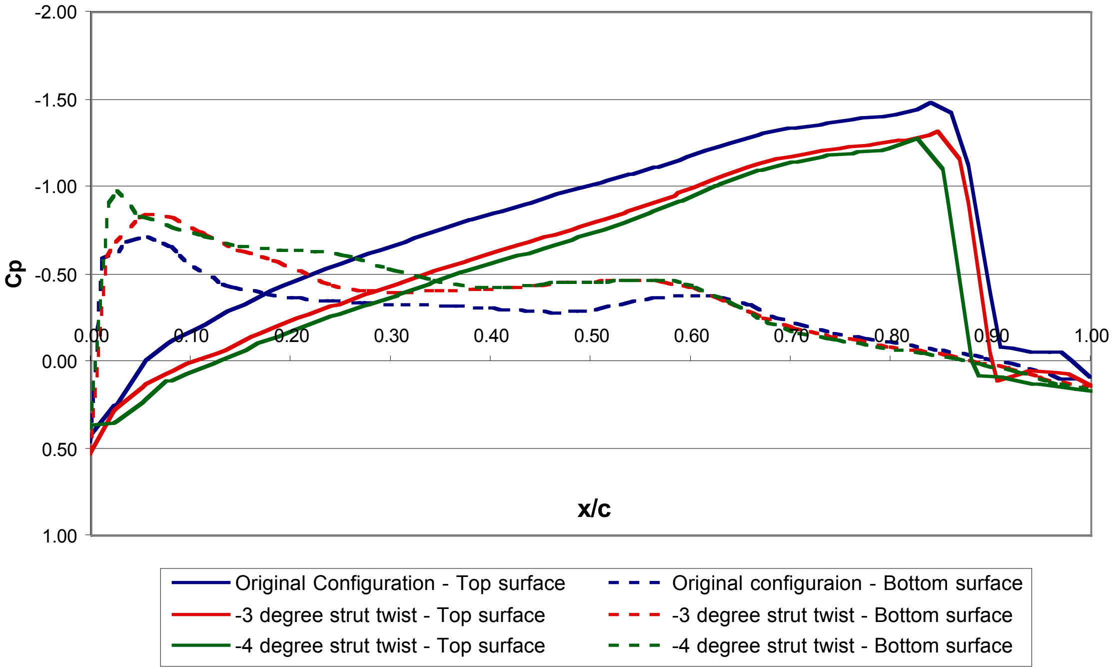

Figure 115: Pressure coefficient distribution on the pylon at $z$=1.5 for the strut twist study. FELISA inviscid solution, M=0.85.

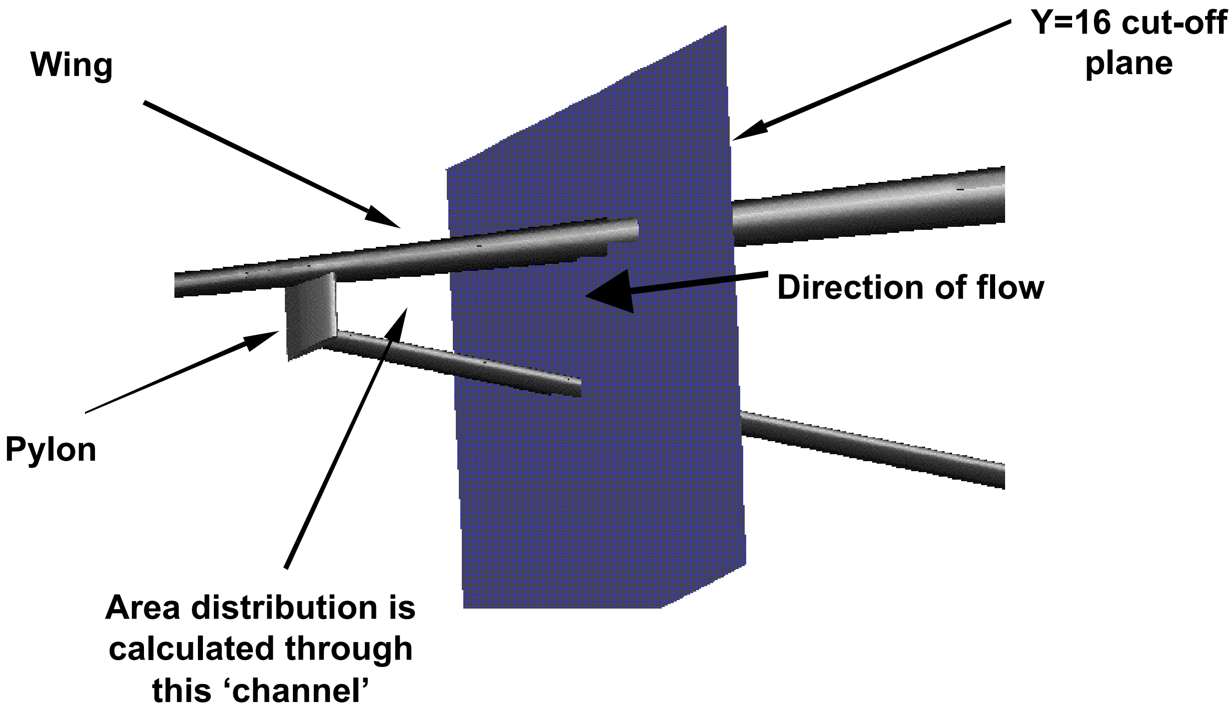

Figure 116: Illustration showing the wing/pylon/strut intersection and how the frontal area distribution is calculated.

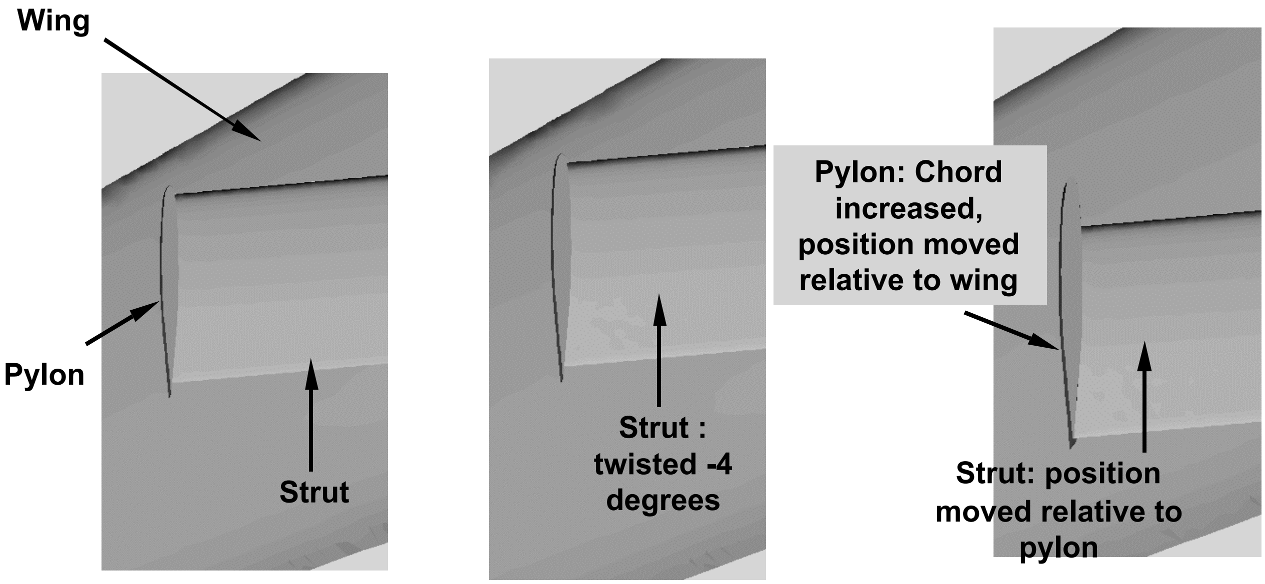

**Reference design : Strut twisted -3 degrees**

**2nd design : Strut twisted -4 degrees**

**3nd design : Strut twisted -4 degrees + other changes**

Figure 117: Illustration shows the differences between the three designs in order to change the intersection area distribution

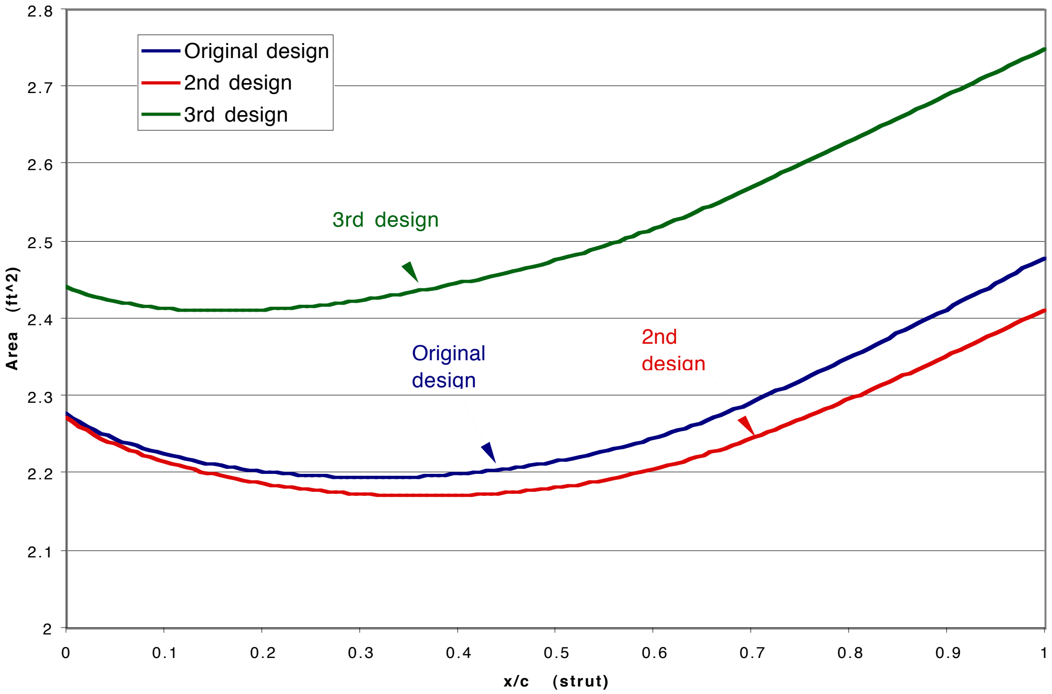

Figure 118: Three-dimensional frontal area distribution through the wing/pylon/strut intersection of the different designs.

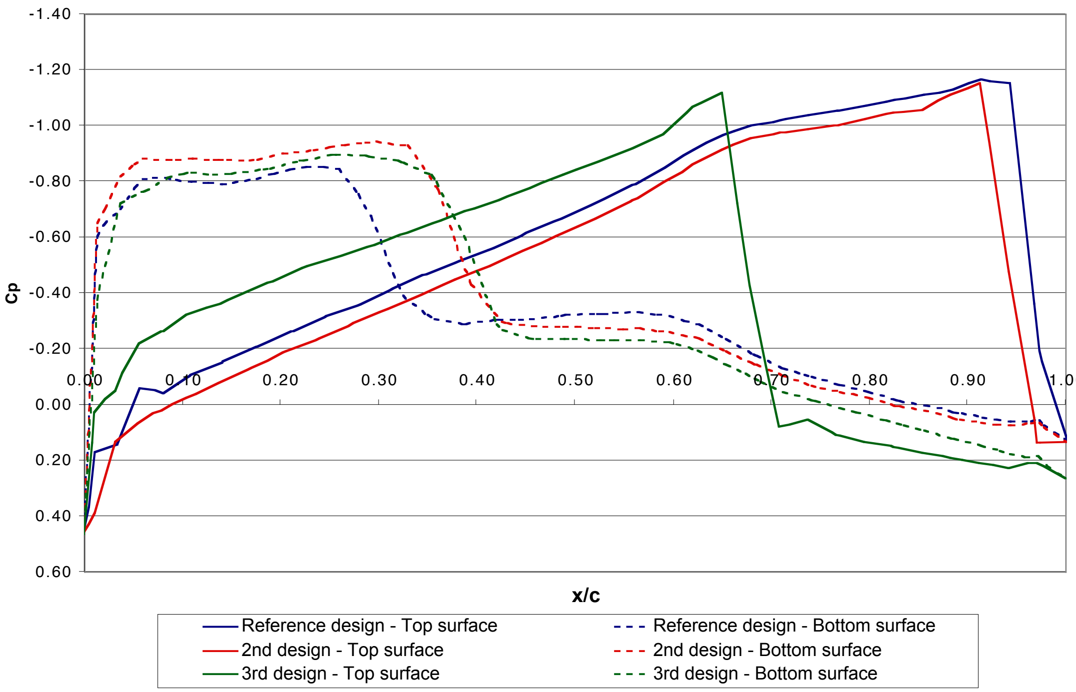

Figure 119: Pressure coefficient distribution on the strut at *y*=18 for the intersection area study. FELISA inviscid solution, M=0.85.

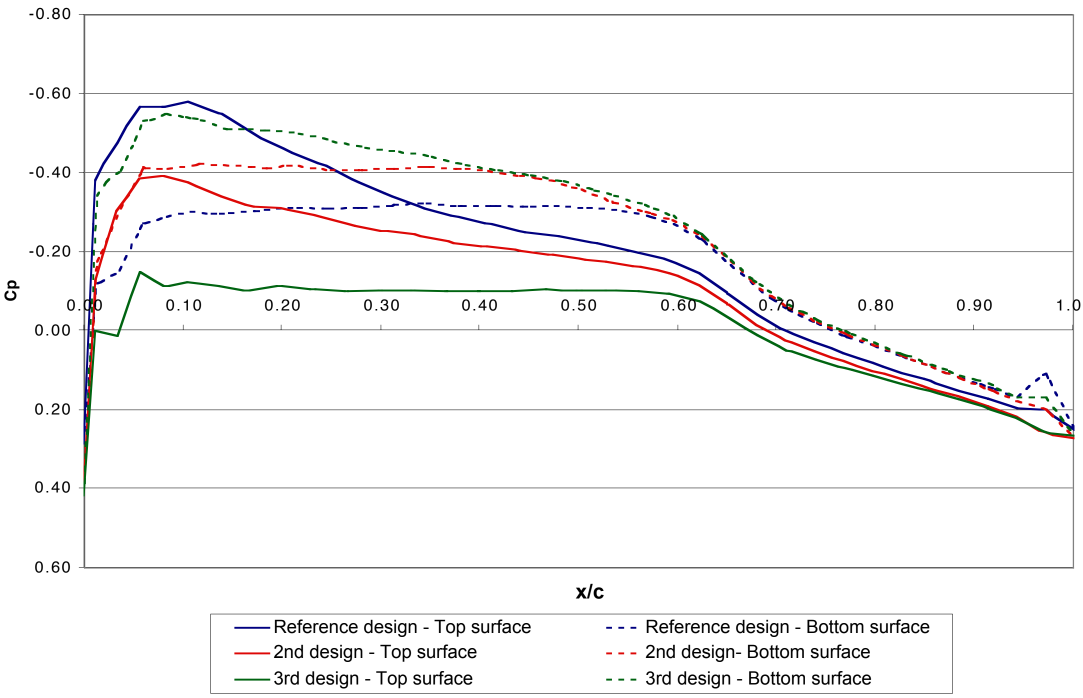

Figure 120: Pressure coefficient distribution on the strut at *y*=12 for the intersection area study. FELISA inviscid solution, M=0.85.

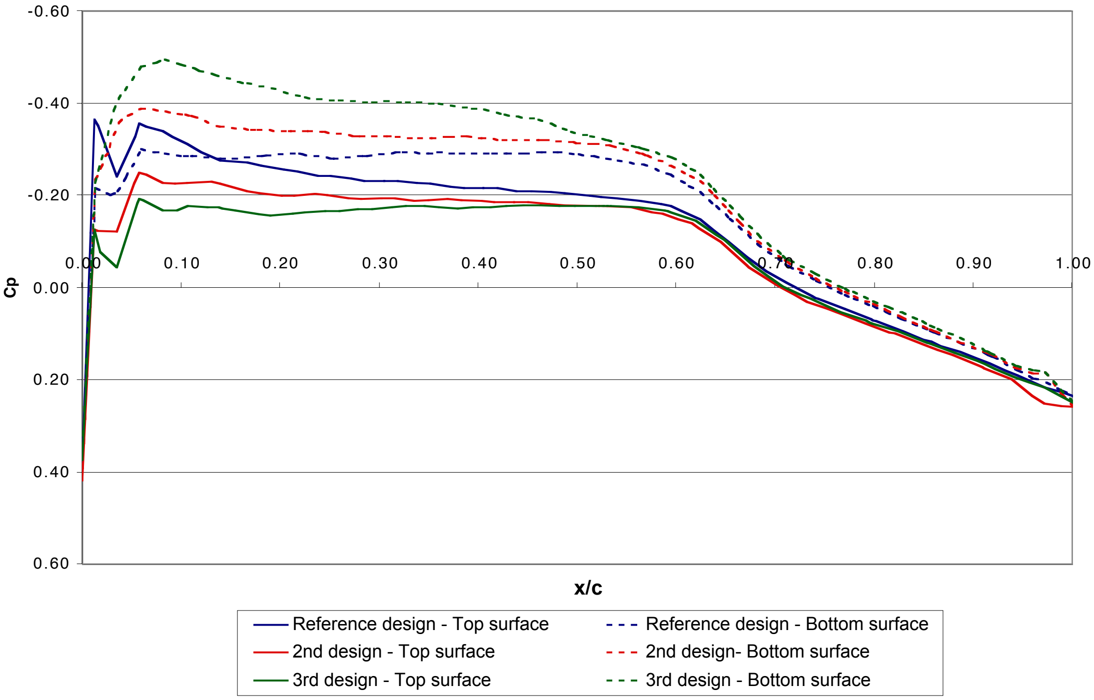

Figure 121: Pressure coefficient distribution on the strut at *y*= 6 for the intersection area study. FELISA invisicid solution, M=0.85.

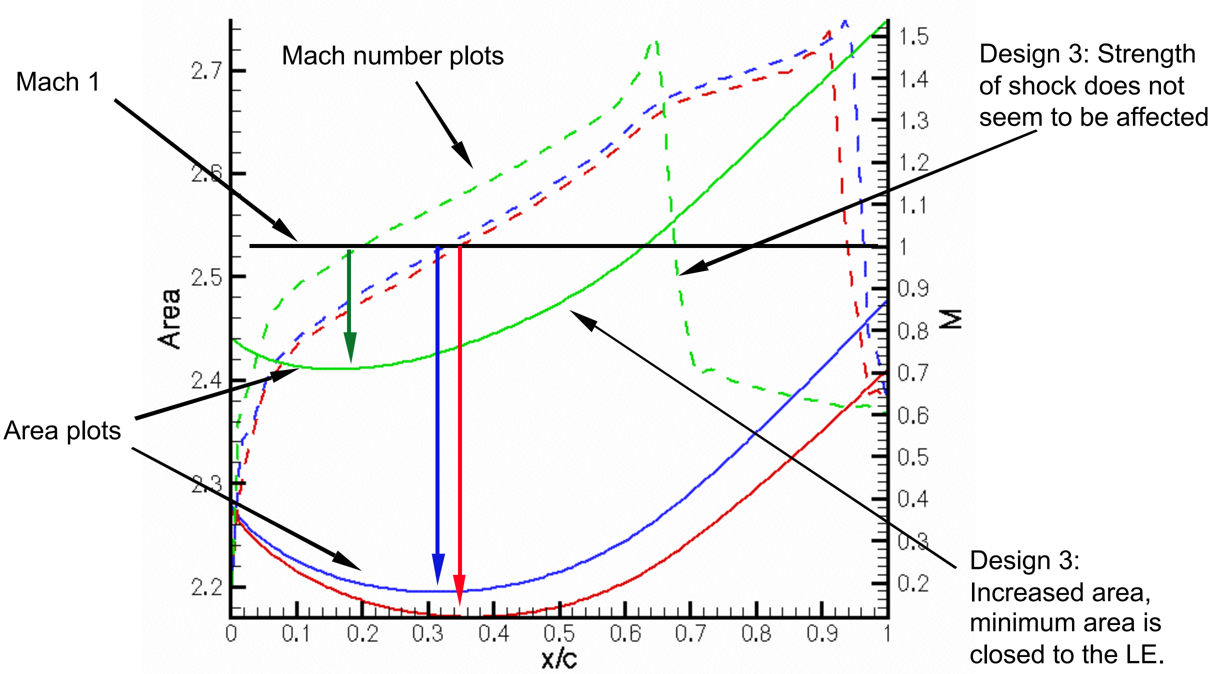

Figure 122: Frontal intersection area and surface flow mach number cross plot. Colored arrows indicate the sonic location in relation to the area distribution.

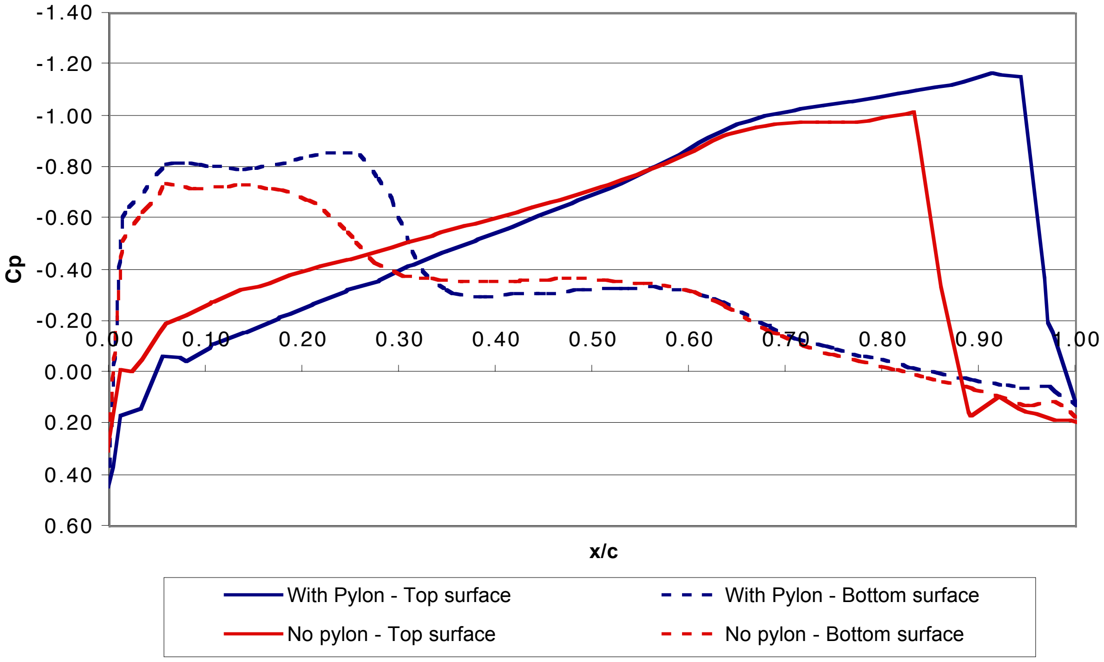

Figure 123: Pressure coefficient distribution on the strut at *y*=18. This plot shows the effect the pylon has on the flow at the intersection. FELISA inviscid solution, M=0.85.

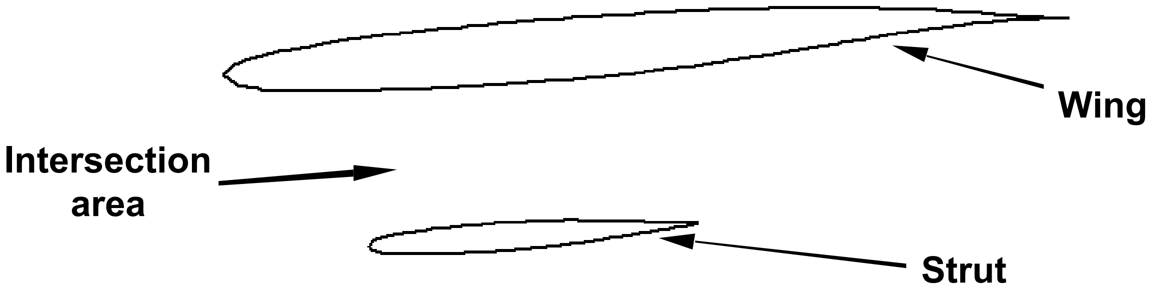

Figure 124: Illustration shows the intersection area between the wing and the strut section.

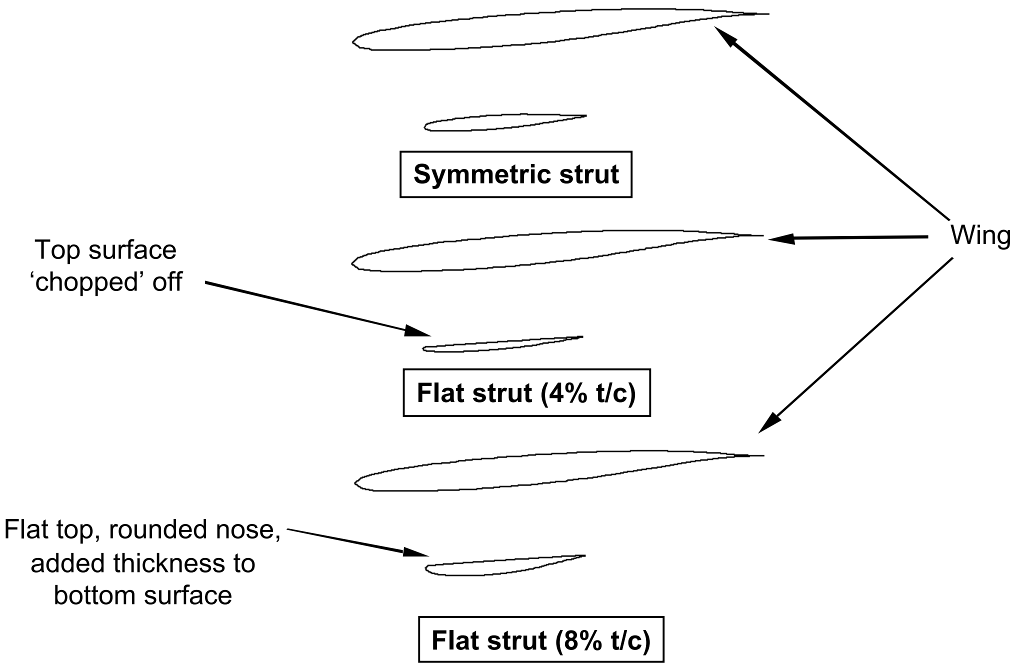

Figure 125: Illustration shows the 3 different designs that were designed to reduced and eliminate the strong shock at the wing/pylon/strut intersection.

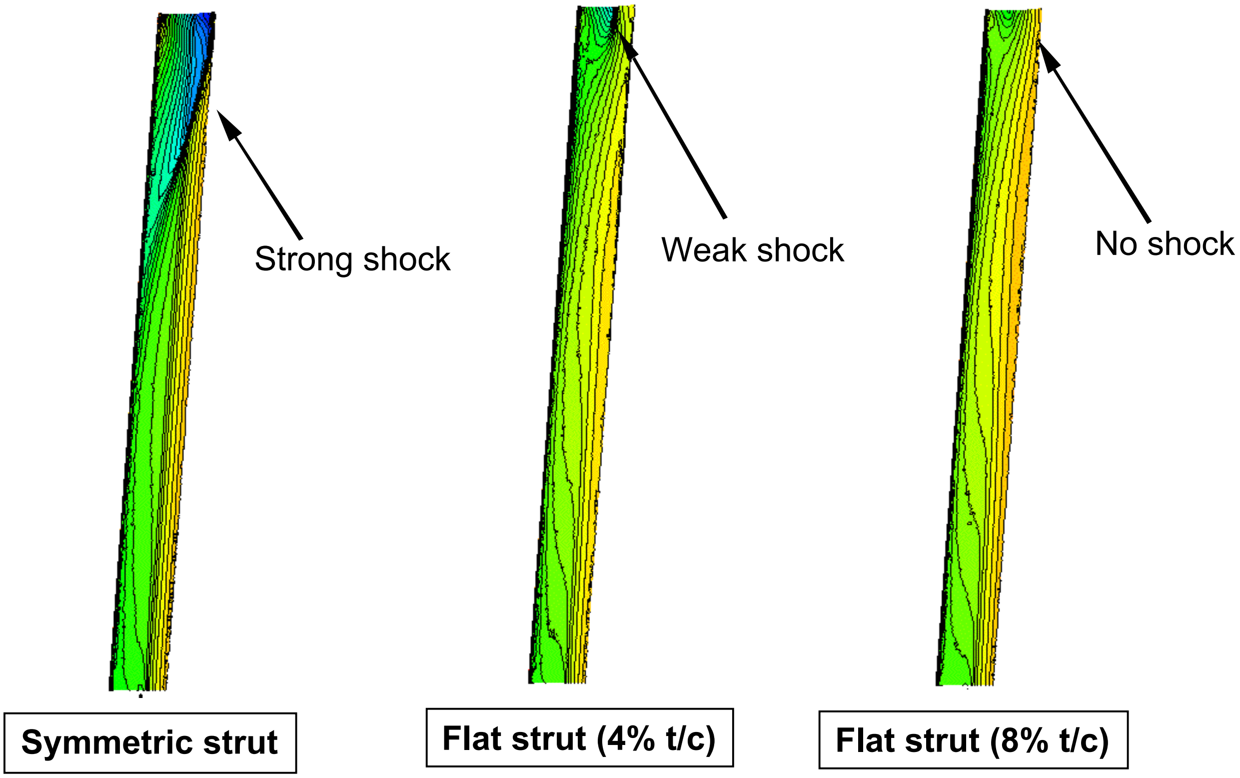

Figure 126: Pressure contours on the upper surface of the strut, comparing the reduction and elimination of the shock at the wing/pylon/strut intersection.

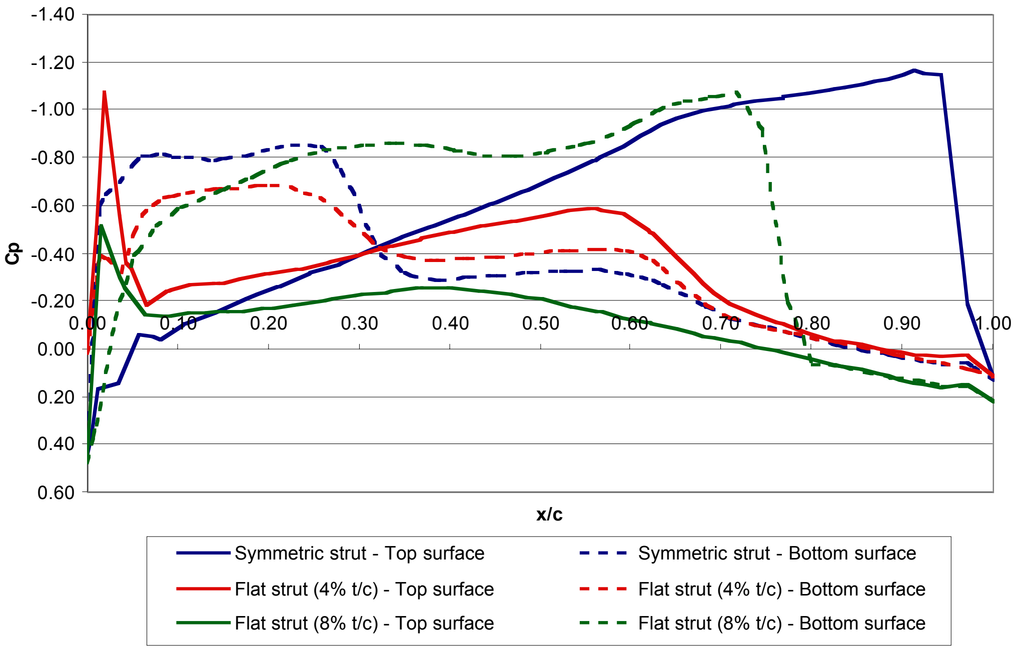

Figure 127: Pressure coefficient distribution on the strut at *y*=18. Plot compares the effect of the flattened strut top surface at the strut tip (intersecting the pylon). FELISA inviscid solution, M=0.85.

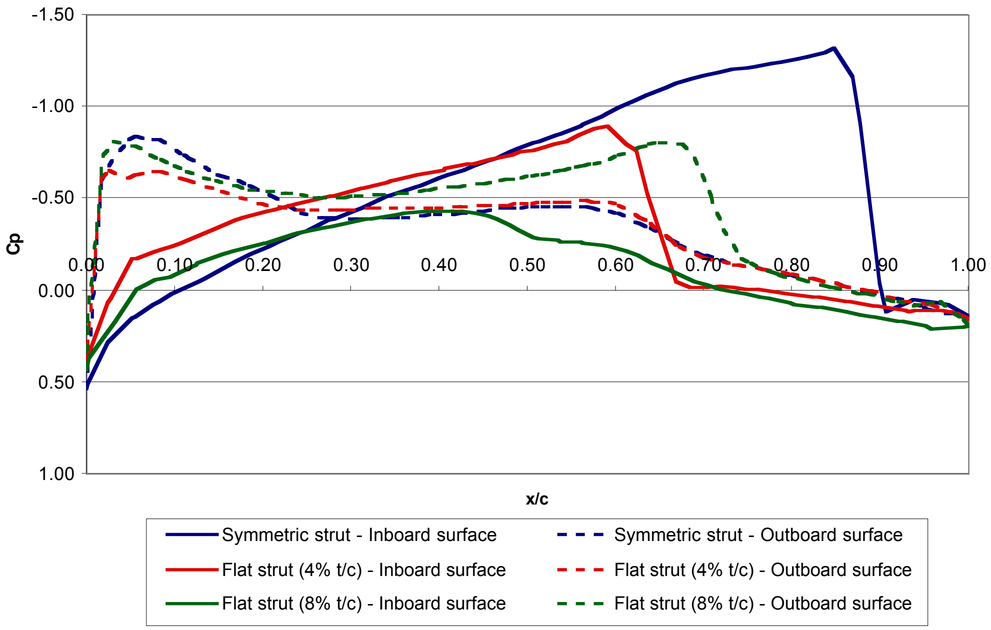

Figure 128: Pressure coefficient distribution on the strut at *y*=18. Plot compares the effect of the flattened strut top surface at the strut tip (intersecting the pylon). FELISA inviscid solution, M=0.85.

# 10. References

[1] Pfenninger, W., "Design Considerations of Large Subsonic Long Range Transport Airplanes with Low Drag Boundary Layer Suction," Northrop Aircraft, Inc., Report NAI-58-529 (BLC-111), 1958. (Available from DTIC as AD 821 759)

[2] Kulfan, R.M., and Vachal, J.D., "Wing Planform Geometry Effects on Large Subsonic Military Transport Airplanes," Boeing Commercial Airplane Company, AFFDL-TR-78-16, February 1978.

[3] Park, H. P., "The Effect on Block Fuel Consumption of a Strutted vs. Cantilever Wing for a Short Haul Transport Including Strut Aeroelastic Considerations," AIAA-78-1454-CP, Los Angeles, California, Aug. 21-23, 1978.

[4] Turriziani, R. V., Lovell, W.A., Martin, G.L., Price, J.E., Swanson, E.E., and Washburn, G.F., "Preliminary Design Characteristics of a Subsonic Business Jet Concept Employing an Aspect Ratio 25 Strut Braced Wing," NASA CR-159361, October 1980.

[5] Grasmeyer, J.M., Naghshineh_Pour, A., Tetrault, P.-A., Grossman, B., Haftka, R.T., Kapania, R.K., Mason, W.H., Schetz, J.A., "Multidisciplinary Design Optimization of a Strut-Braced Wing Aircraft with Tip-Mounted Engines," MAD 98-01-01, 1998.

[6] Grasmeyer, J.M., "Multidisciplinary Design Optimization of a Strut-Braced Wing Aircraft," MS Thesis, Virginia Polytechnic Institute & State University, April 1998.

[7] Grasmeyer, J.M., "Multidisciplinary Design Optimization of a Transonic Strut-Braced Wing Aircraft," 37th AIAA Aerospace Sciences Meeting and Exhibit, Reno, NV, Jan 11-14, 1999, AIAA Paper 99-0010.

[8] Gundlach, J.F., Tetrault, P.A., Gern, F., Nagshineh-Pour, A., Ko, A., Schetz, J.A., Mason, W.H., Kapania, and R.K., Grossman, B, "Multidisciplinary Design Optimization of a Strut-Braced Wing Transonic Transport," AIAA 2000-0420, 2000.

[9] Ko, A., "The Role of Constraints and Vehicle Concepts in Transport Design: A Comparison of Cantilever and Strut-Braced Wing Airplane Concepts," MS Thesis, Virginia Polytechnic Institute & State University, April 2000.

[10] Gern, F.H., Sulaeman, E., Naghshineh-Pour, A., Kapania, R.K., and Haftka, R.T., "Flexible Wing Model for Structural Wing Sizing and Multidisciplinary Design Optimization of a Strut-Braced Wing," AIAA Paper 2000-1427, *41st AIAA/ASME/ASCE/AHS/ASC Structures, Structural Dynamics, and Materials Conference and Exhibit*, Atlanta, GA, April 3-6,2000.

[11] Capone, F.J., *Transonic Strut-Braced Wing Transport Concept*: Proposal for the Flight Research for Revolutionary Aeronautical Concepts (RevCon), NRA 99-LaRC-3, Langley Research Center, Oct., 1999.

[12] Leigh, C., Fromer, J., Haines, C., Kromer, E., Lampman, C., Lessy, A., Norell, T., Rourke, C., Vasquez, J., Werner, K., Woo, H., *Team RevCon: Strut-Braced Wing Demonstrator Aircraft Concept, Final Report*, May 2000.

[13] Tetrault, P.-A., "Numerical Prediction of the Interference Drag of a Streamlined Strut Intersecting a Surface in Transonic Flow," Ph.D. Dissertation, Virginia Polytechnic Institute & State University, January 2000.

[14] Margason, R.J., and Lamar, J.E., "Vortex-Lattice FORTRAN Program for Estimating Subsonic Aerodynamic Characteristics of Complex Planforms", NASA TN D-6142, Feb., 1971.

[15] Lamar, J.E., and Gloss, B.B., "Subsonic Aerodynamic Characteristics of Interacting Lifting Surfaces with Separated Flow around Sharp Edges Predicted by a Vortex-Lattice Method", NASA TN D-7921, Sept., 1975.

[16] Lamar, J.E. and Frink, N.T., "Experimental and Analytic Study of the Longitudinal Aerodynamic Characteristics of Analytically and Empirically Designed Strake-Wing Configurations at Subsonic Speeds", NASA TP-1803, June 1981.

[17] Lamar, J.E., and Herbert, H.E., "Production Version of the Extended NASA-Langley Vortex Lattice FORTRAN Computer Code", – Volume I – User's Guide, NASA TM 83303, April 1982.

[18] Kay, J., Mason, W.H., Durham, W., Lutze, F., Benoliel, A., "Control Authority Issues in Aircraft Conceptual Design: Critical Conditions, Estimation Methodology, Spreadsheet Assessment, Trim and Bibliography", VPI-Aero-200, Department of Aerospace and Ocean Engineering, Virginia Tech, Blacksburg, VA, 1993.

[19] Lamar, J.E., "A Vortex Lattice Method for the Mean Camber Shapes of Trimmed Non-Coplanar Planforms with Minimum Vortex Drag", NASA TN D-8090, June, 1976.

[20] Mason, W.H., "Wing-Canard Aerodynamics at Transonic Speeds – Fundamental Considerations on Minimum Drag Spanloads", AIAA Paper No. 82-0097, Jan., 1982.

[21] Jameson, A. "Acceleration of Transonic Potential Flow Calculations on Arbitrary Meshes by the Multiple Grid Method", AIAA 4th Computational Fluid Dynamics Conference, AIAA Paper No. 1458, Williamsburg, VA, July 1979.

[22] Drela, M., “MSES Multi-element Airfoil Design / Analysis Software – Summary”, http://raphael.mit.edu/projects%26research.html, Massachusetts Institute of Technology, MA, May, 1994.

[23] Peiro, J., Peraire, J., Morgan, K., *FELISA System Version 1.1 (Rev. 1) Reference Manual: Part 1- Basic Theory*, NASA Langley Research Center, VA, Nov., 1996.

[24] Mason, W.H., Applied Computational Aerodynamics Text/Notes, Appendix E, Utility Codes, E.5, Bump, http://www.aoe.vt.edu/aoe/faculty/Mason_f/CAtxtAppE.html

[25] Mason, W.H., and Miller, D.S., "Controlled Supercritical Crossflow on Supersonic Wings - An Experimental Validation," AIAA Paper 80-1421, July 1980.

[26] Drela, M., “XFOIL: An Analysis and Design System for Low Reynolds Number Airfoils”, *Conference on Low Reynolds Number Airfoil Aerodynamic,* University of Notre Dame, June 1989.

[27] Abbot, I.H. and Von Doenhoff, A.E., *Theory of Wing Sections*. Dover, New York. 1959.

[28] Drela, M., “A User’s Guide to MSES 2.95,” MIT Computational Aerospace Sciences Laboratory, Sept., 1996.

[29] Volpe, G. “Inverse Design of Airfoil Contours: Constraints, Numerical Method and Applications”, *Computational methods for Aerodynamic design (Inverse) and Optimization: Papers Presented and Discussions held at the Specialists’ Meeting of the Fluid Dynamics Panel in Loen, Norway*. AGARD CP-463, 1989.

[30] Schmitt, V. and Charpin, F., “Pressure Distributions on the ONERA M6-Wing at Transonic Mach Number”, *AGARD Advisory Report 138*, May 1979.

[31] Harris, C.D., “NASA Supercritical Airfoils: A Matrix of Family Related Airfoils”, NASA TP 2969, March 1990.

[32] Rivers, M.B. and Wahls, R.A., *Comparison of Computational and Experimental Results for a Supercritical Airfoil*, NASA TM-4601, Nov., 1994.

[33] Dam, C.P. van, “Recent experience with different methods of drag prediction”, *Progress in Aerospace Sciences*, Vol. 35, 1999. pp 751-798.

[34] Huyse, L., “Free-form Airfoil Shape Optimization Under Uncertainty Using Maximum Expected Value and Second-order Second-moment Strategies”, ICASE Report No. 2001-18 (NASA/CR-2001-211020), ICASE, Hampton, VA, June 2001.

[35] Drela, M., “Pros & Cons of Airfoil Optimization”, *Frontiers of Computational Fluid Dynamics - 1998* , edited by Caughey, D., and Hafez, M.M., 1998. pp. 364-381.

[36] Lock, R.C., “An Equivalence Law Relating Three- and Two-Dimensional Pressure Distributions”, RAE R&M 3346, May 1962.

[37] Boppe, C.W., “X-29 Aerodynamic Design and Performance”, *AIAA Professional Study Series – Aerodynamic Analysis and Design*, Palo Alto, CA, Oct. 1988.

[38] Van Der Velden, A. and Kroo, I., “A Numerical Method of Relating Two- and Three-Dimensional Pressure Distributions on Transonic Wings”, AIAA 90-3211, 1990.

[39] Braslow, A.L., Maddalon, D.V., Bartlett, D.W., Wagner, R.D., and Collier, F.S., “Applied Aspects of Laminar-Flow Technology”, *Viscous Drag Reduction in Boundary Layers*, edited by D. Bushnell and J.N. Hefner, AIAA, Washington, DC, 1990, pp 47-78.

[40] Roskam, J., *Airplane Design: Part VI Preliminary Calculation of Aerodynamic, Thrust and Power Characteristics*. Roskam Engineering Corp. Ottawa, Kansas, 1988.

[41] Etkin, B., and Reid, L. *Dynamics of Flight: Stability and Control*. John Wiley and Sons Inc., New York, 1996.

# 11. Appendix A : Team RevCon Design Report Verification

One of the main references in the formulation of the tasks involved with this project is the Team RevCon design report [12]. Team RevCon was the Virginia Tech senior design team (year 2000) that designed a wing for the A-7 SBW Revcon proposal. This design was based on the Lockheed-Martin Aeronautical Systems (LMAS) fuselage mounted engines SBW design. Since some of the design selection in this project would involve using data obtained from Team RevCon's design report, it was necessary for us to verify some of the important results presented in that report, especially the static margin calculations.

Team RevCon's design work included the calculation of the stability and control derivatives using several different analysis codes [12]. In the stability and control section of the design team report, results from three different programs for the neutral point location (in terms of % MAC) and static margin were given. This information was verified using the same analysis programs to make sure that the results were correct.

The design team used two Fortran programs, VLM 4.997 and JKayVLM, both of which use the vortex lattice method to perform analysis. Also, the design team used methods found from Roskam [40] and Etkin and Reid [41], which are abbreviated versions of the USAF DATCOM methods. Three different configurations were computed for the design, using the three different analysis methods: wing alone, wing and body, and wing, body and tail configurations. To verify the results, the cases were rerun using VLM 4.997 and JKayVLM. The DATCOM method was not repeated. The results of this verification can be found in Table 6.

Table 6: Neutral point location normalized over the MAC from the leading edge of the MAC

| | Reported VLM4.997 | VLM4.997 | Reported JKayVLM | JKayVLM | Reported DATCOM |
|---|---|---|---|---|---|
| Wing | 0.389 | 0.4117 | 0.413 | 0.4188 | 0.407 |
| Wing-Body | 0.327 | 0.3496 | 0.341 | 0.3441 | 0.4 |
| Wing-Body-Tail | 0.6098 | 0.6195 | 0.602 | 0.6067 | 0.607 |

As a reference, the MAC was calculated to be 5.754 ft, where the leading edge of the MAC is located 20.235 ft aft of the nose (7.4253 ft from the leading edge of the centerline chord). This position is 10.967 ft spanwise from the centerline.

It was also reported that based on a CG position of 23.3 ft from the nose, the A-7 design was 9-10% stable. Based on that CG position, it was verified from VLM4997 that the design was 8.68% stable and from JKayVLM, 9.12% stable.

The neutral point location of the original A-7 aircraft was also calculated so that it could be compared to the design SBW A-7 concept demonstrator. Again, VLM4997 and JKayVLM were used to make the calculations. The results can be found in Table 7.

Table 7: Neutral point location normalized over the MAC, measured from the leading edge of the MAC

| | VLM4.997 | JKayVLM |
|---|---|---|
| Wing Alone | 0.32 | 0.3079 |
| Wing-Body | 0.263 | 0.2615 |
| Wing-Body-Tail | 0.3284 | 0.3812 |

The MAC of the original A-7 aircraft was calculated to be at 10.657 ft. The location of the leading edge of the MAC is 19.7425 ft from the nose.

With the data from Team RevCon’s design report verified, we moved on to the next step of choosing the appropriate wing design for this task.

# 12. Appendix B : Wing sweep and laminar flow parametric studies

In the course of selecting the appropriate wing design for this project, discussions with NASA Langley raised concerns about wing sweep sensitivity and its impact on natural laminar flow. To address these concerns, a wing sweep parametric study was performed to investigate this matter.

The goal of the study was to investigate the amount of laminar flow on the wings and its trade-off with wave drag as a function of wing sweep. To perform this study, the SBW aircraft design was optimized while keeping the wing quarter chord sweep constant. The results of the designs at different wing quarter chord sweeps were then plotted. A laminar flow technology factor of unity was used in this study, corresponding to data from the F-14 glove experiment [39]. This data gives the transition Reynolds number as a function of wing sweep. Figures B-1 to B-3 give the results of the wing sweep study.

It is clear from the figures that the optimum configuration occurs when the wing 1/4 chord sweep is at 28° (which corresponds to 37% laminar flow on the wing). As we would expect, the wave drag decreases and wing friction increases with increasing wing sweep. We also see that the wing *t/c* ratio generally increases with wing sweep. This is a due to the smaller penalty in wave drag with a higher wing sweep, allowing the wing *t/c* ratio to increase, hence reducing the wing weight. The only exception to this observation is the wing tip *t/c* ratio, which decreases after 20° and then remains relatively constant after 30° of sweep. One possible explanation for this is that the tip *t/c* ratio has only a relatively small effect on the wing weight while having a much larger effect on the wave drag. Also note that the minimum drag does not occur at the sweep angle where the wave drag and wing friction drag intersect, as one would expect. Instead, the minimum drag occurs at a higher sweep angle than where the two curves intersect. This is because the contribution of the other drag quantities (such as induced drag and interference drag) also affects the sweep at which minimum drag occurs for this configuration. The other drag quantities are not constant since the aircraft design is re-optimized for every wing sweep investigated. Is should also be noted that it is assumed that there is 100% laminar flow on the strut. With a strut 1/4 sweep of 19.4° and strut chord of 6.1 ft, this is a reasonable assumption.

In addition to the wing sweep parametric study, a laminar flow parametric study was performed. The goal of this study was to find the sensitivity of the aircraft design to the amount of laminar flow on the wings. In this study, the transition location on the wing was fixed and the aircraft configuration was optimized. Figure B-4 shows the result of that study, and provides insight into the potential savings in takeoff gross weight (TOGW) with laminar flow on the wings. There is, however, one flaw in the study that needs to be mentioned. Since the amount of laminar flow on the wing is fixed, it is no longer a function of the wing sweep. The optimizer takes advantage of this change in the optimization problem formulation and sweeps the wing to minimize wave drag (without any penalty in parasite drag). In this case, the wing sweep is only controlled by the structural weight.

## *12.1. Figures*

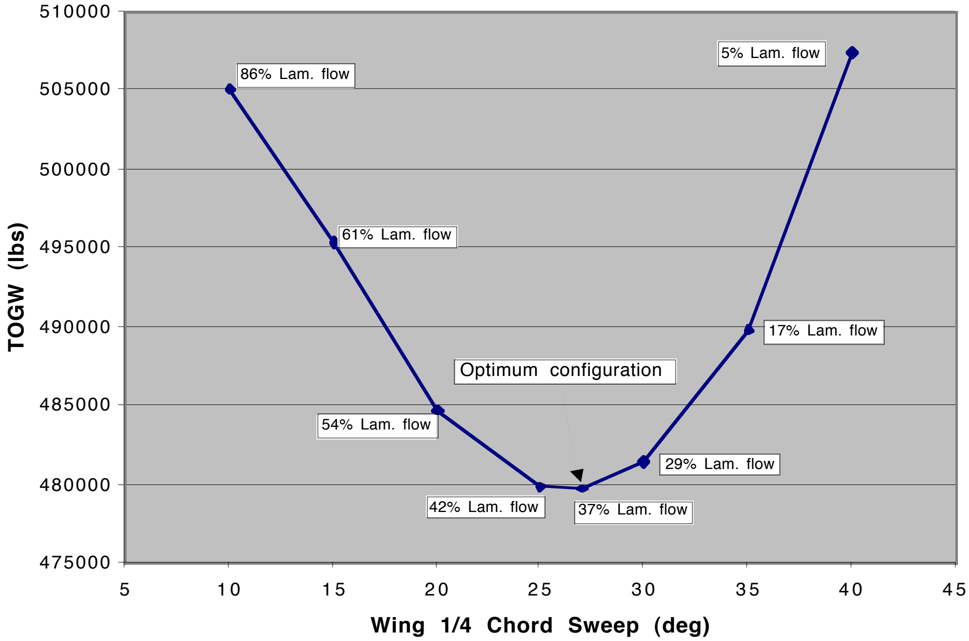

Figure B-1: Variation of TOGW due to % laminar flow caused by wing sweep.

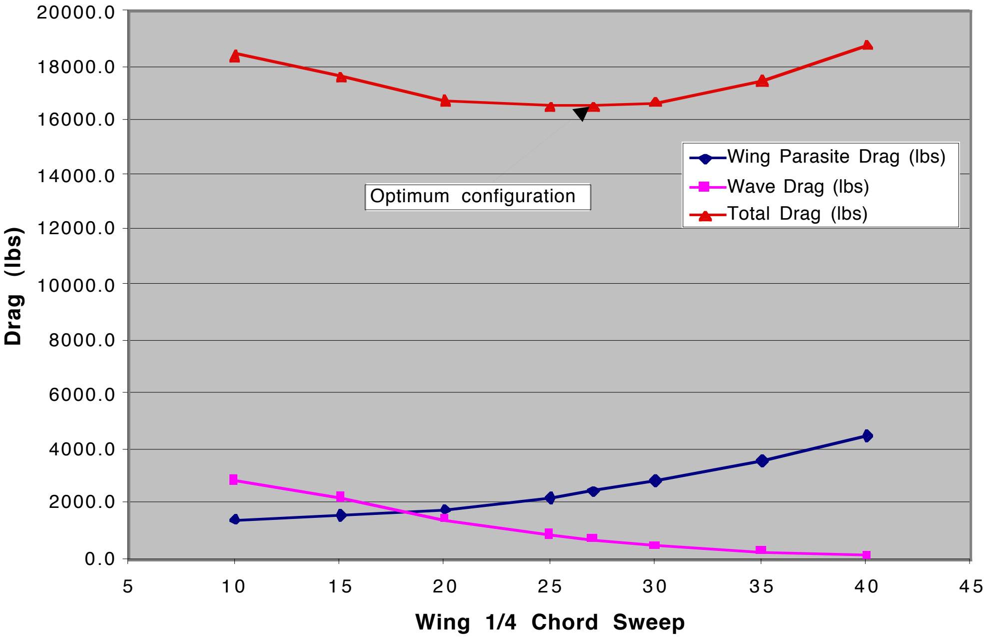

Figure B-2: Variation of wave and wing parasite drag and its contribution to total drag due to the wing sweep.

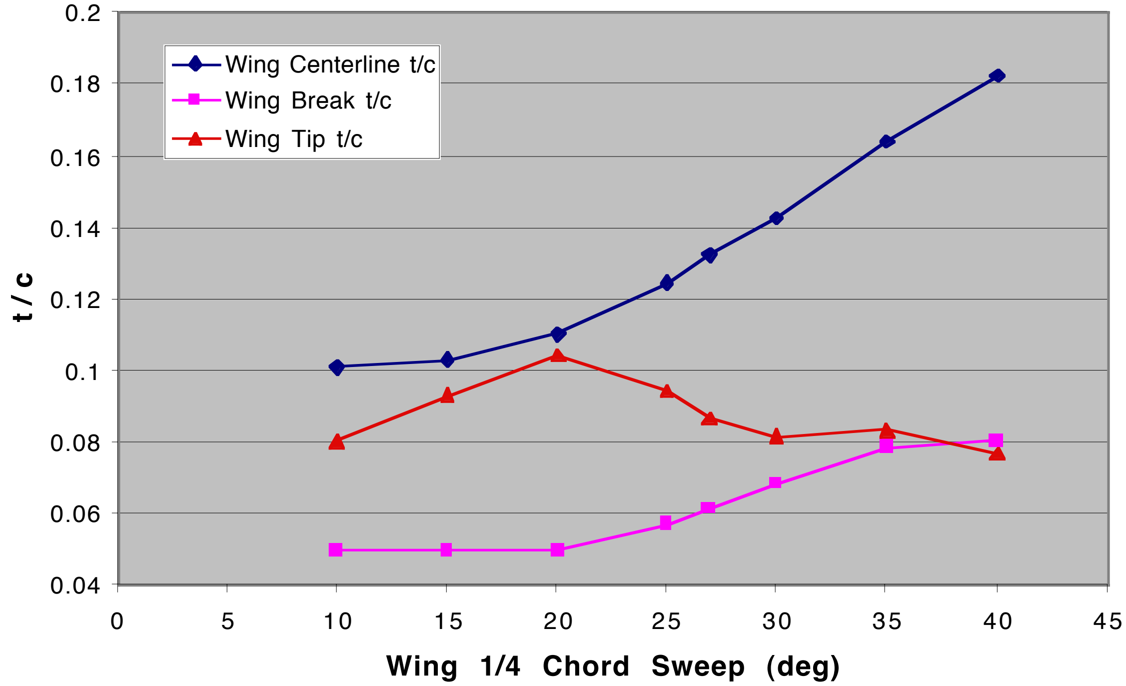

Figure B-3: Variation of the optimized t/c ratio at the different wing stations due to wing sweep.

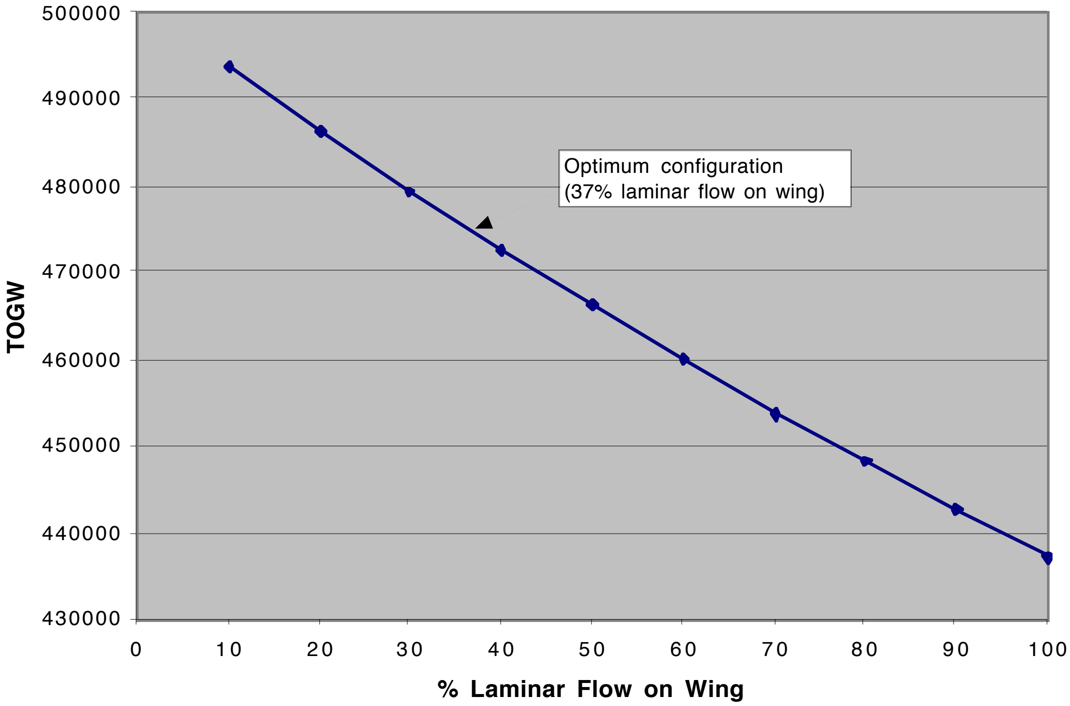

Figure B-4: Variation of TOGW due to % laminar flow on wing.

# 13. Appendix C : Airfoil coordinates

## *13.1. Ko t-133 : Airfoil for wing root station*

Upper surface
Number of point = 5

| | |
|---|---|
| 0.0000 | 0.000E+00 |
| 0.0020 | 1.067E-02 |
| 0.0050 | 1.639E-02 |
| 0.0100 | 2.222E-02 |
| 0.0200 | 2.943E-02 |
| 0.0300 | 3.446E-02 |
| 0.0400 | 3.820E-02 |
| 0.0500 | 4.124E-02 |
| 0.0600 | 4.388E-02 |
| 0.0700 | 4.612E-02 |
| 0.0800 | 4.815E-02 |
| 0.0900 | 4.998E-02 |
| 0.1000 | 5.160E-02 |
| 0.1100 | 5.311E-02 |
| 0.1200 | 5.442E-02 |
| 0.1300 | 5.562E-02 |
| 0.1400 | 5.671E-02 |
| 0.1600 | 5.868E-02 |
| 0.1700 | 5.955E-02 |
| 0.1800 | 6.032E-02 |
| 0.2000 | 6.166E-02 |
| 0.2200 | 6.279E-02 |
| 0.2400 | 6.372E-02 |
| 0.2700 | 6.484E-02 |
| 0.2900 | 6.541E-02 |
| 0.3100 | 6.581E-02 |
| 0.3400 | 6.617E-02 |
| 0.3700 | 6.632E-02 |
| 0.4000 | 6.627E-02 |
| 0.4300 | 6.599E-02 |
| 0.4700 | 6.530E-02 |
| 0.5000 | 6.453E-02 |
| 0.5300 | 6.350E-02 |
| 0.5500 | 6.264E-02 |
| 0.5700 | 6.159E-02 |
| 0.6000 | 5.974E-02 |
| 0.6200 | 5.832E-02 |
| 0.6300 | 5.751E-02 |
| 0.6500 | 5.571E-02 |
| 0.6700 | 5.370E-02 |
| 0.6900 | 5.150E-02 |
| 0.7100 | 4.910E-02 |
| 0.7300 | 4.650E-02 |
| 0.7600 | 4.228E-02 |
| 0.7800 | 3.926E-02 |
| 0.8000 | 3.603E-02 |
| 0.8300 | 3.087E-02 |
| 0.8500 | 2.721E-02 |
| 0.8800 | 2.139E-02 |
| 0.9000 | 1.730E-02 |
| 0.9200 | 1.299E-02 |
| 0.9400 | 8.473E-03 |
| 0.9600 | 3.746E-03 |
| 0.9700 | 1.281E-03 |
| 0.9900 | -3.852E-03 |
| 1.0000 | -6.518E-03 |

Lower surface
Number of points = 78

| | |
|---|---|
| 0.0000 | 0.000E+00 |
| 0.0020 | -1.065E-02 |
| 0.0050 | -1.636E-02 |
| 0.0100 | -2.216E-02 |
| 0.0200 | -2.930E-02 |
| 0.0300 | -3.427E-02 |
| 0.0400 | -3.806E-02 |
| 0.0500 | -4.105E-02 |
| 0.0600 | -4.365E-02 |
| 0.0700 | -4.586E-02 |
| 0.0800 | -4.787E-02 |
| 0.0800 | -4.787E-02 |
| 0.0900 | -4.968E-02 |
| 0.1000 | -5.129E-02 |
| 0.1100 | -5.281E-02 |
| 0.1200 | -5.423E-02 |
| 0.1300 | -5.544E-02 |
| 0.1500 | -5.768E-02 |
| 0.1600 | -5.871E-02 |
| 0.1700 | -5.963E-02 |
| 0.1900 | -6.128E-02 |
| 0.2000 | -6.200E-02 |
| 0.2200 | -6.325E-02 |
| 0.2400 | -6.431E-02 |
| 0.2600 | -6.516E-02 |
| 0.2800 | -6.582E-02 |
| 0.3000 | -6.629E-02 |
| 0.3300 | -6.668E-02 |
| 0.3500 | -6.675E-02 |
| 0.3600 | -6.669E-02 |
| 0.3900 | -6.619E-02 |
| 0.4100 | -6.567E-02 |
| 0.4300 | -6.494E-02 |
| 0.4400 | -6.448E-02 |
| 0.4600 | -6.337E-02 |
| 0.4700 | -6.271E-02 |
| 0.4800 | -6.195E-02 |
| 0.4900 | -6.110E-02 |
| 0.5000 | -6.014E-02 |
| 0.5200 | -5.804E-02 |
| 0.5300 | -5.689E-02 |
| 0.5400 | -5.564E-02 |
| 0.5500 | -5.429E-02 |
| 0.5600 | -5.284E-02 |
| 0.5700 | -5.129E-02 |
| 0.5900 | -4.800E-02 |
| 0.6100 | -4.451E-02 |
| 0.6300 | -4.083E-02 |
| 0.6500 | -3.695E-02 |
| 0.6700 | -3.286E-02 |
| 0.6800 | -3.073E-02 |
| 0.6900 | -2.869E-02 |
| 0.7100 | -2.441E-02 |
| 0.7200 | -2.237E-02 |
| 0.7300 | -2.023E-02 |
| 0.7600 | -1.411E-02 |
| 0.7800 | -1.022E-02 |
| 0.8000 | -6.538E-03 |
| 0.8100 | -4.794E-03 |
| 0.8200 | -3.148E-03 |
| 0.8300 | -1.701E-03 |
| 0.8400 | -3.516E-04 |
| 0.8500 | 8.987E-04 |
| 0.8600 | 1.951E-03 |
| 0.8700 | 2.807E-03 |
| 0.8800 | 3.464E-03 |
| 0.8900 | 3.925E-03 |
| 0.9000 | 4.187E-03 |
| 0.9100 | 4.253E-03 |
| 0.9200 | 4.120E-03 |
| 0.9300 | 3.692E-03 |
| 0.9400 | 3.065E-03 |
| 0.9500 | 2.143E-03 |
| 0.9600 | 9.244E-04 |
| 0.9700 | -4.918E-04 |
| 0.9800 | -2.204E-03 |
| 0.9900 | -4.213E-03 |
| 1.0000 | -6.518E-03 |

## *13.2. Ko t-124 : Airfoil for wing 15% span station*

Upper surface
Number of point = 56

| | |
|---|---|
| 0.0000 | 0.000E+00 |
| 0.0020 | 1.006E-02 |
| 0.0050 | 1.546E-02 |
| 0.0100 | 2.095E-02 |
| 0.0200 | 2.774E-02 |
| 0.0300 | 3.247E-02 |
| 0.0400 | 3.597E-02 |
| 0.0500 | 3.879E-02 |
| 0.0600 | 4.122E-02 |
| 0.0700 | 4.325E-02 |
| 0.0800 | 4.508E-02 |
| 0.0900 | 4.669E-02 |
| 0.1000 | 4.809E-02 |
| 0.1100 | 4.938E-02 |
| 0.1200 | 5.046E-02 |
| 0.1300 | 5.144E-02 |
| 0.1400 | 5.230E-02 |
| 0.1600 | 5.383E-02 |
| 0.1700 | 5.449E-02 |
| 0.1800 | 5.507E-02 |
| 0.2000 | 5.605E-02 |
| 0.2200 | 5.689E-02 |
| 0.2400 | 5.762E-02 |
| 0.2700 | 5.862E-02 |
| 0.2900 | 5.924E-02 |
| 0.3100 | 5.979E-02 |
| 0.3400 | 6.039E-02 |
| 0.3700 | 6.076E-02 |
| 0.4000 | 6.090E-02 |
| 0.4300 | 6.081E-02 |
| 0.4700 | 6.037E-02 |
| 0.5000 | 5.981E-02 |
| 0.5300 | 5.899E-02 |
| 0.5500 | 5.827E-02 |
| 0.5700 | 5.738E-02 |
| 0.6000 | 5.576E-02 |
| 0.6200 | 5.450E-02 |
| 0.6300 | 5.377E-02 |
| 0.6500 | 5.214E-02 |
| 0.6700 | 5.031E-02 |
| 0.6900 | 4.829E-02 |
| 0.7100 | 4.608E-02 |
| 0.7300 | 4.367E-02 |
| 0.7600 | 3.975E-02 |
| 0.7800 | 3.693E-02 |
| 0.8000 | 3.391E-02 |
| 0.8300 | 2.906E-02 |
| 0.8500 | 2.563E-02 |
| 0.8800 | 2.016E-02 |
| 0.9000 | 1.630E-02 |
| 0.9200 | 1.225E-02 |
| 0.9400 | 7.988E-03 |
| 0.9600 | 3.532E-03 |
| 0.9700 | 1.208E-03 |
| 0.9900 | -3.632E-03 |
| 1.0000 | -6.146E-03 |

Lower surface
Number of points = 78

| | |
|---|---|
| 0.0000 | 0.000E+00 |
| 0.0020 | -1.004E-02 |
| 0.0050 | -1.543E-02 |
| 0.0100 | -2.089E-02 |
| 0.0200 | -2.763E-02 |
| 0.0300 | -3.231E-02 |
| 0.0400 | -3.588E-02 |
| 0.0500 | -3.871E-02 |
| 0.0600 | -4.116E-02 |
| 0.0700 | -4.324E-02 |
| 0.0800 | -4.514E-02 |
| 0.0800 | -4.514E-02 |
| 0.0900 | -4.684E-02 |
| 0.1000 | -4.837E-02 |
| 0.1100 | -4.979E-02 |
| 0.1200 | -5.113E-02 |
| 0.1300 | -5.228E-02 |
| 0.1500 | -5.439E-02 |
| 0.1600 | -5.535E-02 |
| 0.1700 | -5.622E-02 |
| 0.1900 | -5.778E-02 |
| 0.2000 | -5.846E-02 |
| 0.2200 | -5.964E-02 |
| 0.2400 | -6.064E-02 |
| 0.2600 | -6.144E-02 |
| 0.2800 | -6.207E-02 |
| 0.3000 | -6.250E-02 |
| 0.3300 | -6.288E-02 |
| 0.3500 | -6.294E-02 |
| 0.3600 | -6.288E-02 |
| 0.3900 | -6.241E-02 |
| 0.4100 | -6.192E-02 |
| 0.4300 | -6.124E-02 |
| 0.4400 | -6.080E-02 |
| 0.4600 | -5.975E-02 |
| 0.4700 | -5.913E-02 |
| 0.4800 | -5.842E-02 |
| 0.4900 | -5.761E-02 |
| 0.5000 | -5.671E-02 |
| 0.5200 | -5.472E-02 |
| 0.5300 | -5.364E-02 |
| 0.5400 | -5.246E-02 |
| 0.5500 | -5.119E-02 |
| 0.5600 | -4.982E-02 |
| 0.5700 | -4.836E-02 |
| 0.5900 | -4.526E-02 |
| 0.6100 | -4.197E-02 |
| 0.6300 | -3.850E-02 |
| 0.6500 | -3.484E-02 |
| 0.6700 | -3.099E-02 |
| 0.6800 | -2.897E-02 |
| 0.6900 | -2.705E-02 |
| 0.7100 | -2.301E-02 |
| 0.7200 | -2.109E-02 |
| 0.7300 | -1.907E-02 |
| 0.7600 | -1.330E-02 |
| 0.7800 | -9.640E-03 |
| 0.8000 | -6.165E-03 |
| 0.8100 | -4.520E-03 |
| 0.8200 | -2.969E-03 |
| 0.8300 | -1.604E-03 |
| 0.8400 | -3.315E-04 |
| 0.8500 | 8.474E-04 |
| 0.8600 | 1.840E-03 |
| 0.8700 | 2.646E-03 |
| 0.8800 | 3.267E-03 |
| 0.8900 | 3.701E-03 |
| 0.9000 | 3.948E-03 |
| 0.9100 | 4.010E-03 |
| 0.9200 | 3.885E-03 |
| 0.9300 | 3.481E-03 |
| 0.9400 | 2.890E-03 |
| 0.9500 | 2.021E-03 |
| 0.9600 | 8.716E-04 |
| 0.9700 | -4.637E-04 |
| 0.9800 | -2.078E-03 |
| 0.9900 | -3.972E-03 |
| 1.0000 | -6.146E-03 |

## 13.3. *Parker t-62: Airfoil for wing 70% span station*

Upper surface
Number of point = 45

| | |
|---|---|
| 0.0000 | 0.000E+00 |
| 0.0001 | 8.999E-04 |
| 0.0003 | 1.800E-03 |
| 0.0007 | 2.700E-03 |
| 0.0013 | 3.600E-03 |
| 0.0022 | 4.500E-03 |
| 0.0034 | 5.399E-03 |
| 0.0048 | 6.299E-03 |
| 0.0064 | 7.199E-03 |
| 0.0082 | 8.099E-03 |
| 0.0102 | 8.999E-03 |
| 0.0125 | 9.899E-03 |
| 0.0152 | 1.081E-02 |
| 0.0182 | 1.171E-02 |
| 0.0216 | 1.262E-02 |
| 0.0255 | 1.353E-02 |
| 0.0300 | 1.444E-02 |
| 0.0350 | 1.538E-02 |
| 0.0407 | 1.631E-02 |
| 0.0469 | 1.726E-02 |
| 0.0541 | 1.824E-02 |
| 0.0617 | 1.923E-02 |
| 0.0701 | 2.026E-02 |
| 0.0800 | 2.133E-02 |
| 0.0910 | 2.246E-02 |
| 0.1027 | 2.362E-02 |
| 0.1162 | 2.485E-02 |
| 0.1312 | 2.613E-02 |
| 0.1475 | 2.745E-02 |
| 0.1667 | 2.883E-02 |
| 0.1900 | 3.025E-02 |
| 0.2400 | 3.249E-02 |
| 0.2900 | 3.381E-02 |
| 0.3500 | 3.479E-02 |
| 0.4100 | 3.552E-02 |
| 0.4800 | 3.546E-02 |
| 0.5400 | 3.447E-02 |
| 0.5900 | 3.298E-02 |
| 0.6400 | 3.092E-02 |
| 0.7000 | 2.787E-02 |
| 0.7600 | 2.431E-02 |
| 0.8300 | 1.902E-02 |
| 0.9100 | 8.919E-03 |
| 0.9700 | 1.533E-03 |
| 1.0000 | -1.604E-03 |

Lower surface
Number of points = 43

| | |
|---|---|
| 0.0000 | 0.000E+00 |
| 0.0020 | -4.295E-03 |
| 0.0050 | -6.380E-03 |
| 0.0100 | -8.857E-03 |
| 0.0200 | -1.212E-02 |
| 0.0300 | -1.427E-02 |
| 0.0400 | -1.592E-02 |
| 0.0500 | -1.728E-02 |
| 0.0600 | -1.842E-02 |
| 0.0700 | -1.936E-02 |
| 0.0900 | -2.103E-02 |
| 0.1000 | -2.175E-02 |
| 0.1200 | -2.298E-02 |
| 0.1400 | -2.399E-02 |
| 0.1700 | -2.519E-02 |
| 0.2000 | -2.607E-02 |
| 0.2400 | -2.685E-02 |
| 0.2800 | -2.729E-02 |
| 0.3300 | -2.745E-02 |
| 0.3700 | -2.729E-02 |
| 0.4100 | -2.684E-02 |
| 0.4400 | -2.626E-02 |
| 0.4800 | -2.514E-02 |
| 0.5200 | -2.366E-02 |
| 0.5600 | -2.175E-02 |
| 0.6000 | -1.940E-02 |
| 0.6400 | -1.696E-02 |
| 0.6900 | -1.331E-02 |
| 0.7400 | -9.614E-03 |
| 0.7900 | -5.916E-03 |
| 0.8400 | -2.726E-03 |
| 0.8700 | -1.105E-03 |
| 0.8900 | -2.317E-04 |
| 0.9100 | 4.455E-04 |
| 0.9200 | 6.861E-04 |
| 0.9300 | 8.286E-04 |
| 0.9400 | 8.643E-04 |
| 0.9500 | 8.019E-04 |
| 0.9600 | 6.415E-04 |
| 0.9700 | 3.831E-04 |
| 0.9800 | -8.019E-05 |
| 0.9900 | -7.395E-04 |
| 1.0000 | -1.604E-03 |

## 13.4. *Parker t-75: Airfoil for wing tip span station*

Upper surface
Number of point = 45

| | |
|---|---|
| 0.0000 | 0.000E+00 |
| 0.0001 | 1.089E-03 |
| 0.0003 | 2.177E-03 |
| 0.0007 | 3.266E-03 |
| 0.0013 | 4.355E-03 |
| 0.0022 | 5.444E-03 |
| 0.0034 | 6.532E-03 |
| 0.0048 | 7.621E-03 |
| 0.0064 | 8.710E-03 |
| 0.0082 | 9.798E-03 |
| 0.0102 | 1.089E-02 |
| 0.0125 | 1.198E-02 |
| 0.0152 | 1.308E-02 |
| 0.0182 | 1.416E-02 |
| 0.0216 | 1.526E-02 |
| 0.0255 | 1.637E-02 |
| 0.0300 | 1.747E-02 |
| 0.0350 | 1.861E-02 |
| 0.0407 | 1.974E-02 |
| 0.0469 | 2.088E-02 |
| 0.0541 | 2.207E-02 |
| 0.0617 | 2.326E-02 |
| 0.0701 | 2.451E-02 |
| 0.0800 | 2.581E-02 |
| 0.0910 | 2.717E-02 |
| 0.1027 | 2.858E-02 |
| 0.1162 | 3.006E-02 |
| 0.1312 | 3.162E-02 |
| 0.1475 | 3.321E-02 |
| 0.1667 | 3.488E-02 |
| 0.1900 | 3.660E-02 |
| 0.2400 | 3.930E-02 |
| 0.2900 | 4.091E-02 |
| 0.3500 | 4.209E-02 |
| 0.4100 | 4.298E-02 |
| 0.4800 | 4.290E-02 |
| 0.5400 | 4.171E-02 |
| 0.5900 | 3.989E-02 |
| 0.6400 | 3.740E-02 |
| 0.7000 | 3.372E-02 |
| 0.7600 | 2.941E-02 |
| 0.8300 | 2.301E-02 |
| 0.9100 | 1.079E-02 |
| 0.9700 | 1.854E-03 |
| 1.0000 | -1.940E-03 |

Lower surface
Number of points = 43

| | |
|---|---|
| 0.0000 | 0.000E+00 |
| 0.0020 | -5.196E-03 |
| 0.0050 | -7.718E-03 |
| 0.0100 | -1.071E-02 |
| 0.0200 | -1.466E-02 |
| 0.0300 | -1.727E-02 |
| 0.0400 | -1.926E-02 |
| 0.0500 | -2.090E-02 |
| 0.0600 | -2.228E-02 |
| 0.0700 | -2.342E-02 |
| 0.0900 | -2.544E-02 |
| 0.1000 | -2.631E-02 |
| 0.1200 | -2.780E-02 |
| 0.1400 | -2.902E-02 |
| 0.1700 | -3.047E-02 |
| 0.2000 | -3.154E-02 |
| 0.2400 | -3.249E-02 |
| 0.2800 | -3.302E-02 |
| 0.3300 | -3.321E-02 |
| 0.3700 | -3.302E-02 |
| 0.4100 | -3.247E-02 |
| 0.4400 | -3.177E-02 |
| 0.4800 | -3.042E-02 |
| 0.5200 | -2.862E-02 |
| 0.5600 | -2.631E-02 |
| 0.6000 | -2.347E-02 |
| 0.6400 | -2.051E-02 |
| 0.6900 | -1.610E-02 |
| 0.7400 | -1.163E-02 |
| 0.7900 | -7.157E-03 |
| 0.8400 | -3.298E-03 |
| 0.8700 | -1.337E-03 |
| 0.8900 | -2.803E-04 |
| 0.9100 | 5.390E-04 |
| 0.9200 | 8.300E-04 |
| 0.9300 | 1.002E-03 |
| 0.9400 | 1.046E-03 |
| 0.9500 | 9.701E-04 |
| 0.9600 | 7.761E-04 |
| 0.9700 | 4.635E-04 |
| 0.9800 | -9.701E-05 |
| 0.9900 | -8.947E-04 |
| 1.0000 | -1.940E-03 |

# 14. Appendix D : Documentation for the 'Bump' program

This subroutine illustrates a means of making smooth changes to airfoil shapes. It is included in PANELv2. It is designed to place a "bump" on the airfoil contour. The shape change starts gradually with zero curvature at point $x_{b_1}$. The bump is setup to be asymmetric about the bump midpoint, $x_{b_2}$, and to blend back into the baseline shape with zero curvature at point $x_{b_3}$. However, if an asymmetric bump is used, the curvature will be discontinuous at the bump maximum. The following plot defines the nomenclature, as well as plotting the output of the sample main program presented below.

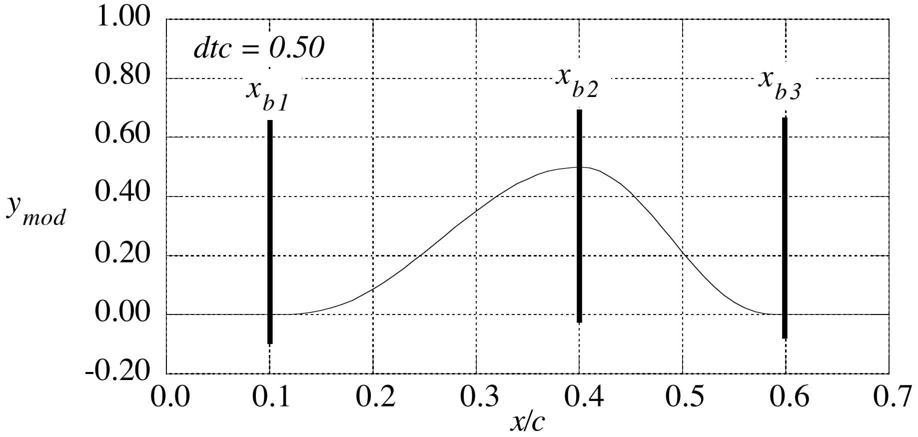

The related slope and curvature are given in the next graph.

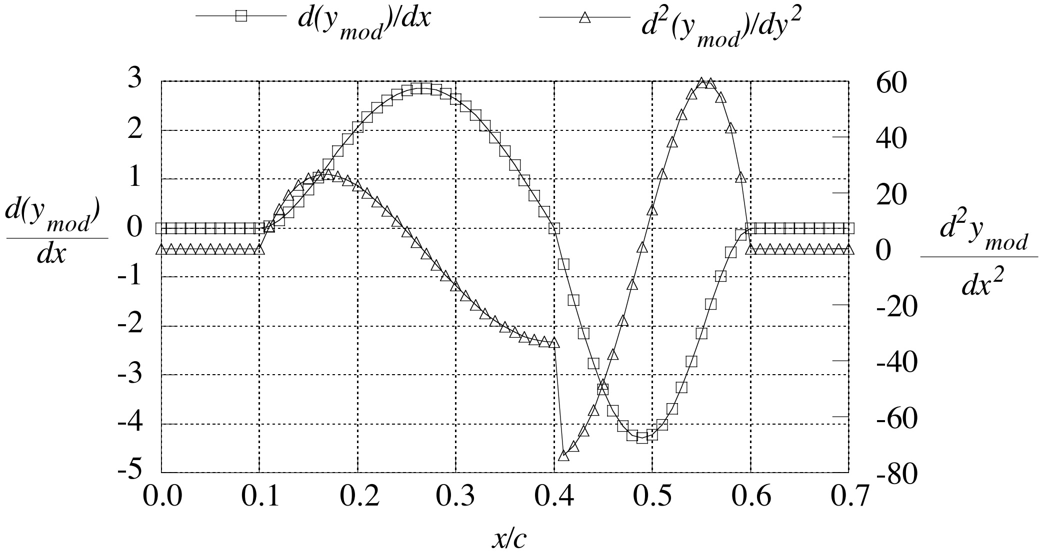

The equation of the bump is:

$$y_{mod} = -64\left(\Delta\frac{t}{c}\right)x_d^3\left(x_d - 1\right)^3$$

$$\frac{d\,y_{mod}}{dx_d} = -64\left(\Delta\frac{t}{c}\right)3x_d^2\left(x_d - 1\right)^2\left(2x_d - 1\right)$$

$$\frac{d^2\,y_{mod}}{dx_d^2} = -64\left(\Delta\frac{t}{c}\right)6x_d\left(x_d - 1\right)\left(5x_d^2 - 5x_d + 1\right)$$

where

$$x_d = \frac{\left(x - x_1\right)}{2\left(x_2 - x_1\right)} \qquad x_1 < x < x_2$$

or

$$x_d = \frac{\left(x + x_3 - 2x_2\right)}{2\left(x_3 - x_2\right)} \qquad x_2 < x < x_3$$

This function is often called a “cubic bump” although it is clearly a sixth order polynomial. The user should examine the subroutine to understand the transformation between the local variable $x_d$ and the global variable $x_{in}$.